Universidad de Valparaíso
Facultad de Ciencias
Instituto de Física y Astronomía

SEARCHING FOR GAS IN DEBRIS DISKS

by

Daniela Paz Iglesias Vallejo

Thesis submitted to the Faculty of Science
of Universidad de Valparaíso, as one of the requirements
to qualify for the academic Ph.D. degree in Astrophysics.

Supervisors	:	Dr. Amelia Bayo (UV, Chile)
		Dr. Johan Olofsson (UV, Chile)
		Dr. Zahed Wahhaj (UV, Chile)
Committee	:	Dr. Amelia Bayo (UV, Chile)
		Dr. Lucas Cieza (UDP, Chile)
		Dr. Johan Olofsson (UV, Chile)
		Dr. Zahed Wahhaj (ESO, Chile)

April, 2020
Valparaíso, Chile

Dedicada a mi esposo Renaud

Abstract

A debris disk is commonly described as a second generation circumstellar disk composed of dust grains, planetesimals and possibly already formed giant planets. It was long thought that debris disks were systems fully depleted of gas, but in the last few years the presence of gas has been detected in a increasing number of them. The nature of this gas is still under debate; it may be residual gas (leftover from earlier stages of the disk) or second generation gas (generated by the sublimation of exocomets or collisions of icy bodies), however, both possibilities would have great implications in the process of planet formation and evolution. An efficient way to search for this gas in debris disks is monitoring gas tracers using multi-epoch high-resolution UV-optical spectroscopy. A detection of gas in the line of sight of the star shows up as a very narrow absorption feature superposed to the photospheric absorption of lines such as Ca II or Na I, which are very sensitive gas tracers. This Thesis is devoted to the search for gas via high-resolution spectroscopy in a sample of 301 debris disks with the purpose of estimating the frequency of gas in debris disks. We collected high-resolution UV-optical spectroscopic data from our own observations and the ESO archive for 273 objects, completing 91% of our sample. We analysed the multi-epoch spectra of each object searching for variable and stable non-photospheric absorption features of circumstellar origin. Firstly, we performed a detailed analysis of a sub-sample of 27 objects having multiple stable absorption features with the aim of determining whether their features were of circumstellar or interstellar origin. In this group we found two objects; c Aql and HR 4796, with variable absorption features attributable to the presence of star-grazing exocomets, and one object; HD 110058 with a stable circumstellar gas absorption. We concluded from these preliminary results that the presence of gas in debris disks might be a common phenomenon. Secondly, we studied the presence of unusually large non-photospheric absorption features found in several ionized lines of the object HD 37306, that lasted for several days. After analysing different possibilities we concluded that the most likely explanation might be an exocometary break-up releasing a stream of gas that remained in orbit for at least a week around the star. Then, we analyzed the variability found in the Ca II K lines of 97 objects with the purpose of distinguishing variable absorption features most likely produced by exocometary activity from variability of a different nature, like stellar pulsations, spots or radial velocity shifts, for instance. We found five candidates with variability consistent with exocometary activity: c Aql, 49 Cet, gam Tri, HR 4796 and HD 37306, two of them with no previous reports of exocomets besides this work. Finally, we studied a sub-sample of 107 objects presenting stable non-photospheric features in their Ca II K lines within our updated database of observations in addition to those in our first sub-sample of analysis. Similarly, the absorption features observed in these objects were analysed in order to determine whether they were of circumstellar or interstellar origin. We confirmed an interstellar origin for the features in 104 of these objects, one of them, 49 Cet having a blended feature of combined circumstellar and interstellar origin. In addition, we found three candidates with features of yet inconclusive origin that might be circumstellar but need further study to confirm it. Putting together our results, we found six debris disks with presence of circumstellar gas, five of them presenting variable absorption features attributable to exocometary activity and one of them with a stable circumstellar gas component. Considering that our sample is unbiased with respect to inclination, that the gas is more likely to be detected when the disk is observed close to edge-on, more easily detected in the spectra of early-type stars, the many detection challenges related to the sporadical nature of exocometary transits, and the interlopers of gas detection, then the evidence of circumstellar gas is significant. Taking into account the currently increasing number of detections, this imply the possibility that most debris disks may harbor some gas, challenging the current paradigm of debris disks.

Citations to previously published work

Iglesias, D., Bayo, A., Olofsson, J., Wahhaj, Z., Eiroa, C., Montesinos, B., Rebollido, I., Smoker, J., Sbordone, L., Schreiber, M. R., and Henning, T. (2018). "Debris discs with multiple absorption features in metallic lines: circumstellar or interstellar origin?". Monthly Notices of the Royal Astronomical Society, 480(1):488–520.

Iglesias, D. P., Olofsson, J., Bayo, A., Zieba, S., Montesinos, M., Smoker, J., Kennedy, G. M., Godoy, N., Pantoja, B., Talens, G. J., Wahhaj, Z., and Zamora, C. (2019). "An unusually large gaseous transit in a debris disc". Monthly Notices of the Royal Astronomical Society, 490(4):5218–5227.

Ackowledgments

I wish to thank all the people who contributed to the completion of this project. First and foremost, I would like to thank my academic supervisor, Dr. Amelia Bayo for her constant support throughout my PhD, her honest feedback, her guidance and her teaching, my co-supervisor, Dr. Johan Olofsson for his advice and feedback, his significant help and contribution to this work, and my co-supervisor at ESO, Dr. Zahed Wahhaj, for his encouragement, his support and his much appreciated advice. I also thank Dr. Lucas Cieza, for being part of the committee of my Thesis project and my PhD defense, I appreciate his good disposition. I want to thank all my collaborators, in particular, to Dr. Jonathan Smoker for his substantial help, feedback and support, Dr. Benjamín Montesinos, Dr. Carlos Eiroa and Dr. Isabel Rebollido, their collaboration was important for the development of this work, and Dr. Matías Montesinos, Sebastian Zieba and Dr. Grant Kennedy, for their contribution to this research. I also want to thank the professors of my institution, Universidad de Valparaíso for their teaching, the skills I learned from them were useful for the development of this research. I would like to show my gratitude also to all the nice people I met at ESO, where I developed part of this Thesis, I particularly thank Dr. Alain Smette for his help, Dr. Lucas Sbordone for his feedback and Dr. Claudio Melo for his advice. I would like to thank the postgraduate students (including former students) and postdocs at UV for their partnership, their friendship, the exchange of tips and assistance, specially to my office mates for their daily companion (and for putting up with my bad mood). These latter thanks also include my office mates at ESO, their friendship and help is very much appreciated. I also wish to include in these acknowledgements the staff working at La Silla, Las Campanas and Paranal for their assistance during the observing runs that provided me with valuable data for this project, special thanks to Dr. Iván Lacerna for his support. I would like to acknowledge too the financial support from Universidad de Valparaíso, the MPTG, and ESO and support from ICM via Núcleo Milenio de Formación Planetaria. And last but not least, I want to thank my parents and close friends for their care and concern, and a very special thanks to my husband for his daily love, patience, help, constant support and encouragement.

On a side note, given the global context at the moment of submitting this Thesis, I take the opportunity to send out my warm regards to all you fellow astronomers and express my sincere condolences to those of you who have lost a beloved one due to the COVID-19.

“Llegará una época en la que una investigación diligente y prolongada sacará a la luz cosas que hoy están ocultas. La vida de una sola persona, aunque estuviera toda ella dedicada al cielo, sería insuficiente para investigar una materia tan vasta... Por lo tanto este conocimiento sólo se podrá desarrollar a lo largo de sucesivas edades. Llegará una época en la que nuestros descendientes se asombrarán de que ignoráramos cosas que para ellos son tan claras... Muchos son los descubrimientos reservados para las épocas futuras, cuando se haya borrado el recuerdo de nosotros. Nuestro universo sería una cosa muy limitada si no ofreciera a cada época algo que investigar... La naturaleza no revela sus misterios de una vez para siempre”

— LUCIO ANNEO SÉNECA, Cuestiones naturales, libro 7, siglo primero

Preface

I imagine that during thousands of years most human beings have stared at the night sky and appreciated its beauty. Centuries ago, we did not know that those beautiful bright dots in the sky were stars similar to our Sun, we did not know that some of those dots were actually planets, we did not know that we were part of a galaxy and that there were many more galaxies far, far away. Today, we know these things, however, this knowledge makes us realize that there are much more things that we do not know.

I also imagine many of us have wondered about our existence; how did we get here? how did "the beginning of all" happen? We are naturally curious about our surrounding Universe and about ourselves being part of it. We want to know how things work, what things are made of, what is their purpose, why are they like that. These questions have motivated many of us to investigate and transfer our knowledge from generation to generation since thousands of years. Astronomers in particular, we want to investigate things far beyond our planet in order to better understand our own tiny world and its role in the Universe. Myself, as many of you, want to understand the origin of life and find out whether it exists somewhere else outside of this small rock called Earth. This is my motivation to go towards the research of planetary systems. I want to understand how they formed and evolved, and what are all the parameters that, combined in the right way, might favour the origin of life. The research presented in this Thesis is meant to help us know a little bit more about the building blocks of planetary systems and about part of their evolutionary process; the debris disk stage.

Contents

Chapter 1

Introduction

There is a long and complex evolutionary process from the moment that a star is born until it becomes a planetary system. This whole process is not yet well understood to date and many researchers around the world are working with theoretical simulations and observations trying to understand at least part of this process. With the research presented in this Thesis, we want to contribute to the understanding of debris disks, the late stage of planet formation. Not so long ago, these disks were thought as gas free disks, composed only by dust and rocks of different sizes. During the last decade, this paradigm has changed considerably by the increasing number of discoveries of gaseous debris disks. In the present work, we aim to understand how frequent this phenomenon is. Are all debris disks gaseous in the end? Or are these only rare, exceptional cases? Do gaseous debris disks share some particular characteristics? These are questions that we will try to answer in the following Chapters.

1.1 Debris Disks

Circumstellar disks are the natural consequences of the star formation process. The formation of a star starts with the gravitational collapse of a molecular core. The conservation of angular momentum triggers the quick formation of a rotating disk around the star called a "protoplanetary disk". These disks of gas and dust rapidly evolve, flattening and extending their outer radii to tens or even hundreds of AU around the star (Williams and Cieza, 2011). Planets are believed to form in protoplanetary disks. The mass of these disks is thought to be initially composed of 99% gas and 1% dust (interstellar-like ratios, Bohlin et al. 1978; but see, among others, Williams and Best 2014). After a few Myrs (e.g. Hernández et al. 2007 and Fedele et al. 2010) these protoplanetary disks evolve from optically thick gas-rich systems into transition disks, and later, at a stellar age of about 10 Myrs, they are transformed into a collection of rocks, dust, planetesimals and maybe gaseous giant planets known as debris disks (see Fig. 1.1 for a schematic picture and description of a circumstellar disk evolution). At this stage, the disk is supposed to be fully depleted of gas due to gas removal processes such as photoevaporation, accretion and radiation pressure (e.g. Pontoppidan et al. 2014 and Alexander et al. 2006 for reviews on volatiles and photoevaporation in protoplanetary disks, respectively). Therefore, the current paradigm is that the majority of debris disks do not harbour gas and contain very little second generation dust produced by collisions among planetesimals; gas giants would have to form during the earlier gaseous stage of the disk; and rocky planets can form or continue to grow later during the gas-poor phase of the disk (Wyatt, 2008).

As mentioned, the study of debris disks help us understand planet formation, in particular, the formation and evolution of rocky planets. By studying how planets form in other systems we can better understand the formation of our own planetary system. The Solar System is an evolved planetary system of $\sim$4.5 Gyrs (Bouvier and Wadhwa, 2010) and still possess a debris disk composed by the Kuiper belt, asteroid belts and Zodiacal dust. However, the Solar System's debris disk is less massive and less collisionally active than other observed debris disks, and therefore it would be impossible to detect with the current instrumentation from the distance of any other star with a known debris disk (Wyatt 2020, Kral et al. 2017a).

In this section we will shortly review some aspects of debris disks, such as their evolution, structure, composition and their observation in order to set the context for the next section, in which we discuss the presence of gas in debris disks.

1.1.1 Evolution: From Protoplanetary Disks to Debris Disks

It is argued that the physical distinction between protoplanetary disks and debris disks relies mainly on the presence of primordial gas in sufficient quantity to dominate the motion of small dust grains, rather than on the primary or secondary nature of the dust, or on the stirring levels of the disk (Wyatt et al., 2015). The opening of a gap in the inner regions of protoplanetary disks

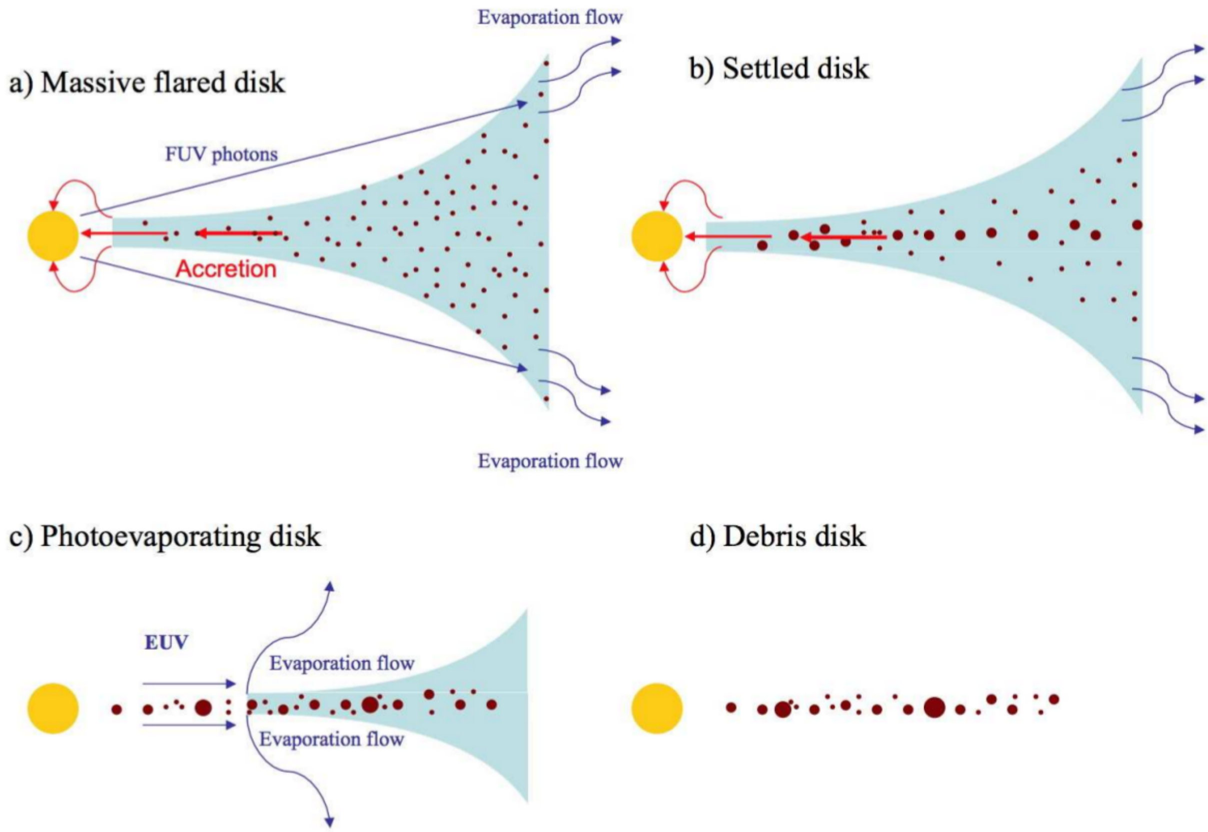

Figure 1.1: Figure 6 and caption from Williams and Cieza (2011): "The evolution of a typical disk. The gas distribution is shown in blue and the dust in brown. (a) Early in its evolution, the disk loses mass through accretion onto the star and FUV photoevaporation of the outer disk. (b) At the same time, grains grow into larger bodies that settle to the mid-plane of the disk. (c) As the disk mass and accretion rate decrease, EUV-induced photoevaporation becomes important, the outer disk is no longer able to resupply the inner disk with material, and the inner disk drains on a viscous timescale ($\sim 10^5$ yr). An inner hole is formed, accretion onto the star ceases, and the disk quickly dissipates from the inside out. (d) Once the remaining gas photoevaporates, the small grains are removed by radiation pressure and Poynting-Robertson drag. Only large grains, planetesimals, and/or planets are left. This debris disk is very low mass and is not always detectable."

would be the first observable step in the evolution from a continuous primordial disk towards a more radially concentrated disk, and can be triggered by processes such as photoevaporation or planet formation. The following steps in the evolution of the disk are not well constrained, particularly with respect to the timescales on which gas and dust should disappear. Wyatt et al. (2015) identified five key steps in the evolution from protoplanetary to debris disks, which we will summarize below. It is worth noting that since there are aspects of the evolution that may depend on the stellar mass, the following description will focus mainly on the evolution of intermediate mass stars, i.e. A-type stars, which comprise the majority of the stars in our sample of study, as can be seen in Fig. 1.11. This division of the evolutionary stages is meant to help our understanding of each transition, but does not claim that the order of the evolution is uniquely determined, indeed we expect the evolution to be rather chaotic and different for each system.

Transition disk

The carving of an inner hole in a protoplanetary disk transforms it into a “transition disk”. However, nowadays this definition of a transition disk has certain caveats. Transition disks were initially discovered by the lack of warm dust in their spectral energy distribution (SED), but recent studies have shown that gaps and substructures are ubiquitous in circumstellar disks and, in some cases, no cavities are detected in disks that were classified as transition disks according to their SED (e.g. Huang et al. 2018, Facchini et al. 2019). Nevertheless, following the traditional definition of transition disk, the presence of this inner gap can be observed in their SED and in high resolution imaging. The mechanism responsible of carving this gap or hole is still under debate. A planet (or multiple planets) might be able to sculpt a gap in the disk while keeping the same accretion levels observed in some transition disks (Williams and Cieza 2011, Zhu et al. 2012). However, given that only few stars are found to have giant planets at large distances they do not provide a good explanation for clearing in all the transition disks, specially for those with larger gaps. On the other hand, photoevaporation is expected to produce a hole in the disk (e.g. Alexander and Armitage 2007), but it is not the best explanation for the most massive transition disks as photoevaporation operates after depletion of disk mass and is not in good agreement with accreting transition disks. Probably a more realistic scenario might include both processes;

for instance, planet-induced clearing very close to the star could trigger photoevaporation that further opens the gap thus there is no need to have planets close to the outer edge of the gap.

Depletion of millimetre-sized dust in the outer disk

The most straightforward difference that can be observed between protoplanetary and debris disks is the excess emission between infrared and millimetre wavelengths. Signs of grain growth to millimetre sizes is observed at early stages of protoplanetary disks and most of the dust mass in the disk remain within this grain size range as it evolves (Wyatt et al., 2015). There is a clear division at $\sim$10 Myr between younger protoplanetary disks having > 1 $M_{\oplus}$ of dust and older debris disks having < 1 $M_{\oplus}$ of dust (Panić et al., 2013). We must remind though, that we should not generalize and that there are uncertainties on the nature of the stages, for instance, there are some optical depth effects like self-obscuration that must be taken into account (e.g. Galván-Madrid et al. 2018) and several mechanisms competing. Radial drift would remove grains quickly when there is still enough gas, but at the same time, we know that planetesimals must be forming, so a significant fraction of the mm-sized grains must be incorporated in them, and therefore most of their mass is "locked down" in those larger bodies that we cannot detect, thus we cannot know the true total mass of the disks.

The reduction of mm-sized grains must occur rather fast, as their mass do not show evidence of changing throughout the protoplanetary disk stage (Carpenter et al., 2014). The ending of these grains is undetermined and several possibilities have been discussed. One of them suggests that, since these grains represent a significant fraction of the solid mass in the protoplanetary disk, and thus they cannot be dragged away by photoevaporation, and Poynting-Robertson drag would take much longer than 10 Myr to deplete them, then their reduction must be achieved through collisions. If these dust grains are grinded down through destructive collisions, then the smaller grains can be removed by other mechanisms, such as radiation pressure or coupling to the photoevaporative wind. A different outcome could be these grains to end up (again through collisions) in larger bodies, either accreting onto already formed planetesimals or planets, or growing into planetesimals. This latter assumption implies masses of solid material in the debris disks comparable to those present in the protoplanetary disk. Either way, this leave us with two potential sources for dust in debris disks: pre-existing planetesimals that accreted grains during this stage, and the dust resulting from the destruction of whatever structure those mm-sized grains may have formed.

Evolution of hot dust in inner regions

Some debris disks have been observed to have hot dust, at a temperature that locates it at a few au from the star (e.g. Smith et al. 2009, Smith et al. 2012). However, the origin of this hot component is unclear; it is questioned whether they are asteroid belt analogues, sublimation of comets scattered in from outer regions, or evidence for the ongoing formation of rocky planets. Systems with ages over 100 Myrs having both cold and hot dust give an indication that the hot dust in some of these systems may have a cometary origin (Kennedy and Wyatt, 2014), since the outer belts provide a suitably enduring source population.

High levels of hot dust is a phenomenon observed mainly in young ($\ll$ 100 Myr) stars (Kennedy and Wyatt, 2013). This is in agreement with an asteroid belt and with a planet formation scenario, since fast collisional evolution close to the star means that asteroid belts quickly becomes undetectable (Wyatt et al., 2007) and provides an explanation for the ultimate ending of planet formation processes. The formation of rocky planets is an interesting argument for the origin of the hot dust because models of such processes that are successful at reproducing the Solar System's terrestrial planets predict that hot dust should be easily detectable at the current age of the Solar System.

Disappearance of gas

This is arguably one of the most puzzling stages in the evolution from protoplanetary to debris disk. In first place, it is very difficult to measure the total amount of gas present either in protoplanetary disks or in debris disks. Gas detections, either in emission or absorption, can only trace a minor fraction of the total gas mass (Thi et al. 2001b, Carmona et al. 2011). Gas emission detections in protoplanetary disks provide a poor measurement of the total gas mass because of the gas being optically thick. In the case of debris disks, although they are in general optically thinner than protoplanetary disks, since CO is the main gas tracer, there is a large uncertainty in its mass given that CO freezes out onto dust grains in the outer regions of the disk and thus remains undetectable. Gas detected in absorption is limited by the fact that it can only trace the gas that is crossing the line of sight of the star. It has been shown that, in general, there seems to be a transition at ∼10 Myrs where the primordial gas disappears and the second generation gas starts to appear (Wyatt et al., 2015). However, there are several counterexamples that contradict this age limit. Although the origin of the gas detected in debris disks is debated, secondary gas is thought to be chemically different from primordial gas, as it is released from ices that reside in dust and planetesimals (e.g. Zuckerman and Song 2012) and thus it should be likely dominated by CO and water instead of H_2, the main component of primordial gas. Another indication of the possible origin of the gas is its spatial distribution. When the gas is observed to match the distribution of the dust it is assumed to be second generation as CO is expected to be short-lived due to photo-dissociation and thus it must be constantly replenished by planetesimals collisions or sublimation of exocomets (e.g. the case of β Pic; Dent et al. 2014, Telesco et al. 2005). A different case is observed, for instance, in HD 21997, where the observations show that CO is not co-located with the dust, but it rather extends towards the inner regions very close to the star (Kóspál et al. 2013, Moór et al. 2013), suggesting it cannot be produced by collisions of planetesimals thus it must be primordial. This raises the question of how this gas can persist in the disk at an age of ∼30 Myr.

Formation of ring-like planetesimal structures

The concentration of planetesimals into a narrow ring (or several narrow rings) is the most common outcome of the evolution (instead of a broad disk). This general condition of debris disks being narrow (with a fractional radial width of $\Delta r/r \approx$10%) does not imply that broad disks (of $\Delta r/r >$1) do not exist (Wyatt et al., 2015). Besides, it is possible that the μm-sized dust may be confined in a narrow ring while the planetesimals from which the dust is produced are distributed in a broader disk. In this case, the dust production may happen either in a narrowly confined region, or throughout the whole disk but the smallest dust particles are being dragged by residual gas into a narrow region (Kenyon and Bromley 2002, Takeuchi and Artymowicz 2001, Lyra and Kuchner 2013). The timing and mechanism of the concentration of planetesimals into narrow rings remains unclear. There is the possibility that this structure was defined early during the protoplanetary disk stage. If so, the few observed broader disks may be the result of a strong interaction with planets (Beust et al. 2014, Pearce and Wyatt 2014, Wyatt 2006).

Alternatively, it is also possible that these planetesimals got confined into rings during dispersal of the protoplanetary disk. It may be that the presence of planets could induce the concentration of planetesimals into a narrow radial distribution, especially if there were planets at both the inner and outer edges of the planetesimal belt (Rodigas et al., 2014). However, new studies suggest that scattered light observations show narrower structures likely due to a sensitivity effect, where observations are more sensitive to detect higher surface-brigtness regions and thus the contrast enhances the narrow ring, and possibly post-processing methods also contribute to sharpen the structures (Hughes et al., 2018).

1.1.2 Structure and Composition of Debris Disks

Recent advances in imaging techniques have revealed previously unknown details of debris disks structure and have provided us with a multi-wavelength picture that allows us to connect the morphology to the physical processes that shape the disk structure. In this section, we summarize the properties of spatially resolved structure in Kuiper belt analogues. The diversity of the structure can be divided into the following categories, described below.

Radial Structure

Debris disks, in general, could be characterized as an assembly of circumstellar rings. These rings can be broad or narrow, some systems may have multiple rings while others may have a very broad ring (or disk) with gaps in between (see Fig. 1.2 for examples of different radial structures). The extrasolar Kuiper belts that have been resolved so far contain far more dust than the Solar System's belt and they are also much younger. In fact, the dust in our Solar System's Kuiper belt remains undetectable from Earth with current technology (only Kuiper belt objects have been detected). However, the radial extent of these debris disks is comparable to our Solar System's, which has an inner radius of 40 au and a width of $\sim$10 au (Barucci et al. 2008, Poppe et al. 2019).

There seem to be no strong correlation between disk radius or disk width and the spectral type of the host star. Also dust temperatures seem to be constant across all spectral types (e.g. Morales et al. 2011). However, the maximum radial extent of debris disks shows some trends with stellar luminosity; the more luminous the star the more extended its debris disk, although

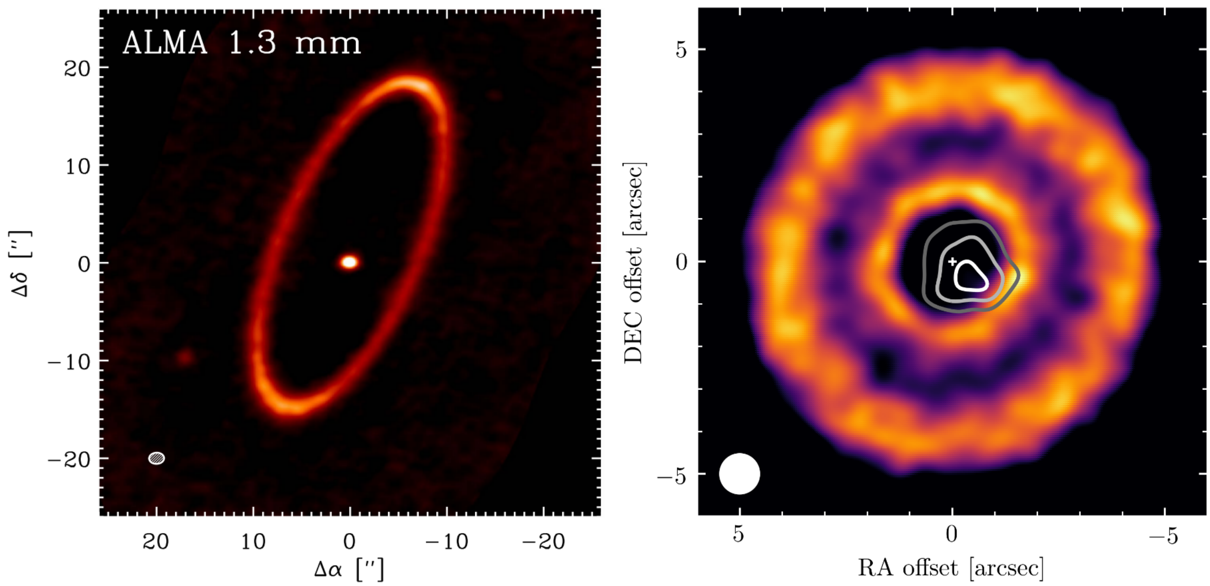

Figure 1.2: Examples of debris disks with different radial structure. **Left:** Example of a narrow ring structure: Fomalhaut. Figure 1 from MacGregor et al. (2017), ALMA image of the 1.3 mm continuum emission from Fomalhaut. **Right:** Example of a broad disk with gaps: HD 107146. Figure 9 from Marino et al. (2018). ALMA image at 1.1 mm (band 6).

in most cases the larger outer radii is composed of a "halo" of smaller grains blown away by radiation pressure or the stellar wind. Although these extended halos are more common for debris disks around A-type stars, they can also be found in less luminous stars, like, for instance, AU Mic, a debris disk surrounding an M star which presents a halo reaching hundreds of au (Kalas et al., 2004). A model that would explain this configuration was proposed by Strubbe and Chiang (2006): a "birth ring" of planetesimals start a collisional cascade and the resulting smallest grains are blown out by radiation pressure or stellar winds into an extended halo. Some disks have been observed to have dust halos inside the parent ring, which might be the result of grains spiriling inwards due to Poynting-Robertson drag (Löhne et al. 2012, Schüppler et al. 2016, Ren et al. 2018).

Narrow rings structures (with $\Delta r/r \lesssim 0.5$, halos aside) are quite common among debris disks (e.g. Fomalhaut: Kalas et al. 2005, HR 4796A: Perrin et al. 2015 and HD 181327: Schneider et al. 2014). But there are also some examples of radially broad debris disks (e.g. the cases of 49 Ceti: Hughes et al. 2017, HD 107146: Ricci et al. 2015 and AU Mic: MacGregor et al. 2013). What makes a debris disk narrow or broad is still unclear, as discussed in the previous section.

We must also take into account the presence of warps in debris disks. The best example of this is the disk surrounding β Pic, which showed a clear warp in the inner region that seemed to point towards the planet β Pic b (Mouillet et al. 1997, Heap et al. 2000, Golimowski et al. 2006, Lagrange et al. 2009). Similar warps have also been observed in the disks around AU Mic (Wang et al. 2015, Wisniewski et al. 2019) and HD 110058 (Kasper et al., 2015). Models suggest that multiple planets or other mechanisms would be necessary to maintain warped structures in the disk (e.g. Lee and Chiang 2016, and references therein). Another kind of characteristic observed in some debris disks that shares both radial structure and departures from axisymmetry are spiral arms. For instance, the debris disks surrounding TWA 7 was observed to present a spiral arm, possibly explained by the presence of an undetected planet (Olofsson et al., 2018).

Azimutal Structure

The azimutal structure (or departures from axisymmetry) is particularly interesting because something beyond the star-debris disk system is required in order to break the axisymmetry (see Fig. 1.3 for examples). There are several theories about what might cause these breaks; it might be gravitational disruptions by a planet, or a companion, or a stellar flyby, interactions with the interstellar medium, instabilities due to gas and dust interactions, or collisions of planetesimals. There are several categories of azimutal structure in debris disks:

a) Eccentricity: Most narrow debris disks have been found to present an eccentric structure which implies an offset from the central position of the star. Eccentricities have been observed to range between ∼0.06 and ∼0.2 (Hughes et al. 2018 and references therein). An eccentric distribution of the dust around the star translate into the grains having different temperatures: hotter towards the pericenter (the closest point to the star) and colder towards the apocenter (the most distant point). Therefore, the disks may exhibit different flux distributions when observed at different wavelengths: mid- to far-infrared observations can show a "pericenter glow", while observations in the submillimiter can result in an "apocenter glow" (e.g. Wyatt et al. 1999, Wyatt 2005). This characteristic can help us understand the grain size density distribution in the disk as different grain sizes behave differently in scattered light and thermal emission observations. The origin of eccentricity in debris disks is not yet clear. The proposed mechanisms must break

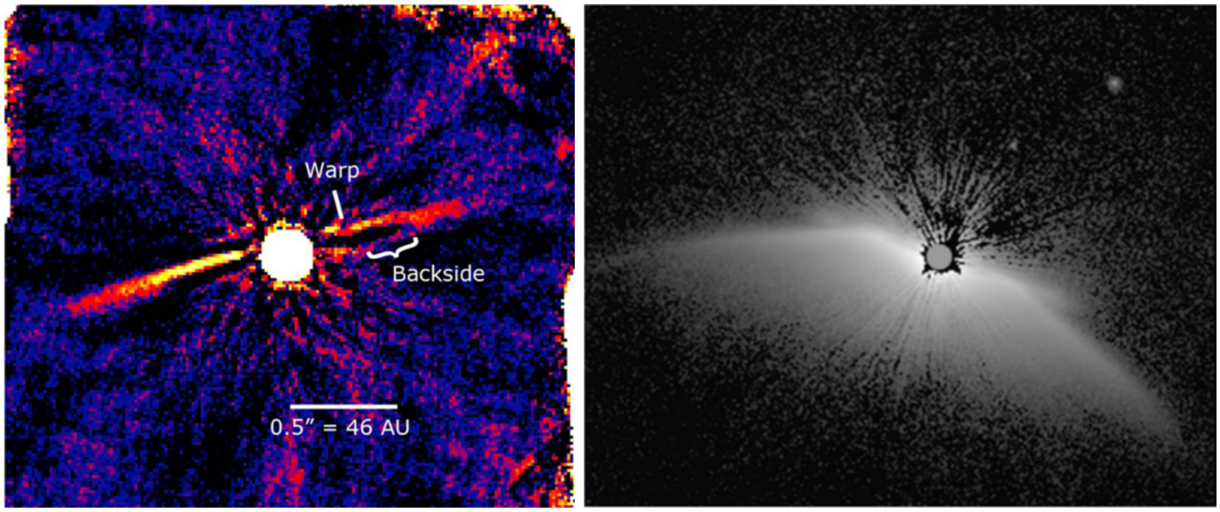

Figure 1.3: Examples of debris disks with different azimutal structure. **Left:** Example of an asymmetric debris disk: HD 106906. Figure 1 from Kalas et al. (2015), GPI H-band ADI image of HD 106906. **Right:** Example of a debris disks with swept-back wings: HD 61005. Figure 7 from Schneider et al. (2014). STIS scattered light image of HD 61005.

the intrinsic symmetry of the disk, e.g. eccentric planets, interactions between gas and dust and giant collisions of planetesimals.

b) Swept-back Wings: Asymmetric swept-back features are also observed in dust rings. The best example is the system HD 61005, also called "The Moth" because of the look of its swept-back "wings" as seen in scattered light images (Schneider et al. 2014, Olofsson et al. 2016: see Fig: 1.3, right panel). The most accepted explanation for this kind of asymmetry is interactions with the interstellar medium (e.g. Maness et al. 2009, Debes et al. 2009). Another method involving torque to break the axisymmetry in the disk requires an eccentric, inclined planet. This was proposed for the case of HD 61005 by Esposito et al. (2016). Another plausible explanation to explain these swept-back features could be a recent collision (Mazoyer et al., 2014). However, there is no definitive answer yet to explain these observed swept-back wings in debris disks.

c) Clumps: The formation of clumps in debris disks has been speculated long ago to be the result of resonant interactions between dust and planets (e.g. Liou and Zook 1999, Ozernoy et al. 2000). This prediction is based on an analogy with Neptune and the resonant structure it produces on Kuiper belt objects in the Solar System. However, recent modeling of debris disk evolution shows that resonant structure can be broken by collisions (Kuchner and Stark 2010, Nesvold and Kuchner 2015). Clumpy features are most easily observed at long wavelengths which better trace the larger dust grains, as smaller grains are affected by radiation pressure smoothing the clumpy structure (Wyatt, 2006). Clumpy structure may appear ambiguous in some systems as different observations do not always show the clumpy features, but a system that shows clear signs of clumps is β Pic. It shows a relatively weak departure from axisymmetry in dust continuum emission and a stronger azimutal variation in CO emission (Dent et al. 2014, Matrà et al. 2017a). β Pic has shown so far to be an exception to the principle that debris disks are generally azimutally smooth at millimiter wavelengths.

Vertical Structure

The analysis of the vertical structure of debris disks can provide us with plenty of information about the physical processes involved in sculpting the structure of the disks (see, for instance, Fig. 1.4). However, given the degeneracy between the radial and vertical structure in optically thin disks observed at intermediate inclinations, vertical height is often difficult to constrain. The most favorable disk inclination for studying the vertical structure of a disk is when observed edge-on, although interpreting the radial distribution becomes challenging. The vertical structure deduced from modeling imaging observations is frequently expressed as an h/r ratio, where h is the scale height and r is the disk radius. Some observations of debris disks with sufficiently high resolution seem to show a trend where the projected FWHM perpendicular to the disk major axis is either constant or decreases with radius close to the star, but then increases with radius far from the star (Hughes et al., 2018). Good examples of this are the cases of AU Mic and β Pic (Graham et al. 2007, Kalas and Jewitt 1995). This structure might be the result of a forward-scattering phase function inside the debris belt and an effect of the degeneracy between radial and vertical structure in the outer region of the disk. The most reliable estimates of h are the ones where the modeling of the scattered light takes into account the phase function. This has been done for several systems (e.g. HD 15115: Sai et al. 2015, HD 61005: Olofsson et al. 2016 and HD 36546: Currie et al. 2017) and the obtained h/r values range between 0.02–0.12, with 0.06 being the median.

The vertical structure of debris disks can be interpreted as a measurement of dynamical

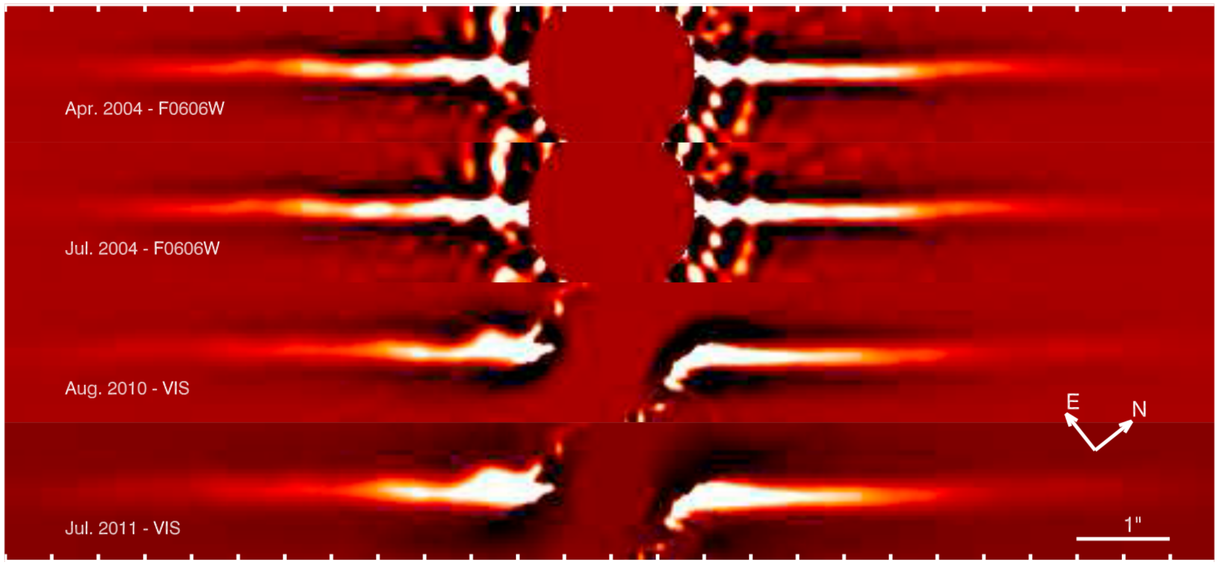

Figure 1.4: Example of a debris disk with an interesting vertical structure: AU Mic. This object presents fast moving features observed in its vertical structure. Figure 4 from Boccaletti et al. (2018), HST images of the disk from 2004, 2010, and 2011 showing changes in its structure.

excitation as it is the most direct way of assessing the velocity dispersion in the system, along with the processes and masses of the bodies that shape its structure. The massive bodies that stir the collisional cascade in the disk have a gravitational impact on the small dust grains and increase their eccentricity and inclination through collisions, bringing all the bodies into equilibrium with high impact velocities. Therefore, the disk thickness can be directly related to the mass of the largest bodies stirring the collisional cascade (e.g. Thébault and Augereau 2007, Quillen et al. 2007). However, Thébault (2009) shows that the vertical structure as observed at optical and infrared wavelengths seems to have a “natural” h of $0.04{\pm}0.02$ attributed to radiation pressure from the star, which has an impact on the small grains, thus scale height values must be interpreted with caution when trying to assess the dynamical state of debris disks.

1.1.3 Observations of Debris Disks

Debris disks are usually discovered by an excess of infrared emission above that expected from the star itself. Far-IR surveys such as Herschel have shown that $\sim$20% of stars host detectable amounts of dust (Eiroa et al. 2013, Matthews et al. 2014, Sibthorpe et al. 2018), although this number could be much higher if it was possible to detect fainter dust emission. The first evidence of circumstellar dust was found over 30 years ago with the InfraRed Astronomical Satellite (IRAS). Aumann et al. (1984) reported the first detection of a large infrared excess from a main-sequence star. After this discovery, hundreds of stars have been searched for infrared excesses. Debris disks surveys of nearby stars such as DUNES (Eiroa et al. 2010, Montesinos et al. 2016) and DEBRIS (Sibthorpe et al., 2018) performed with Herschel have shown that detection rates decrease for later spectral types. Indeed, few debris disks have been detected around M stars (Matthews et al., 2014). However, it is not clear whether this is due to a detection bias or intrinsic to the system properties and evolution. The fractional luminosity of debris disks also declines with age, which is expected because of their collisional evolution (Montesinos et al., 2016). Morey and Lestrade (2014) shows that the fractional dust luminosity in M stars could be analogous to those of earlier spectral-types and thus, consistent with the lack of detections in surveys.

There are several different ways of observing a debris disk. As mentioned, the infrared excess emission has been the primary diagnostic used to infer the presence of a dusty belt around the star. Although, recently this diagnostic has been challenged with, for example, the discovery of a debris disk around the GSC 07396-00759 M star, which did not have any sign of excess in the SED (Sissa et al., 2018). In addition, images of their thermal emission and scattered light can also be obtained and provide further details of the structure and composition of the disks. We will describe these observational methods in the following subsections. Here, we will focus only on the observation of the dust, as observations of the gas component will be discussed in the next section.

Thermal Emission

The dust grains in a debris disk are heated by absorbing the stellar radiation. The absorbed energy is re-radiated as thermal radiation, typically in the infrared (IR). IR surveys have been performed with IRAS, the Spitzer Space Telescope, the Herschel Space Observatory, Akari and the Wide-field Infrared Surver Explorer (WISE), allowing the detection of the thermal IR radiation generated by a debris disk.

The Spectral Energy Distribution (SED) is used to characterize the excess luminosity of the disk over the stellar photosphere (see example shown in Fig. 1.5). By modeling the SED one is

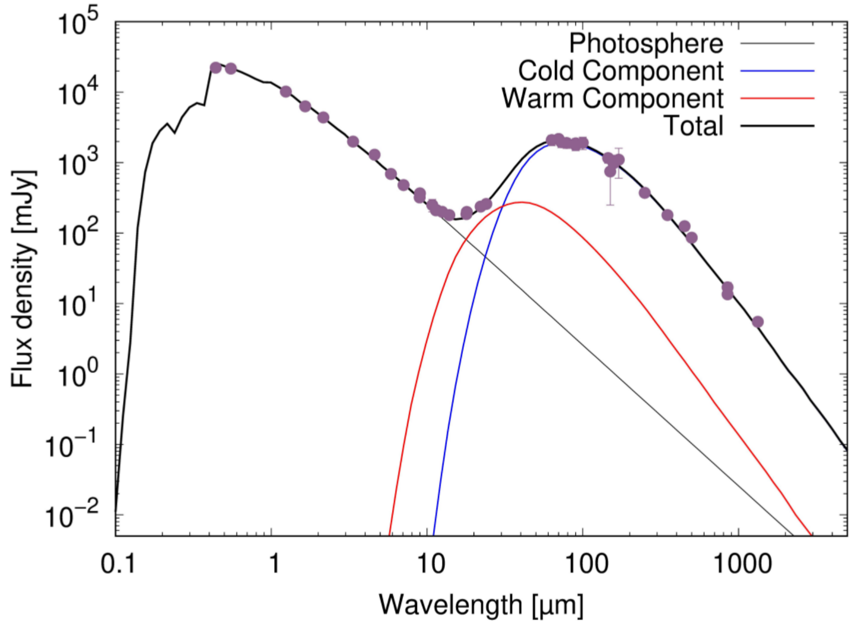

Figure 1.5: Spectral Energy Distribution (SED) of 49 Cet. The thin black line represents the stellar photosphere, the red line shows the warm inner ring while the blue line shows the outer belt (Fig. 6 from Pawellek et al. 2019). The estimated temperatures for the warm and cold components are 125±2 K and 63±3, respectively.

able to estimate the dust temperature in the disk as well as its possible location around the star, although one is not able break the degeneracies between disk temperature, grain distribution and location of those grains. The SED can be modeled by multiple components with different temperatures when the dataset available is rich, or by a simple blackbody excess if the data is sparse. Since the absorptivity and emissivity of a dust grain depends strongly on its size and shape, a modified blackbody model that considers the decrease in emission and absorption efficiency of the smaller dust grains should be used when photometric data points in the long-wavelength (sub-millimeter) tail of the SED are present (Hughes et al., 2018). This is because observations mainly probe grains that have a size comparable to the wavelength of observations.

While the excess emission observed in the SED of a stellar source is the primary method of detection of circumstellar dust around a star, an image of the thermal emission generated by a debris disk can also be obtained and provides us with better constraints on the morphology and extension of the disk. Indeed, the thermal image can reveal that the expected disk radius inferred from the SED may differ from the observed, and this difference may offer some constraints re-

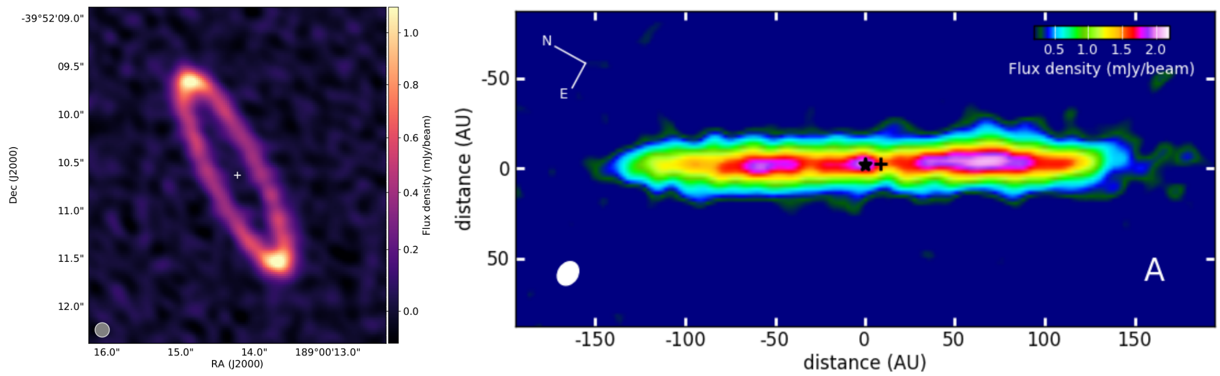

Figure 1.6: Left: Thermal image of HR 4796 taken with ALMA (Figure 1 from Kennedy et al. 2018). **Right:** Continuum image of β Pictoris obtained using ALMA. The disk has been rotated by +29 degrees (Figure 1 (A) from Dent et al. 2014).

garding grain size, as the smaller grains tend to be the hottest and dominate the thermal emission (Hughes et al., 2018). Spatially (or only partially) resolved thermal observations of debris disks have been obtained with the Herschel/PACS, the Submillimiter Array (SMA), Spitzer/MIPS and ALMA (see, for instance, Fig. 1.6 showing two disks resolved with ALMA). These observations provide us with important information about the overall structure of the disk, including size, eccentricity, inclination, gaps, asymmetries, warps, scale height, wings and halos and some additional information regarding the dust properties of the disks, such as its composition, porosity and grain size distribution.

Scattered Light

Similarly to thermal images, scattered light images can also reveal the morphology of the disk and provide constraints on the properties of the dust grains. However, scattered light images offer additional information such as the color of the disk, dust albedo, the degree of forward scattering of the dust particles and their linear polarization induced by scattering. The light emitted by the star is unpolarized, but the light scattered by the circumstellar dust is polarized and its degree of polarization can be imaged with instruments such as the Gemini Planet Imager (GPI), the Spectro-Polarimetric High-contrast Exoplanet REsearch instrument (SPHERE), NICMOS, NACO, NICI, HST/STIS and HST/ACS/HRC. Two examples of scattered light images of debris disks are shown in Fig. 1.7 (these are the same two disks shown previously in thermal images for comparison).

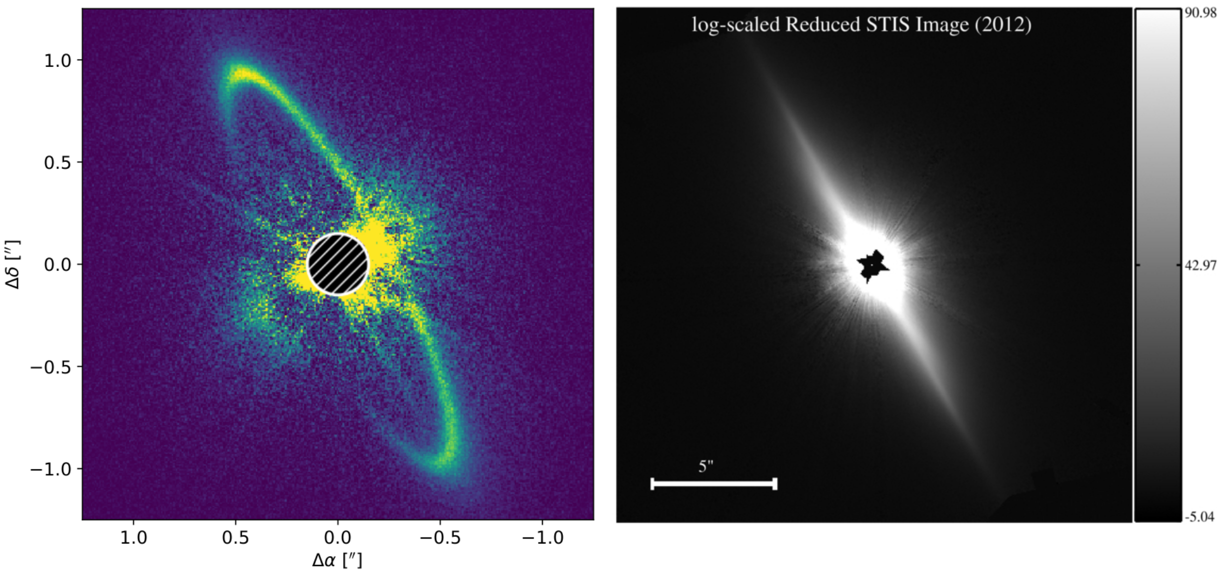

Figure 1.7: Left: Scattered light image of HR 4796 obtained with SPHERE/ZIMPOL (Figure 3 from Olofsson et al. 2019). **Right:** Scattered light image of β Pictoris taken with HST/STIS (Figure 1 (right) from Apai et al. 2015).

The scattering phase function is the angular distribution of light intensity scattered by a particle at a given wavelength. There are several methods to analyse scattering phase functions, each one having advantages and disadvantages. The most commonly used is the Henyey-Greentein prescription, which is characterized by the asymmetry parameter g (Henyey and Greenstein, 1941). However, inferring dust properties from g is not straightforward as it depends significantly on the scattering theory. Scattered light images mainly trace micron-sized dust grains. The smaller grains scatter light nearly isotropically whereas larger grains tend to scatter forward (Hughes et al., 2018). Therefore, scattered light analysis can provides us with additional constraints on the dust properties.

1.2 Gas in Debris Disks

The idea that debris disks should be gas free has been challenged in the past few years by the discovery of a (currently increasing) number of debris disks containing some gas detected either in the (sub-)mm, far-infrared (FIR), infrared (IR), optical or UV wavelengths. These gaseous debris disks have been found mainly around young A type stars, like the well-studied β Pictoris (Brandeker et al., 2004), 49 Ceti (Roberge et al., 2014), HD 32297 (Redfield, 2007), HD 172555

(Riviere-Marichalar et al., 2012), HD 21997 (Moór et al., 2011), some B type stars like σ Her (Chen and Jura, 2003) and HD 142926 (Jaschek et al. 1969, Slettebak 1982), few F type stars like HD 181327 and η Corvi (Marino et al. 2016, Marino et al. 2017) and only two M stars: AU Mic and CE Ant (France et al. 2007, Matrà et al. 2019). Although in this work we mainly focus on the presence of gas in debris disks surrounding main sequence stars, it is worth mentioning that white dwarfs also harbour debris disks and seven of them have been found to contain gas (Manser et al., 2020). Several tracers have been used to this end, for instance CO, C and O emissions at mm wavelengths (Greaves et al. 2016, Kral et al. 2017b), C and O emissions in the farIR (Cataldi et al. 2015, Brandeker et al. 2016), Ca II and Na I absorptions in the optical (Kiefer et al., 2014c) and different C species (C I, C II) and Fe I absorptions in the far-UV, among others (Brandeker et al. 2004, Roberge et al. 2006, Roberge et al. 2014).

Possibly the most fundamental question about the gas in debris disk is: what is its origin? Is it primordial material leftover from the earlier gas-full phase of the disk, or it is of second-generation origin, and thus constantly replenished by outgassing mechanisms? In the next sections, we will refer to this question as well as the detection of this gas and the implications of its presence in planet formation processes.

1.2.1 Gas Detection Methods

There are two main ways to detect the presence of gas in debris disks. It can be detected directly by observing emission of gas species, or it can be detected in an indirect manner by observing the stellar spectrum and detect non-photospheric absorption features produced by the presence of gas. Below, we describe each of these methods.

Direct Method: Emission

We can directly observe the presence of gas in a debris disk by detecting emission lines of species that produce energy transitions mainly in the far-IR and millimeter wavelengths. Within this range, only cold gas having excitation temperatures in the order of tens of K can be detected. These emissions are due to low-energy rotational transitions in the mm regime and fine-structure forbidden lines from atomic species in the far-IR. Given that the total gas mass present in a gas-rich debris is much smaller than the amount of gas in a protoplanetary

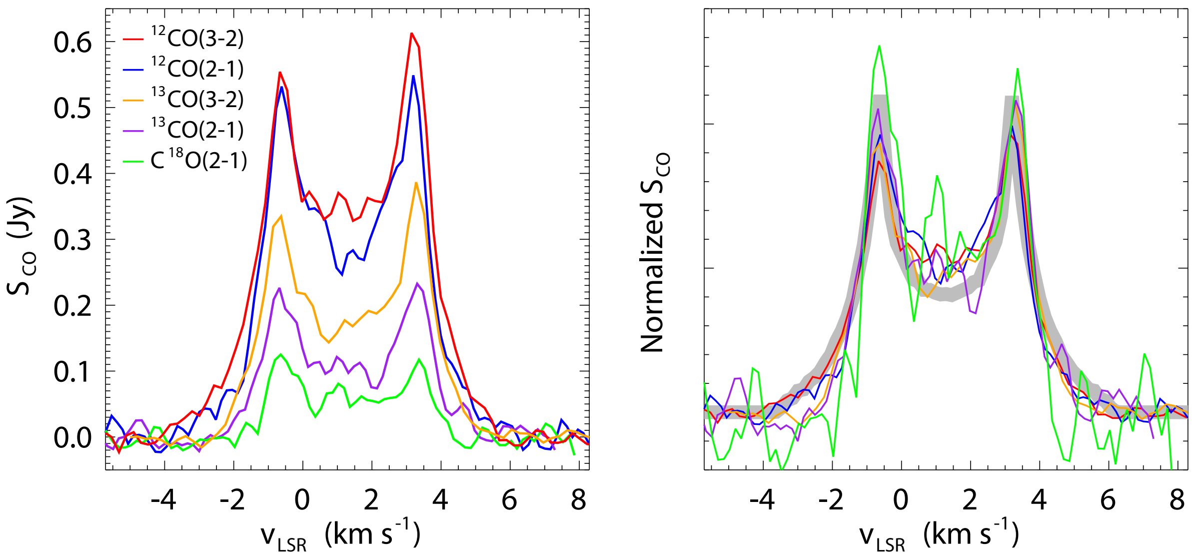

Figure 1.8: CO emission of HD 21997 observed with ALMA (Figure 1 from Kóspál et al. 2013). **Left:** Integrated flux densities in Jy of different CO transitions. **Right:** Spectra normalized to their respective line areas to compare the line profiles.

disk (between 10^{-6} and 10^{-2} $M_{\oplus}$, Kral et al. 2017b), these detections are quite challenging and high-sensitivity instruments are required. Facilities such as ALMA, APEX, IRAM and Herschel have the capability of detecting gas-phase species including CO, O, C and H_2. An example of several CO transitions detected with ALMA in the debris disk surrounding HD 21997 is shown in Fig. 1.8 (Kóspál et al., 2013). The double peak emission is typical for rotating material seen with a certain inclination; one side being redshifted (with respect to the radial velocity of the system) as moving away from us while the material moving towards us appears blueshifted. High angular resolution observations of emission lines can also show the spatial distribution of gas in the disk and thus can reveal whether the gas is co-located with the dust or not, providing a hint about the origin of the gas. A special case of spatially resolved gas observations is the study of the β Pictoris debris disk performed by Brandeker et al. (2004). Unlike other far-IR and mm observations, Brandeker et al. (2004) used VLT/UVES to study the well known gas-rich surrounding β Pic in the optical by placing the slit in different positions and orientations along the disk and offset from the star. β Pictoris is the only debris disk so far whose gas has been spatially resolved at optical wavelengths allowing the detection of emission lines from species such as Fe, Na, Ca and Ti (typically detected in absorption).

Indirect Method: Absorption

Traces of gas in debris disks can also be detected in an indirect manner through absorption spectroscopy. This method uses the stellar spectrum to study the material that crosses the line of sight of the star. The caveat is that this method restricts the detections to a narrow range of inclination angles in order for the material to pass through the line of sight from the observer's perspective and thus it is only useful for disks seen close to edge-on. However, this method is more sensitive to small amounts of gas than emission line studies and thus it allows the detection of a larger variety of species, such as Ca, Mg, Mn, O, Fe, N, Na, Ti, C, S, Si, Cl, Al, Cr and Sc (e.g. Roberge et al. 2014, Grady et al. 2018, Jaschek et al. 1969). These absorption lines are typically narrow (depending on the velocity dispersion of the gas) and, therefore, are more easily detected when found superposed on rotationally broadened spectral lines, such as those of early-type stars (for instance, see Fig. 1.9 showing the detection of Ca II in HD 172555, an A-type star surrounded by a debris disk; Kiefer et al. 2014a). Gas absorption features are mainly detected at UV and optical wavelengths and since they are produced at higher excitation temperatures than emission lines it indicates that this gas should be closer to the star and thus hotter. Therefore, it is sometimes referred to as "hot" gas, unlike the "cold" gas detected in emission (Rebollido et al., 2018). Given that these absorption features are very narrow, having FWHM in the order of 10 km.s^{-1} or less (Kiefer, 2014), it is necessary to use high-resolution spectrographs (R>10,000) in order to detect them. Instruments such as HARPS, UVES, FEROS, MIKE, HERMES, FIES, the Sandiford Echelle Spectrograph, the HST Imaging Spectrograph and COS have been used to detect these gas features in debris disks and other kind of stars. Since these instruments require much shorter integration times than emission line observations (minutes versus hours), it is possible to perform much larger surveys and to monitor the variability (or stability) of the gas absorptions. Therefore, this is the method used throughout this Thesis. Further details about the interlopers of gas detections using this method and about the detection of variable absorption features produced by the so-called "Falling Evaporating Bodies" (FEBs) are given in the following subsections.

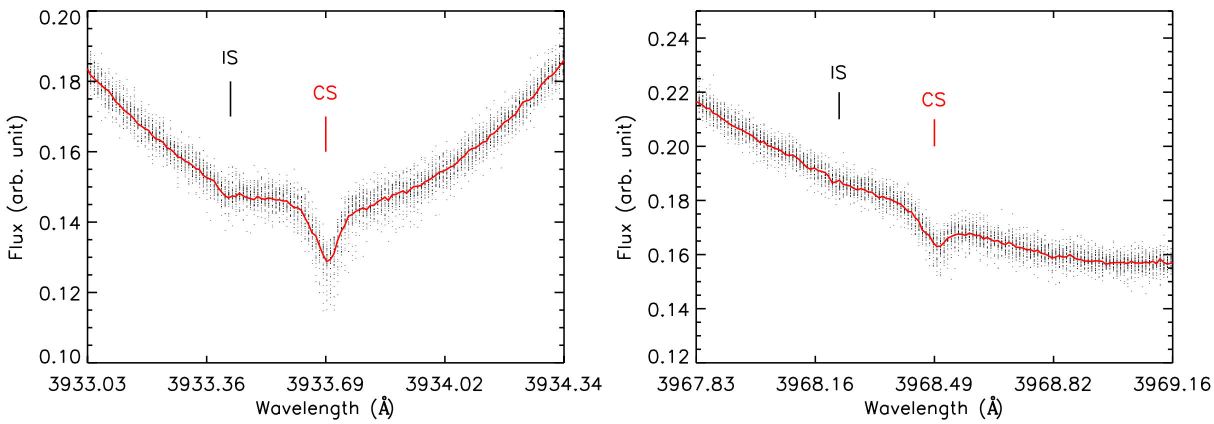

Figure 1.9: Ca II absorption in the K (left) and H (right) lines of HD 172555 observed with HARPS (Figure 1 from Kiefer et al. 2014a). Reference spectrum in red and dispersion from all the combined spectra in black dots. The position of the circumstellar (CS) absorption is marked in red and the position of an interstellar (IS) absorption in black.

1.2.2 Interlopers of Gas Detection Through Absorption Spectroscopy

Circumstellar gas is not the only source of absorption features and variability in the spectral lines of the stars. They can also be produced by other phenomena and therefore, can be easily misidentified. Here we describe those other processes that might be confused with circumstellar gas and the methods that can help to discriminate between them.

Interstellar Medium

Interstellar clouds in the line of sight of stars produce narrow absorption features superimposed on the stellar spectra that are very similar to circumstellar gas features. Same as for circumstellar gas, these features are more easily detected in early-type radiative stars (Redfield and Linsky, 2008).

There are several criteria that can be helpful to determine the origin of non-photospheric features. Here we describe some general prescriptions to follow when studying the origin of these narrow absorptions:

- Circumstellar gas should be found near the radial velocity of the star since it belongs to the system and thus it moves together with it. However, interstellar clouds are often also found at similar velocities, so this characteristic does not necessarily rule out interstellar origin. On the other hand, FEB-like events, which are of circumstellar origin, are often detected at redshifted or blueshifted velocities with respect to the star's (Kiefer et al. 2014b, Rebollido et al. 2020).

- Following on the previous statement, if there is short term (night to night) variability in the absorptions there is a high probability that it is caused by FEBs, thus this is a strong sign of circumstellar origin. Interstellar clouds are not likely to present short term variability. Only mid to long term (months to years) variations have been reported in the interstellar medium (ISM)ranging from small to large variations in column density (e.g. McEvoy et al. 2015).

- As a very general rule, column density CaII/NaI and equivalent width $K/D2$ ratios have values > 1 for circumstellar and < 1 for interstellar gas (Kiefer et al., 2014c). This rule might be helpful when determining the origin, however we need to be careful as it not a strict border. In this Thesis we have found several exceptions (shown in Chapter 3), for instance η Cha, having both absorptions with ratios > 1 while its nearby stars show clear confirmation of interstellar origin, and in the other side, HD 110058, presenting the complete opposite case in its circumstellar absorption at $\sim$12 km/s.

- If we find a known interstellar cloud traversing the line of sight of the star and its radial velocity matches the feature's, then the most likely possibility is that we are observing an absorption due to such a cloud, therefore the origin is interstellar. Throughout this Thesis, we often use the Local Interstellar Medium (LISM) database of clouds within 15pc from the Sun compiled by Redfield and Linsky (2008) to compare against the absorptions found in our database of debris disks.

- If we analyse other rotationally broadened stars with a similar line of sight and they present similar absorption features at similar velocities, this is a strong confirmation of interstellar origin of the features since the same cloud must be covering all the stars within a certain radius and therefore they show the same absorptions. On the opposite side, the same rule applies if the feature is not observed in any other nearby star; this strongly suggests circumstellar origin, as in the case of HD 110058's feature at $\sim$12 km/s discussed in Chapter 3. However, some caution must be taken as we cannot be certain about the spatial extent of the clouds. It would be best, if possible, to analyse nearby stars distributed at different locations around the target to make sure to cover all the surrounding area.

- If we detect absorptions from Diffuse Interstellar Bands (DIBs), this confirms the presence of ISM in the line of sight of the star, as DIBs are only found in the ISM (Farhang et al., 2019).

Variability

As mentioned in the previous subsection, the detection of variable absorption features superimposed to the stellar spectra can be a sign of exocometary activity or the so-called FEB-like events. Although the variable nature of these features immediately rules out an interstellar origin, they can be confused with other sources of variability in the stellar spectra. Spectral lines can present, for instance, changes in their overall shape, or intensity or radial velocity shifts, and since those lines are the base upon we detect non-photospheric features, the characteristics of the latter can be "artificially altered" by the variations of the former. These variations can be the result of different factors, such as multiplicity, stellar pulsations, hot/cold spots, accretion/ejection activity or flares. Photospheric pulsations can produce travelling absorption features superimposed on the photospheric profile, which can look very similar to the absorptions produced by transiting FEBs. However, these so-called "migrating subfeatures" induced by pulsations have a certain periodicity and can be detected simultaneously in several lines (e.g. Nazé et al. 2020). Another thing that must be taken into account is that the Ca II doublet, in particular, being the most sensitive circumstellar gas tracer in the optical and, therefore, the most used one to detect exocometary activity, is also a sensitive magnetic activity indicator (Lovis et al. 2011, Wise et al. 2018, Karoff et al. 2019). An interesting case of variability wrongly attributed to exocomets is the case of HR 10. This system, previously reported to present FEB-like events (e.g. Lagrange-Henri et al. 1990a, Redfield 2007, Welsh et al. 1998) was later identified to be a spectroscopic binary and the variability attributed to each star having a circumstellar shell Montesinos et al. (2019).

Similarly to the interstellar case, below we describe some general indications that might help discriminate between variability caused by exocometary activity or other kinds of activity. It is worth noting that, in order to better assess the origin of the variability, several epochs are necessary. In this work, we have established a minimum of three observations for our analysis. However, in an ideal case, it would be best to have a large number of epochs covering a variety of temporal samplings in order to study the variability at different times-scales and be able to better understand it and reach a reliable conclusion. It is also advisable to use as many tracers as possible, but due to time constraints in Chapter 5 we focus mainly on the most intense, the Ca II K line, for a first order identification.

- It is very helpful to search in the literature about any report that could be related to variability in the spectral lines of the object. For instance, whether this is a known spectroscopic binary or a variable star. A possible co-relation to those scenarios must be checked. Previous reports of FEB-like events and/ or the presence of gas emissions must also be taken into account as they further strengthen the exocomets scenario.

- In the FEBs (or exocomets) scenario, the variability must be caused be variable absorption features superposed to the stellar spectral lines. Other kinds of variations such as radial velocity shifts, oscillation of the lines, or changes in the overall shape of the lines are likely caused by other phenomena.

- Variations due to circumstellar gas should only be observed in certain spectral lines such as Ca II, Fe II, Na I or Ti II, for instance. If variability is observed in all the spectral lines at the same time, an exocometary origin is likely discarded.

- Variability presenting certain periodicity is likely attributable to other phenomena such as stellar hot/cold spots, pulsations, magnetic fields or multiplicity (e.g. Cunha et al. 2019). FEB-like events have a sporadic nature and are not likely to be periodic.

- Variable emission lines within the optical range, especially those observed in the Balmer lines are indicators of other phenomena such as accretion, stellar activity or radiative processes rather than exocomets.

- Transiting exocometary gas usually produces an absorption feature that remains detectable for at least a few hours (Kiefer et al. 2014b, Tobin et al. 2019). If an absorption feature is observed to appear and disappear completely in a matter of seconds, it might be probably an instrumental artifact.

1.2.3 Demographics of Debris Disks with Gas

As described in previous sections, gas has been detected in an increasing number of debris disks either in emission or absorption spectroscopy. Here we provide an inventory of all (to the best of our knowledge) reported detections of gas in these dusty circumstellar disks. In Table 1.1, we list all debris disks having public records of traces of gas. This list includes disks having confirmed gas detections (i.e. multiple detections in several gas tracers) and disks with weak hints of gaseous features. This means that we have compiled all the reports of gas detections in debris disks, however, it is possible that not all of them are 'reliable' detections. Also, it is worth noting that this list includes both stable gas components and transient gas detections.

As can be seen in Table 1.1, a total of 21 debris disks present cold gas emission; 16 of them surrounding A-type stars, 3 of them around F stars and 2 around M stars. Regarding hot gas absorptions, they have been reported for 31 debris disks systems (including those being reported in this work, a total of six systems), 24 of them being A stars, 7 of them being B stars and none of them being of later spectral types. According to our inventory, a total of 44 debris disks have been reported to present some gas content, eight of them having reports of both gas emission and absorption (all of which are A-type stars). It is not well understood why there is a gas detection bias favoring earlier spectral types. It might be related to the fact that detections of debris disks are also biased towards earlier types. Hughes et al. (2018) compares all the searches and detections of CO, O I and C II by subdividing in AB, FGK and M spectral types and also compared between young and old ages. The three species show the same trend, favouring AB stars and young ages. These trends still remain in our updated inventory. On the other hand, Matrà et al. (2019) demonstrates that the release of secondary gas in M stars by a collisional cascade is different from the process in early-type stars because in M stars the collisional cascade is affected by removal of the smallest grains by the stellar wind as opposed to radiation pressure in more massive stars, which might be an explanation for the lack of detections in low mass stars.

As mentioned before, our study focuses on the presence of gas in debris disks around main sequence stars. Therefore, in Table 1.1 we present only detections towards main sequence stars. However, it is worth mentioning that a similar study has been performed for debris disks surrounding white dwarfs. Manser et al. (2020) studied the frequency of gaseous debris disks around white dwarfs by determining the occurrence rate of emission detected in the Ca II triplet. They showed that a $4\pm_2^4$ percent of white dwarfs having a dusty debris disks present an observable gaseous component in emission.

Table 1.1: Inventory of gas detections in debris disks. Spectral types were taken from Simbad (Wenger et al., 2000). The systems included in our sample are flagged with a *. Weak (3σ) detections are flagged with a (?). Detected species are listed according to their detection method 'Ab'= absorption or 'Em'=emission.

Object	Spectral Type	Age [Myr]	Detected Species	Detection Method	References
β Pictoris	A6V	23±3 [49]	Ca, Na, Fe, Mg	Ab	e.g. [1], [2], [3]
			CO, C, O	Em	e.g. [4], [5]
			Fe, Na, Ca, Ni, Ti, Cr	Em	[6]
49 Ceti*	A1V	40 [50]	CO, C, H_2	Em	e.g. [7], [8], [9]
			C, O, Fe, S, Si, Cl, Al, Ca	Ab	[10], [11]
σ Her	B9V	140 [12]	C, N	Ab	[12]
HD 32297	A0V	30 [51]	Na	Ab	[13]
			C, CO	Em	[14], [15]
HD 141569	A2VekB9mB9(_lB)	5 [16]	C, O, CO	Em	[16]
			Mg, Fe, Mn	Ab	[17]
HD 172555	A7V	23±3 [49]	O	Em	[18]
			Ca, Si, C, O	Ab	[19], [20]
HD 21997*	A3IV/V	30 [22]	CO	Em	[21], [22]
AU Mic*	M1VeBa1	23±3 [52]	H_2	Em	[23]
η Tel*	A0V+M7/8V	23±3 [49]	C / Ca	Em / Ab	[24] / [25], [26]
HD 131835*	A2IV	16 [27]	CO, C	Em	e.g. [27], [28]
HD 158352*	A8Vp	750±150 [53]	Ti, Ca(?)	Ab	e.g. [29], [30]
24 CVn*	A4V	804 [54]	Ti, Ca	Ab	e.g. [29]
HD 21620	A0Vn	80 [55]	Ca	Ab	[31]
HD 142926*	B9pe	78 [56]	Fe, Cr, Sc, Ca, Na	Ab	e.g. [32], [33]
			Mg, Ti, Si	Ab	e.g. [34], [35]
c Aql*	A1V	448 [57]	Ca	Ab	e.g. [36], [37]
HR 4796*	A2V	10 [57]	Ca	Ab	[38], [37]
HD 110058*	A0V	15 [57]	CO(?) / Ca	Em / Ab	[39] / [37], [40]
CE Ant*	M2Ve	10 [58]	CO	Em	[41]
HD 37306*	A1V	30 [52]	Ca, Fe, Ti	Ab	[42]
HD 138813*	A0V	10 [59]	CO	Em	[39]

Continued on next page

Table 1.1 – continued from previous page

Object	Spectral Type	Age [Myr]	Detected Species	Detection Method	References
HD 146897*	F2/3V	10 [59]	CO	Em	[39]
HD 156623	A0V	10 [59]	CO	Em / Ab	[39] / [26]
HD 181327*	F6V	23 [59]	CO	Em	[43]
η Crv*	F2V	1400 [44]	CO	Em	[44]
Fomalhaut	A4V	440 [45]	CO	Em	[45]
HD 95086*	A8III	17 [46]	CO(?)	Em	[46]
HD 121191	A5IV/V	15-16 [60]	CO	Em	[47]
HD 121617	A1V	16 [60]	CO	Em	[47]
HD 131488	A1V	16 [60]	CO	Em	[47]
α Pic	A8VnkA6	700 [61]	Ca	Ab	[48]
λ Gem	A4IV	550 [61]	Ca	Ab	[38]
HD 58647	B9IV	0.4±0.1 [62]	Ca	Ab	[38]
ϕ Gem	A5IV	637±111 [54]	Ca	Ab	[38]
HD 85905	A1IVn	481 [63]	Ca	Ab	[48]
δ Crv	A0IV(n)kB9	260 [61]	Ca	Ab	[38]
ρ Vir*	A0Va_lB	10 [64]	Ca	Ab	[31]
HD 145964*	B9V	5 [64]	Ca	Ab	[31]
5 Vul*	A0V	100 [64]	Ca	Ab	[11]
HD 24966*	A0V	10 [65]	Ca	Ab	[25]
HD 38056*	B9.5V	250 [66]	Ca	Ab	[25]
θ Hya*	B9.5V+DA1.6	90 [54]	Ca	Ab	[25]
HD 225200*	A1V	90 [67]	Ca	Ab	[25]
HD 36546	B8	10 [69]	Ca	Ab	[68]
gam Tri	A1Vnn	160 [61]	Ca	Ab	[70]

[1] Ferlet et al. (1987), [2] Kiefer et al. (2014b), [3] Vidal-Madjar et al. (2017) [4] Roberge et al. (2006), [5] Dent et al. (2014), [6] Brandeker et al. (2004), [7] Zuckerman et al. (1995), [8] Roberge et al. (2013), [9] Thi et al. (2001b), [10] Roberge et al. (2014), [11] Montgomery and Welsh (2012), [12] Chen and Jura (2003), [13] Redfield (2007), [14] Donaldson et al. (2013), [15] MacGregor et al. (2018), [16] Thi et al. (2014), [17] Malamut et al. (2014), [18] Riviere-Marichalar et al. (2012), [19] Kiefer et al. (2014a), [20] Grady et al. (2018), [21] Moór et al. (2011), [22] Kóspál et al. (2013), [23] France et al. (2007), [24] Riviere-

Marichalar et al. (2014), [25] Welsh and Montgomery (2018), [26] Rebollido et al. (2018), [27] Moór et al. (2015), [28] Kral et al. (2019), [29] Abt and Moyd (1973) [30] Lagrange-Henri et al. (1990b), [31] Welsh and Montgomery (2013), [32] Jaschek et al. (1969), [33] Harmanec et al. (1976), [34] Slettebak (1982), [35] Koubsky et al. (1993), [36] Montgomery and Welsh (2017), [37] Iglesias et al. (2018), [38] Welsh and Montgomery (2015), [39] Lieman-Sifry et al. (2016), [40] Hales et al. (2017), [41] Matrà et al. (2019), [42] Iglesias et al. (2019), [43] Marino et al. (2016), [44] Marino et al. (2017), [45] Matrà et al. (2017b), [46] Booth et al. (2019), [47] Moór et al. (2019), [48] Welsh et al. (1998), [49] Mamajek and Bell (2014), [50] Zuckerman and Song (2012), [51] Kalas et al. (2005), [52] Torres et al. (2006), [53] Moór et al. (2006), [54] David and Hillenbrand (2015), [55] Roberge and Weinberger (2008), [56] Zorec et al. (2005), [57] Nielsen et al. (2019), [58] Bell et al. (2015), [59] Kral et al. (2017b), [60] Pecaut and Mamajek (2016), [61] Vican (2012), [62] Montesinos et al. (2009), [63] Gontcharov (2012), [64] Morales et al. (2009), [65] Rhee et al. (2007), [66] Morales et al. (2016), [67] Su et al. (2006), [68] Rebollido et al. (2020) [69] Currie et al. (2017), [70] Iglesias et al. (in prep.)

1.2.4 Origin of Gas in Debris Disks: Residual or Second Generation?

The possible origin of the gas detected in debris disks has been widely discussed (Moór et al. 2011, Wyatt et al. 2015, Kóspál and Moór 2016, Kral et al. 2017a). In short, it could be residual gas that remained from the earlier gaseous stage of the disk, which would imply that the efficiency of gas removal processes may be lower than we thought. Or, it could be second generation gas, produced by icy comets that, either orbiting or as they approach the star, begin to “evaporate” (or, more correctly, sublimate) and release small amounts of gas. Gas of secondary origin could also be produced by collisions among volatile-rich dust grains or comet-like bodies (Higuchi et al. 2017 and references therein) or even by photon-stimulated desorption of solids (Matthews et al., 2014). These latter two processes could replenish the disk with a stable gaseous component likely to be located in the outer regions of the disk (Brandeker et al., 2004). On the other hand, the idea of the “falling evaporating bodies” (FEBs) has been gaining more acceptance in the last few years, since FEB-like events have been detected (mostly) around A-type stars with debris disks and some shell stars (e.g., Beust et al. 1998, Kiefer et al. 2014a, Eiroa et al. 2016).

While the general consensus is that the origin of the gas is due to the sublimation of icy bodies, this is not a satisfactory explanation for the detection of colder CO found at tens of

AU from the star (Marino et al., 2020). In some cases, the large amount of gas found in the system is more consistent with primordial origin (e.g. Kóspál et al. 2013). The timescale for photodissociation of CO is of the order of 100 years, orders of magnitude too quick compared to the ages of the systems (>10 Myrs, Visser et al., 2009). Therefore, it is not clear how the gas can survive for so long in the disk. It could be that CO and other gas species are being constantly replenished by outgassing processes or that the gas is shielded somehow from the UV radiation that induces photo-dissociation. Since debris disks are optically thin (regarding the dust), it is not well understood how CO is shielding and surviving. Some possibilities are that sufficient amounts of CO could become self-shielded, or that H_2 is serving as a shield (although it has not been found to have enough density), or maybe the C product of dissociation can protect CO from photons and become ionized (Kral et al. 2017b, Wyatt 2018). We know of at least 17 systems with CO detections and additional C I emission has been detected for 4 of them (e.g. Dent et al. 2014, Moór et al. 2019, Cataldi et al. 2015, 2020). In these cases, it has been possible to calculate the C I/CO column density ratio and the results suggest a strong over-abundance of atomic carbon with respect to CO, supporting the hypothesis that quite quickly after being produced, CO is photo-dissociated. Therefore, since multiple species have been detected in only a handful of systems, current surveys aim to study a larger number of gas tracers in order to improve our understanding about the origin and composition of gas in debris disks.

1.2.5 Falling Evaporating Bodies (FEBs)

The first evidence of exocometary gas features dates back to 1975, when Slettebak (1975) reported the detection of very strong, sharp absorption features in the Ca II H & K line of an interesting early-type star called β Pictoris. A decade later, Ferlet et al. (1987) detected drastic changes in the narrow absorption features observed in the Ca II K line of β Pic, attributing them for the first time to the presence of cometary-like objects falling towards the star. Since then, this variable infalling material in β Pic was studied extensively and the term "Falling Evaporating Bodies" (FEBs) was coined (e.g. Lagrange-Henri et al. 1988, Beust and Tagger 1993, Beust et al. 1998, Beust and Morbidelli 2000). Nowadays, evidence of star-grazing exocomets has been reported in close to 30 debris disks (e.g. Iglesias et al. 2018, Rebollido et al. 2018, Welsh and Montgomery 2018). These events manifest as stochastic absorption features usually at redshifted or blueshifted velocities with respect to the radial velocity of the star. Variable absorption features have been detected over short time windows of hours or night to night as well as over months (Barnes et al. 2000, Thébault and Beust 2001, Welsh and Montgomery 2013). The case of β Pictoris remains to this day the most studied case of exocometary activity, both theoretically and observationally, with thousand of observations tracing hundreds of exocometary transits and the most extensive evidence of different gaseous species detected in both emission and absorption (e.g. Beust et al. 2001, Brandeker et al. 2004, Thébault and Beust 2001, Dent et al. 2014, Beust et al. 2014, Vidal-Madjar et al. 2017, Tobin et al. 2019). Kiefer et al. (2014b) reported the presence of two different families of exocomets in the disk of β Pic determined from the statistical analysis of $\sim$6,000 variable absorption features, one corresponding to shallow absorptions attributed to old, exhausted comets depleted in volatiles and the other one corresponding to deep absorptions related to recently fragmented exocomets (see Fig. 1.10). β Pictoris is also the only system where exocomets have been detected in both high-resolution spectroscopy and broadband photometry (Zieba et al., 2019).

One interesting by-product of studying FEBs is posing the question on the cause of such instabilities in the debris disk. A possible cause for such instabilities could be the presence of a larger body like a planetesimal or a planet disturbing the disk (Dvorak et al. 2020, Raymond et al. 2012). The inward scattering of exocomets in β Pic being triggered by the presence of a massive planet was early suggested by Beust et al. (1998) and this was confirmed years later by the detection of a giant planet (Lagrange et al., 2009). Therefore, detecting FEB-like events could be seen as an indirect hint for the presence of at least one giant planet embedded in the debris disk system. The study of exocomets over large samples, with improving cadence and number of species traced is a recently open research field that will likely further develop with the JWST, WFIRST and PLATO missions in the future (Matra et al., 2019). Its development will allow the study of the composition of exocomets in comparison to the comets in the Solar System and the study of volatiles transport to the inner regions of forming planetary systems (Strøm et al. submitted, Dvorak et al. 2020, Matra et al. 2019). So far a number of surveys searching for exocomets in early-type stars has been performed (e.g. Welsh and Montgomery 2013, Welsh and Montgomery 2015, Welsh and Montgomery 2018, Rebollido et al. 2020) demonstrating they are mainly detected in A-type stars, either shell stars or debris disks stars, and that there is an

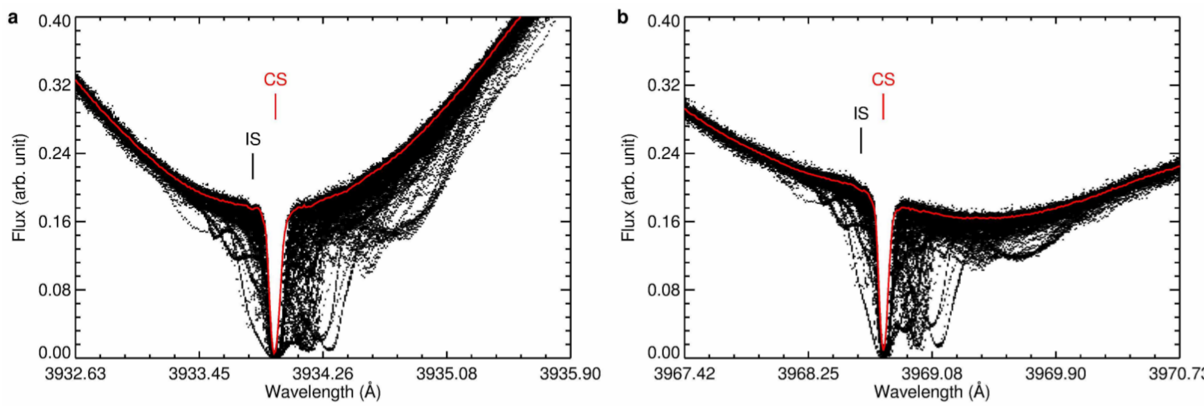

Figure 1.10: Ca II absorption in the K (**a**) and H (**b**) lines of β Pictoris observed with HARPS (Extended Data Figure 2 from Kiefer et al. 2014b). Reference spectrum in red and all the different observations are shown in black dots. The position of the stable circumstellar (CS) absorption is marked in red.

expected correlation with them being detected in debris disks with a near edge-on inclination with respect to the observer. As mentioned, this sub-field of planetary science is rapidly evolving with an increasing number of detections in the last few years and likely more are yet to come in the future allowing us to better understand their role in planetary systems.

1.2.6 Implications of the Presence of Gas in Debris Disks and its impact in Planet Formation

Independently of its origin, whether primordial or secondary, the implications of the presence of gas in debris disks are many (see, for a recent review, Hughes et al. 2018). It can change our understanding of gas removal processes by setting new constraints on their efficiency (Williams and Cieza, 2011), particularly for photoevaporation, thought to be the main cause of gas removal in protoplanetary disks (Alexander et al. 2006, Canovas et al. 2017). In addition, gas can influence the morphology of the dust in the disk providing us with a possible answer to the formation of the observed gaps in some debris disks (Lyra and Kuchner, 2013). Gas can also imprint changes in the dynamics of the system since even small amounts of gas can drag dust and pebbles (Wyatt, 2008), and dust grains can couple to the gas component which acts as a fluid affecting rocky planet formation processes (Fernández et al. 2006, Cleeves et al. 2016, Kenyon et al. 2016). It can also affect the interpretation of the observed dust properties of the disk since it might prevent radiation pressure from expelling micron-sized dust grains and thus might provide an explanation for the overheated dust temperatures observed in some disks (Wyatt 2018, Moór et al. 2017). Sufficient amount of gas can dampen planetary eccentricities and inclinations and thus can lead to planet migration (Wyatt 2018, Morbidelli 2018).

In a recent study by Kral et al. (2020), the presence of gas in debris disks was shown to produce the formation of a secondary atmosphere on terrestrial planets. If rocky planets are already formed in a gaseous debris disk they can accrete this gas forming a new atmosphere with a composition similar to that of the gas. Furthermore, debris disks with a considerable gas content can even produce massive atmospheres forming sub-Neptune-like planets.

Since the presence of gas can have a strong impact on the formation and evolution of planetary systems it is essential to understand its frequency and how gas detections relate to properties of debris disk systems, such as age, multiplicity, stellar type, metallicity, dust content and disk-planet interaction. The study of this gas also gives us information regarding the composition of volatile-rich planetesimals and whether they could transport this volatile material to planets in the habitable zone, opening the question to whether they contribute to the development of life.

1.3 This Thesis

1.3.1 Aim of This Work

In this work we studied a robust sample of 301 debris disk (Olofsson et al. in prep.) to learn what percentage of debris disks contains gas, how the gas is physically related to the dust and what properties characterize the stars that possess circumstellar gas in their surrounding debris disks. Instruments such as ALMA and APEX can provide us with a plethora of information about disks besides being able to detect gas emission. However, observing such a large sample with either facility would be extremely expensive in terms of telescope time. In comparison, the analysis of UV-optical ground-based spectra provides a very efficient way to find debris disks with gas to be followed-up with other instruments (Montgomery and Welsh 2012, Welsh and Montgomery 2013, Kiefer et al. 2014c). Just as a simple illustration, integration times of CO surveys with ALMA or APEX are $\sim$1 hour per target (Kóspál et al. 2013, Hales et al. 2014), while optical high-resolution high-signal-to-noise-ratio spectroscopic observations of similar targets conforming our sample take only a few minutes or even seconds (making for perfect filler /

poor weather condition programs on class 2 to 8 meter telescopes). Thus the number of spectra taken during one night ranges from ∼50 to ∼100, depending on the telescope/instrument and the targets.

1.3.2 Our Sample

The full sample of debris disks we studied in this Thesis consists of 301 systems selected from an original list compiled by Olofsson et al. (in prep). The original list, was assembled via a thorough literature search for debris disks that had been observed with the IRS instrument (Houck et al., 2004) on board of the Spitzer space telescope (Werner et al., 2004). This search resulted in ∼ 500 objects that were then filtered down to 301 imposing different criteria on the significance of the excess in the mid-infrared and excluding debris disks that display strong emission features in their IRS spectra (e.g., Olofsson et al., 2012), as these objects are not really representative of "classical" debris disks. It follows then that the selection criteria applied to achieve our database of 301 debris disks are unbiased with respect to disk inclinations as the disks are optically thin and, since most inclinations are unknown, they can be assumed to be following a uniform distribution.

The sample is presented in Table A.1 in the Appendix. This Table contains the main identifier used in Simbad database (Wenger et al., 2000), other commonly used identifiers such as the "HD" from the Henry Draper Catalogue (Cannon and Pickering, 1918), the "HR" (Harvard obs., Revised photometry) from the Bright Star Catalogue (Hoffleit, 1964), and "HIP" from the Hipparcos Catalogue (HIP, 1997). In addition, the Table presents "My ID", an identifier used through the whole Thesis process to manage the objects database. The names were chosen with a preference for the designation used in Simbad. Finally, ICRS (ep=J2000) coordinates of the targets obtained from Simbad are also given.

The main parameters of the sample are given in Table A.2, found in the Appendix. All these parameters were obtained from Simbad, except for the $L_{\text{disk}}/L_\star$ luminosity ratio which were obtained from the SED model fitting (Olofsson et al. in prep.) and ages, which were estimated using a very simplistic approach based on either the system belongs to a moving group or not. If the system is a "field star", then it is assumed to be older than 100 Myrs and thus is classified as "old" (O). On the other hand, if the system is likely to belong to a moving group, it is assumed

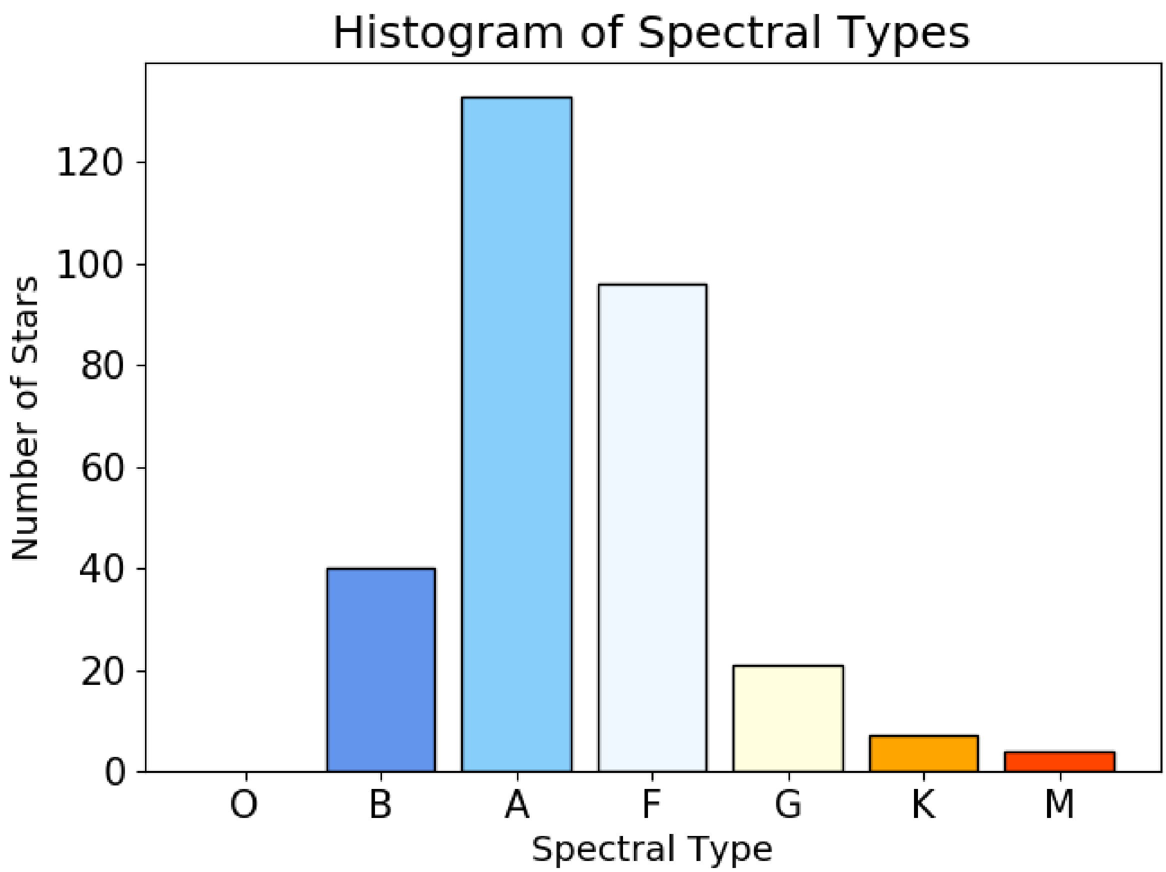

Figure 1.11: Histogram of the spectral types of the host stars of the debris disks in our sample. Colors are only a representation of the spectral types.

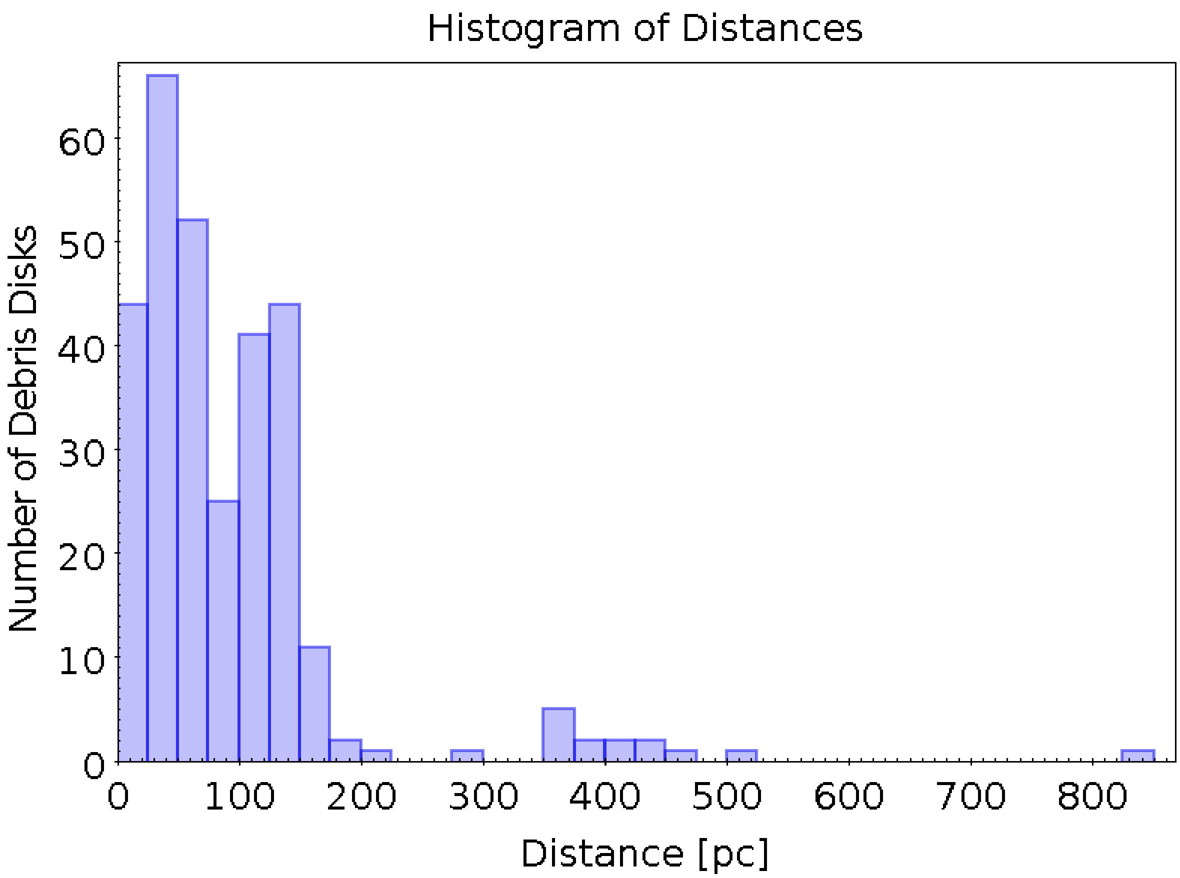

Figure 1.12: Histogram of the distances of the debris disks in our sample.

to be younger than 100 Myrs and is categorized as “young” (Y). About 27% of the sample was classified as “young” debris disks. A histogram of the spectral types of the host stars in our sample is shown in Fig. 1.11 and a histogram of the distances of all the systems is presented in Fig. 1.12. It can be appreciated from these figures that most of the host stars in the sample are A-type stars and that most of the systems are located within $\sim$200 pc.

Chapter 2

Spectroscopic data

We collected high-resolution, high-signal-to-noise UV-optical spectroscopic data for our sample by obtaining our own observations, exploiting the ESO archive and exchanging data with collaborators. The purpose of collecting these observations was to analyse the sample in the wavelength ranges covering the Ca II H and K lines at 3968.5Å and 3933.7Å, and the Na I D1 and D2 lines at 5895.9Å and 5889.9Å, as these are the most sensitive gas tracers in the UV-optical range. We were able to collect adequate data for 273 objects in our sample, missing mainly the northern targets, as shown in Fig. 2.1.

We obtained spectroscopic observations with UVES (Dekker et al., 2000) on the VLT UT2 telescope at Paranal Observatory, Chile, FEROS (Kaufer et al., 1999) on the MPG/ESO 2.2m telescope at the La Silla Observatory in Chile, and MIKE (Bernstein et al., 2003) mounted on the Magellan-Clay telescope at Las Campanas Observatory, Chile. We also queried the ESO archive searching for all relevant high-resolution spectra covering the UV-optical wavelength ranges. In particular data from HARPS (Mayor et al., 2003), UVES and FEROS instruments were searched for. Additionally, data from FEROS, HERMES and FIES were shared to this project by two teams of collaborators. All the collected observations are summarized in Table B.1, found in the Appendix. Proprietary observations are flagged with a *. Since UVES and MIKE spectrographs can take simultaneous observations of different wavelength coverage using a dichroic, a single observation consists of two spectra (usually one covering the blue wavelength ranges and one covering the red wavelength ranges). Therefore, in Table B.1 we only present the number of

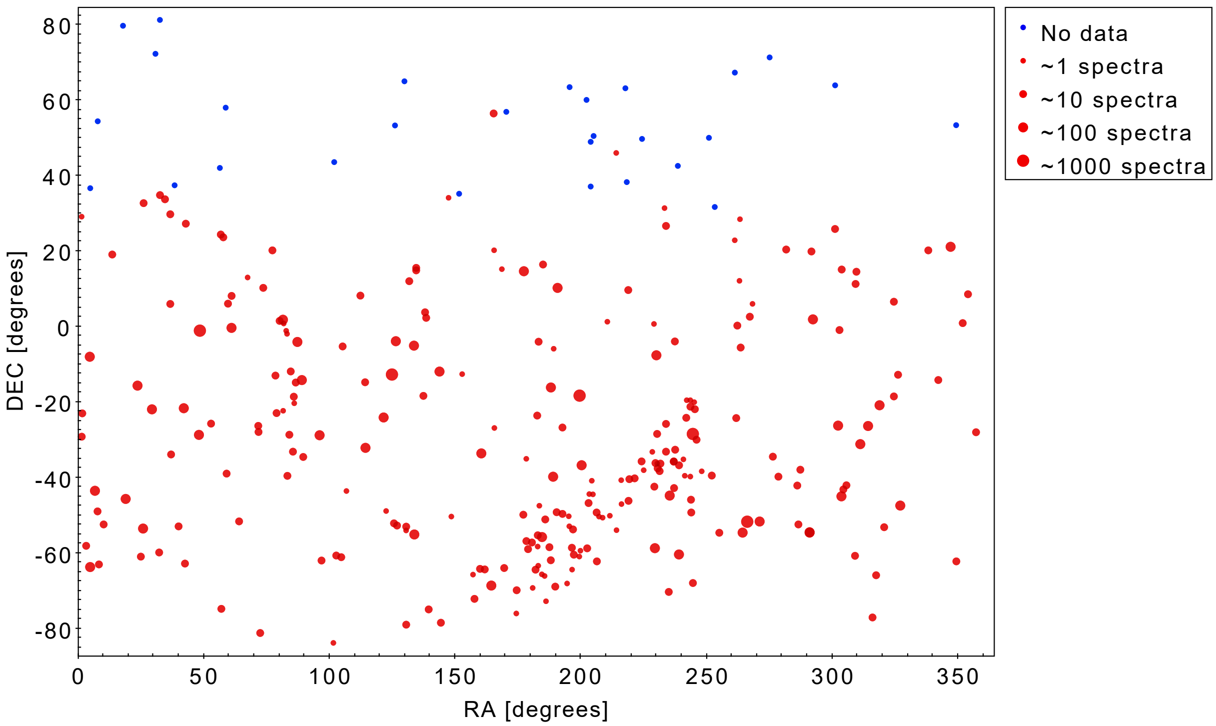

Figure 2.1: Coordinates of all the objects in our sample. Spectroscopic data were obtained for all the objects shown in red.

observations covering the Ca II doublet to better assess the number of single observations we have collected (although, in some cases we collected UVES observations covering other ranges). The actual total amount of spectra covering all the different ranges used in this Thesis reaches ~17'500 spectra.

2.1 Proprietary data

2.1.1 FEROS observations

We performed observations with the FEROS Échelle spectrograph during two nights under the ESO Programme ID 096.A-9018(A). The instrument choice was motivated by its characteristics: large wavelength range (the complete optical spectral region from ~3500Å to ~9200Å in only one exposure), high resolution (R = 48,000) and high spectral stability, which makes it suitable for detecting narrow absorption features in a wide variety of spectral lines. The spectra were taken with exposure times computed with the online FEROS Exposure Time Calculator[1] to obtain a signal-to-noise ratio (S/N hereafter) of about ∼150 around the blue wavelength range. Standard calibrations were taken and the FEROS DRS[2] (Data Reduction Software) with the default parameters was used to reduce the data. The reduced spectra were corrected for telluric contamination (see Sec. 2.3).

Additional proprietary data from FEROS obtained from the Programmes 0101.A-9012(A), 0102.A-9008(A) and 0103.A-9010(A) were used for this project. These observations were reduced using the CERES pipeline (Brahm et al., 2017). In this case, wavelengths were transformed from the default vacuum wavelength calibration to observed wavelength in air. All these proprietary FEROS data are shown in Table B.1 with a *.

2.1.2 UVES observations

We obtained UVES spectra in service mode during periods under the ESO Programme IDs: 096.C-0238(A), 097.C-0409(A), 097.C-0409(B), 098.C-0463(A), 098.C-0463(B), 098.C-0463(C), 0102.C-0547(A), and 0102.C-0564(A). These spectra are listed in Table B.1 with a *. Data from Programme 096.C-0238(A) were observed with the blue arm centred at 4370Å and with a spectral coverage of 3731–4999Å and data from all the other Programmes were observed in dichroic mode with the blue arm centred at 3900Å and the red arm centred at 5800Å, covering the spectral ranges 3282–4562Å and 4726–6835Å, respectively. The narrowest slits were used in order to achieve the maximum resolution possible; the 0.4″ slit in the blue arm and the 0.3″ slit in the red arm, yielding resolutions of 80,000 and 110,000, respectively. Exposure times were computed with the online UVES Exposure Time Calculator[3] aiming to obtain a S/N ∼150 (achieved for most of the spectra) around the blue wavelength range under thick (very low transparency) sky conditions. Standard calibrations were also taken and the ESO pipeline[4] with the default parameters was used to reduce the data. The spectra were a posteriori corrected for telluric contamination (see Sec. 2.3) and barycentric radial velocity shifts were corrected by the value provided in the header by the ESO pipeline.

[1]https://www.eso.org/observing/etc/bin/gen/form?INS.NAME=FEROS+INS.MODE=spectro
[2]https://www.eso.org/sci/facilities/lasilla/instruments/feros/tools/DRS.html
[3]https://www.eso.org/observing/etc/bin/gen/form?INS.NAME=UVES+INS.MODE=spectro
[4]http://www.eso.org/sci/software/pipelines/

2.1.3 MIKE observations

We obtained observations with MIKE double echelle spectrograph in visitor mode during two runs (a total of three nights) awarded for this project. These observations are listed in Table B.1 with a *. We took our observations using the dichroic in the standard configuration, which reaches a wavelength coverage from about 3350-5000Å in the blue arm and 4900-9500Å in the red arm. We used the 0.35″ slit (the smallest slit available) in order to achieve the highest resolution; 83,000 on the blue side and 65,000 on the red side. Since the objects we observed are very bright (Vmag<11) we used no binning and fast readout mode as it is possible to achieve high S/N within short exposure times. The exposure times were computed following the MIKE User Manual[5] aiming a S/N ∼200. Standard calibrations were taken, including a bright B-type star during twilight using a "milky flat" diffuser for flat field corrections. The spectra were reduced with the Carnagie CarPy pipeline (Kelson et al. 2000, Kelson 2003) and barycentric radial velocity shifts were corrected using the PyAstronomy package (Czesla et al., 2019).

2.1.4 FIES observations

We collected observations from FIES spectrograph (Telting et al., 2014), mounted at the 2.5m Nordic Optical Telescope (NOT) located at El Roque de los Muchachos Observatory in Canary Islands, Spain (shown in Table B.1 with a *). The instrument counts with a 1.3″ fibre offering a maximum spectral resolution of R=67,000, which was used for these observations, and covers a spectral range of 370-830nm. Observations reach a S/N in the order of ∼100 near the Ca II doublet. Data reduction were performed with the dedicated reduction software (FIEStool[6]) and barycentric corrections were applied a posteriori.

2.1.5 HERMES observations

Observations from HERMES spectrograph (Raskin et al., 2011) attached at the 1.5 m Mercator Telescope at El Roque de los Muchachos Observatory in Canary Islands, Spain, were also collected for this Thesis, as shown in Table B.1 (marked with a *). HERMES covers a wavelength range from 380 to 900nm with a spectral resolution of R∼85,000 in a single exposure.

[5] http://www.lco.cl/Members/magins/mike-kb/mike-user-manual
[6] http://www.not.iac.es/instruments/fies/fiestool/

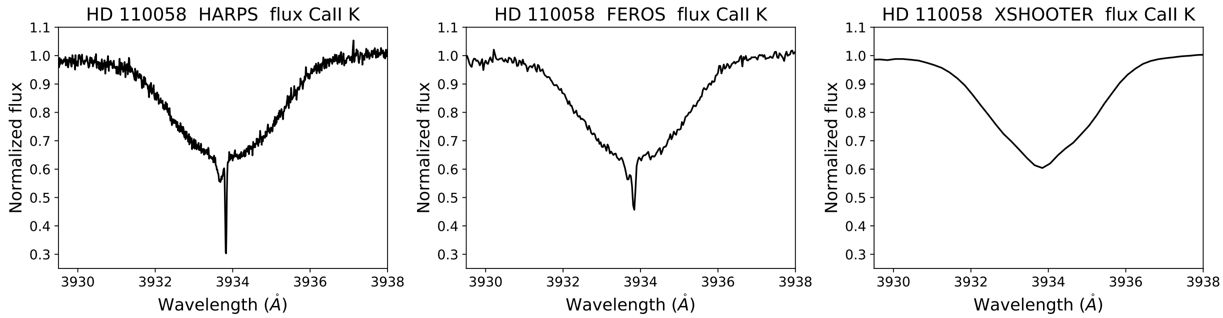

Figure 2.2: Absorption profiles of the Ca II K of the object HD 110058 taken with HARPS, FEROS and XSHOOTER spectrographs, respectively.

The collected observations have a S/N of ∼100 near the Ca II H & K lines. Data reduction were performed using a dedicated automated data reduction pipeline and radial velocity toolkit (HermesDRS[7]) and barycentric corrections were applied to the reduced spectra.

2.2 Archival data

We queried the ESO archive looking for optical spectra with resolution high enough to detect narrow absorption features with widths in the order of ∼0.1Å. This restricted the instruments to HARPS, UVES and FEROS. Initially, we had considered including XSHOOTER data in our analysis, but soon we realized that its resolution (which reaches a maximum of 9'700 in the UV) is not capable of resolving the narrow features we are searching for. An example of this is given in Fig. 2.2. Here we show a comparison of the Ca II K line of the object HD 110058, which presents both an interstellar absorption (shallow feature at the left) and a circumstellar absorption (deep feature at the right) observed with HARPS, FEROS and XSHOOTER. Clearly the features (which are stable) are not detected with XSHOOTER. FEROS has the lowest resolution among all the spectrographs used in this study (while HARPS provides the highest) but its resolution is high enough (R=48,000) to detect narrow absorptions. Our targets have been observed multiple times (e.g., searching for planets via radial velocity variations), hence we found a large number of spectra (from one spectrum up to 3000 spectra). Consequently, a considerable fraction of our dataset comes from archival data.

[7]`https://www.aao.gov.au/science/software/2dfdr`

2.2.1 HARPS data

HARPS is an echelle spectrograph fed by a pair of fibres, one of them collects the star light, while the second is used to either record simultaneously a Th-Ar reference spectrum or the background sky. HARPS spectra covers the wavelength range 3780–6910Å, has a spectral resolution of 120,000 and has been optimised for mechanical stability, which makes it ideal for our study. We retrieved several epochs of HARPS data for the debris disks listed in Table B.1. All these observations were already reduced with the HARPS DRS[8] (Data Reduction Software) and corrected for heliocentric radial velocity shifts, and we then corrected for telluric contamination (see Sec. 2.3).

2.2.2 UVES data

Additional to the HARPS data, we found a considerable number of UVES observations for our sample (see Table B.1). UVES is a two-arm cross-dispersed echelle spectrograph, its blue arm covers the wavelength range 3000–5000Å and the red arm covers 4200–11000Å. Overall, the spectral coverage depends on the instrumental set-up used for the observations since UVES allows the use of dichroic beam splitters, but in general we have spectra covering the ranges 3043–3916Å, 3236–4563Å, 3731–4999Å, 4549–6686Å, 4726–6835Å and 6650–10426Å. These UVES data had already been reduced with dedicated ESO pipelines but additional corrections of heliocentric radial velocity shifts and telluric contamination were necessary.

2.2.3 FEROS data

We also retrieved FEROS archival data for some of our targets (Table B.1). Similarly to the HARPS data, the FEROS observations were reduced with the available instrument pipelines and corrected for heliocentric radial velocity shifts. Posterior corrections for telluric contamination were performed.

[8] `https://www.eso.org/sci/facilities/lasilla/instruments/harps/doc/DRS.pdf`

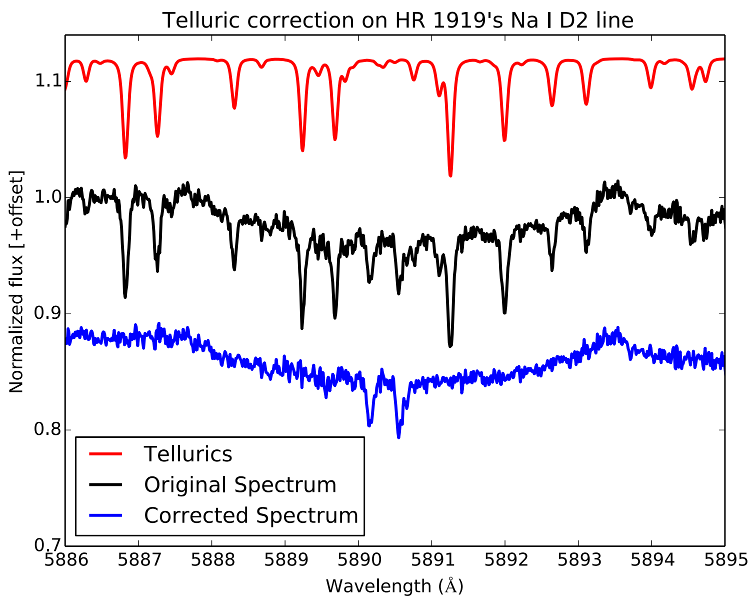

Figure 2.3: Example of telluric correction in HR 1919's Na I D2 line. Telluric lines modeled by molecfit in red, original spectrum in black, and corrected spectrum in blue. The different spectra are shifted with respect to each other for clarity.

2.3 Telluric lines correction

The red domain of the spectra contains many telluric absorption features mostly due to water vapour, O_2 and O_3. Since one of our main tracers is the sodium doublet at 5895.9 and 5889.9Å, it is imperative to perform a correct subtraction of telluric contamination. To this end, we used `Molecfit`[9] (Smette et al. 2015, Kausch et al. 2015), a tool developed to correct observations for telluric absorption which can be used for any kind of spectra without the need to observe a standard star. We used the wavelength range 5902.5-5927.0Å to fit the continuum but excluded gas absorption features to ensure that they do not affect our best-fitting result. We successfully removed telluric absorptions and reduced them to the noise level (i.e. they were reduced by about 99%). An example of the telluric correction is shown in Figure 2.3.

[9] http://www.eso.org/sci/software/pipelines/skytools/molecfit

Chapter 3

Debris disks with multiple absorption features in metallic lines: circumstellar or interstellar origin?

This chapter is a slightly improved version of the paper: Iglesias, D., Bayo, A., Olofsson, J., Wahhaj, Z., Eiroa, C., Montesinos, B., Rebollido, I., Smoker, J., Sbordone, L., Schreiber, M. R., and Henning, T. (2018). “Debris discs with multiple absorption features in metallic lines: circumstellar or interstellar origin?”, published in Montly Notices of the Royal Astronomical Society, 480(1): 488–520.

The main change we made with respect to the publication was including the analysis of four additional objects: HD 144981, HD 145554, HD 145631 and HR 6051. Thus here we present the analysis of a sample of 27 objects instead of 23 as in the paper. The introduction of the paper was not included in this chapter as the scientific context is already given in the introduction of this Thesis. The inclusion of the four new objects in this chapter did not affect the overall conclusions with respect to the previously published.

3.1 Sub-sample

In this chapter, we present a sub-sample of 27 gas-bearing debris disk candidates characterized by showing detections of non-photospheric absorption features at different radial velocities within our database of observations prior to December 2016. The main properties of this sub-sample are detailed in Tables 3.1 and 3.2. Unless otherwise indicated, most of the stellar parameters reported in Table 3.2 were retrieved from the Simbad database (Wenger et al., 2000). In particular, distances came from the Tycho-Gaia Astrometric Solution (TGAS) from the Gaia data-release 1 (Gaia Collaboration et al., 2016) or from the Hipparcos new reduction of van Leeuwen (2007) when the former were not available. Luminosities are estimated via SED fitting (assuming the previously mentioned distances) with Kurucz models (Castelli et al., 1997) using VOSA[1] (Bayo et al., 2008). Isochronal ages are estimated with VOSA based on the SED fitted parameters and different sets of isochrones (Siess et al. 2000, Baraffe et al. 1998). Note that the large uncertainties in isochronal ages are attributable to uncertainties in the distance to the objects and/or the set of isochrones assumed for the estimates (further discussion on the ages of the sample will be given in Olofsson at al. in prep.). For those objects confirmed to belong to young moving groups (i.e. β03 Tuc, 66 Psc, ν Hor, HD 24966, HD 54341, η Cha, HD 110058, HD 144981, HD 145554, HD 145631, HR 6051 and HR 6507), we have adopted the literature age commonly assigned to those moving groups (in principle more precise than isochronal dating). The multiplicity column highlights objects reported in the literature to be multiple systems.

As mentioned before, the 27 candidates presented in this chapter have been chosen because they display particularly interesting gas absorption features: they all have not only one, but multiple, stable, absorptions at different radial velocities with respect to the star within the 15 years of baseline considered for this analysis. Merely by statistical arguments, this multiplicity increases the chances of a circumstellar gas detection, and for the cases that a circumstellar origin for several simultaneous features could be confirmed, it would imply a very interesting disk configuration and/or geometry. For instance, a disk containing several gas rings at different distances from the star or different populations of exocomets, which would require further study and possible follow-up with high angular resolution instruments like ALMA. A description of the

[1] http://svo2.cab.inta-csic.es/theory/vosa/

Table 3.1: Sub-sample of gas-bearing debris disk candidates with multiple absorption features and their respective coordinates.

Name	HD Id	R.A. [J2000]	Dec. [J2000]
β03 Tuc	HD 3003	00:32:43.9	-63:01:53.4
66 Psc	HD 5267	00:54:35.2	+19:11:18.3
ν Hor	HD 17848	02:49:01.5	-62:48:23.5
HD 24966	HD 24966	03:56:29.4	-38:57:43.8
HD 290540	HD 290540	05:31:31.4	-01:49:33.3
HD 36444	HD 36444	05:31:40.5	-01:07:33.3
HD 290609	HD 290609	05:33:05.6	-01:43:15.5
HR 1919	HD 37306	05:37:08.8	-11:46:31.9
HD 54341	HD 54341	07:06:20.9	-43:36:38.7
HD 60856	HD 60856	07:35:56.9	-14:42:39.0
HR 3300	HD 71043	08:22:55.2	-52:07:25.4
η Cha	HD 75416	08:41:19.5	-78:57:48.1
HD 92536	HD 92536	10:39:22.8	-64:06:42.4
3 Crv	HD 105850	12:11:03.8	-23:36:08.7
HD 106036	HD 106036	12:12:10.3	-63:27:14.8
HR 4796	HD 109573	12:36:01.0	-39:52:10.2
HD 110058	HD 110058	12:39:46.2	-49:11:55.5
HD 112810	HD 112810	12:59:59.9	-50:23:22.5
HD 126135	HD 126135	14:24:43.9	-40:45:18.6
HD 141378	HD 141378	15:48:56.8	-03:49:06.6
HD 141327	HD 141327	15:49:43.1	-32:48:29.8
HD 144981	HD 144981	16:09:20.9	-19:27:25.9
HD 145554	HD 145554	16:12:21.8	-19:34:44.6
HD 145631	HD 145631	16:12:44.1	-19:30:10.3
HR 6051	HD 145964	16:14:28.9	-21:06:27.5
HR 6507	HD 158352	17:28:49.7	+00:19:50.3
cAql	HD 183324	19:29:00.9	+01:57:01.6

Table 3.2: Stellar parameters for the sample.

Name	$v\sin i$ [km.s^{-1}]	Spectral Type	radV [km.s^{-1}]	distance [pc]	Isochronal Age [Myr]	Literature Age [Myr]	$\log(L_{bol}(L_\odot))$ [dex]	Multi-plicity
β03 Tuc	93	A0V	7.70±0.80	45.56±0.394[b]	$115.48\pm^{137.30}_{115.48}$	30.0[d] $\pm^{0.0}_{20.0}$	$1.19\pm^{0.01}_{0.01}$	✓[j]
66 Psc	144	A1Vn	8.50±2.80	108.11±7.48[b]	$5.00\pm^{0.98}_{0.31}$	200[e]	$1.46\pm^{0.06}_{0.07}$	✓[k]
ν Hor	143.7	A2V	30.90±2.00	52.13±1.76[c]	$529.02\pm^{103.10}_{129.08}$	100[e]	$1.23\pm^{0.04}_{0.05}$	–
HD 24966	–	A0V	–	105.82±4.03[b]	$195.41\pm^{102.01}_{195.41}$	10[e]	$1.13\pm^{0.04}_{0.04}$	–
HD 290540	–	A2	–	357.32±54.90[c]	$11.57\pm^{338.74}_{11.57}$	112[f]	$1.23\pm^{0.12}_{0.17}$	–
HD 36444	–	B9V	–	458.20±98.20[c]	$4.33\pm^{603.23}_{1.33}$	101[f]	$1.57\pm^{0.16}_{0.26}$	–
HD 290609[1]	–	A0	–	23.86±11.43[b]	–	5[g]	$2.41\pm^{0.44}_{0.00}$	–
HR 1919	148.1	A1V	23.00±0.70	70.76±4.15[c]	$28.52\pm^{307.72}_{28.52}$	453[f]	$1.10\pm^{0.06}_{0.07}$	–
HD 54341	–	A0V	–	102.35±3.77[b]	$7.94\pm^{391.30}_{0.97}$	10[e]	$1.34\pm^{0.05}_{0.05}$	–
HD 60856	44	B5V	31.20±1.90	363.83±88.54[c]	$2.19\pm^{595.55}_{0.20}$	196[f]	$1.84\pm^{0.17}_{0.29}$	–
HR 3300	224	A0V	22.50±1.10	70.03±1.13[b]	$710.26\pm^{111.03}_{701.81}$	404[f]	$1.11\pm^{0.02}_{0.02}$	–
η Cha	296[a]	B8V	14.00±7.40	94.97±1.44[b]	$3.09\pm^{297.86}_{0.09}$	6.0[d] $\pm^{1.0}_{0.0}$	$1.80\pm^{0.03}_{0.03}$	–
HD 92536	–	B8V	10.00±1.00	145.13±8.75[c]	$4.04\pm^{0.49}_{0.90}$	231[f]	$1.66\pm^{0.07}_{0.08}$	–
3 Crv	126.8	A1V	11.00±4.20	58.82±1.94[b]	$907.37\pm^{92.96}_{899.21}$	465[f]	$1.14\pm^{0.04}_{0.05}$	–
HD 106036	–	A2V	7.70±1.30	99.00±3.87[c]	$463.25\pm^{238.95}_{463.25}$	17[h]	$0.98\pm^{0.05}_{0.05}$	–
HR 4796	152.0	A0V	7.10±1.10	72.78±1.75[b]	$69.59\pm^{30.88}_{69.59}$	378[f]	$1.56\pm^{0.05}_{0.05}$	✓[l]
HD 110058	–	A0V	5.00±1.20	188.76±34.11[c]	$560.29\pm^{48.08}_{560.29}$	10[e]	$1.24\pm^{0.19}_{0.34}$	–
HD 112810	82	F3/5IV/V	4.20±1.20	134.60±7.22[c]	$1997.73\pm^{1012.17}_{1997.73}$	10[i]	$0.46\pm^{0.05}_{0.05}$	–
HD 126135	–	B8V	12.00±6.00	165.02±16.34[b]	$5.00\pm^{692.27}_{0.80}$	103[f]	$1.44\pm^{0.10}_{0.08}$	–
HD 141378	107	A5IV-V	-16.40±2.00	55.54±2.32[c]	$10.05\pm^{0.65}_{0.15}$	587[f]	$0.99\pm^{0.04}_{0.04}$	–
HD 141327	–	B9V	-5.10±2.40	213.29±22.48[c]	$4.88\pm^{794.54}_{0.88}$	196[f]	$1.46\pm^{0.09}_{0.12}$	–
HD 144981	155.20	A0V	-1.30±1.90	148.05±10.17[c]	$8.69\pm^{1.17}_{1.53}$	11[m]	$1.11\pm^{0.08}_{0.07}$	✓[n]
HD 145554	340	B9V	-6.15±2.57	153.85±11.26[c]	$4.00\pm^{76.72}_{4.00}$	11[m]	$1.99\pm^{0.10}_{0.13}$	–
HD 145631	287.00	B9V	-5.56±0.21	144.39±8.88[c]	$4.02\pm^{93.26}_{4.02}$	11[m]	$1.90\pm^{0.07}_{0.08}$	–
HR 6051	306	B9V	-7.80±1.70	108.70±6.85[b]	$7.16\pm^{737.63}_{1.59}$	11[m]	$1.30\pm^{0.06}_{0.06}$	–
HR 6507	180	A8Vp	-36.10±2.00	59.63±0.93[b]	$7.83\pm^{0.22}_{0.72}$	600[e]	$1.17\pm^{0.01}_{0.01}$	–
cAql	110	A0IVp	12.00±4.30	61.20±1.35[b]	$60.55\pm^{0.00}_{60.55}$	506[f]	$1.29\pm^{0.05}_{0.06}$	–

[a]Zorec and Royer (2012), [b]van Leeuwen (2007), [c]TGAS, [d]Torres et al (in prep.), [e]Rhee et al. (2007), [f]Gontcharov (2012), [g]Hernández et al. (2006), [h]Mittal et al. (2015), [i]Ballering et al. (2013), [j]Dommanget and Nys (2002), [k]Docobo and Ling (2007), [l]Jura et al. (1993), [m]Pecaut et al. (2012), [n]Andrews et al. (2017).

[1]Distances reported for this object range from ∼24 pc (van Leeuwen, 2007) to ∼775 pc (Kharchenko, 2001); both of those estimates report huge uncertainties (above 50%), and propagate to unrealistic luminosities and thus isochronal ages. For this reason we do not include this object in any comparative analysis that involves age, luminosity and/or distance.

data used in this study is shown in Table 3.3.

3.2 Methods and results

We analysed the calcium H & K lines at 3968.47 and 3933.66Å and the sodium D1 & D2 lines at 5895.92 and 5889.95Å, respectively. The aim is to detect narrow absorption lines superimposed on the photospheric line. These "extra" absorption lines indicate the presence of gas in the line of sight of the star. To determine the nature of the gas we followed different approaches, that we detail in the following sub-sections.

The first step in our analysis is to measure the radial velocity of the stars. Afterwards, we determined the photospheric contribution for each line either by performing spectral synthesis or by finding a "spectral twin". Then, we identified additional (stable or transient) components by removing the photospheric contribution before characterizing their properties.

Additionally, we also searched for signatures of Diffuse Interstellar Bands (DIBs), compared the radial velocity of the absorption features to the radial velocities of known local clouds and searched for similar extra absorption lines in nearby stars to better assess their nature.

3.2.1 Radial velocities

Since five of our objects did not have any reported radial velocity measurements in the literature, we performed our own estimates for all objects aiming at a homogeneously determined set of values and to assess the accuracy of our results.

In a first attempt to obtain the radial velocities, we computed the cross correlation function for every epoch of each object using a synthetic model as a template. Unfortunately, since most of our objects are fast rotators, their absorption lines have very wide profiles, and we did not obtain consistent results between all the epochs, with dispersions up to $30\,\mathrm{km.s^{-1}}$. Therefore, we decided to take a different approach and use a simpler but, in this case, more suitable technique. For every epoch of each object we fit Lorentzian profiles to the most prominent absorption lines in our spectra: Hα, Hβ, Hγ and Hδ. We excluded Hϵ because it is blended with the Ca II H line. We used a range of 1000 $\mathrm{km.s^{-1}}$ for the profile fitting of each (previously normalized) line in velocity space and obtained the radial velocity of the line from the position of the profile with

Table 3.3: Number of spectra for each star per date, instrument, ESO observing period and dates of observations. Observations from our programmes are flagged with a *.

Name	Number of Spectra	Instrument	Period	Observation dates
β03 Tuc	6, 4, 2, 2, 2	HARPS	P73, P75, P77, P77, P77	2004-09-30, 2005-08-19, 2006-05-[20, 25, 26]
	2, 2, 2, 2, 2, 2	HARPS	P84, P84, P84, P84, P84, P84	2009-11-[12, 13, 14, 15], 2009-12-[05, 08]
	2, 2, 2, 2	HARPS	P85, P86, P86, P87	2010-07-07, 2011-01-[06, 07], 2011-07-23
	1, 1	FEROS	P96, P96	2015-10-[23, 24]
66 Psc	1, 2	UVES	P96, P97	2015-11-14*, 2016-07-23*
ν Hor	6, 2, 2	HARPS	P75, P75, P77	2005-08-19, 2005-09-09, 2006-09-11
	2, 2, 2, 6, 2	HARPS	P80, P80, P80, P94, P94	2007-12-[05, 06, 10], 2015-01-[18, 20]
HD 24966	1	FEROS	P96	2016-01-04*
	2, 2, 2	UVES	P97, P97, P97	2016-07-23*, 2016-08-[21, 29]*
HD 290540	1, 1	FEROS	P96, P96	2016-01-[03, 04]*
HD 36444	1	FEROS	P96	2016-01-04*
HD 290609	1	FEROS	P96	2016-01-04*
HR 1919	4, 2, 2, 2, 2, 2	HARPS	P76, P76, P76, P76, P76, P76	2006-02-[08, 09, 10, 11, 13], 2006-03-12
	2, 2, 2, 2	HARPS	P78, P80, P80, P80	2006-11-18, 2007-12-[05, 06, 10]
	2, 1, 1	FEROS	P96, P96, P96	2015-10-23, 2016-03-[28, 29]
HD 54341	3, 1	HARPS	P94, P94	2015-01-[19, 20]
HD 60856	1	FEROS	P96	2016-01-04*
HR 3300	6, 2, 2	HARPS	P94, P4, 94	2015-01-[18, 20, 21]
	1, 2, 3, 3	FEROS	P82, P82, P82, P88	2008-11-[18, 21, 22], 2011-12-07
	1, 1	FEROS	P96, P96	2015-10-23, 2016-03-26
η Cha	2, 3	UVES	P66, P66	2001-02-[16, 18]
	3, 6, 2	HARPS	P60, P94, P94	2005-02-12, 2015-01-[19, 20]
	2, 2, 5	FEROS	P60, P60, P60	2006-10-24, 2006-12-08, 2007-01-01
	4, 4, 4	FEROS	P60, P60, P60	2007-2-[16, 23, 24]
	1, 1, 1	FEROS	P84, P84, P84	2009-11-30, 2009-12-[05, 07]
	1, 1, 1, 1, 1, 1	FEROS	P84, P84, P84, P84, P85, P85	2010-01-[27, 28, 29, 30], 2010-06-[01, 14]
HD 92536	3, 3, 2, 1	HARPS	P94, P94, P94, P94	2015-01-[18, 19, 20, 21]
3 Crv	6, 2, 2, 2, 2	HARPS	P77, P77, P77, P80, P84	2006-05-[20, 21, 25], 2007-12-10, 2009-12-05
	4, 2, 6, 2	HARPS	P85, P85, P86, P86	2010-07-[08, 09], 2011-01-[04, 07]
	2, 2, 2, 2	HARPS	P86, P86, P86, P87	2011-02-[4, 5, 6], 2011-07-21
	1, 1	FEROS	P96, P96	2016-03-[26, 29]
HD 106036	2	UVES	P96	2016-02-21*
HR 4796	74, 152, 76, 76, 92, 16	UVES	P68, P79, P79, P79, P79, P79	2002-01-19, 2007-05-[07, 08, 13, 14, 15]
	2, 3, 2, 3	HARPS	P80, P94, P94, P94	2007-12-06, 2015-01-[19, 20, 21]
	1, 1, 2, 1, 1	FEROS	P79, P79, P79, P79, P79	2007-03-09, 2007-05-[01, 04, 12, 27]
	2, 3, 4, 3	FEROS	P96, P96, P96, P96	2016-03-[26, 27, 28, 29]
HD 110058	2, 1	FEROS	P84, P87	2010-01-31, 2011-04-16
	6, 2, 2, 2	HARPS	P94, P94, P94, P94	2015-01-[18, 19, 20, 21]
HD 112810	2	UVES	P96	2016-03-23*
HD 126135	1, 1, 2	HARPS	P94, P94, P94	2015-01-[18, 20, 21]
HD 141378	1	FEROS	P92	2014-02-18
HD 141327	1, 1, 2	FEROS	P79, P81, P82	2007-04-02, 2008-04-01, 2009-02-06
HD 144981	1	FEROS	P96	2016-03-28
HD 145554	1	FEROS	P96	2016-03-29
HD 145631	1	FEROS	P96	2016-03-29
HR 6051	1, 1, 1, 1	FEROS	P96, P96, P96, P96	2016-03-[26, 27, 28, 29]
HR 6507	4, 2, 2, 2	HARPS	P75, P77, P77, P77	2005-08-20, 2006-05-[20, 25], 2006-09-12
	2, 5, 2, 2	HARPS	P80, P80, P84, P84	2008-03-[17, 21], 2010-07-[08, 09]
	6	UVES	P83	2009-04-16
c Aql	10, 38	UVES	P79, P87	2007-06-30, 2011-05-27
	1, 1, 1	FEROS	P83, P83, P83	2009-06-[02, 03], 2009-08-24
	1, 1, 1	FEROS	P85, P85, P85	2010-07-22, 2010-08-[23, 31]

respect to the rest frame.

In order to address possible changes in the estimates of radial velocities due to activity, we checked all our objects for emission features in the Balmer lines (not only for emission dominated lines, but also for shallow core emissions). Only one object, namely HD 60856, presents emission features in these lines. This emission is dominating the full line in the case of Hα and thus it was not possible to model the photospheric profile. Therefore, only for this object, we decided to exclude Hα from the radial velocity measurements. In addition, we bootstrapped each of the remaining Balmer lines to estimate the impact of a core emission in our fitting procedure. The standard deviation for the radial velocity from this procedure with 1000 realizations was $\sim$1.6 km.s^{-1}. This object has only one epoch of observations, therefore our estimated uncertainty for the radial velocity takes into account the individual line fitting uncertainties and the dispersion found among the different lines.

For all the other objects, since the cores of the lines appeared purely photospheric, we averaged over all the epochs and lines, and the uncertainties were derived propagating the estimated errors.

In most cases, our radial velocity measurements are in good agreement with the ones found in the literature (see Table 3.2), having average differences of $\sim$3 km.s^{-1}. However, the radial velocity value we determined for ν Hor differed by $\sim$17 km.s^{-1} with respect to the literature. We compared both radial velocity values when fitting Kurucz (Castelli et al., 1997) models (see Section 3.2.2) and concluded that our estimate provides a better match to our data. In general, although differences with the literature were relatively small, in the model fitting process we always obtained a better fit when shifting the model to our own estimates of radial velocity. In any case, the large difference found for ν Hor is not that surprising given the high dispersion in the measurements provided from different datasets in Wilson (1953), the reference adopted in Simbad. Finally, we must also note that, for the whole sample, no significant shifts were found between epochs, obtaining velocity dispersions per object of the order of $\sim$2 km.s^{-1}. Our resulting radial velocity estimates are shown in Table 3.4.

3.2.2 Spectral synthesis

For most objects (except HD 112810, see Sec. 3.2.3), we used Kurucz models (Castelli et al., 1997) to fit and normalize the photospheric absorption, thus isolating the additional absorp-

Table 3.4: Stellar parameters determined from the synthetic model fitting and radial velocity estimates computed as described in Section ??. Radial velocity of stars in multiple or binary systems are flagged with *. The typical uncertainties for the estimates of $v\sin i$ and $T_{\rm eff}$(Ca II K), are of ∼5 km.s^{-1} and 5-10%, respectively. Dispersion values come from the measurements in the four different lines or from the grid step size (entries marked with ^{g}) when the four lines yielded the same values.

Name	$v\sin i$ [km.s^{-1}]	radV [km.s^{-1}]	$T_{\rm eff}$(Ca II K) [K]	$\log g$ [dex]	[Fe/H]
β03 Tuc	100	6.05 ± 1.60*	9550	4.00 ± 0.50	+0.17 ± 0.20
66 Psc	150	4.32 ± 2.66*	10750	3.90 ± 0.23	-0.38 ± 0.54
ν Hor	140	13.58 ± 1.67	8300	4.25 ± 0.25	-0.20 ± 0.31
HD 24966	210	15.70 ± 3.15	9250	4.38 ± 0.22	-0.03 ± 0.58
HD 290540	200	27.26 ± 3.12	10500	4.25 ± 0.25	-0.88 ± 0.22
HD 36444	360	26.72 ± 4.50	10250	4.00 ± 0.35	-0.62 ± 0.65
HD 290609	100	25.87 ± 1.65	10500	3.88 ± 0.41	-0.07 ± 0.26
HR 1919	140	23.49 ± 1.28	8800	4.15 ± 0.38	-0.12 ± 0.22
HD 54341	140	41.03 ± 0.95	10500	4.50 ± 0.25^g	-0.12 ± 0.22
HD 60856	40	34.78 ± 3.58	14000	4.12 ± 0.22	-0.38 ± 0.41
HR 3300	210	22.35 ± 0.72	9550	4.25 ± 0.25	+0.10 ± 0.37
η Cha	280	15.21 ± 1.41	11750	3.75 ± 0.25	-0.88 ± 0.22
HD 92536	180	15.45 ± 0.44	11150	3.88 ± 0.41	-0.45 ± 0.55
3 Crv	130	14.41 ± 1.09	8500	4.12 ± 0.22	+0.17 ± 0.41
HD 106036	160	9.37 ± 2.34	9000	4.50 ± 0.25^g	+0.00 ± 0.25^g
HR 4796	150	5.35 ± 2.94*	9800	4.25 ± 0.25	-0.07 ± 0.26
HD 110058	150	11.20 ± 0.81	9000	4.03 ± 0.36	-0.33 ± 0.47
HD 112810	–	5.25 ± 2.24	–	–	–
HD 126135	310	11.73 ± 0.67	11250	3.88 ± 0.41	-0.62 ± 0.65
HD 141378	80	-14.68 ± 2.62	8750	4.50 ± 0.25^g	+0.42 ± 0.13
HD 141327	250	-4.65 ± 2.40	10550	4.00 ± 0.35	-0.50 ± 0.50
HD 144981	210	-6.47 ± 1.59	10000	4.38 ± 0.22	-0.12 ± 0.41
HD 145554	250	-9.66 ± 1.49	10750	3.88 ± 0.41	-1.00 ± 0.25^g
HD 145631	300	-9.86 ± 1.90	9750	4.00 ± 0.35	-1.00 ± 0.25^g
HR 6051	320	-7.26 ± 4.11	10250	3.77 ± 0.28	-1.00 ± 0.25^g
HR 6507	140	-36.13 ± 2.49	7750	4.25 ± 0.25	+0.28 ± 0.13
c Aql	90	17.29 ± 2.61	9700	4.35 ± 0.26	-0.57 ± 0.49

tion lines. The models were computed using the spectral synthesis codes `SYNTHE` and `ATLAS 9` (Sbordone et al., 2004).

For each line we computed the normalized median spectrum from all the epochs, to use it as a robust reference for the fitting process. Since the radial velocity dispersion along all the epochs is small ($\sim$2 km.s^{-1}), the median can be used as a good reference. For each of the median spectrum, the uncertainties are derived using the standard deviation of all epochs if there are more than 2 epochs. For objects with only one or two epochs, the pipelines do not always provide uncertainties. Therefore, for each wavelength point, we estimate the standard deviation in a moving box with a width of 33 wavelength points. Then, we computed a grid of models with different stellar parameters for the wavelength ranges containing the Ca II and Na I doublets. The free parameters that can be investigated in the modelling process are: the effective temperature $T_{\rm eff}$, the surface gravity $\log g$, the metallicity [Fe/H], turbulent velocity, additional turbulence, opacity threshold for the lines, and projected rotational velocity $v\sin i$. We adopted standard values for the turbulent velocity, additional turbulence and opacity threshold; and explored the remaining parameters: $T_{\rm eff}$, $\log g$, [Fe/H] and $v\sin i$. Table 3.5 summarizes the fixed values and range of parameters that we explored in the fitting process. Those ranges were chosen according to previous estimates available in the literature. Our model fitting procedure consists of a simple two-step χ^2 minimization. The fits were performed for each line independently since, possibly due to non-Local Thermodynamic Equilibrium (non-LTE) effects (Mashonkina et al. 2000, Plez 2013 and Sitnova et al. 2017), it is hardly possible to obtain good matches for all of them simultaneously. The only parameter determined using all the lines at once is $v\sin i$. The first step consists of estimating approximate values for all the parameters, within a coarse grid of models. The step sizes are reported in Table 3.5. Afterwards, we used a simplex downhill method with finer interpolations for $T_{\rm eff}$ and $\log g$, with steps of 50 K and 0.1 dex, respectively. To avoid local minima, we repeated the simplex downhill algorithm several times (6–10 times, depending on the convergence of each object), initializing it from different regions of the parameter space that yielded similar (a factor 2 with respect to the minimum) χ^2 values in the coarse grid. The convergence criterion for the downhill algorithm was set to an improvement in the goodness of fit by 10^{-4}. Given that Ca II K is the most sensitive photospheric temperature tracer among all the lines studied (Gray and Corbally, 2009), in Table 3.4 we report as the best fitting temperature

Table 3.5: Adopted and explored values for the parameters of the Kurucz models.

Parameter	Values
Turbulent Velocity	2.0 km.s^{-1}
Additional Turbulence	0.0 km.s^{-1}
Opacity Threshold	0.001
$T_{\rm eff}$	6000–13000 K, with Δ=250 K
$\log g$	[3.5, 4.0, 4.5]
$[Fe/H]$	[-1.0, -0.5, 0.0, +0.2, +0.5]
$v\sin i$	20–400 km.s^{-1}, with Δ=10 km.s^{-1}

the one obtained for that line. A rather conservative confidence interval is estimated from all the models that returned a relative change in χ^2 smaller than 50% compared to the best fitting model. On the other hand, for $\log g$ and [Fe/H], we provide an average of the values obtained for the four lines, and the associated uncertainties correspond to their standard deviations.

Once the best fitting model per line is found, it is used to isolate the extra absorption lines from the photospheric profile. The best fits for each object and lines are displayed in Figures 3.1 (below) and C.1 to C.4 (in the Appendix).

We were able to find matching photospheric models for all the objects except for one, and the resulting parameters are consistent with their spectral types from the literature. The only exception is HD 112810, which is an F3/5IV/V spectral type according to the literature and the only F-type star within the sample presented in this chapter (we further discuss this object in Section 3.2.3). Otherwise, for each individual object, the dispersion in $T_{\rm eff}$ for the four different lines is of the order of ~ 300 K, which is expected when accounting for non-LTE effects (Przybilla et al. 2011, Plez 2013 and Sitnova et al. 2017).

3.2.3 Spectral twins

As an alternative to the synthetic spectrum, we also performed a search for the closest spectral match within all the objects in our sample for which we have spectra (i.e. 234 objects). In particular, we compared the median spectrum (the same as the reference spectrum) of each candidate against the median spectrum of each object in the sample with similar spectral types. We used a range of 11 subtypes (e.g. between A0 and F0 for an A5 candidate) for the spectral twin search.

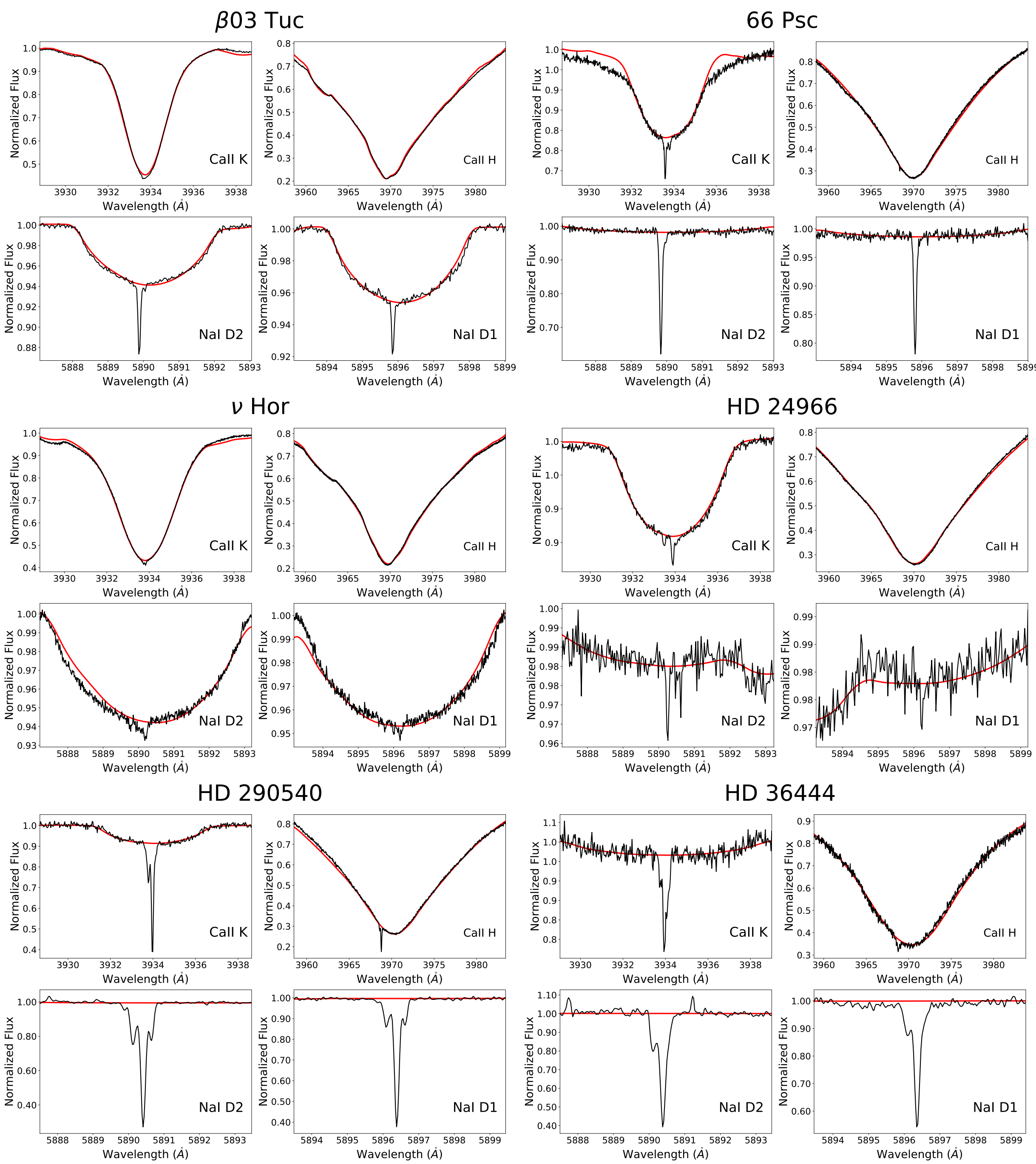

Figure 3.1: Best-fit models for β03 Tuc's, 66 Psc's, ν Hor's, HD 24966's, HD 290540's and HD 36444's Ca II H&K and Na I D1&D2 lines. Median from the real spectra in black, synthetic spectrum in red.

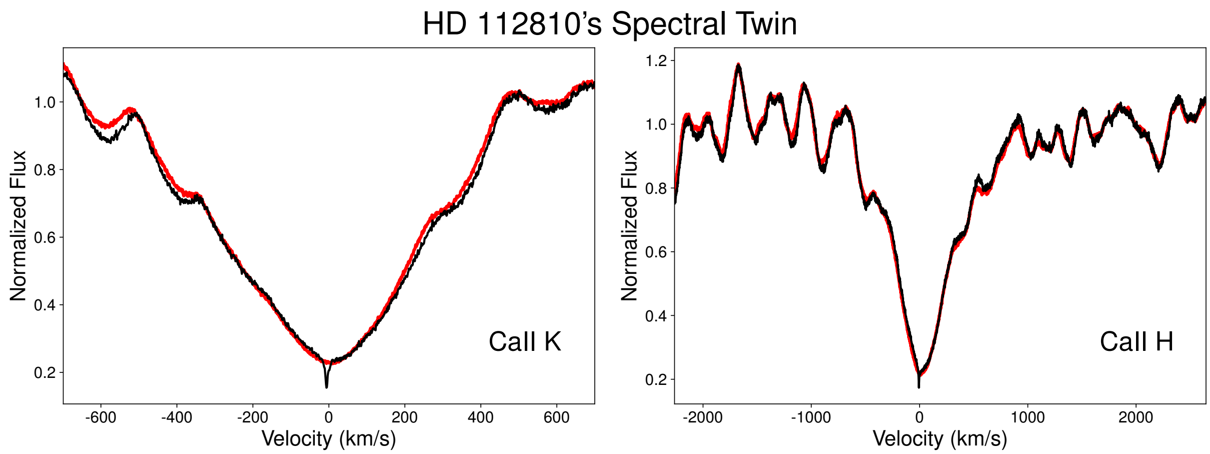

Figure 3.2: Spectral twin found for HD 112810 (in black): the F4IV type star HD 15115 (in red). The radial velocities of both stars have been shifted to zero for a better comparison. No additional broadening has been added to the spectra of any of the two objects.

Similar to the synthetic model fit, we selected the best fitting "template" in terms of minimum χ^2. The only difference is that in the χ^2 calculation we neglected the wavelength regions containing the 10% most distant data points between the two spectra being compared, in order to avoid a bias induced by the presence of extra features in either spectra.

In the case of HD 112810, since we were not able to find a satisfactory Kurucz model, we used the spectral twin we found for the object as a photospheric model to isolate the absorption feature. As can be seen in Fig. 3.2, HD 15115 is a good match to the spectrum of HD 112810.

3.2.4 Identification and characterization of features

We started by normalizing the reference (median) spectrum by the synthetic model (or spectral twin for HD 112810) to isolate the extra absorption features. In some cases when the model is not a perfect match (often the case in the wings of the photospheric lines), the normalized spectrum shows a "wavy" pattern, that makes the characterization of the extra features more challenging. In those cases we performed a polynomial fit to the normalized spectrum to remove this wavy pattern.

Afterwards, we performed Gaussian fitting to each of the extra absorption features in order to derive radial velocities, equivalent widths and apparent column densities. In the case of blended absorption lines, we modelled a combined Gaussian profile with the minimum number of Gaussians that would finely fit the profile, as shown in Figs. 3.3 (below) and C.5–C.12 (in the Appendix). We only considered as "real absorption features" those with significance above 3σ over the residual spectrum, the significance being measured from the amplitude of the Gaussian fit. We considered a feature to be "the same" as that present in another line of the same object when the absolute difference of the radial velocity of both features is $\leqslant 2\sigma$, where $\sigma = \sqrt{\sigma_1^2 + \sigma_2^2}$, being σ_1 and σ_2 the uncertainty of the radial velocity of each feature.

Radial velocities and equivalent widths were estimated from the best Gaussian(s) fit. In addition, apparent column densities were estimated following Savage and Sembach (1991) and using the oscillator strength values f from Morton (1991). We checked our own estimates for three stars against results produced by the `Vapid` code (Voigt Absorption Profile Interstellar Dabbler Howarth et al., 2002, which can model interstellar absorption lines) and they agreed within the uncertainties. Apparent column density (Ca II/Na I) ratios were also computed as they can help to discriminate the origin of the features.

We noticed that for some of the objects with Na I column densities exceeding 12.0, the column density in Na I D1 is larger by about 0.2 dex than the one for Na I D2. This is likely caused by saturation, i.e. the line with the weaker transition yields a higher column density. Although this problem affects the precision of the measurements in these particular cases, in the end it does not strongly bias the final verdict on the origin of the gas, since we have performed several independent kinds of analysis in order to reach our conclusions.

The parameters for each line and feature are presented in Table 3.6. The average radial velocity of each feature and their N(Ca II/Na I) are shown in Table 3.8. As can be seen in the Tables, the range of properties is very wide, including blue and red-shifted components, weak and intense features, either Ca II or Na I rich. The detailed discussion on the impact of these parameter in determining the origin of the gas responsible for the feature is left to Section 3.3.

Table 3.6: Absorption feature parameters. Heliocentric radial velocity, apparent column density and equivalent width of the features present in each line. Uncertainties for the radial velocities are in the order of 2.3 km.s^{-1} for the Ca II lines and 1.5 km.s^{-1} for the Na I lines. Apparent column densities and equivalent widths have uncertainties of 3–4% for the Ca II lines and 1–2% for the Na I lines.

	Ca II K			Ca II H			Na I D1			Na I D2		
Name	radV [km.s^{-1}]	$\log_{10} N$ [cm^{-2}]	EW [mÅ]	radV [km.s^{-1}]	$\log_{10} N$ [cm^{-2}]	EW [mÅ]	radV [km.s^{-1}]	$\log_{10} N$ [cm^{-2}]	EW [mÅ]	radV [km.s^{-1}]	$\log_{10} N$ [cm^{-2}]	EW [mÅ]
β03 Tuc	-12.23	9.78	0.52	–	–	–	–	–	–	-10.21	9.24	0.34
	-3.52	10.03	0.91	-4.41	10.14	0.60	-3.50	10.50	3.10	-3.51	10.51	6.25
	1.89	10.57	3.19	1.72	10.29	0.84	–	–	–	3.18	9.64	0.85
66 Psc	-5.14	11.10	10.38	-6.01	11.05	4.72	-5.83	11.28	17.49	-5.85	11.27	31.64
	2.58	10.25	1.51	–	–	–	-1.44	10.48	2.93	0.32	10.18	2.93
	10.74	10.56	3.09	–	–	–	12.23	9.71	0.51	–	–	–
ν Hor	5.41	10.55	3.04	4.18	10.35	0.96	3.86	9.52	0.33	2.97	9.78	1.20
	13.03	10.46	2.46	12.35	10.36	1.00	13.02	10.02	1.03	12.57	9.86	1.43
	–	–	–	–	–	–	-8.91	9.67	0.46	-9.27	9.41	0.51
HD 24966	-13.10	10.52	2.79	–	–	–	–	–	–	–	–	–
	17.00	10.89	6.55	15.04	10.71	2.23	15.34	9.90	0.78	15.32	9.87	1.45
	30.21	10.37	1.98	–	–	–	–	–	–	34.08	9.55	0.69
HD 290540	9.51	11.61	32.77	9.27	11.50	13.29	9.09	11.45	26.23	9.26	11.44	49.67
	23.96	12.00	64.17	24.15	12.14	49.91	23.47	12.13	98.75	23.56	11.96	123.98
	33.78	11.13	11.33	37.80	10.67	2.02	35.16	11.30	18.97	35.30	11.29	35.55
	–	–	–	–	–	–	-4.17	10.28	1.86	-3.82	10.44	5.31
HD 36444	7.27	11.16	12.03	6.91	11.28	7.96	9.02	11.44	25.95	8.79	11.30	36.31
	21.96	11.70	38.88	21.72	11.82	27.16	22.13	11.95	72.57	22.15	11.87	109.98
	31.40	11.11	10.57	31.98	11.13	5.79	30.81	11.23	16.26	31.00	10.98	18.06
	38.79	11.21	13.46	42.23	11.33	9.06	–	–	–	–	–	–
HD 290609	-9.23	10.91	6.86	–	–	–	-8.56	10.43	2.61	–	–	–
	9.65	11.98	71.21	9.35	12.04	44.61	8.46	11.62	38.92	8.50	11.54	61.20
	24.00	12.01	69.05	24.08	12.06	43.66	22.92	12.26	125.13	23.02	12.08	149.96
	34.38	11.62	33.45	37.31	11.85	29.57	35.39	11.33	20.65	32.52	11.12	24.87
	49.65	11.63	35.35	55.24	11.63	17.92	53.69	10.78	5.84	46.45	10.75	11.01
HR 1919	10.92	11.20	12.71	10.56	11.11	5.48	10.39	10.44	2.71	10.63	10.36	4.44
	32.17	11.57	28.28	30.84	11.37	9.74	30.92	10.46	2.80	30.51	10.34	4.27
	38.79	10.64	3.66	35.43	11.12	5.61	36.77	9.69	0.48	35.58	9.97	1.82
HD 54341	10.32	10.07	1.01	–	–	–	–	–	–	–	–	–
	24.49	10.36	1.96	26.17	10.50	1.35	24.95	9.91	0.79	25.91	10.05	2.22
	–	–	–	–	–	–	–	–	–	3.31	9.85	1.39
HD 60856	20.39	11.69	36.77	20.14	11.82	26.63	20.38	12.25	118.41	20.38	12.03	134.94
	30.65	10.71	4.37	31.10	10.82	2.85	28.72	10.70	4.86	29.47	10.42	5.13
HR 3300	5.62	10.77	4.99	4.95	10.50	1.38	7.52	10.18	1.49	5.72	10.19	3.01
	15.83	10.21	1.37	16.04	10.28	0.83	17.66	10.20	1.57	17.45	10.22	3.27
	20.82	10.30	1.69	–	–	–	–	–	–	–	–	–
η Cha	-3.37	10.13	1.16	-3.46	10.11	0.55	-1.05	9.57	0.36	-3.46	9.84	1.36
	10.09	10.77	4.97	9.55	10.76	2.49	11.92	10.46	2.85	12.20	10.44	5.34
HD 92536	2.81	10.60	3.36	1.57	10.22	0.72	-0.23	9.50	0.31	-0.56	9.74	1.07
	9.94	11.40	19.84	9.59	11.45	11.85	9.19	11.55	31.90	9.18	11.53	56.67
	18.21	11.27	15.18	18.31	11.22	6.96	17.59	10.90	7.77	17.25	10.90	15.15
3 Crv	-6.64	11.05	9.23	-7.69	10.83	2.89	-6.81	10.76	5.53	-6.86	10.71	9.60
	-1.45	10.67	3.86	-3.19	11.01	4.35	-1.22	9.83	0.67	-1.71	9.91	1.60
	2.21	10.54	2.95	3.70	9.69	0.21	–	–	–	–	–	–
HD 106036	-6.17	11.03	9.13	-3.40	11.20	6.78	–	–	–	–	–	–
	9.97	11.30	16.57	10.39	11.08	5.13	–	–	–	–	–	–
HR 4796	-14.40	10.41	2.18	-14.60	10.49	1.33	-11.10	9.89	0.76	-11.76	9.85	1.40
	-5.57	10.40	2.14	-5.84	10.26	0.79	-5.01	10.51	3.19	-5.11	10.54	6.75

Continued on next page

Table 3.6 – continued from previous page

Name	Ca II K			Ca II H			Na I D1			Na I D2		
	radV [km.s^{-1}]	$\log_{10} N$ [cm^{-2}]	EW [mÅ]	radV [km.s^{-1}]	$\log_{10} N$ [cm^{-2}]	EW [mÅ]	radV [km.s^{-1}]	$\log_{10} N$ [cm^{-2}]	EW [mÅ]	radV [km.s^{-1}]	$\log_{10} N$ [cm^{-2}]	EW [mÅ]
	5.20	9.78	0.52	–	–	–	–	–	–	–	–	–
HD 110058	1.85	11.47	24.38	0.97	11.45	12.04	0.56	11.23	16.31	0.42	11.24	32.67
	12.50	11.50	21.89	12.19	11.77	20.79	12.36	11.76	41.72	12.34	11.49	43.52
HD 112810	-12.11	11.07	9.76	-10.86	10.88	3.23	–	–	–	–	–	–
	-3.76	11.60	29.69	-4.49	11.57	14.99	–	–	–	–	–	–
	3.77	11.01	8.46	2.28	11.25	7.58	–	–	–	–	–	–
HD 126135	-22.78	10.25	1.51	–	–	–	-22.49	10.01	1.01	-22.12	10.06	2.23
	-14.89	10.73	4.45	-15.59	10.60	1.71	-13.47	10.84	6.73	-14.36	10.67	9.03
	-8.32	10.59	3.27	-9.90	10.56	1.57	-7.83	10.02	1.04	-10.23	10.46	5.64
	4.16	10.92	6.83	3.83	10.85	3.05	4.25	11.59	33.50	4.36	11.57	58.21
	–	–	–	–	–	–	–	–	–	26.30	9.63	0.84
HD 141378	-30.03	10.79	5.16	–	–	–	–	–	–	–	–	–
	-15.02	10.36	1.93	–	–	–	–	–	–	–	–	–
HD 141327	-18.37	11.33	18.11	-21.23	11.22	7.07	-23.48	10.42	2.58	-23.69	10.41	4.97
	-1.43	11.95	66.92	-2.40	11.97	37.57	-4.17	12.51	203.27	-4.20	12.43	260.97
	14.78	11.80	47.59	14.23	11.82	26.94	14.66	10.77	5.73	14.16	10.77	11.18
	22.92	11.04	9.25	21.83	10.97	4.06	23.11	10.60	3.90	22.75	10.75	10.90
HD 144981	-27.17	10.86	6.15	-30.40	10.81	2.77	-21.05	11.09	11.84	-22.45	11.01	19.47
	-8.20	11.69	36.90	-8.63	11.75	22.69	-9.81	12.52	181.35	-10.01	12.33	208.88
HD 145554	-26.55	10.87	6.22	-23.03	11.00	4.25	-26.91	11.60	35.07	-26.96	11.47	49.80
	-9.45	11.81	44.49	-9.64	11.83	25.87	-12.01	12.36	141.27	-12.20	12.13	155.45
HD 145631	-28.32	10.86	6.17	-29.29	10.61	1.74	-26.75	11.31	19.19	-26.80	11.25	32.55
	-8.51	11.72	37.67	-8.77	11.82	25.33	-11.14	12.37	143.45	-11.41	12.16	163.49
HR 6051	-26.76	11.05	9.43	-27.04	11.02	4.50	-24.12	11.67	40.88	-24.20	11.53	56.64
	-9.38	10.73	4.57	-10.08	10.78	2.60	-11.17	11.73	46.34	-11.34	11.56	59.13
HR 6507	-38.93	10.32	1.78	-39.26	11.02	4.49	-38.62	10.39	2.40	-39.01	9.97	1.82
	-30.41	11.12	10.98	-29.52	11.29	8.22	-29.80	10.26	1.80	-29.10	10.42	5.09
	-24.86	11.25	14.00	-25.05	11.22	6.84	-25.08	10.97	8.71	-25.09	10.91	14.68
c Aql	-31.19	10.49	2.64	-31.67	10.52	1.44	–	–	–	–	–	–
	-19.67	10.34	1.88	-19.88	10.44	1.21	–	–	–	–	–	–

3.2.5 Variability of the extra absorption features

We investigated the variability of additional absorption lines in two ways: first by analysing their stability when they are detected in all the epochs and second by looking for transient absorption features that appear in a handful of epochs. For the first method, we performed the same Gaussian fitting described above, but on each individual epoch and we searched for variations in flux and velocity of those "stable" components (since they are present in all the epochs they also appear in the reference spectrum). For the second method, we searched for additional variable detections above a 3σ level that might appear in some of the epochs. Such transient detections could be related to FEB-like events.

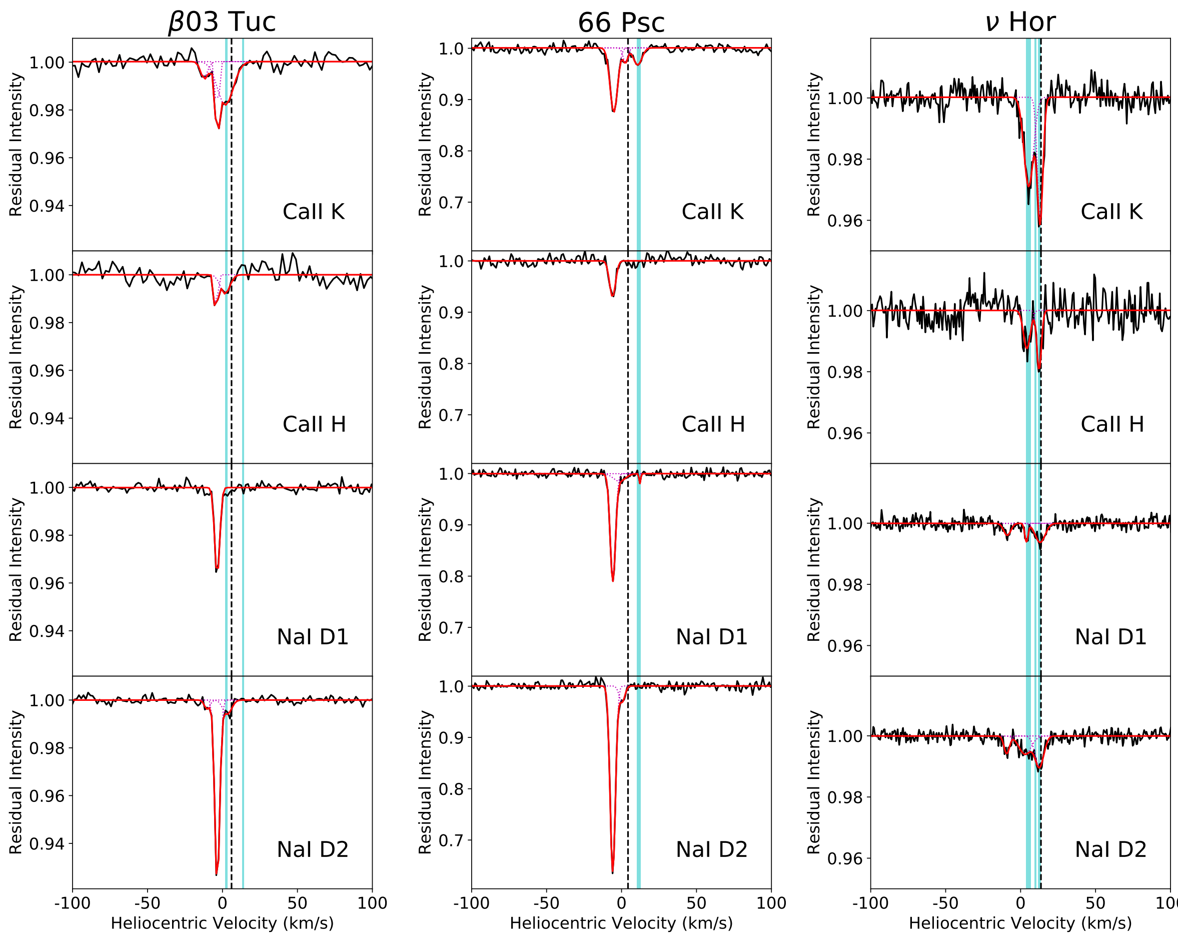

Figure 3.3: Absorption profiles of the Ca II H & K and Na I D1 & D2 lines for β03 Tuc, 66 Psc and ν Hor. Photospheric absorptions have been subtracted and the remaining extra components have been modelled by gaussian profiles. Individual gaussian fits are shown in dotted magenta lines and the combined profile is shown in red. Dashed black line marks the estimated radial velocity of the star and cyan lines mark the velocity of the traversing clouds in the line of sight with their respective errors as their line widths.

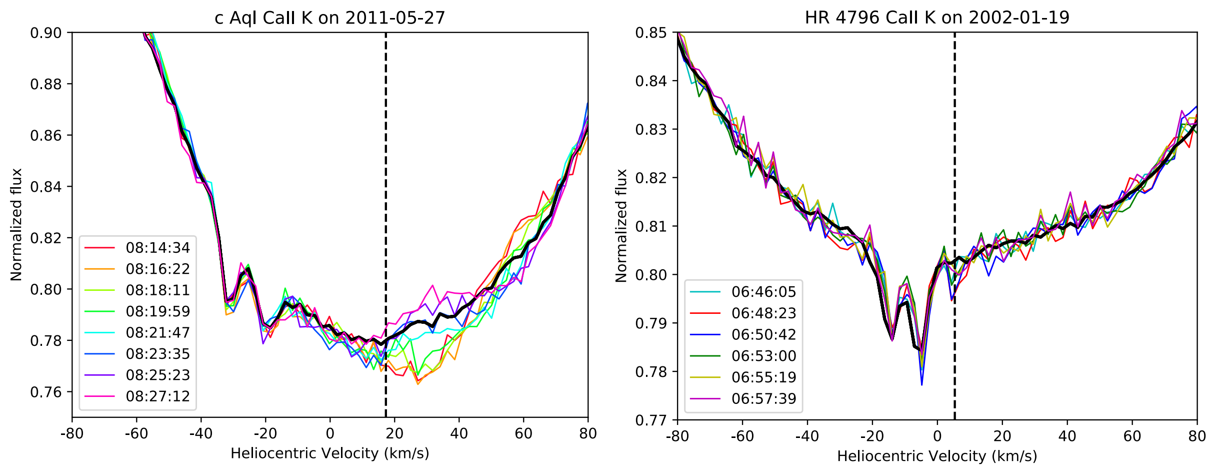

Figure 3.4: Left: Variability in the Ca II K line of c Aql during the night of 2011-05-27, the UT of each observation is shown in the legend. Right: Example of variability detected in HR 4796 at the stellar radial velocity along a selection of spectra taken on 2002-01-19. The thick black line in each Figure shows the median spectrum for comparison. The radial velocity of the star is marked with a dashed black line in both Figures.

We found variable absorption features attributable to FEB-like events in specific epochs of the objects c Aql and HR 4796. In particular, in the case of c Aql we detected very short-term variations from within a few nights to within a few minutes. Variations detected on the night of 2011-05-27 are shown in Fig. 3.4 for the Ca II K line, and they are also present in the Ca II H and Na I lines for some of the observations. These variations, likely attributable to intense exocometary activity, are detected at $\sim$35 km.s^{-1}, red-shifted with respect to the radial velocity of the star.

We have also detected variability in the Ca II K line of HR 4796. The observed variations appear as a small feature detected at 5.30 km.s^{-1}, matching the radial velocity of the star (5.35 km.s^{-1}). Since we have collected over 200 individual spectra of HR 4796, in Fig. 3.4 we only show a selection of a few epochs as examples of the variability observed around this star. These detections are narrow and only slightly over 3σ. Since the strength of Ca II H line is roughly half that of the Ca II K line, we do not expect to have a significant detection in the latter (as was the case). However, it is reassuring (in the circumstellar gas scenario) that all the detections in the Ca II K line match the radial velocity of the star.

In addition, we have detected low-level ($\sim 2\sigma$) variability in the residual spectra of HR 6507. However, this variability presents itself as a very broad component covering the full range of

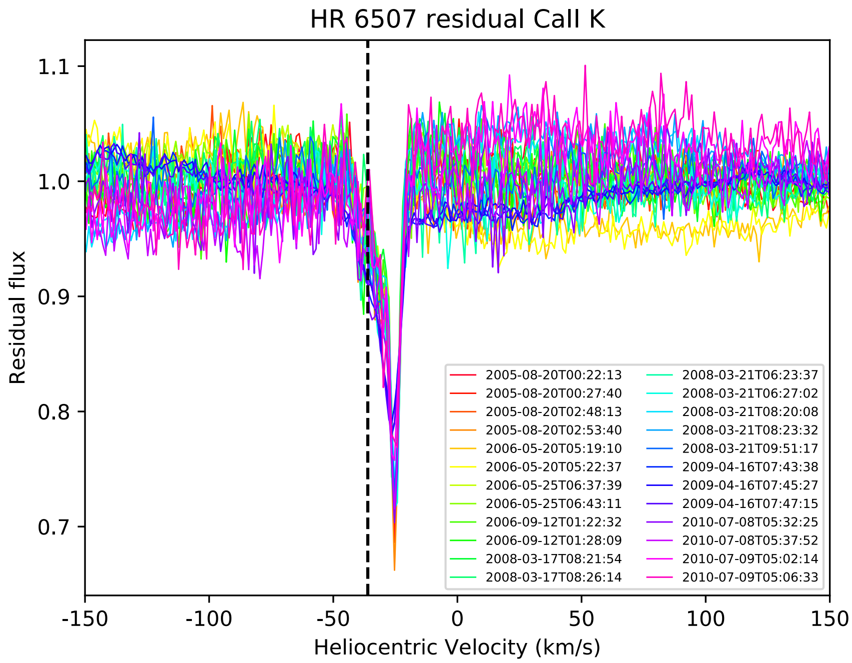

Figure 3.5: Variability in the residuals of the CaII K line of HR 6507 after normalizing all the epochs by the reference spectrum. The date of each observation is shown. The radial velocity of the star is marked with a dashed black line.

velocities of the photospheric line, as can be seen in Fig. 3.5. In order to determine if this variability was produced by circumstellar gas or the star itself, we also analysed the H_α line. Neither narrow emission nor absorption were detected in this line. However, the same broad variability was found, more consistent with photospheric variation. This star is classified as a shell star in (Hauck and Jaschek 2000, Jaschek et al. 1991), but even the shell classification is questioned in Jaschek et al. (1988) and Jaschek and Andrillat (1998). From the velocity field involved, this variability is more likely due to the presence of spots (as described in Figueira 2013).

3.2.6 Local Interstellar Medium features

Objects with known clouds in the line of sight

We looked for local interstellar clouds in the line of sight of the stars, as this clouds could explain the presence of the extra absorption lines that we observe. We used the online Local

InterStellar Medium (LISM) Kinematic Calculator[2] (Redfield and Linsky, 2008) which predicts the radial and transverse velocities of LISM clouds in any direction and calculates which clouds are traversed by any given line of sight.

We found traversing known clouds from the Redfield and Linsky (2008) catalogue for 18 of our objects and, in most cases, the radial velocity of the clouds matched the velocity of some of the absorption features. In Table 3.8 we present the clouds traversing the line of sight of each object, their heliocentric radial velocities and whether they match one of the absorption lines or not. As can be seen in the Table, a significant number of our features are attributable to gas located in the G cloud, which is an interstellar cloud located next to the Local Interstellar Cloud (LIC).

Objects with Diffuse Interstellar Bands

We have analysed the Diffuse Interstellar Bands (DIBs) at wavelengths 5780.5Å and 5797.1Å. DIBs are absorption features caused by the ISM and they can be detected in the UV, optical and IR wavelengths. DIBs are much broader than the atomic interstellar lines, having full width at half maximum ranging from ∼0.8-30 Å, presumably due to unresolved rotational structure of large carbon-bearing molecules, which are common in the interstellar medium (Herbig, 1995). The DIBs we have chosen to analyse are some of the strongest DIBs detectable in optical spectra. The presence of absorption features at any of these particular wavelengths might indicate the presence of ISM in the line of sight of the star, as DIBs are hardly attributable to circumstellar gas around pre-main sequence or main sequence stars (as opposed to objects that have departed the main sequence, see for e.g. Díaz-Luis et al. 2015).

We detected the presence of absorption lines likely to be due to DIBs in the 12 objects listed in Table 3.7. These absorption lines are broad and diffuse, making it difficult to obtain precise measurements of their radial velocities. Therefore we use this criteria mostly to confirm the presence of ISM within a certain velocity range. We note that although in most cases we have identified diffuse bands at both wavelength locations, for HR 3300, HD 92536, and HD 126135 we have detected DIBs at only one of the wavelengths. This can be explained by the fact that the intensity of the bands detected for those three sources is much lower than in the other cases;

[2]http://lism.wesleyan.edu/LISMdynamics.html

Table 3.7: Summary of the detection of absorptions consistent with DIBs at either 5780.5Å or 5797.1Å.

Name	DIB at 5780.5 Å	DIB at 5797.1 Å
β03 Tuc	✗	✗
66 Psc	✗	✗
ν Hor	✗	✗
HD 24966	✗	✗
HD 290540	✓	✓
HD 36444	✓	✓
HD 290609	✓	✓
HR 1919	✗	✗
HD 54341	✗	✗
HD 60856	✓	✓
HR 3300	✗	✓
η Cha	✗	✗
HD 92536	✓	✗
3 Crv	✗	✗
HD 106036	✗	✗
HR 4796	✗	✗
HD 110058	✗	✗
HD 112810	✗	✗
HD 126135	✓	✗
HD 141378	✗	✗
HD 141327	✓	✓
HD 144981	✓	✓
HD 145554	✓	✓
HD 145631	✓	✓
HR 6051	✓	✓
HR 6507	✗	✗
c Aql	✗	✗

therefore we interpret the difference as a sensitivity issue rather than a physical one.

Nearby stars analysis

Similarly to the analysis performed on the objects in our sample, we analysed the Ca II K lines of nearby stars searching for the presence of absorption features at similar velocities to the ones observed in our objects. Finding these similar absorption lines in the line of sight towards nearby stars would strongly suggest an ISM origin for the gas feature(s). We chose to analyse the Ca II K line since its absorption is more intense and easier to detect than the H line and it is the main tracer of circumstellar gas in the optical.

For each star of our sample, we searched for high resolution spectra of nearby stars within a search-box of up to 6 degrees ($\sim$ 3 degrees radius). Considering the distances of the objects, the equivalent projected separations between the targets and their neighbours range between $\sim$0.1 pc and $\sim$30 pc. From the gathered data, we only considered objects having early spectral types, ideally between B0 and F5, since absorption features are harder to detect in later spectral types. Non-photospheric gas absorptions are easily spotted when superimposed on fast rotators having wider (and fewer) spectral lines.

We found suitable nearby stars for all the candidates except for 66 Psc and HD 24966. The observations used for this analysis are described in Table C.1 found in the Appendix. We found absorption features present in all the nearby stars and they match most of the absorption features found in our objects, confirming the interstellar origin for the majority of the features. In the case of HD 110058, we found that three nearby stars presented one absorption feature matching HD 110058 absorption line at $\sim$1 km.s^{-1}, one star shows a weak absorption matching the radial velocity of the G cloud, but none of the nearby stars shows any signs of absorption lines matching the one at $\sim$12 km.s^{-1}, which also happens to be near the estimated radial velocity of this star. Therefore we propose a circumstellar origin for this feature.

A comparison of the nearby stars absorption lines against our objects and their respective angular separations are shown in Figs. 3.6, below, and C.13 to C.15, in the Appendix.

3.2.7 General results

We present a summary of our results regarding stable features in Table 3.8, in which we report the radial velocity of the star, the traversing clouds, their radial velocities and whether they match one of the observed features, the average velocities of each absorption feature, its Ca II/Na I density ratio, whether it has a matching absorption in a nearby star and our verdict on its origin; ISM (InterStellar Medium) or CS (CircumStellar).

Most of the stable features are likely produced by clouds in the line of sight and not by the circumstellar medium, except in the cases of HR 4796 and HD 110058. We find that two objects present variability: HR 4796 shows flux variations in its feature located at the same velocity as the star and c Aql exhibits transient red-shifted absorption lines with characteristics of FEB-like events. Another interesting case is that of HR 6507, for which a clear diagnostic cannot be

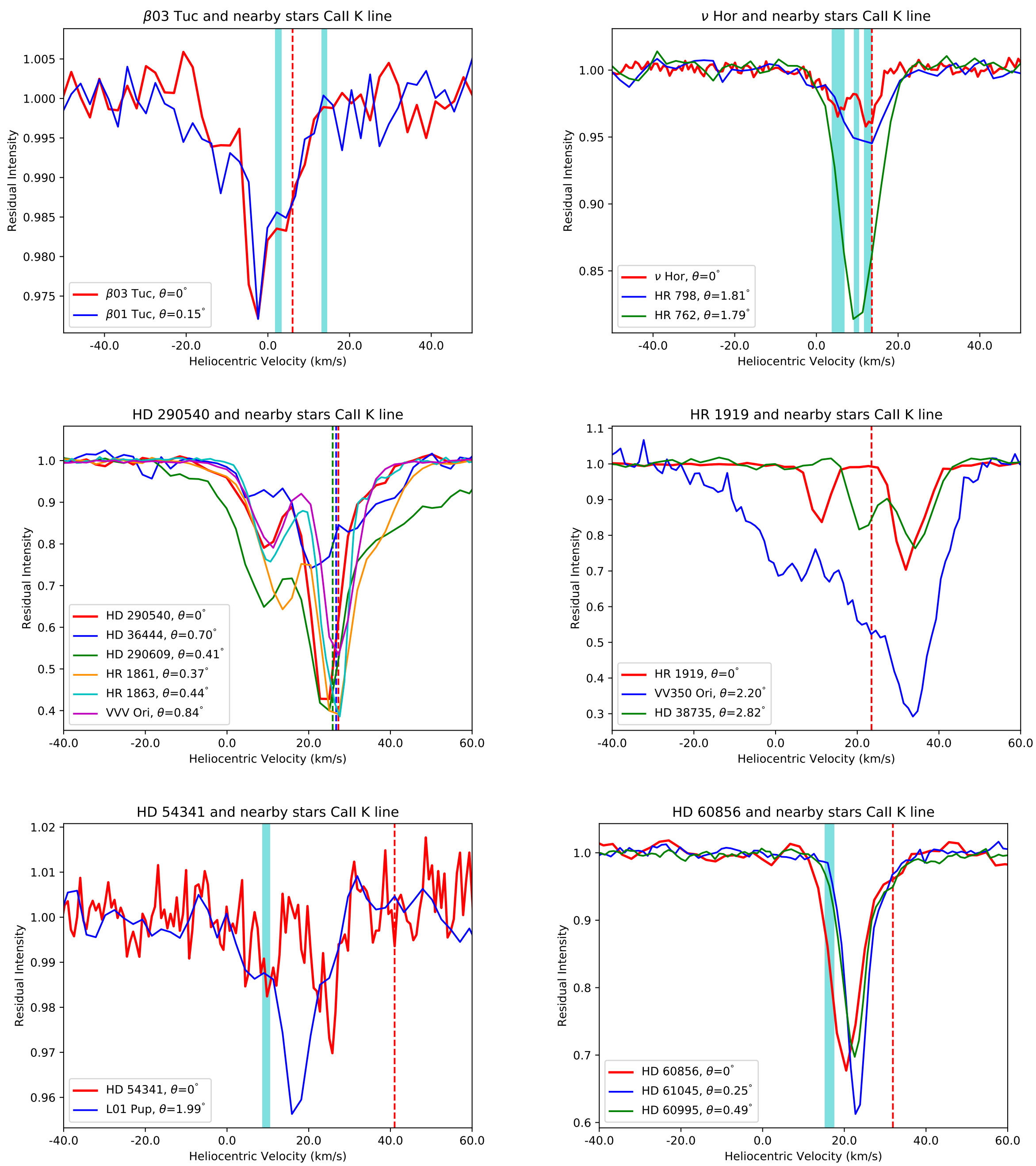

Figure 3.6: Nearby stars around β03 Tuc, ν Hor, HD 290540 (along with HD 36444 and HD 290609), HR1919, HD 54341 and HD 60856. Dashed line marks the estimated radial velocity of the star and cyan lines mark the velocity of the traversing clouds in the line of sight with their respective errors as their line widths.

attained with the available data as discussed in Sec. 3.3.2.

Table 3.8: Absorption components and their mean radial velocity, CaII/NaI density ratio, absorption feature detection in a nearby star and proposed origin.

Name	Stellar RV [km.s^{-1}]	Cloud Name	Cloud RV [km.s^{-1}]	Match Feat.?	Feat. RV [km.s^{-1}]	$\frac{N(\mathrm{Ca\,II})}{N(\mathrm{Na\,I})}$	Nearby star	Origin
β03 Tuc	6.05 ± 1.60	–	–	–	-11.22	3.47	✓	ISM
		Dor	13.85 ± 0.65	✗	-3.74	0.38	✓	ISM
		Vel	2.54 ± 0.78	✓	2.26	13.08	✓	ISM
66 Psc	4.32 ± 2.66	–	–	–	-5.71	0.63	–	ISM
		–	–	–	0.49	0.40	–	ISM
		LIC	11.44 ± 1.29	✓	11.49	7.03	–	ISM
ν Hor	13.58 ± 1.67	G	5.33 ± 1.52	✓	4.11	6.16	✓	ISM
		Vel	12.65 ± 0.93	✓	12.74	2.94	✓	ISM
		Cet	9.85 ± 0.63	✗	-9.09	< 1	✓	ISM
HD 24966	15.70 ± 3.15	Blue	10.59 ± 1.30	✗	-13.10	> 5	–	ISM
		G	17.51 ± 1.38	✓	15.68	8.40	–	ISM
		Dor	32.11 ± 0.85	✓	32.15	6.58	–	ISM
HD 290540	27.26 ± 3.12	–	–	–	9.28	1.31	✓	ISM
		–	–	–	23.78	1.04	✓	ISM
		–	–	–	35.51	0.46	✓	ISM
		–	–	–	-3.99	< 1	✓	ISM
HD 36444	26.72 ± 4.50	–	–	–	8.00	0.70	✓	ISM
		LIC	22.75 ± 0.96	✓	21.99	0.72	✓	ISM
		–	–	–	31.30	1.00	✓	ISM
		–	–	–	40.51	> 5	✓	ISM
HD 290609	25.87 ± 1.65	–	–	–	-8.89	3.05	✓	ISM
		–	–	–	8.99	2.70	✓	ISM
		–	–	–	23.50	0.73	✓	ISM
		–	–	–	34.90	3.24	✓	ISM
		–	–	–	51.26	7.33	✓	ISM
HR 1919	23.49 ± 1.28	–	–	–	10.63	5.59	✓	ISM
		–	–	–	31.11	11.97	✓	ISM

Continued on next page

Table 3.8 – continued from previous page

Name	Stellar RV [km.s^{-1}]	Cloud Name	Cloud RV [km.s^{-1}]	Match Feat.?	Feat. RV [km.s^{-1}]	$\frac{N(\text{Ca II})}{N(\text{Na I})}$	Nearby star	Origin
		–	–	–	36.64	12.35	✓	ISM
HD 54341	41.03 ± 0.95	–	–	–	3.31	< 1	✓	ISM
		Blue	9.59 ± 0.93	✓	10.32	> 5	✓	ISM
		–	–	–	25.38	2.80	✓	ISM
HD 60856	31.89 ± 1.59	LIC	16.37 ± 1.18	✗	20.32	0.40	✓	ISM
		–	–	–	29.98	1.55	✓	ISM
HR 3300	22.35 ± 0.72	G	4.62 ± 0.94	✓	5.95	2.97	✓	ISM
		Vel	15.00 ± 0.97	✓	16.75	1.08	✓	ISM
		Cet	20.50 ± 0.87	✓	20.82	> 5	✓	ISM
η Cha	15.21 ± 1.41	G	-4.07 ± 1.17	✓	-2.84	2.47	✓	ISM
		Vel	0.02 ± 0.75	✗	10.94	2.07	✓	ISM
HD 92536	15.45 ± 0.44	G	-6.09 ± 0.97	✗	0.90	6.52	✓	ISM
		–	–	–	9.47	0.77	✓	ISM
		–	–	–	17.84	2.21	✓	ISM
3 Crv	14.41 ± 1.09	Leo	-5.36 ± 1.05	✓	-7.00	1.65	✓	ISM
		–	–	–	-1.89	9.91	✓	ISM
		Gem	2.54 ± 0.95	✓	2.96	> 5	✓	ISM
HD 106036	9.37 ± 2.34	G	-11.13 ± 0.98	✗	-4.78	–	✓	ISM
		–	–	–	10.18	–	✓	ISM
HR 4796	5.35 ± 2.94	–	–	–	-12.97	3.79	✓	ISM
		–	–	–	-5.38	0.64	✓	ISM
		–	–	–	5.20	> 5	✗	CS
HD 110058	11.20 ± 0.81	G	-14.46 ± 0.97	✗	0.95	1.68	✓	ISM
		–	–	–	12.35	1.02	✗	CS
HD 112810	5.25 ± 2.24	G	-15.70 ± 0.97	✗	-11.48	–	✓	ISM
		–	–	–	-4.12	–	✓	ISM
		–	–	–	3.02	–	✓	ISM
HD 126135	11.73 ± 0.67	NGP	-24.28 ± 1.22	✓	-22.46	0.82	✓	ISM
		Gem	-14.33 ± 1.01	✓	-14.58	0.80	✓	ISM
		–	–	–	-9.07	1.89	✓	ISM

Continued on next page

Table 3.8 – continued from previous page

Name	Stellar RV [km.s^{-1}]	Cloud Name	Cloud RV [km.s^{-1}]	Match Feat.?	Feat. RV [km.s^{-1}]	$\frac{N(\text{Ca II})}{N(\text{Na I})}$	Nearby star	Origin
		–	–	–	4.15	0.20	✓	ISM
		–	–	–	26.30	< 1	✓	ISM
HD 141378	-14.68 ± 2.62	G	-28.37 ± 1.18	✓	-30.03	> 5	✓	ISM
		–	–	–	-15.02	> 5	✓	ISM
HD 141327	-4.65 ± 2.40	G	-27.31 ± 1.08	✗	-21.69	7.32	✓	ISM
		–	–	–	-3.05	0.31	✓	ISM
		–	–	–	14.46	11.08	✓	ISM
		–	–	–	22.65	2.12	✓	ISM
HD 144981	-6.47 ± 1.59	G	-29.16 ± 1.10	✓	-26.16	0.83	✓	ISM
		–	–	–	-10.32	0.20	✓	ISM
HD 145554	-9.66 ± 1.49	G	-29.20 ± 1.10	✓	-28.23	0.33	✓	ISM
		–	–	–	-12.23	0.36	✓	ISM
HD 145631	-9.86 ± 1.90	G	-29.21 ± 1.10	✓	-28.51	0.50	✓	ISM
		–	–	–	-11.21	0.32	✓	ISM
HR 6051	-7.26 ± 4.11	G	-29.14 ± 1.10	✓	-26.55	0.29	✓	ISM
		–	–	–	-11.49	0.13	✓	ISM
HR 6507	-36.13 ± 2.49	–	–	–	-38.95	3.72	✓	ISM
		–	–	–	-29.71	7.33	✓	ISM
		–	–	–	-25.02	1.99	✓	ISM
c Aql	17.29 ± 2.61	Mic, Aql	-26.86, -25.26	✗	-31.43	> 5	✗	ISM
		Eri	-20.11 ± 1.14	✓	-19.77	> 5	✓	ISM

3.3 Discussion

Gas absorption features superimposed on photospheric lines look fairly similar whether they are caused by clouds in the line of sight of the star or by the presence of stable gas in the circumstellar environment. Therefore, a detailed analysis, involving multiple criteria, has to be performed in order to discriminate between the two scenarios. Below we discuss our results regarding the origin of the features in "interstellar" and "circumstellar" categories.

3.3.1 Interstellar-like features

Most of the absorption features found in this study are classified as "interstellar" as they do not present significant time variability beyond the noise level or attributable to different instrument or resolution. In addition, all these features posses other characteristics such as having a composition consistent with typical ISM values, matching clouds in their line of sight, or detection of a similar feature in a nearby star with velocities matching within 3σ.

Overall, we found 24 absorption features matching the radial velocity of known clouds traversing the lines of sight of the stars. A summary of the traversing clouds, their radial velocities and the matching absorptions is provided in Table 3.8. The evidence for these features to be caused by those clouds in the line of sight, is strengthened by the fact that they are also detected in nearby stars around our science targets. A particular case of this phenomenon is observed in the groups of objects HD 290540, HD 36444, and HD 290609 and HD 144981, HD 145554, and HD 145631.

HD 290540, HD 36444 and HD 290609: These three stars are located within an angular separation of 0.7° of each other. As can be seen in Fig. 3.6, the three objects present similar absorption features at similar velocities, which are also detected for three other nearby stars within an angular radius of 1°. We obtained comparable radial velocities for these three objects, around $26\,\mathrm{km.s^{-1}}$. As noticeable in Fig. 3.6, they all have a deep absorption line close to $23\,\mathrm{km.s^{-1}}$, which corresponds to the Local Interstellar Cloud (LIC, Redfield and Linsky, 2008). Although this absorption line is found to be close to the radial velocity of the stars, its interstellar origin is clear as it is confirmed by being present in other three stars with a similar line of sight and having a N(Ca II/Na I) ratio consistent with ISM ($\lesssim$1). The other absorption lines seen in the three objects at ~ 9 and $\sim 34\,\mathrm{km.s^{-1}}$ also seem to have a common interstellar origin. The one at $\sim 9\,\mathrm{km.s^{-1}}$ is possibly attributable to the Hyades cloud at $\sim 11\,\mathrm{km.s^{-1}}$, which according to Redfield and Linsky (2008) crosses near ($< 20^{\circ}$) the line of sight of these three stars. We did not find any known cloud traversing a similar line of sight at a radial velocity close to $\sim 34\,\mathrm{km.s^{-1}}$, however, since this absorption line is present in several stars at a similar velocity we also conclude that it is of interstellar origin.

There is a fourth feature at $\sim 41\,\mathrm{km.s^{-1}}$ for HD 36444 detected only in the Ca II lines which, due to its mostly Calcium composition (N(CaII/NaI)> 5) could be consistent with having a circumstellar origin. However, a similar feature is observed in the nearby star HR 1863, and therefore it is likely to be another feature of interstellar origin, possibly warm ISM, which has been reported to have a composition richer in Calcium than cold ISM (Bertin et al., 1993). Unfortunately we have obtained only one epoch for HD 36444 therefore we were not able to investigate the variability of this feature. Further data is thus necessary in order to fully rule out circumstellar origin.

HD 290609 also presents a fourth feature, but it is detected around $\sim 51\,\mathrm{km.s^{-1}}$. However, we point out that this group of stars is located within the Orion OB1 association (Hernández et al., 2006) making it likely that environmental nebular gas is observed at different velocities (Brown et al., 1994). In any case, although we conclude an ISM origin for HD 290609's fourth feature because of the high frequency of interstellar clouds observed in the surroundings; as in the previous case, there is only one spectrum available for HD 290609 and it would be interesting to perform further analysis gathering more epochs in order to better assess the origin of this feature.

Similar to the previous case, HD 144981, HD 145554 and HD 145631 are located within 0.72° of each other and present similar absorption features. As shown in Fig. C.14, the three objects along with the nearby star HR 6026, present remarkably similar absorption lines in terms of depth and velocity. In this case, the three objects present two features with all the characteristics pointing towards an interstellar origin. The radial velocities of the absorption lines are blueshifted with respect to the radial velocities of the stars, all the features present column density CaII/NaI ratios <1, the three objects present absorptions attributable to DIBs and, more importantly, the three of them have matching features in other nearby stars. In addition, the component at ∼-28 km/s matches well with the radial velocity of the G cloud, which traverses the line of sight at ∼-29 km/s (Redfield and Linsky, 2008). We did not find any nearby cloud at a radial velocity similar to the deep absorption feature at ∼-11 km/s, but the similarity of the feature present in the three objects and also in the fourth nearby star is clear, therefore we conclude interstellar origin with high certainty.

3.3.2 Circumstellar-like features

Stable features with no matching absorptions in nearby stars

In the case of HD 110058, we found that three nearby stars present one absorption feature matching HD 110058's absorption at $\sim 1\,\mathrm{km.s^{-1}}$, thus we propose an interstellar origin for this feature. This interstellar feature was also reported by Hales et al. (2017), who analysed MIKE spectra of HD 110058 and three nearby stars (at angular separations between 1.2° and 2.8°) and found matching features for the absorption at $\sim 1\,\mathrm{km.s^{-1}}$. We obtained further spectra for four different nearby stars in the ESO archive (at angular separations between 0.74° and 2.16°) and confirmed the matching absorption lines in three stars, in agreement with the findings by Hales et al. (2017). Given the distance to this star (188.7 ± 34.1 pc), both studies cover a region of $2.4 - 9.2$ pc in radius. Considering a typical radius of 1.5 pc for the warm local ISM material located within 15 pc from the Sun (Redfield and Linsky, 2008), the projected coverage at the distance of HD 110058 would be about 19 pc, thus the local ISM material would likely cover the region in which the nearby stars are located. On the other hand, our measurements of the equivalent widths of this feature is in agreement with a more recent work by Rebollido et al. (2018), where the authors report that the strength measured for this blue-shifted component varies with respect to Hales et al. (2017) measurement, proposing a possible circumstellar origin for the blue-shifted feature at $\sim 1\,\mathrm{km.s^{-1}}$. Considering the scenario of variability in the blue-shifted component and a possible overlap of circumstellar feature over the interstellar it would be worth performing follow-up observations of this object to better assess the origin of this feature. There is a fourth nearby star analyzed which does not present a feature at said velocity, but shows a weak absorption line at $\sim -15\,\mathrm{km.s^{-1}}$ matching the radial velocity of the G cloud.

HD 110058 presents an additional absorption feature at $\sim 12\,\mathrm{km.s^{-1}}$ which is very near our estimate of the radial velocity of this star ($11.20\,\mathrm{km.s^{-1}}$). None of the nearby stars analyzed show any sign of absorption matching HD 110058's absorption line at $\sim 12\,\mathrm{km.s^{-1}}$. Therefore we propose a circumstellar origin for this feature. This circumstellar feature was also proposed by Hales et al. (2017) and confirmed by Rebollido et al. (2018), thus our analysis is in agreement with their conclusions.

Variable features

We detected variable absorption features attributable to FEB-like events in the objects c Aql and HR 4796. The detection of FEB-like events in c Aql was previously reported by Montgomery and Welsh (2017), where they detected high variations from night to night and attributed them to exocometary activity. Furthermore Welsh and Montgomery (2013) reported some nightly changes but no FEBs-like events. With the data collected from the ESO archive we found, in addition to night to night variations, strong variability within very short time scales of only a couple of minutes. To our knowledge, this is the shortest-term variability detected to date in such systems. This object is known to be a pulsating star with a period of 30.39 minutes (Kuschnig et al., 1994) but a phase analysis of the Ca II K and the Hα lines does not indicate any such periodicity. In addition, the residual absorption events are not associated with a counterpart in emission at a mirrored velocity with respect to the radial velocity of the star (even taking into account the uncertainty in the latter), as one would expect from pulsations. In the left panel of Fig. 3.4, we show the variability detected in c Aql through eight individual spectra taken within a time span of ~ 20 minutes. Similar short term variability has only been observed so far in β Pictoris (Kiefer et al., 2014b) and the shell star ϕ Leo (Eiroa et al., 2016), with reported variability within hours.

Variability in the Ca II K line of HR 4796 at the same radial velocity of the star is reported here for the first time. Previously, only a sporadic absorption at $\sim 60\,\mathrm{km.s^{-1}}$ during the night of 2007-05-04 was reported by Welsh and Montgomery (2015). A more detailed analysis of the variability detected in these two objects will be presented in Iglesias et al. (in prep).

Regarding other objects in our sample with claims of variability in the literature, there are also HR 6051, (Welsh and Montgomery, 2013), HR 6507 (Welsh and Montgomery, 2015) and HD 24966 (Welsh and Montgomery, 2018). For the case of HR 6051, Welsh and Montgomery (2013) reported the detection of weak absorption features on specific nights, which the authors attributed to the evaporation of exocomets. Their spectra were taken on May 2011 with the Sandiford Echelle Spectrograph at the McDonald Observatory, Texas. In our data of HR 6051 taken on March 2016 with FEROS, we do not detect any significant additional absorption line besides the stable interstellar ones. Since both observations are similar in terms of S/N and resolution, we suspect our non detections could be due to the lack of events during those particular nights. It would be worth analysing more observations to confirm the activity observed in this object by previous works.

In the case of HR 6507, Welsh and Montgomery (2015) modelled the absorption lines using two components at radial velocities $\sim -37\,\mathrm{km.s^{-1}}$ and $\sim -28\,\mathrm{km.s^{-1}}$. The observations were taken with the Sandiford Echelle Spectrograph at the McDonald Observatory, Texas, with $\sim$ 60000 resolution. We combined HARPS and UVES spectra (with higher resolution, $\sim$ 100000 and $\sim$ 80000, respectively) and were able to distinguish and fit three absorption features at radial velocities $\sim -39\,\mathrm{km.s^{-1}}$, $\sim -29\,\mathrm{km.s^{-1}}$ and $\sim -25\,\mathrm{km.s^{-1}}$. Welsh and Montgomery (2015) attributed a circumstellar origin for the feature observed at $\sim -37\,\mathrm{km.s^{-1}}$ because of its proximity to the radial velocity of the star ($\sim -36\,\mathrm{km.s^{-1}}$). However, for the corresponding feature, which we measure at $\sim -39\,\mathrm{km.s^{-1}}$, we found absorption lines of similar velocity and intensity in nearby stars, suggesting ISM origin.

HR 6507 has also been reported to posses shell star signatures (Hauck and Jaschek 2000, Jaschek et al. 1991), although in other works no clear indication of a shell has been found, attributing this to a weakening or disappearing of the shell (Jaschek et al. 1988, Jaschek and Andrillat 1998). Nevertheless, considering the possibility of HR 6507 being a shell star, it is likely that it possesses circumstellar gas and therefore shows gas signatures at its radial velocity. As mentioned in 3.2.5, we found small variability in the overall residuals of all the lines observed for HR 6507. In Hauck and Jaschek (2000), they report the star as variable and possibly micro-variable, which might explain the observed variations. Taking all this into account, we do not attribute the variability to FEBs-like events, but a more detailed study of this source is needed to achieve stronger conclusions.

In the case of HD 24966, Welsh and Montgomery (2018) recently proposed the detection of exocomets at different velocity ranges in two out of three observations. The significance and interpretation of such variable transient FEB absorption features will be further investigated in Iglesias et al. (in prep).

Relationship between circumstellar-like features and system properties

Gas absorptions features of presumed circumstellar origin were found in the systems HD 110058, HR 4796 and c Aql.

The debris disk around HD 110058 has been resolved with SPHERE by Kasper et al. (2015), where they determined an inclination of $\sim 90^\circ$. This edge-on orientation reinforces the circumstellar verdict on the gas origin, as this is the most favourable orientation for potentially detecting gas lines in absorption. Since the absorption line that we detect is deep, narrow, stable, and close to the radial velocity of the star, it is consistent with a stable gas component, possibly located in the outer regions of the disk (Beust et al. 1998, Brandeker et al. 2004).

HR 4796 has an inclination of 76.5° (Milli et al. 2017, Kennedy et al. 2018) which is fairly close to edge-on. Since somewhat small misalignments in cometary orbits with respect to the parental disk are common (Nesvorný et al., 2017), it is not necessarily unlikely to detect FEB events.

Regarding the disk around c Aql, it has only been marginally resolved with Herschel by Morales et al. (2016). They estimated an inclination of $21^\circ \pm 42^\circ$. Although this inclination does not seem favourable for circumstellar gas detections using optical spectroscopy, the estimated uncertainty on the inclination is very large as the disk was only marginally resolved. The possibility of a much higher inclination cannot be ruled out. Even if the shallower inclination is confirmed, we could still be spotting the activity of bodies with highly inclined orbits. Overall, it is reassuring that two of our candidates with gas detections are close to edge-on, with very robust inclination determinations.

Regarding the rest of the sample, only two other objects have been marginally resolved (with Herschel): ν Hor, modelled with $73.4^\circ \pm 6.5^\circ$ inclination (Moór et al., 2015), and HD 141378, with an estimated inclination of $60^\circ \pm 37^\circ$ (Morales et al., 2016). We did not detect signs of circumstellar gas in these objects. Nevertheless, it would be worth performing follow-up studies to be able to analyse more epochs and therefore increase the chances of detecting stochastic activity or provide more robust evidence of the lack of such activity.

3.4 Conclusions

In this work we have analysed the multiple absorption features present in the Ca II H & K and Na I D1 and D2 lines of 27 debris disks systems using optical high-resolution spectroscopy in order to determine if their origin is of circumstellar or interstellar nature.

We found gas absorptions of circumstellar nature in three objects: HD 110058, HR 4796 and c Aql. HD 110058 presents a strong stable absorption consistent with a gaseous disk, possibly residual gas leftover from the earlier gas-rich stage of the disk or from very active planetesimal collision episodes.

Variable absorption features were found in the spectra of HR 4796 and c Aql. A weak circumstellar absorption was found in HR 4796 at the same radial velocity as the star with flux variations over 3σ, possibly due to photo-dissociation processes or collisions of icy bodies producing changes in the gas content of the disk. Highly variable red-shifted absorptions were detected in c Aql, with substantial variations observed on time scales shorter than two minutes, which is the shortest variability detected so far in this type of lines. These fast changing signatures are likely due to exocometary activity within the disk surrounding c Aql. For these two objects, HR 4796 and c Aql, we will present a more detailed analysis of the variable features in a future work. The circumstellar gas detections are in agreement with the near edge-on inclinations of the two objects with robust inclination measurements: HD 110058 with an inclination of $\sim 90^\circ$ and HR 4796 with an inclination of 76.5°.

Given h, r and i the scale-height, radial distance and inclination of a circumstellar disk, respectively, and assuming a typical scale-height/distance ratio of h/r $\sim$0.1 for debris disks (Thébault, 2009), the typical angle subtended by the disk should be $\sim 5.7^\circ$. For a uniform distribution of $\sin(i)$ between 0 and 1, the probability of i $\geqslant (90^\circ - 5.7^\circ)$ is $\sim$10%, and therefore, the probability for a randomly inclined system to be found close to edge-on or with an inclination suitable to detect circumstellar gas absorptions is $\sim$10%.

However, the sample analyzed in this chapter cannot, a priori, be considered “random” because of the selection criterion of “having multiple absorption features” (that may bias the sample towards objects with circumstellar gas on close to edge-on orientation). On the other hand, this sample is actually unbiased with respect to stochastic detections such as FEBs (we remind the reader that the selection function was performed on the reference spectra, i.e. only stable components are considered).

Bearing in mind that the inclination constraints could be more relaxed regarding the detection of FEBs (as discussed in Sec. 3.3.2); that FEBs, given their stochastic nature, may not be detected by mere chance at our epochs of observations; and that, in any case, we do detect circumstellar gas in three cases out of 27 objects (one stable and two variables); our results definitely point towards gas in debris disks not being a rare phenomenon. We will, however, have more quantitative and robust results on this matter once the full sample of 301 debris disks is analyzed.

Chapter 4

HD 37306: An unusually large gaseous transit in a debris disk

4.1 Introduction

Debris discs were long thought to be second generation dusty discs completely devoid of gas. However, this paradigm has changed in the last few years with the detection of gas in a growing number of young debris discs (e.g. Kóspál et al. 2013, Moór et al. 2015, Rebollido et al. 2018 and the references in Kral et al. 2017b). In our ongoing survey to robustly estimate the fraction of debris discs harboring circumstellar gas (described in Iglesias et al. 2018), we have followed the methodology described in Kiefer et al. 2014a. In short, we searched for narrow absorption features superimposed onto the photospheric absorption lines in the Ca II doublet H & K. These absorption features, when variable, can be interpreted as arising from comets falling towards the star (hence the term Falling Evaporating Bodies, FEBs).

Our survey sample consists of ∼300 objects selected with a methodology that is unbiased in terms of disc inclination. We have gathered several epochs of observations for ∼91% of them, compiling a rich database of thousands of spectra. The full variability analysis will be presented in Iglesias et al. (in prep), but in this work, we focus on a particularly intriguing object: HD 37306.

HD 37306, a bright A1V-type star, was previously studied by our team in Iglesias et al. (2018). With the data available at the time, we concluded that the two stable "extra" components in the Ca II lines that the object presented, were of interstellar origin. In that study we analysed 26 high-resolution observations from February 2006 to March 2016 where no variability was detected. Recently, we updated our database collecting new publicly available observations of our sample from the ESO archive. We found eight new observations of HD 37306 taken in 2017 where remarkable additional absorption features in several metallic lines (also reported in Rebollido et al. submitted) were detected, particularly large in the Ca II lines. In this study we complement this data with additional spectroscopy and time series photometry and present different scenarios to explain the origin of these transient features.

4.2 HD 37306: Stellar parameters and Spectral Energy Distribution (SED)

In Iglesias et al. (2018) we estimated some of the stellar properties by fitting Kurucz models (Castelli et al., 1997) to the Ca II (at 3933.66 & 3968.47 Å) and Na I (at 5889.95 & 5895.92 Å) doublets. We estimated a $v \sin i$ of 140 ± 5 km.s^{-1} (consistent with previous estimates), a $T_{\rm eff}$ of 8800 ± 50 K (in agreement with Gaia DR2 estimate of $9138\pm^{297}_{386}$ K, Gaia Collaboration 2018), $\log g$ of 4.15 ± 0.38 *dex* and *[Fe/H]* of -0.12 ± 0.22. We also estimated a heliocentric radial velocity of 23.49 ± 1.28 km.s^{-1}, consistent with the previous measurement found in the literature of 23.00 ± 0.70 km.s^{-1} (Gontcharov, 2006). HD 37306 is located at a distance of 70.46 ± 0.39 pc (Gaia Collaboration, 2018) and it has been reported to be a member of the Columba Association (Zuckerman and Song, 2012). We assessed the probability of belonging to the Columba Association with the BANYAN Σ[1] (Bayesian Analysis for Nearby Young AssociatioNs Σ) tool (Gagné et al., 2018) and confirmed its membership with a 99.3% probability. Incidentally, an isochronal age of $28.53\pm^{307.72}_{28.52}$ Myrs was estimated for the object using VOSA[2] (Bayo et al., 2008) based on the SED fitted parameters and different sets of isochrones (Baraffe et al. 1998, Siess et al. 2000). Thus we adopt the age of 30 Myrs of the Columba Association (Torres et al., 2006). Ages from the literature range between 10 Myrs (e.g. Ballering et al. 2013, De Rosa et al. 2014, David and Hillenbrand 2015) and 453 Myrs (Gontcharov, 2012).

[1]http://www.exoplanetes.umontreal.ca/banyan/banyansigma.php
[2]http://svo2.cab.inta-csic.es/theory/vosa/

Regarding its known local properties, HD 37306 is surrounded by a debris disc (Zuckerman and Song, 2012), confirmed by the excess emission in the SED (see Fig. 4.1). We have fit model grids for the star and disc to the data. We used synthetic photometry of the models to fit the photometry, and resampled model spectra to fit the IRS spectrum. The model is composed of a PHOENIX model atmosphere (Husser et al., 2013) at a given temperature, which is normalized to the optical photometry by solid angle, and a model for the thermal emission depending on the temperature of the dust, where the Planck function is normalized to the mid-/far-infrared emission by, basically, the dust mass in the disc. The best fitting model parameters are found with the *MultiNest* code (Feroz et al., 2009), with both the stellar and disc parameters found simultaneously. The best fit model has a stellar $T_{\rm eff}$ = 9100K, consistent with the previous estimates. The dust component has a temperature of 120K and fractional luminosity $L_{\rm disc}/L_\star = (7 \pm 0.2) \times 10^{-5}$. Based on this temperature and the stellar luminosity of $17L_\odot$, the blackbody radius for the dust is 21au. A weak silicate feature is visible in the IRS spectrum when the best fitting model is subtracted, indicating that at least some small ($\sim \mu$m sized) dust is present, and therefore that the dust is not entirely comprised of grains large enough to behave as blackbodies. Thus, the true distance of the dust from the star is likely larger than 21au, probably of the order of 50au.

4.3 Observations and data analysis

4.3.1 Spectroscopic Data

We have collected a total of 35 high-resolution (R = 48,000 – 115,000) optical spectra from different instruments with wavelength coverages within a range $\lambda \sim 3350 - 9500$Å, combining our own observations and others from the ESO archive. Our data set includes spectra taken with HARPS (Mayor et al., 2003) mounted on the ESO 3.6m telescope and FEROS (Kaufer et al., 1999) on the MPG/ESO 2.2m telescope, both at La Silla Observatory in Chile, and MIKE (Bernstein et al., 2003) mounted on the Magellan-Clay telescope at Las Campanas Observatory, Chile. The dates of the observations, the instruments used and the number of spectra per night are summarized in Table 4.1.

All the observations were reduced using the standard pipelines of each instrument. The ESO

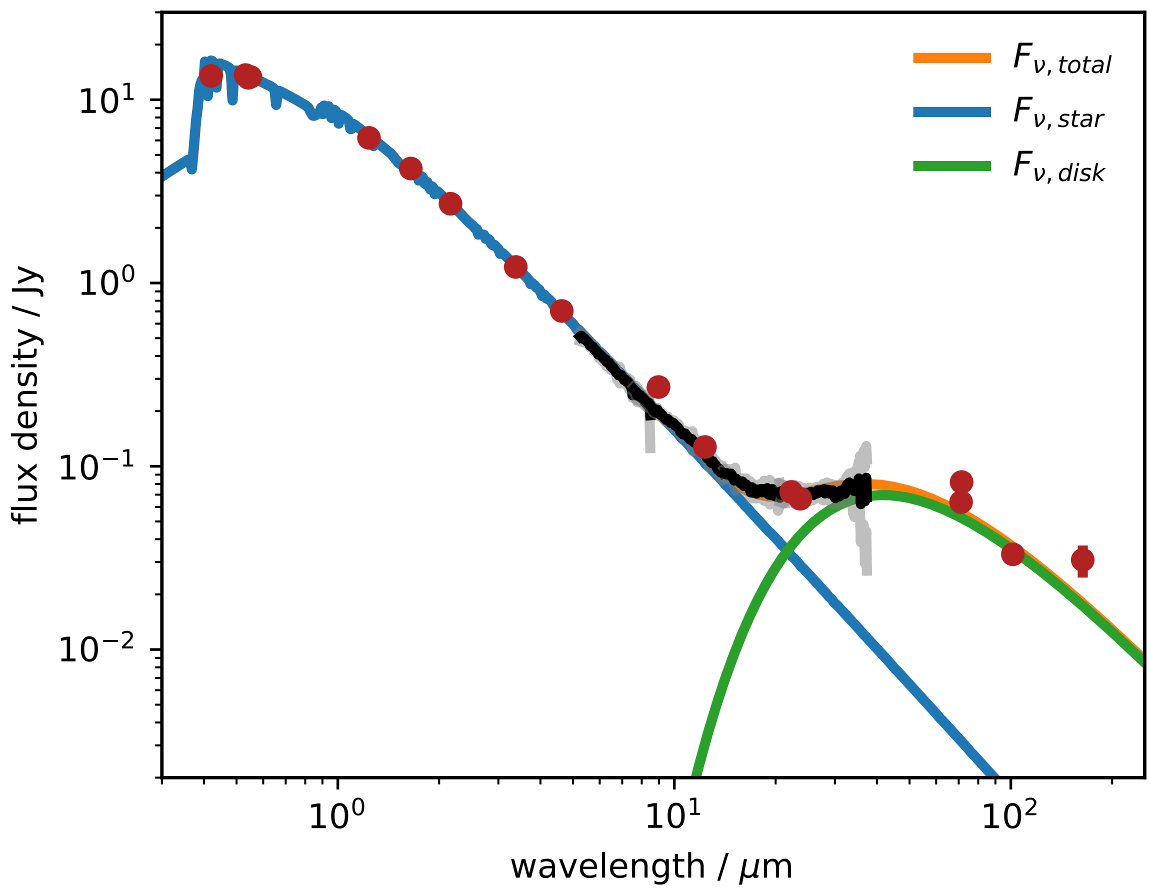

Figure 4.1: Flux distribution for HD 37306. Dots show photometry and the black and grey lines show the *Spitzer* IRS spectroscopy and uncertainty. The blue line shows the best-fit stellar photosphere, and the green line the best-fit modified blackbody for the disc.

spectra were downloaded from the Phase 3 portal, and the MIKE spectra were reduced with the CarPy pipeline (Kelson et al. 2000, Kelson 2003). Barycentric radial velocity corrections were applied to the MIKE spectra as these corrections are not included in its pipeline. Telluric line contamination was removed using MOLECFIT[3] (Smette et al. 2015, Kausch et al. 2015) in the same way as in Iglesias et al. (2018).

In order to quantify the extra absorption features detected in September 2017, we normalized each spectral line and computed a median from all the observations without the absorption along with another median from all the observations where the additional absorption was detected. An example for the Ca II K line can be seen in Fig. 4.2. Then, we divided the median containing the absorption by the median with no detection to analyse the properties of the feature isolated from the photospheric line and additional interstellar features.

We consider as a "detection" those absorptions in the residual spectrum (resulting from the division of the medians) that exceed 3σ. As these residual features are unusually wide, and thus, seem to be dominated by Doppler broadening we fit Gaussian profiles to these absorptions in order to estimate their parameters (see Table 4.2). Examples of these residual absorptions and their Gaussian fits are shown in Fig. 4.3 for the Ca II lines and Fig. 4.4 for Ti II and Fe II.

The observed wavelength of each transition in air values were taken from the NIST Atomic Spectra Database[4]. The heliocentric radial velicities of the absorptions were estimated from the center of the Gaussian fits. The apparent column densities N were computed following Savage and Sembach (1991) using oscillator strength values from Morton (1991) in the case of Ca II and from the NIST Atomic Spectra Database for Ti II and Fe II. Equivalent width and Doppler broadening parameter b were also derived from the Gaussian fit, with $b = FWHM/2\sqrt{\ln 2}$. The instrumental effects on b are negligible in this case.

4.3.2 Photometric Data

In order to complement our spectroscopic observations, we mined photometric databases for simultaneous observations. In particular, we collected photometric measurements from MASCARA North (Talens et al. 2017, Talens et al. 2018), ASAS-SN (Shappee et al. 2014, Kochanek

[3] http://www.eso.org/sci/software/pipelines/skytools/molecfit
[4] https://www.nist.gov/pml/atomic-spectra-database

Table 4.1: Spectroscopic data used in this work. Instrument, number of spectra per night and UT dates of each observation.

Instrument	N Spectra	Dates
HARPS	4, 2, 2, 2, 2	2006-02-[08, 09, 10, 11, 13]
HARPS	2, 2	2006-03-12, 2006-11-18
HARPS	2, 2, 2	2007-12-[05, 06, 10]
FEROS	2	2015-10-23
FEROS	1, 1	2016-03-[28, 29]
FEROS	2, 1, 2, 1, 1, 1	2017-09-[23, 24, 25, 26, 27, 30]
MIKE	1	2019-03-18

Table 4.2: Parameters of the observed absorption lines. Element, observed wavelength of the transition in air, heliocentric radial velocity of the absorption, logarithm of the apparent column density N, equivalent width and Doppler broadening parameter b. Errors in $V_{\odot}$ are in the order of 2–3 $km\,s^{-1}$ and for $\log_{10} N$, EW and b are in the order of 10–15%.

Elem.	Wavel. (Å)	$V_{\odot}$ ($km\,s^{-1}$)	$\log_{10} N$ (cm^{-2})	EW (mÅ)	b ($km\,s^{-1}$)
Ti II	3759.30	26.11	12.16	35.21	26.58
Ti II	3761.33	25.49	11.88	23.62	26.47
Ca II	3933.66	22.00	12.57	276.11	31.95
Ca II	3968.47	26.54	12.87	273.05	29.92
Fe II	4233.16	25.12	13.75	22.71	30.98
Fe II	4549.47	26.85	13.82	27.63	34.75
Fe II	4555.89	18.90	14.12	17.05	46.76
Fe II	4583.83	25.08	13.90	26.51	32.72
Fe II	4629.33	28.17	14.04	11.50	35.16
Fe II	4923.92	22.43	13.13	30.10	35.41
Fe II	5018.44	25.59	13.40	41.39	33.95
Fe II	5169.03	24.14	12.98	50.60	33.88
Fe II	5197.57	25.27	13.50	11.20	28.23
Fe II	5234.62	25.96	13.89	14.17	30.51
Fe II	5275.99	24.76	13.62	13.20	28.24
Fe II	5316.61	28.40	13.89	26.69	30.87
Fe II	6247.56	24.39	13.68	9.86	36.40
Fe II	6456.38	24.43	13.67	13.64	31.25
Ca II	8498.02	22.49	13.17	99.65	36.37
Ca II	8542.09	22.32	13.00	379.12	34.51
Ca II	8662.14	24.72	12.90	264.05	33.64

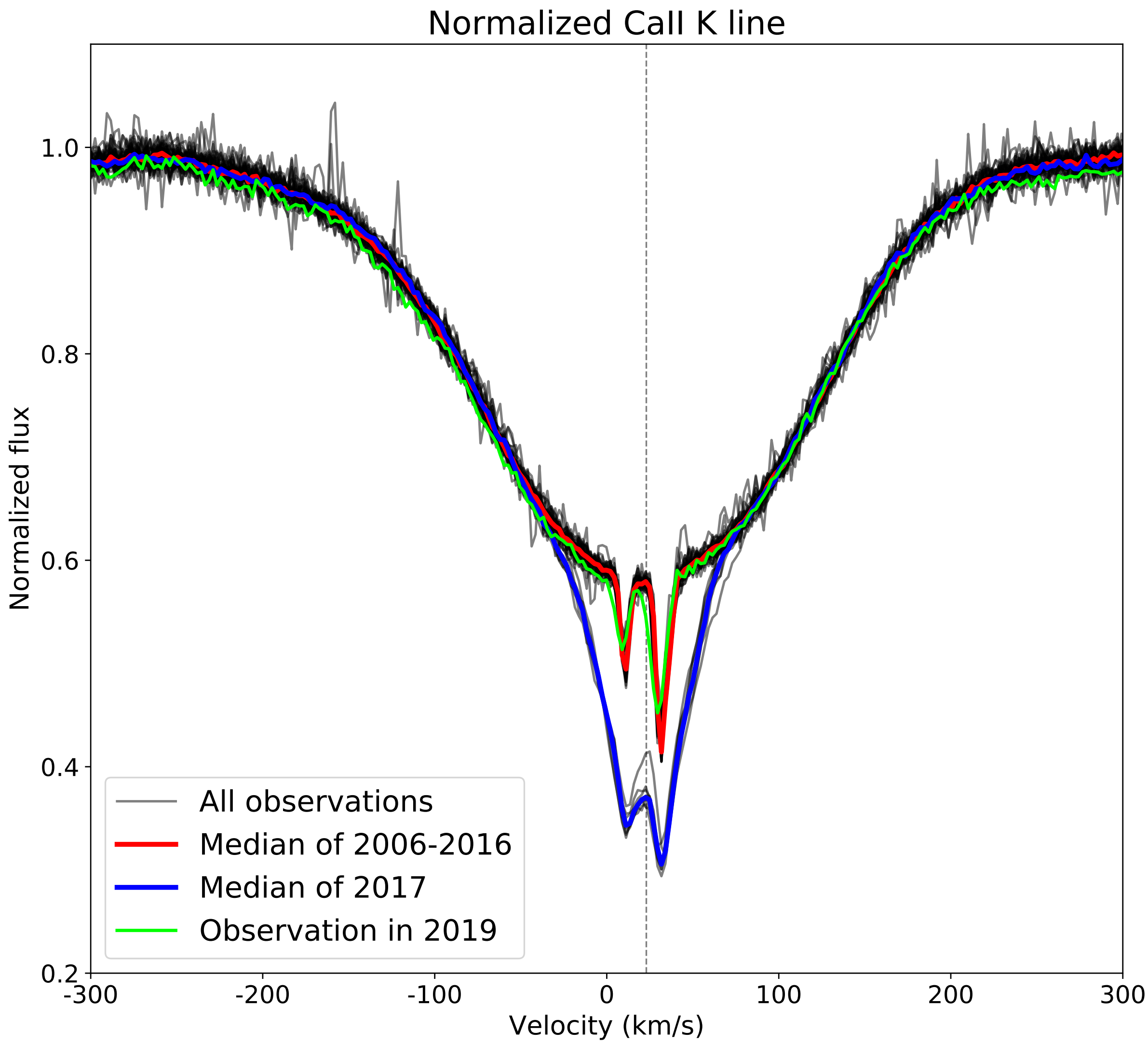

Figure 4.2: All the Ca II K line observations of HD 37306 normalized and over-plotted for comparison. The median spectra of all the epochs before and during the event are shown in red and blue, respectively. The spectrum taken in 2019-03-18 is highlighted in green. The stellar radial velocity is marked with a dashed line.

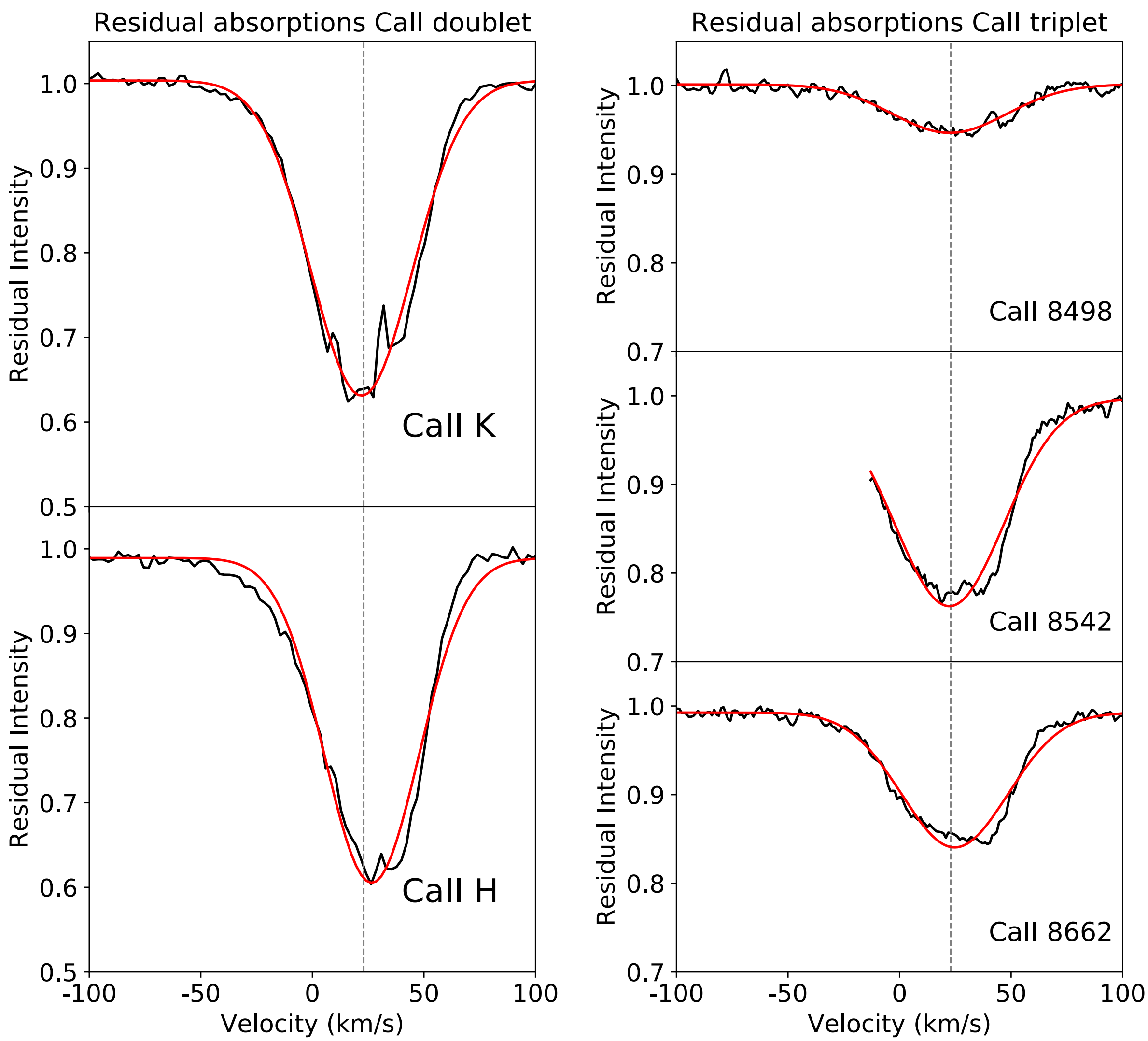

Figure 4.3: Median of the residuals of the Ca II doublet and triplet of HD 37306. Gaussian fits in red. The Ca II line at 8542Å is truncated due to an instrumental gap. Again, the radial velocity of the star is marked with a gray dashed line.

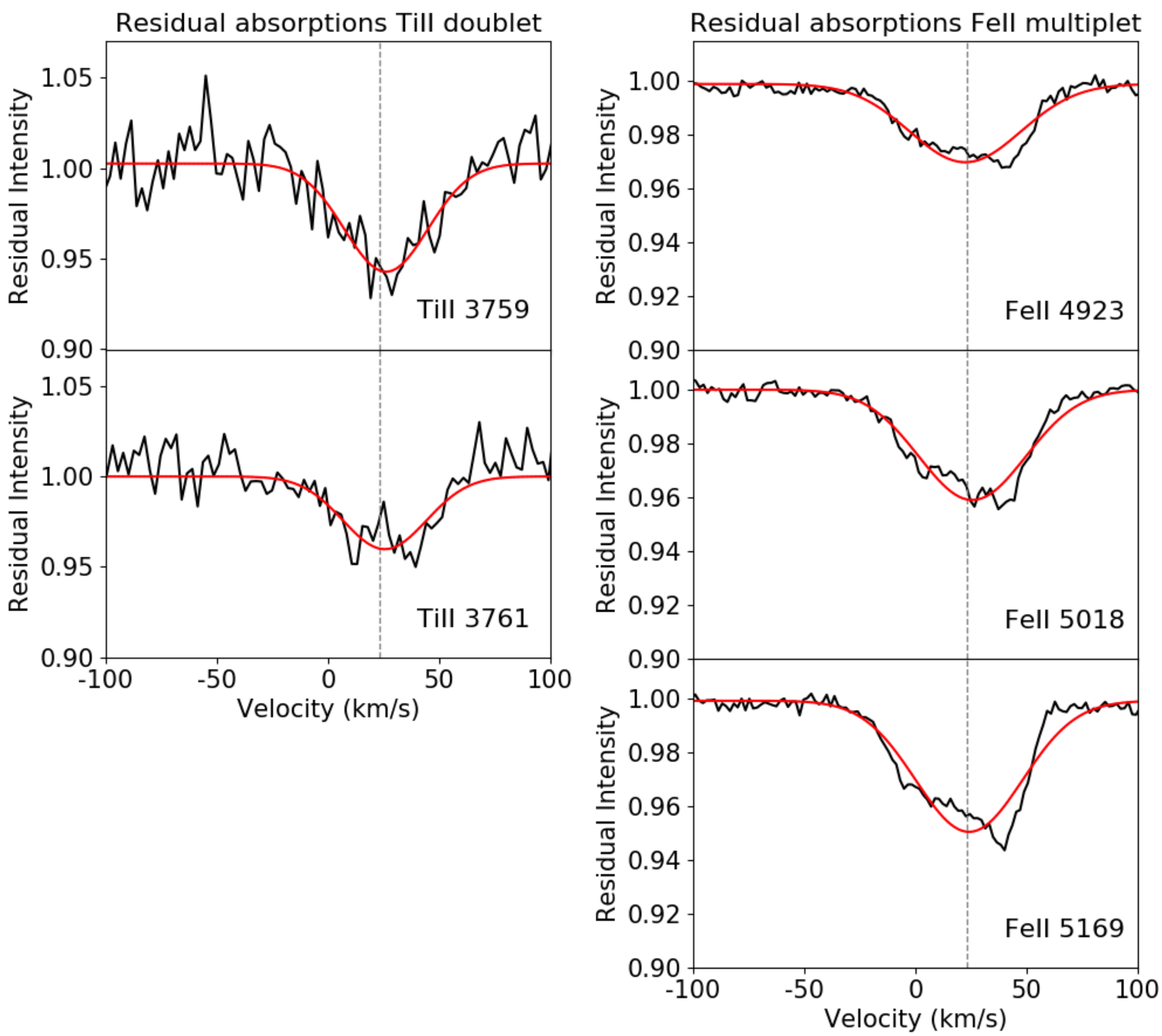

Figure 4.4: Median of the residuals of the Ti II doublet and Fe II multiplet of HD 37306.

et al. 2017) and TESS (Ricker, 2015).

Multi-site All-Sky CAmeRA

MASCARA North (Multi-site All-Sky CAmeRA; Talens et al. 2017, Talens et al. 2018), located at the Observatorio del Roque de los Muchachos on La Palma, observed HD 37306 between February 2015 and April 2019 for several hours each night the star was visible. Photometry was extracted from the 6.4 seconds cadence observations and processed using the primary calibration procedure outlined in Talens et al. (2018), which uses groups of stars to correct for systematics common to many light curves. This primary calibration corrects for the effects of the variable atmosphere, the camera transmission and intra-pixel variations before binning the data to a cadence of 320 seconds. After binning, a secondary calibration step is used to remove residual systematics in the light curves of individual stars. The fully calibrated light curve is shown in Fig. 4.5 (upper panel).

Part of the observations were taken simultaneously with the 2017 spectroscopic campaign, as can be seen in Fig. 4.5 (zoom in the lower panel). These observations started mid September 2017. No significant change in flux was observed during or after this time.

ASAS-SN

The "All-Sky Automated Survey for Supernovae" (ASAS-SN) project (Shappee et al. 2014, Kochanek et al. 2017) consists of 24 telescopes in different locations around the globe. This survey has taken multiple observations of HD 37306 from 2013-09-19 up to date. In this case, we took into account the fact that the observations were taken with several different instruments and normalized each light curve per instrument by its median value for better comparison. However, similar to the observations taken with MASCARA, no significant changes were detected in the light curves.

TESS

The Transiting Exoplanet Survey Satellite (TESS; Ricker 2015) observed HD 37306 in its 6^{th} Sector from 12 December 2018 to 6 January 2019 (unfortunately not within the spectroscopic transient event). HD 37306 (TIC 287842651, T = 6.08 mag) is one of the preselected targets

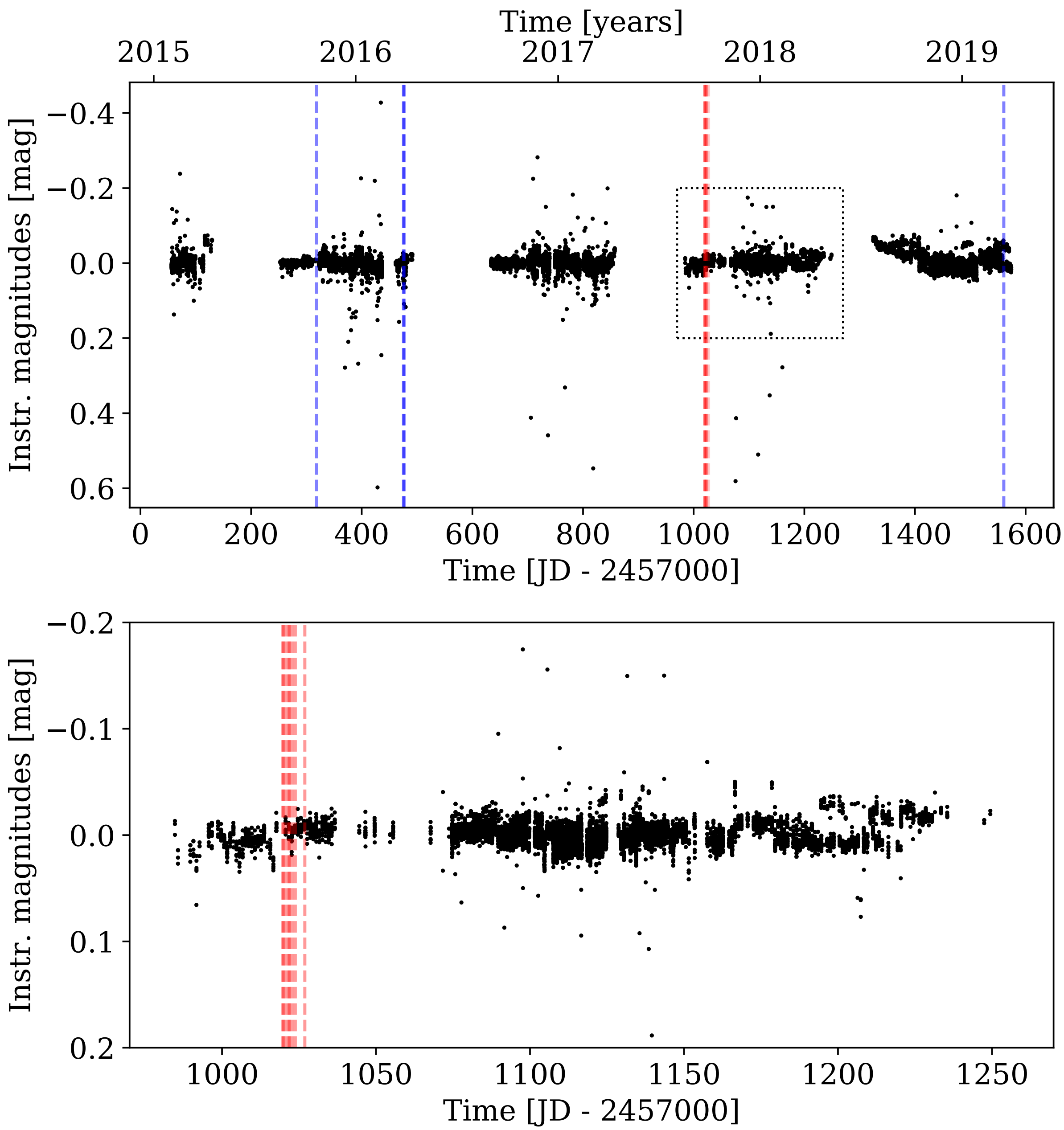

Figure 4.5: *Upper panel*: The full MASCARA light curve of HD 37306. The blue and red vertical dashed lines indicate the times of spectroscopic observations as seen in table 4.1. The marks in red correspond to the spectroscopic observations presenting the event. No variations were detected in spectroscopic observations of the epochs marked in blue. *Lower panel*: Zoom into the black dotted box seen in the upper panel.

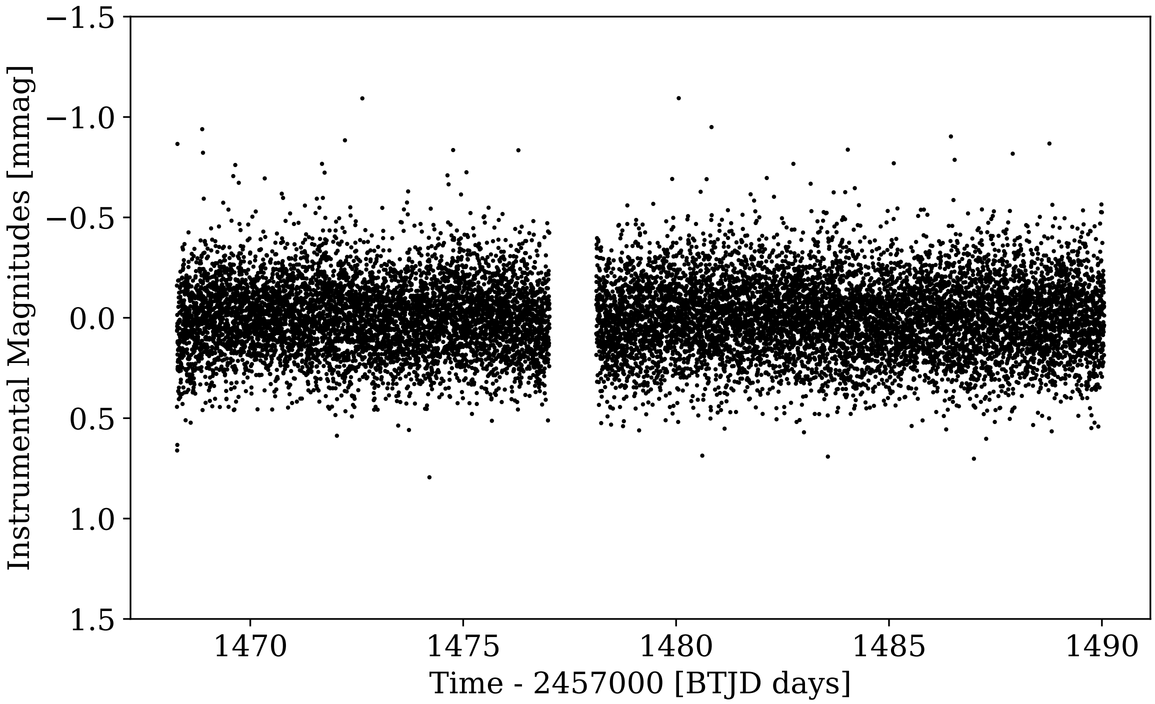

Figure 4.6: The full TESS light curve of the star HD 37306. The gap of about one day in the light curve is caused by a pause in observations due to TESS downlinking the data to Earth.

for which short cadence (i.e. 2-minute) data is provided. We use the 2-minute Presearch Data Conditioning (PDC; Smith et al. 2012; Stumpe et al. 2012) light curve from the Science Processing Operations Center (SPOC) pipeline (Jenkins et al. 2016; Jenkins 2017), which was originally developed for the Kepler mission (Jenkins et al., 2010). These light curves are corrected for systematics by the SPOC pipeline. We also remove every measurement with a non-zero "quality" flag (see §9 in the TESS Science Data Products Description Document[5]) which mark anomalies like cosmic ray events or instrumental issues. This finally gives as a time span of 21.8 days and a duty cycle of 95%. The resulting full light curve can be seen in figure 4.6.

A frequency analysis using the software package Period04 (Lenz and Breger, 2005) that combines Fourier and least-squares algorithms was conducted. It reveals no significant frequencies down to a signal-to-noise ratio of 4 (following the analysis in Breger et al. 1993).

[5]`https://archive.stsci.edu/missions/tess/doc/EXP-TESS-ARC-ICD-TM-0014.pdf`

4.3.3 Imaging Data

Additionally, we collected publicly available SPHERE (Beuzit et al., 2019) observations of HD 37306 from the ESO archive (program ID 095.C-0212). The observations were performed using the dual-band imaging mode IRDIFS ($H2H3$, Vigan et al. 2010, Dohlen et al. 2008, Claudi et al. 2008). Basic data reduction was performed using the SPHERE Data Reduction Handling pipeline (Pavlov et al., 2008), to perform background subtraction, flat-field and bad pixels corrections, and to determine the position of the star behind the coronograph. To try to detect the debris disc we processed the data using the angular differential imaging technique (Marois et al. 2006, Gomez Gonzalez et al. 2017) by performing a principal component analysis before de-rotating and stacking the pupil-tracking observations. The sky rotation achieved during the observations was of 29.2°. We removed between 1 and 25 principal components, but did not detect the disc in the reduced images. The 5σ contrast achieved were in the order of 14.6mag at 1 arcsec and 16.8mag at 3 arcsec. The FOV of 11"x11" considering the star is located at ∼70pc yields a coverage of $\sim (775au)^2$. Given the extra absorption detected in the Ca II, Fe II and Ti II lines, if the event is related to a body belonging to the debris disc, the disc is most likely close to edge-on, the most favorable case for a detection using angular differential imaging (Milli et al., 2012). Despite this possible favorable orientation, the non detection of the disc with SPHERE can most likely be explained either with a very small disc close to the star, or a low surface disc brightness (either an intrinsically faint disc or a radially very extended one).

4.4 Transient spectroscopic Event

In every observation of HD 37306 taken in September 2017 with the FEROS spectrograph, unusually large additional absorption features were present in the Ca II lines and other metallic lines such as Ti II and Fe II. These observations cover a range of eight consecutive nights and the absorptions are consistently present during the whole time range. Once we analysed this data-set, on March 2019, we took a new epoch of data with MIKE, and found that the additional absorptions had disappeared, going back to the "quiescent" stage. Unfortunately, we cannot determine the duration of the event detected in HD 37306 because previous and posterior data were taken ∼1.5 years apart. Therefore, we can only state that the event lasted at least eight days, but less than three years. A detailed view of the Ca II K line is shown in Fig. 4.2. The large additional absorption detected in 2017 can be appreciated in blue, while previous and posterior data only show two narrow features of interstellar origin (Iglesias et al., 2018).

We analysed other typical gas tracers such as Na I, O I and the Balmer lines, not finding any change to our 3σ threshold (see Sec. 4.3.1). We also studied SiO bands as collision (hyper-velocity impact) released gas would be expected to re-condense, but we observed no change on those bands either.

The absorptions in the H and K lines are equally intense due to saturation, suggesting optically thick material. Based on the absorption depth of the Ca II H & K lines and following the guidelines in Kiefer et al. (2014b), we estimated that the stellar fraction covered by the gas would be ∼37% and that the gas could be roughly located at about 15 stellar radii (or about 0.14 AU for the typical size of an A1V-type star of 2.0 $R_{\odot}$, Pecaut and Mamajek 2013). The higher temperature closer to the star is consistent with the detection of only ionized species and not neutral, and is also consistent with the feature exhibiting broader components due to thermal broadening.

The FWHM of the absorption features are in the order of $\sim 50\,\mathrm{km.s^{-1}}$, much larger than the typical values observed during exocometary transits ($10 - 15\,\mathrm{km.s^{-1}}$, Kiefer et al. 2014b, Beust et al. 2001) and their radial velocities are centered close to the stellar one, as can be seen in Figs. 4.3 and 4.4, and in Table 4.2. There are no significant changes either in the intensity of the absorptions or their radial velocities during the September 2017 period. Regarding the duration and stability of this event, although we do not know exactly how long it lasted, a duration $\geqslant$8 days is remarkably high in the context of exocometary transits, as they usually evolve in less than 1 day (Kiefer et al. 2014c, Welsh and Montgomery 2018). Considering the characteristics of the features, we expect that the gas producing them would be close to the star, as the radiation pressure on the ions is larger and acts more efficiently at shorter distances. A high radiation pressure could be responsible for a higher velocity dispersion of the ions, leading to broader components (Beust et al., 1991). Recent work by Lin and Chiang (2019) highlights the possibility that gas released from bodies that are on eccentric orbits, whether they be planetesimals or smaller dust, should also reside on an eccentric orbit. Thus, it is possible that some or all of the gas velocity dispersion is related to its origin, rather than radiation pressure acting solely on the gas.

4.5 Discussion

We here explore different possibilities that might explain the observed absorptions and evaluate which one could be the most likely scenario.

4.5.1 Instrumental Artifact

In order to discard the possibility that the absorption might be due to an instrumental issue, we also analysed spectra from other A-type stars taken during the same nights with the same instrumental set-up. We did not detect any similar event in these other sources, thus firmly ruling out any possible instrumental artifact.

4.5.2 Circumstellar Shell

A possible explanation for the observed spectroscopic event could be a circumstellar shell. This scenario could explain the long duration and stability of the absorptions. In addition, absorption features in the Ti II and Fe II lines are usually present in shell stars. However, shell stars typically present narrow absorption features at the core of the Hydrogen lines (Slettebak, 1986; Gray and Corbally, 2009). As previously mentioned, we analysed the Balmer H lines of HD 37306, not finding any sign of non-photospheric absorption or emission or any variation at all (to a 3σ level) through all the observations. The relatively low projected rotational velocity of HD 37306 (considering we are discussing fast rotators given the spectral type) of 140 km.s^{-1} also argues against this scenario, since, according to Abt (2008) and Abt et al. (1997), evidence of “shell-like” circumstellar gas is mainly detected for stars with $v \sin i > 200$ km.s^{-1}. Although the origin of circumstellar shells is unclear, some studies suggest they are accreted by rapidly rotating stars ($v \sin i \geqslant 200$ km.s^{-1}) from the interstellar medium (Abt 2015). In this particular case, it would be unlikely that HD 37306 accreted and lost such a shell within three years. On the other hand, considering the possibility of the shell being expelled from the star, as it seems to be the case for fast rotating super giants (e.g. Gvaramadze et al. 2018, Kourniotis et al. 2018), the lack of signs of stellar activity in the Balmer lines and the not high enough projected rotational velocity do not favour this possibility either.

4.5.3 Exocometary Break-up

Another reasonable model for the week-long absorptions might be similar to what was proposed for the star KIC8462852 (Boyajian et al. 2016, Wyatt et al. 2018): a family of exocomets observed after breakup. We consider the possibility of an optically thick "stream" of ionized gas that fills out some fraction of its orbit.

To have a better estimate of the configuration that could lead to an event lasting over several days, we tried to model the extra absorption line with a "toy model" of an eccentric gaseous disc. This model does not properly calculate the optical depth for different velocities but rather computes a histogram of the number of particles that have a certain velocity and are passing in the line of sight of the star.

A given model is fully described by the following parameters, the inner semi-major axis r_0, the radial width of the disc Δr, the eccentricity e, inclination i, position angle ϕ, argument of periapsis ω, opening angle ψ, stellar mass $\mathrm{M}_\star$ stellar radius $\mathrm{R}_\star$, and stellar radial velocity R_v (the latter three values being fixed to $2.15\,\mathrm{M}_\odot$, $2.0\,\mathrm{R}_\odot$, and $23.5\,\mathrm{km.s}^{-1}$, $\mathrm{M}_\star$ and $\mathrm{R}_\star$ taken from Pecaut and Mamajek 2013[6] and R_v from Iglesias et al. 2018). We then draw 2 000 000 particles, and each particle has the following orbital parameters; a semi-major axis r drawn uniformly between r_0 and $r_0 + \Delta r$, an inclination (and position angle) drawn from a normal distribution centered at i (and ϕ, respectively) with a standard deviation of ψ, with all the particles sharing the same argument of periapsis ω. Then, we take the mean anomaly uniformly between $[0, 2\pi)$, solve Kepler's equation for the eccentric anomaly and compute the true anomaly ν from it. We can then compute the positions and velocities $(x, y, z, v_\mathrm{x}, v_\mathrm{y}, v_\mathrm{z})$ of each particle (z being the direction towards the observer). The code checks which one is passing in the line of sight of the star ($\sqrt{x^2 + y^2} \leqslant \mathrm{R}_\star$ and $z > 0$) and saves its radial velocity v_z. We compute the histogram F_mod of all v_z (with the same binning as the observations) that satisfied the aforementioned criteria and try to fit it to the observations F_obs. We first compute the scaling factor that minimizes the χ^2,

[6] http://www.pas.rochester.edu/~emamajek/EEM_dwarf_UBVIJHK_colors_Teff.txt

as

$$f_{\text{scale}} = \frac{\sum\left(\dfrac{F_{\text{mod}} \times (F_{\text{obs}} - 1)}{\sigma^2}\right)}{\sum\left(\dfrac{F_{\text{mod}}}{\sigma}\right)^2}. \tag{4.1}$$

We subtract -1 from F_{obs} because the observations are normalized to 1 while the histogram starts at 0. The final model is then obtained as $F_{\text{mod}} = 1 + F_{\text{mod}} \times f_{\text{scale}}$. As already mentioned, this approach really is a "toy model" as we do not compute the optical depth in the photospheric line as a function of the radial velocity. Therefore we cannot really constrain the vertical extent of the disc for instance, but this allows us to have a first order approximation of where the gas should be to reproduce the velocity dispersion that we observe around HD 37306.

The problem is highly degenerate, and after several tests we settled on the following free parameters: the inner radius r_0, the ratio between the width of the disc and the inner radius $\Delta r/r_0$, the eccentricity e, and the argument of periapsis ω. The value of the position angle does not matter for the modeling, and we fix $i = 90^\circ$ and $\psi = 0.05$. To find the best fit solution, we use an affine invariant ensemble sampler Monte-Carlo Markov Chain, implemented in the `emcee` package (Foreman-Mackey et al., 2013), using 100 walkers, a burn-in phase of 1 000 steps and a final length of 2 500 steps. At the end of the run, we find an acceptance fraction of 0.26 and the maximum auto-correlation length among the four free parameters is 43 steps. Figure 4.7 shows the best fit model to the observations, Figure 4.8 shows the top view of the same model, and the probability distributions are shown in Figure 4.9 (using the `corner` package, Foreman-Mackey, 2016). From those probability distributions we derive the 16$^{\text{th}}$ and 84$^{\text{th}}$ percentiles to estimate the uncertainties, which are reported in Table 4.3. From Figure 4.9 it is clear that the inner edge of the disc (r_0) and the eccentricity of the disc (e) are coupled, as expected, given that we are only modeling the radial velocity dispersion. Furthermore, one should note that because the input parameter is $\Delta r/r_0$ (and not simply Δr), there is also a degeneracy between the latter value and r_0 (and hence with e as well). We find that the gaseous disc should have inner and outer edges with semi-major axis between 8.5 and 19.6 $\mathrm{R}_\star$, and hence should be quite extended in the radial direction. Those values yield orbital periods between $5.5^{+2.7}_{-1.6}$ and $19.4^{+5.6}_{-5.1}$ days, suggesting that

Table 4.3: Free parameters, priors, and best fit results for the modeling of the observations assuming a gaseous disc around HD 37306.

Parameters	Prior	Best-fit
r_0 [$R_\star$]	[1, 20]	$8.5^{+2.6}_{-1.7}$
$\Delta r/r_0$	[0.1, 5]	$1.3^{+0.1}_{-0.1}$
e	[0.3, 0.98]	$0.6^{+0.1}_{-0.1}$
ω [°]	[80, 100]	$88.7^{+0.3}_{-0.3}$

overall, the gaseous disc would have to survive between half and one full orbit. Considering that the chances of detection increase for longer periods and that the gas does not present significant variations over the 8 days it was observed, it is more likely that the disc should have survived close to one full orbit. The eccentricity should be around 0.6, and we find that the pericenter of the disc should lie in between the star and the observer. This is because this configuration produces the largest radial velocity dispersion, and we do not find exactly 90° because of the slight asymmetry of the profile. If we consider the inclination of the orbiting material is close to 90° and that the lower limit on the stellar fraction covered by the gas is ~37%, then a lower limit on the opening angle of the disc should lie between 0.015 and 0.035, at the outer and inner edges of the disc, respectively. We should note that the model ignores the possible effect of radiation pressure, which might accelerate the dissipation of the gas.

Because the vast majority of the 2 000 000 particles do not pass in front of the star, the final modeled spectrum can be relatively noisy. Instead of increasing significantly the number of particles we smooth the modeled spectrum using a moving box; each velocity bin is the mean value of the 3 neighbours before and 3 neighbours after (including the bin that is evaluated). Because the observed spectrum is also noisy, especially close to the minimum, we also smooth it in a similar fashion.

As can be appreciated in Fig. 4.7, the model reproduces the absorption profile quite closely and the scenario is compatible with the duration of the event. In addition, the lack of detection in the simultaneous photometric observations taken with MASCARA and ASAS-SN could be explained by not reaching the sensitivity required to detect an exocomet transiting an A-type star. For instance, the first photometric detection of exocomets crossing in front of β Pictoris (also an A-type star) were performed using TESS observations and the dips were reported to

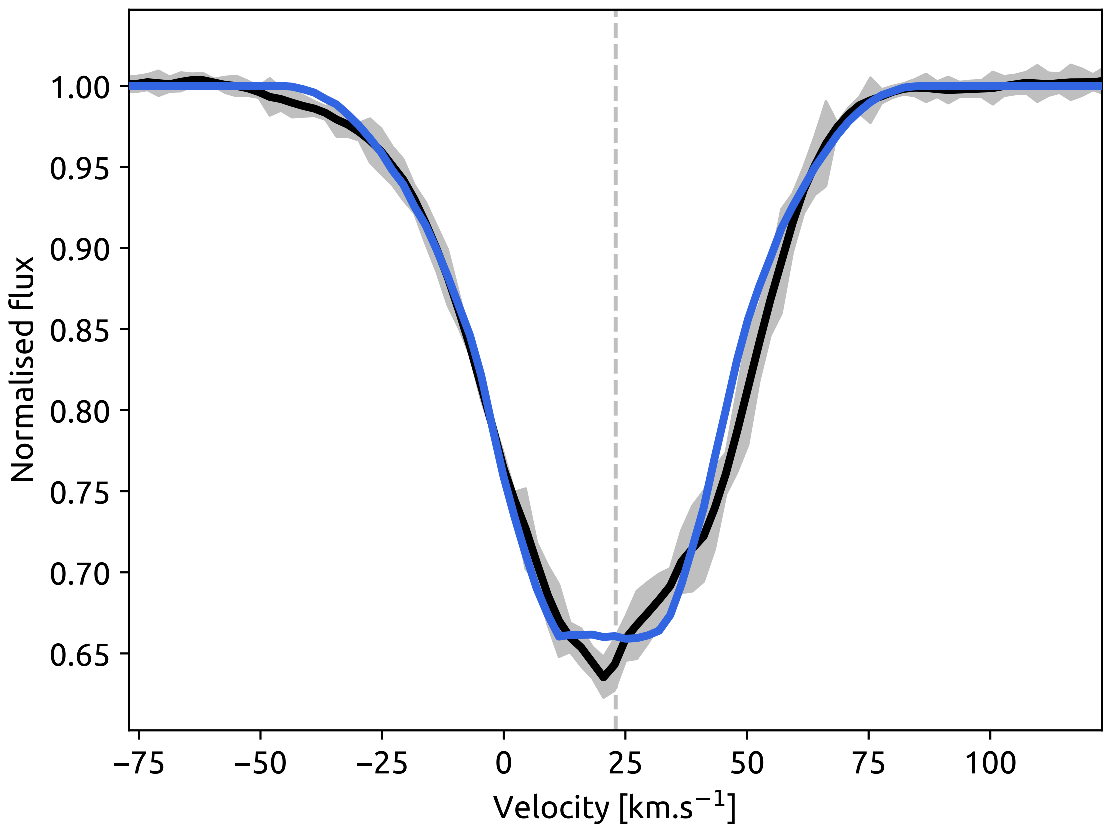

Figure 4.7: Model of the exo-cometary break-up (blue) to the Ca II K line absorption during the event (black).

have depths between 0.5 and 2 millimagnitudes (Zieba et al., 2019). Between MASCARA and ASAS-SN, MASCARA reached the best sensitivity with σ=17.7 millimagnitudes, clearly not sensitive enough to have a detection similar to those in β Pictoris. Unfortunately, the available TESS observations of HD 37306 were not simultaneous with the spectroscopic event.

4.5.4 Colliding Trojans

We studied the possibility of such a long lasting absorption being due to colliding trojans producing gas in the Lagrangian points of a possible hidden planet. But, in order to be so close to the star and transit for so long, the orbit of the planet needs to be highly eccentric. We performed hydrodynamical simulations of a gaseous disc with an embedded Jupiter mass planet

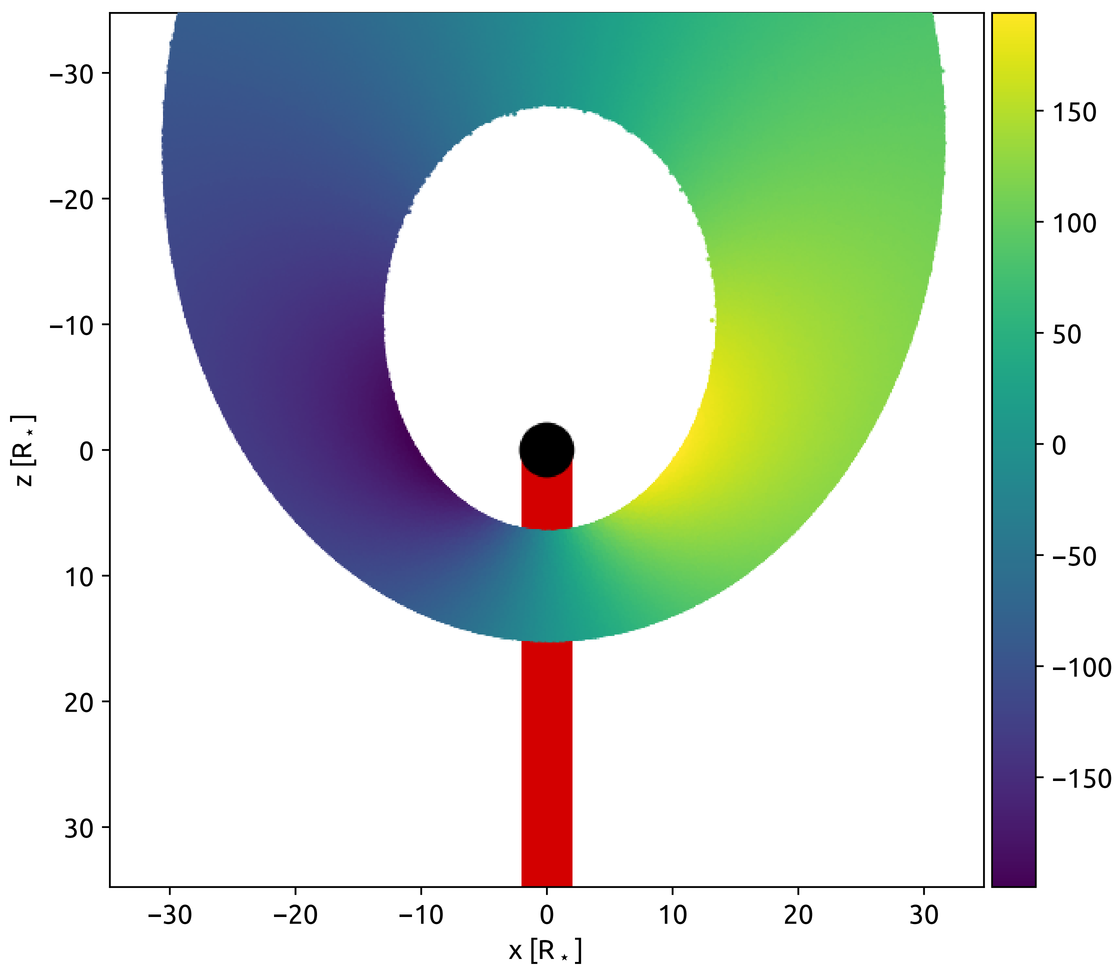

Figure 4.8: Top view of the best fit model. Observer located at the bottom. The color scale shows the radial velocity and the red shaded area shows where we estimate the velocity dispersion to fit the observations (the radial velocity of the star has been subtracted in this plot).

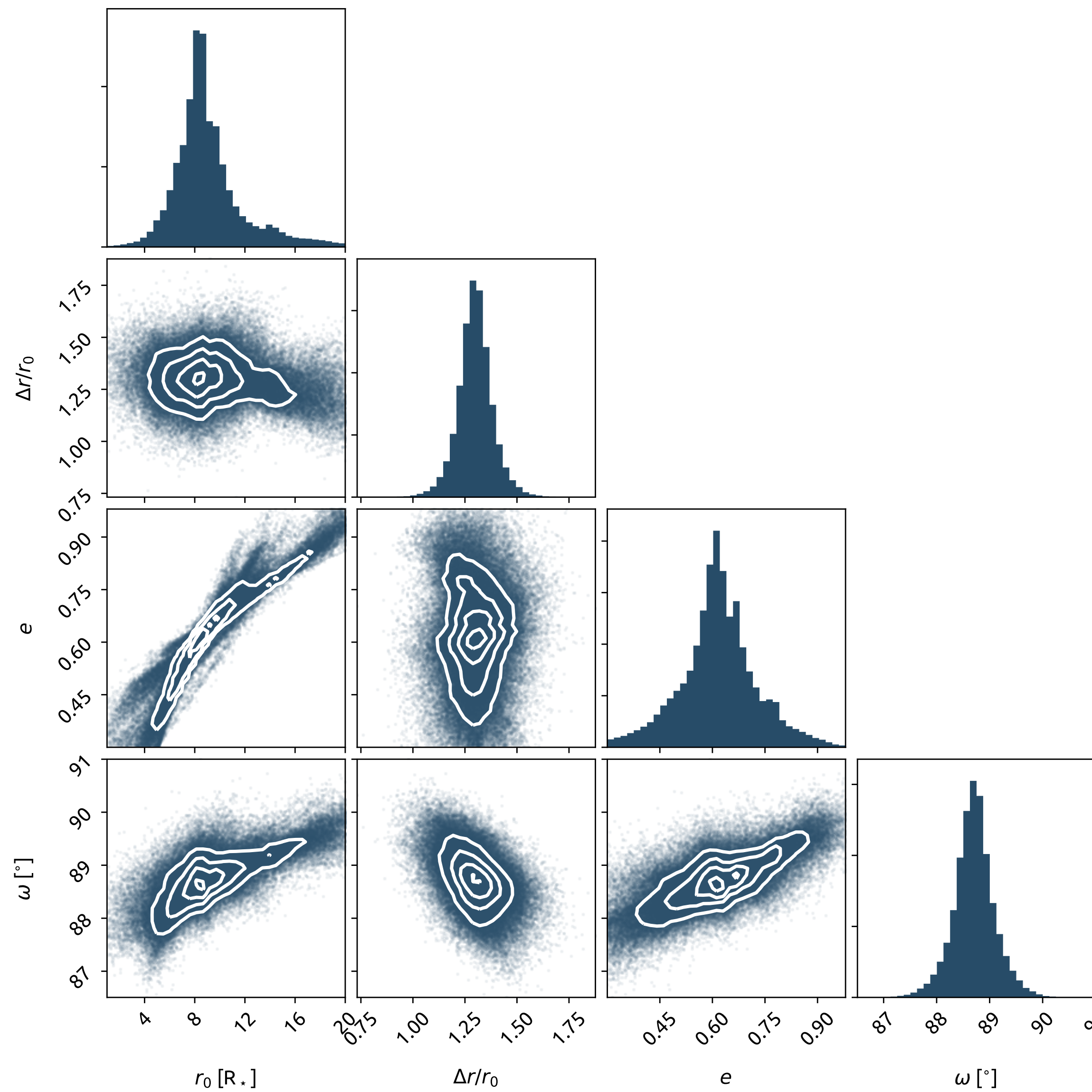

Figure 4.9: Probability distribution for the modeling results of the gaseous disc.

using our modified version (Montesinos et al., 2015) of the Fargo code (Baruteau and Masset, 2008). The surface disc density is defined by $\Sigma(r) = \Sigma_0 \frac{[1\text{au}]}{r}$, where $\Sigma_0 = 0.1$ g.cm^{-2}, and r the distance to the star in au. We assume a viscous fluid with a turbulent visocosity (Shakura and Sunyaev, 1973) given by $\alpha = 10^{-3}$. Under these circumstances, most of the gas is accreted during the simulation (10^5 yrs), remaining an optically thin layer of gas with a gap (carved by the planet). The resulting low density disc could be compatible with the lack of detection of a stable gas component. The quantification of the lack of detection is, however, out of the scope of this paper, since stability arguments discard this scenario (see below). On top of that simulation, we followed the evolution of (100,000) dust particles with different sizes ranging from microns to cms, where the dust is affected by the gas dynamics due to drag and drift forces. In addition to these forces, the dust particles feel the gravitational potential from the star. The self-gravity of the disc was neglected (details of our dust code can be found in Cuello et al., 2019).

We found that the presence of a Jupiter mass planet in a circular orbit carves a gap in the gaseous disc with a large dust particle concentrations ($\sim$ 1 Earth-mass) located at the Lagrangian points (L4 and L5) of the giant planet (in agreement with Lyra et al., 2009). In this case, the dusty trojans rotate at Keplerian velocity with zero eccentricity. For Jupiter mass planets with eccentricities higher than 0.1, we found that the dust is not able to accumulate in the Lagrangian points. It is worth mentioning that in order to explain the observations, trojan eccentricities should be at least 0.6.

4.5.5 Planetary Transit

Planetary transits are very difficult to detect in A-type stars using photometry given the brightness of the star compared to the shadow produced by a planet. However, the brighter the star, the higher the signal to noise of the transiting planet atmospheric spectrum. Here we propose a couple of scenarios involving a transiting planet.

A possible scenario could invoke a planet passing at close enough distance to the star allowing sublimation of its atmosphere (or even surface) to occur. To better understand the possible location and size of what could be causing the observed absorptions, we explore the scenario-independent constraints, similar to the analysis done in Boyajian et al. (2016). Fig. 4.10 (analog to Fig. 10 in Boyajian et al. 2016) shows constraints for the duration of the transit, assuming that the clump causing the dip is opaque and moves in circular orbits around the star. As mentioned in previous sections, for the stellar parameters we assume $R_\star = 2.0R_\odot$ and $M_\star = 2.15M_\odot$ (Pecaut and Mamajek, 2013). Following Boyajian et al. (2016), if the clump is much less massive than the star of mass $M_\star$ and orbits at a distance d from the star, then the relation between the clump radius r and the duration of the transit t is given by,

$$r \approx 1.85t\sqrt{\frac{M_\star}{d}} - R_\star. \tag{4.2}$$

In this scenario, we are assuming the clumps to be spherical and, basically, formed by a planet (or planetesimal) and the accumulation of sublimating material (gas and dust) inside its Hill sphere of radius $R_{\rm Hill} = d(M_{\rm pl}/[3M_\star])^{1/3}$.

Having no significant dip detected in the light curves ($> 3\sigma$), the clump size must be under this detection limit (dotted red line in Fig. 4.10), which, considering $R_\star = 2.0R_\odot$, translates into $r \approx 0.44R_\odot$. In order for the duration of the transit to be of at least eight days and be under the photometric detection limit, the clump should orbit at a distance $\geqslant\sim 100$ au. At this distance, the temperature would be too low for the planet to sublimate producing large dense clouds around it, and for the gas to ionize. In addition, if the probability of having a planetary transit is $\sim R_\star/d$, then at ~ 100 au this probability would be of 9.3×10^{-5}, making the probability of the detection very low.

We could also consider the case of a forming planet having a Hill sphere full of gas. At the very early phase of planet formation, the planet has an intrinsic luminosity due to accretion (peaking in L, L' bands), and what we would see would be actually the circumplanetary disc (not the planet itself). In this case, a forming (accreting) planet should be very bright (one should expect $10^{-3} - 10^{-6}$ $L_\odot$ during the first million years of formation; Mordasini et al. 2012). This scenario only makes sense in a gas-rich environment, therefore this is not likely to be the right explanation taking into account the debris disc nature and age range of the system. In addition, as discussed in the first case, to explain an eight days transit the forming planet would have to be far away from the star but, at the same time, the gas would have to be ionized, making the second possible explanation in this section very unlikely as well.

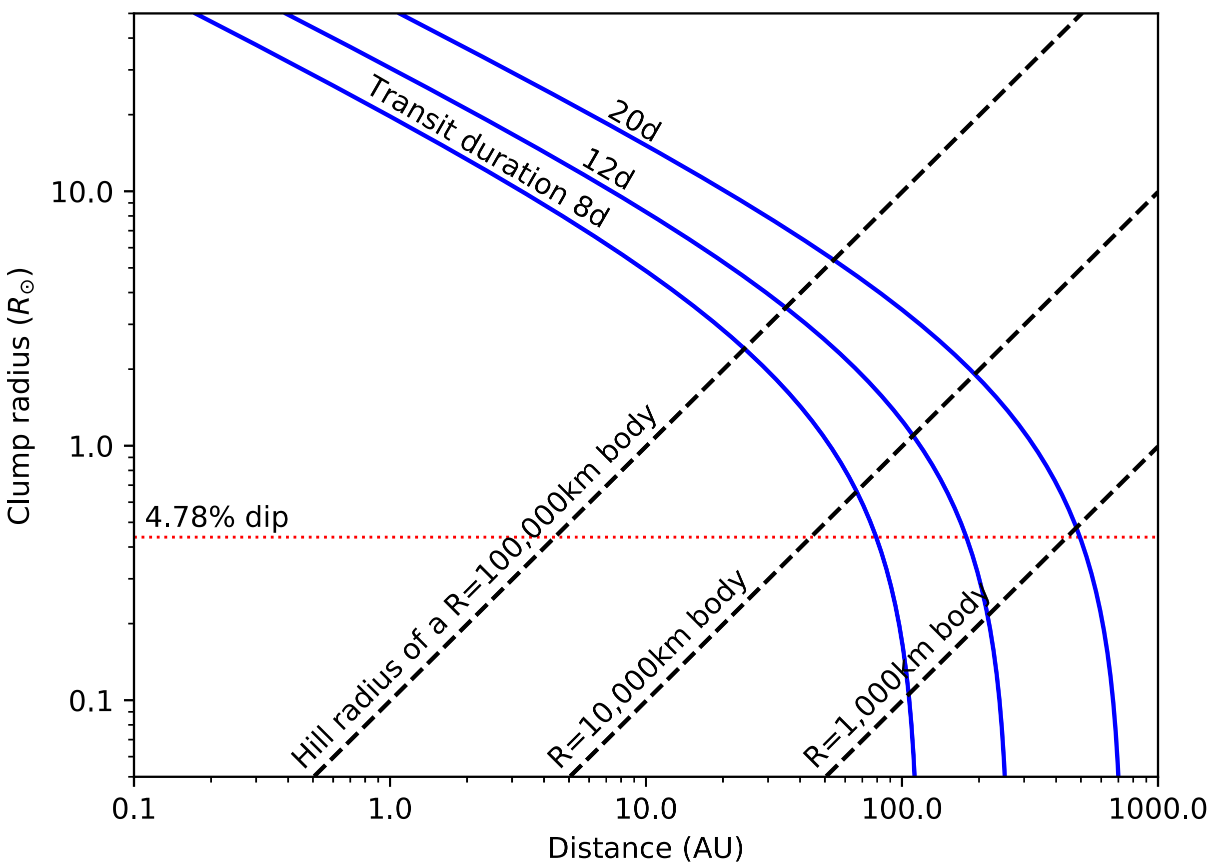

Figure 4.10: Distance to the star versus size of an optically thick, spherical dusty clump on circular orbits around the star. The solid blue lines show the transit duration, diagonal black dashed lines show Hill radii of planets of different sizes, and the red dotted line shows the minimum size the clump should have in order to have a 3σ detection in the MASCARA photometry, which corresponds to a 4.78% dip in the light curve.

4.5.6 Possible interstellar origin

In the diffuse interstellar medium (ISM), Ca II and Ti II are pretty well correlated (Hunter et al., 2006) and the Na I/Ca II ratio ranges from 0.1 to 1000 (Siluk and Silk 1974, Vallerga et al. 1993) depending on the dust and ionization state of the Ca II, which is not in disagreement with our detection. However, the median value of the b value for Ca II components is 1.3 km.s^{-1} in the diffuse ISM, corresponding to a kinetic temperature of around 4100 K (Welty et al., 1996). Our b values for the Ca II components are of 33.2 km.s^{-1} on average, which would correspond either to very high turbulent velocities (> 20 km.s^{-1}) or extremely high kinetic temperatures ($> 2 \times 10^6$ K). More importantly, interstellar features do not show such strong variations within short periods (e.g. Smith et al. 2013 and McEvoy et al. 2015), thus the appearance and disappearance of a large component within three years would be very unlikely. Besides, the star is at ~ 70 pc, thus it is located inside the local bubble where column densities do not reach such high values. For instance, at 100pc $\log N(\text{Ca II}) \sim 11.5\,\text{cm}^{-2}$ (Hunter et al., 2006), and the observed absorptions have on average a $\log N(\text{Ca II})$ of $\sim 12.9\,\text{cm}^{-2}$.

4.6 Conclusions

We detected unusually broad spectral absorption features from ionized gas species in the debris disc system HD 37306. The stellar spectra present stable non-photospheric absorption lines superimposed onto several Ca II, Fe II and Ti II lines over a time range of at least eight days.

We analysed simultaneous spectroscopic and photometric observations of HD 37306 before, during and after the event and found no significant change in the photometric data that might be correlated with the spectroscopic event. We also analysed high angular resolution SPHERE images of the target but the disc was not detected.

We evaluated several scenarios aiming to determine which one would provide the most likely explanation for the particular features detected in HD 37306. We were able to reasonably discard some possibilities such as an instrumental artifact, colliding trojans or an interstellar origin. Other options such as a circumstellar shell or a planetary transit cannot be completely ruled out, but remain as very unlikely possibilities.

We conclude that the most likely scenario would be the transit of a family of exocomets observed after breakup releasing a large amount of gas close to the star, at a few stellar radii. Our model reproduces satisfactorily the broad profile of the absorption feature and is in agreement with the duration of the event. A rather strong limitation of this scenario is that radiation pressure should dissipate Ca II on short timescales and this effect is not considered in our model.

Due to the stochastic nature of the event we reported in this study, it will be challenging to further characterize what happened during 2017. Future ALMA observations may help detect other gas tracers in emission, such as CO, that could have been released during this event, and may help us figure out the processes involved in this unusual week-long event. We will perform further high resolution spectroscopic observations of this system aiming to possibly detect any kind of additional events and characterize them to have a better understanding of the system. Given the rarity of this event, we aim to obtain an estimate of the occurrence rate of such phenomenon in debris disc stars.

Chapter 5

Variability in the Ca II K line of debris discs: stellar or exocometary activity?

This Chapter is based on a paper in preparation (Iglesias et al. in prep.), which is meant to be published under the same title.

5.1 Identification of variable objects

We analyzed a total of 269 objects having at least three observations of the Ca II K spectral line searching for those exhibiting any kind of variability in this line. We included publicly available and private observations taken up to March 31, 2019, which corresponds to ∼90% of the full sample. However, we have excluded a set of observations taken with MIKE spectrograph on September 2018 because of missing calibration lamps, which are important to assess wavelength shifts between observations which induce false variability detections.

In order to detect the variability, we normalized each epoch of the Ca II K line by fitting the continuum at both sides of the line. We selected a portion of the spectrum covering a range of 5Å at each side of the Ca II K emission or absorption (depending on the spectral type of the star), fit a straight line to this range and divided by this line in order to obtain the continuum flux normalized to one for every observation. Then, we obtain a median spectrum from all the Ca II K line spectra to use it as a reference spectrum; variability will be measured with respect to this median spectrum. After this, we divided each individual observation by this reference spectrum to analyze the residual flux.

Table 5.1: Sub-sample of debris discs presenting variability and their respective coordinates.

Name	HD Id or Other	R.A. [J2000]	Dec. [J2000]	Name	HD Id or Other	R.A. [J2000]	Dec. [J2000]
HD 1466	HD 1466	00:18:26.1	-63:28:38.9	CD-54 4621	MML 8	12:12:35.7	-55:20:27.2
HD 1461	HD 1461	00:18:41.8	-08:03:10.8	HD 107146	HD 107146	12:19:06.5	+16:32:53.8
kap Phe	HD 2262	00:26:12.2	-43:40:47.3	HD 108857	HD 108857	12:30:46.2	-58:11:16.7
lam01 Phe	HD 2834	00:31:24.9	-48:48:12.6	eta Crv	HD 109085	12:32:04.2	-16:11:45.6
HD 3670	HD 3670	00:38:56.7	-52:32:03.3	HR 4796	HD 109573	12:36:01.0	-39:52:10.2
nu. Phe	HD 7570	01:15:11.1	-45:31:54.0	HD 110058	HD 110058	12:39:46.1	-49:11:55.5
49 Cet	HD 9672	01:34:37.7	-15:40:34.8	rho Vir	HD 110411	12:41:53.0	+10:14:08.2
q01 Eri	HD 10647	01:42:29.3	-53:44:26.9	V MO Hya	HD 111786	12:51:57.8	-26:44:17.7
q02 Eri	HD 10939	01:46:06.2	-53:31:19.3	HD 113556	HD 113556	13:05:32.6	-58:32:07.9
V DK Cet	HD 12039	01:57:48.9	-21:54:05.3	HD 114082	HD 114082	13:09:16.1	-60:18:30.0
HD 13246	HD 13246	02:07:26.1	-59:40:45.9	iot Cen	HD 115892	13:20:35.8	-36:42:44.2
bet Tri	HD 13161	02:09:32.6	+34:59:14.2	lam Boo	HD 125162	14:16:23.0	+46:05:17.9
gam Tri	HD 14055	02:17:18.8	+33:50:49.8	HD 128311	HD 128311	14:36:00.5	+09:44:47.4
alf For	HD 20010	03:12:04.5	-28:59:15.4	HD 131835	HD 131835	14:56:54.4	-35:41:43.6
94 Cet	HD 19994	03:12:46.4	-01:11:45.9	bet Cir	HD 135379	15:17:30.8	-58:48:04.3
HD 21997	HD 21997	03:31:53.6	-25:36:50.9	BD-07 4003	HIP 74995	15:19:26.8	-07:43:20.1
V1229 Tau	HD 23642	03:47:29.4	+24:17:18.0	HD 137057	HD 137057	15:25:16.0	-38:09:28.4
28 Tau	HD 23862	03:49:11.2	+24:08:12.1	alf CrB	HD 139006	15:34:41.2	+26:42:52.8
HD 25457	HD 25457	04:02:36.7	-00:16:08.1	HD 138813	HD 138813	15:35:16.1	-25:44:02.9
gam Dor	HD 27290	04:16:01.5	-51:29:11.9	HD 140817	HD 140817	15:47:04.4	-35:30:37.2
V EX Eri	HD 30422	04:46:25.7	-28:05:14.8	HD 144587	HD 144587	16:07:29.9	-23:57:02.4
HD 30447	HD 30447	04:46:49.5	-26:18:08.8	HR 6051	HD 145964	16:14:28.8	-21:06:27.4
pi.01 Ori	HD 31295	04:54:53.7	+10:09:02.9	HR 6037	HD 145689	16:17:05.4	-67:56:28.6
HD 35367	HD 35367	05:24:20.7	+01:35:26.5	HD 146897	HD 146897	16:19:29.2	-21:24:13.2
HD 287861	HD 287861	05:25:10.2	+01:15:31.3	HR 6507	HD 158352	17:28:49.7	+00:19:50.3

Continued on next page

Table 5.1 – continued from previous page

Name	HD Id or Other	R.A. [J2000]	Dec. [J2000]	Name	HD Id or Other	R.A. [J2000]	Dec. [J2000]
HD 290609	HD 290609	05:33:05.5	-01:43:15.5	HD 159082	HD 159082	17:32:14.8	+11:55:48.1
HR 1915	HD 37286	05:36:10.2	-28:42:28.8	HR 6534	HD 159170	17:33:29.8	-05:44:41.2
HD 37306	HD 37306	05:37:08.7	-11:46:31.8	mu. Ara	HD 160691	17:44:08.7	-51:50:02.5
HR 1975	HD 38206	05:43:21.6	-18:33:26.9	HD 164249	HD 164249	18:03:03.4	-51:38:56.4
HD 38858	HD 38858	05:48:34.9	-04:05:40.7	eps Sgr	HD 169022	18:24:10.3	-34:23:04.6
HD 45184	HD 45184	06:24:43.8	-28:46:48.4	HR 6948	HD 170773	18:33:00.9	-39:53:31.2
HD 46190	HD 46190	06:27:48.6	-62:08:59.7	rho Tel	HD 177171	19:06:19.9	-52:20:27.2
HD 52265	HD 52265	07:00:18.0	-05:22:01.7	HD 181327	HD 181327	19:22:58.9	-54:32:16.9
HD 61005	HD 61005	07:35:47.4	-32:12:14.0	5 Vul	HD 182919	19:26:13.2	+20:05:51.8
HD 69830	HD 69830	08:18:23.9	-12:37:55.8	c Aql	HD 183324	19:29:00.9	+01:57:01.6
HD 71722	HD 71722	08:26:25.2	-52:48:26.9	HD 190470	HD 190470	20:04:10.0	+25:47:24.8
HD 76151	HD 76151	08:54:17.9	-05:26:04.0	kap01 Sgr	HD 193571	20:22:27.5	-42:02:58.4
HR 3570	HD 76653	08:55:11.7	-54:57:56.7	phi01 Pav	HD 195627	20:35:34.8	-60:34:54.3
HD 82943	HD 82943	09:34:50.7	-12:07:46.3	iot Del	HD 196544	20:37:49.1	+11:22:39.6
HR 3927	HD 86087	09:54:51.2	-50:14:38.2	V AU Mic	HD 197481	20:45:09.5	-31:20:27.2
HR 4138	HD 91375	10:30:20.1	-71:59:34.0	HR 8013	HD 199260	20:56:47.3	-26:17:46.9
V CE Ant	TWA 7	10:42:30.1	-33:40:16.2	alf Oct	HD 199532	21:04:43.0	-77:01:25.5
HD 95086	HD 95086	10:57:03.0	-68:40:02.4	HD 202206	HD 202206	21:14:57.7	-20:47:21.1
bet UMa	HD 95418	11:01:50.4	+56:22:56.7	HD 207129	HD 207129	21:48:15.7	-47:18:13.0
HD 98363	HD 98363	11:17:58.1	-64:02:33.3	39 Peg	HD 213617	22:32:35.4	+20:13:48.0
HD 101088	HD 101088	11:37:14.6	-69:40:27.2	tau01 Aqr	HD 215766	22:47:42.7	-14:03:23.1
HD 102458	HD 102458	11:47:24.5	-49:53:03.0	V342 Peg	HD 218396	23:07:28.7	+21:08:03.3
HD 104231	HD 104231	12:00:09.4	-57:07:01.9	HR 8843	HD 219482	23:16:57.6	-62:00:04.3
HD 106906	HD 106906	12:17:53.1	-55:58:31.8				

A residual spectrum which does not present any variability with respect to the reference spectrum should be flat and only dominated by its overall noise. Therefore, we searched for signs of variability by identifying the presence of narrow absorption or emission features having at least two data points over the 3σ level in this residual spectrum. We also include a constrain for the FWHM of these features: they must be wider than twice the resolution of the spectra in order to avoid selecting artifacts, and the must be narrower than 100 km.s^{-1} based on the widest FWHM of absorption features produced by exocomets reported in β Pic (Kiefer et al., 2014b). In addition, we searched for wide "wavy" patterns in this residual spectrum, which should be at least wider than 50 km.s^{-1} but not necessarily over the 3σ level. For this, we fit Gaussian profiles to the residual and any spectrum that differed from being "flat" (i.e. the amplitude of the Gaussian profile is different than zero) is considered as a "wavy" pattern (which are typically seen in pulsating stars). After visually analysing each residual spectrum for the 269 objects having at least three observations and searching for these signs of variability, we selected 97 objects exhibiting some kind of variation in at least one of their observations.

The main goal of selecting this sample is to determine whether the variability detected in their Ca II K spectral line is due to exocometary activity and thus there is presence of second generation circumstellar gas in the disk, or if it is attributed to a different cause, such as stellar activity, presence of companions, stellar spots, multiplicity, rotation/differential rotation, magnetic fields or pulsations. We have chosen to analyse mainly the Ca II K spectral line since it is the most sensitive circumstellar gas tracer in the UV-optical wavelength range and thus it is the main line used to search for exocometary activity (e.g. Ferlet et al. 1987, Kiefer et al. 2014b, Eiroa et al. 2016, Welsh and Montgomery 2018).

The sample is presented in Table 5.1. The main parameters of the sample are shown in Table D.1, in the Appendix. All parameters are taken from Simbad (Wenger et al., 2000), except for luminosity ratio $L_{\text{disk}}/L_{\star}$ which were obtained from the SED model fitting (Olofsson et al. in prep.) and age, which was categorized with a flag "O" for disks older than 100 Myr and "Y" for those younger than 100 Myrs. Since ages are very difficult to estimate, we have made a very rough estimation based on whether the disks belong to a moving group or not. If they likely belong to moving groups, then they are assumed to be "young", and if they are likely field stars, they are assumed as "old".

As previously mentioned, the sample was selected under the condition of having at least three observations in order to be able to identify any sign of variability. The number of observations per object ranges from a minimum of 3 up to a maximum of 2985 observations, as shown in Table 5.2. The cadence of the observations varies from one object to another, but they are, in general pattern-less. The minimum and maximum separation between epochs per object are also given in Table 5.2.

5.2 Methods and Results

5.2.1 Variability Analysis

Sources in the sample exhibiting signs of variability was classified into five categories of "type of variability" by visual inspection, as shown in Table 5.3. In these categories we describe the main characteristics of the variability observed in the residual spectra. If narrow emission or absorption features are observed, they are classified whether they are observed close to the radial velocity of the star (i.e. within 3σ of the features width from the stellar radial velocity, although this is a rather conservative estimate since the accuracy of the stellar RV could be worst and wider) or at any other velocity (random RV). As mentioned, in addition to narrow features, "wavy" patterns are also observed. Thus, these are classified into "symmetrical" or "asymmetrical", depending on whether a "wave" (or wide feature) is observed at any random position in the spectrum or if they show a symmetrical pattern centered at the radial velocity of the star (similar to a $\sin x$ function). Finally, a fifth category is assign to those objects that show (visually) noticeable radial velocity shifts in their spectra, likely due to a massive companion. These objects likely show something similar to a symmetrical wavy pattern in their residual profile but with a much higher amplitude and accompanied by evident shifts observed in the normalized spectral lines. These categories can be observed simultaneously in many cases, for instance, one object can exhibit wavy-like variations in addition to narrow absorption features, thus more than one variability classification can be assigned to any object. Examples of the types of variability observed in the sample are shown in Figures 5.1 to 5.5.

Table 5.2: Number of spectra for each star per date, minimum and maximum separation between observations. Spectra from UVES and MIKE include both blue and red arm and, in general, half of them correspond to the blue arm and half to the red arm.

Object	N° of Spectra	Min. Separ. [days]	Max. Separ. [days]	Object	N° of Spectra	Min. Separ. [days]	Max. Separ. [days]
HD 1466	55	4.25×10^{-3}	5.03×10^{3}	HD 106906	94	1.97×10^{-3}	2.93×10^{3}
HD 1461	462	1.04×10^{-3}	3.69×10^{3}	HD 107146	19	4.06×10^{-3}	3.61×10^{3}
kap Phe	73	1.11×10^{-3}	2.25×10^{3}	HD 108857	8	4.03×10^{-3}	4.40×10^{3}
lam01 Phe	10	1.46×10^{-3}	2.79×10^{2}	eta Crv	52	1.11×10^{-3}	4.40×10^{3}
HD 3670	23	2.25×10^{-3}	1.13×10^{3}	HR 4796	245	1.24×10^{-3}	5.56×10^{3}
nu. Phe	93	6.95×10^{-4}	6.11×10^{3}	HD 110058	23	7.31×10^{-3}	2.62×10^{3}
49 Cet	97	1.44×10^{-3}	3.85×10^{3}	rho Vir	61	1.62×10^{-3}	4.08×10^{3}
q01 Eri	151	8.38×10^{-4}	3.70×10^{3}	V MO Hya	15	9.91×10^{-4}	3.48×10^{3}
q02 Eri	13	4.18×10^{-3}	1.07×10^{3}	HD 113556	4	2.66×10^{-3}	2.85×10^{3}
V DK Cet	96	1.18×10^{-3}	5.07×10^{3}	HD 114082	21	2.25×10^{-3}	3.26×10^{3}
HD 13246	15	6.42×10^{-2}	4.72×10^{3}	iot Cen	62	6.05×10^{-4}	2.21×10^{3}
bet Tri	3	9.87×10^{-1}	1.99	lam Boo	4	1.18×10^{-1}	3.51×10^{1}
gam Tri	14	2.23×10^{-3}	9.97×10^{2}	HD 128311	7	2.25×10^{-3}	4.42×10^{3}
alf For	202	5.73×10^{-4}	2.01×10^{3}	HD 131835	18	5.90×10^{-2}	2.18×10^{3}
94 Cet	1709	8.41×10^{-4}	4.04×10^{3}	bet Cir	92	9.93×10^{-4}	2.58×10^{3}
HD 21997	39	1.42×10^{-2}	2.93×10^{3}	BD-07 4003	249	1.19×10^{-1}	2.91×10^{3}
V1229 Tau	13	1.76×10^{-3}	1.10×10^{1}	HD 137057	5	5.22×10^{-3}	2.67×10^{3}
28 Tau	6	6.19×10^{-2}	1.06×10^{3}	alf CrB	7	1.19×10^{-3}	5.37×10^{2}
HD 25457	130	9.40×10^{-4}	4.09×10^{3}	HD 138813	28	1.07×10^{-3}	4.11×10^{2}
gam Dor	18	6.18×10^{-4}	5.16×10^{3}	HD 140817	4	3.48×10^{-3}	2.62×10^{3}
V EX Eri	24	9.01×10^{-4}	3.58×10^{3}	HD 144587	5	6.01	3.78×10^{2}
HD 30447	25	1.47×10^{-3}	2.57×10^{3}	HR 6051	21	1.79×10^{-2}	4.01×10^{2}
pi.01 Ori	22	1.06×10^{-3}	3.31×10^{3}	HR 6037	38	1.04×10^{-3}	5.83×10^{3}
HD 35367	6	7.58×10^{-3}	2.31×10^{2}	HD 146897	10	2.14×10^{-2}	4.14×10^{2}
HD 287861	3	2.01	1.09×10^{3}	HR 6507	24	1.25×10^{-3}	1.78×10^{3}
HD 290609	3	2.04	1.09×10^{3}	HD 159082	4	9.97×10^{-1}	3.95×10^{3}
HR 1915	9	1.37×10^{-2}	3.86×10^{2}	HR 6534	10	2.80×10^{-3}	1.15×10^{2}
HD 37306	43	3.86×10^{-3}	4.25×10^{3}	mu. Ara	2985	7.67×10^{-4}	4.66×10^{3}

Continued on next page

Table 5.2 – continued from previous page

Object	N° of Spectra	Min. Separ. [days]	Max. Separ. [days]	Object	N° of Spectra	Min. Separ. [days]	Max. Separ. [days]
HR 1975	33	1.53×10^{-3}	1.50×10^{3}	HD 164249	52	8.53×10^{-4}	4.49×10^{3}
HD 38858	203	1.81×10^{-3}	3.81×10^{3}	eps Sgr	11	1.12×10^{-3}	2.56×10^{3}
HD 45184	308	1.23×10^{-3}	3.82×10^{3}	HR 6948	8	8.37×10^{-3}	2.71×10^{3}
HD 46190	13	1.39×10^{-2}	2.17×10^{3}	rho Tel	39	1.30×10^{-3}	1.81×10^{3}
HD 52265	13	3.25×10^{-3}	4.20×10^{3}	HD 181327	77	3.25×10^{-3}	4.46×10^{3}
HD 61005	78	5.57×10^{-3}	4.73×10^{3}	5 Vul	19	4.74e-03	5.81e+02
HD 69830	685	1.04×10^{-3}	3.77×10^{3}	c Aql	44	9.90×10^{-4}	3.57×10^{3}
HD 71722	17	3.47×10^{-2}	4.35×10^{2}	HD 190470	6	1.02×10^{-2}	3.79×10^{1}
HD 76151	42	8.14×10^{-4}	5.52×10^{3}	kap01 Sgr	14	3.74×10^{-2}	3.68×10^{3}
HR 3570	49	1.80×10^{-3}	2.60×10^{3}	phi01 Pav	8	1.36×10^{-2}	7.87×10^{2}
HD 82943	197	1.04×10^{-3}	3.74×10^{3}	iot Del	7	3.60×10^{-3}	3.79×10^{1}
HR 3927	4	9.62×10^{-1}	3.63×10^{3}	V AU Mic	50	2.93×10^{-3}	5.05×10^{3}
HR 4138	47	1.26×10^{-3}	4.18×10^{3}	HR 8013	73	1.62×10^{-3}	5.19×10^{3}
V CE Ant	56	1.45×10^{-2}	3.35×10^{3}	alf Oct	31	1.36×10^{-3}	4.14×10^{3}
HD 95086	141	1.97×10^{-3}	2.25×10^{3}	HD 202206	66	3.48×10^{-3}	2.95×10^{3}
bet UMa	14	1.30×10^{-3}	4.00×10^{1}	HD 207129	344	1.04×10^{-3}	1.74×10^{3}
HD 98363	9	7.51×10^{-3}	4.74×10^{3}	39 Peg	6	8.80×10^{-3}	3.67×10^{1}
HD 101088	13	1.42×10^{-2}	1.12×10^{3}	tau01 Aqr	4	9.98	2.71×10^{2}
HD 102458	47	1.08×10^{-2}	4.79×10^{3}	V342 Peg	307	1.51×10^{-3}	3.67×10^{3}
HD 104231	24	9.82×10^{-3}	5.17×10^{3}	HR 8843	38	1.64×10^{-3}	3.62×10^{3}
CD-54 4621	6	2.86×10^{-2}	4.37×10^{3}				

5.2.2 Identification of Candidates to Exocometary Activity

With the aim of identifying which objects that show signs of variability in their Ca II K spectral lines are more likely to be due to exocometary activity, in addition to analysing and classifying their type of variability we searched for the previously known properties of the systems that could be related to variations in their spectra. These properties are shown in Table 5.4 and include information on whether the star is known to be variable, what kind of variable star it is and the variability period (if known), whether the star is known to be a binary or multiple system, and any other relevant information like, for instance, if it has been reported to have substellar companions. Most of the information was retrieved from Simbad database, except when otherwise indicated in the Table. These properties will help us to assess the possible origin of the spectral variations.

In order to identify the candidates which may show signs of variable exocometary gas features, we started by selecting the spectral types that are more favourable for these detections. So far, detection of transient gas features attributed to the transit of FEBs of exocomets in UV-optical spectroscopy has been observed mostly in A-type stars, a few late B-type stars and white dwarfs, and (to the best of our knowledge) only one early F star (e.g. Montgomery and Welsh 2012, Welsh and Montgomery 2015, Welsh and Montgomery 2018, Welsh and Montgomery 2019, Melis et al. 2012, Debes et al. 2012). No detections through this method have been reported in later spectral types. It is not clear whether this bias is due to the spectral characteristics of early types making detections easier to spot, or due to the lack of exocometary activity in later types. However, it is worth noting that narrow absorption features of interstellar origin are also only reported in early, radiative stars, thus it is likely that the detection bias is due to a detection limit given that interstellar gas can be found in the line of sight of any star, independently of its spectral type.

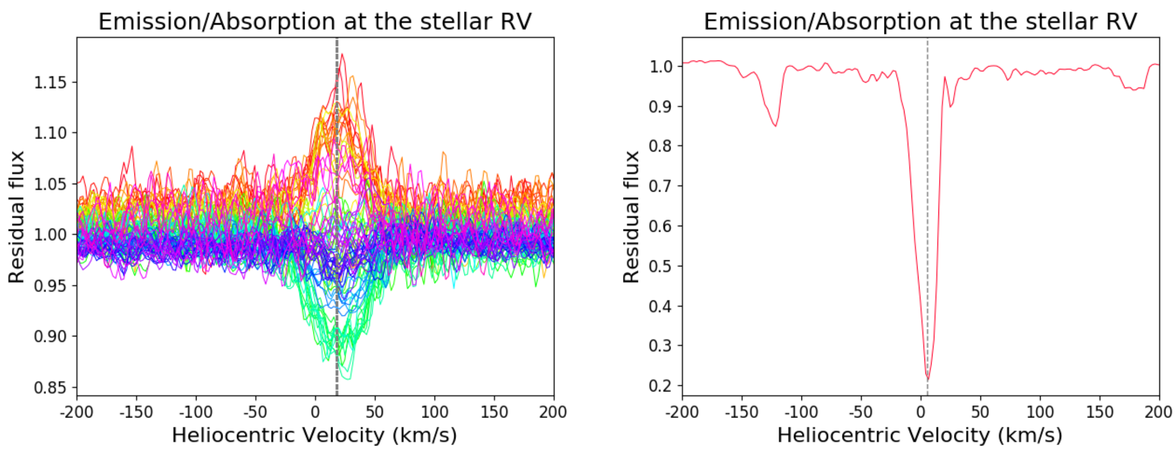

Figure 5.1: Emission and/or absorption at the radial velocity of the star. **Left:** some epochs present residual emission while others present residual absorption at the radial velocity of the star. **Right:** example of a single epoch presenting a strong absorption matching the stellar radial velocity.

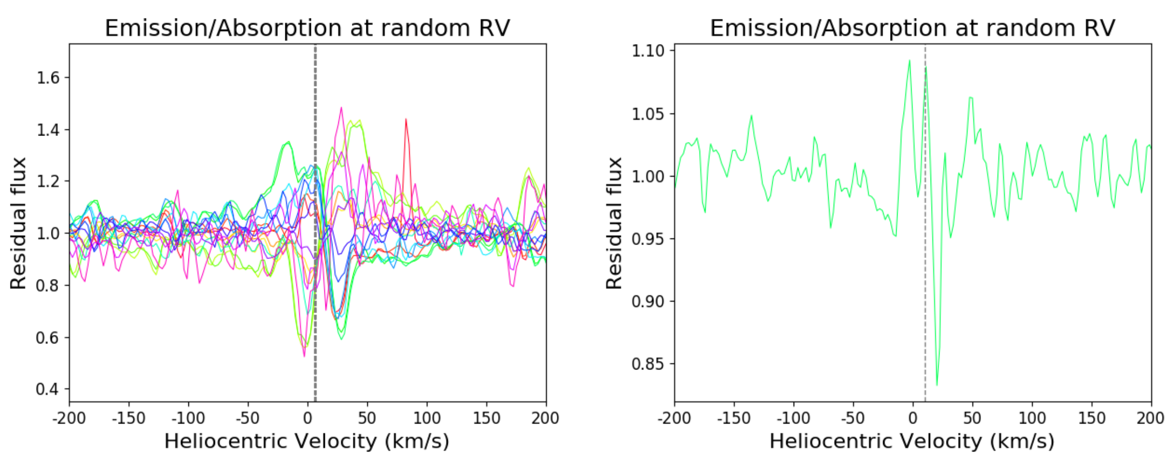

Figure 5.2: Emission and/or absorption at random radial velocities. **Left:** some epochs present residual emission while others present residual absorption at different radial velocities. **Right:** example of a single epoch presenting a narrow absorption.

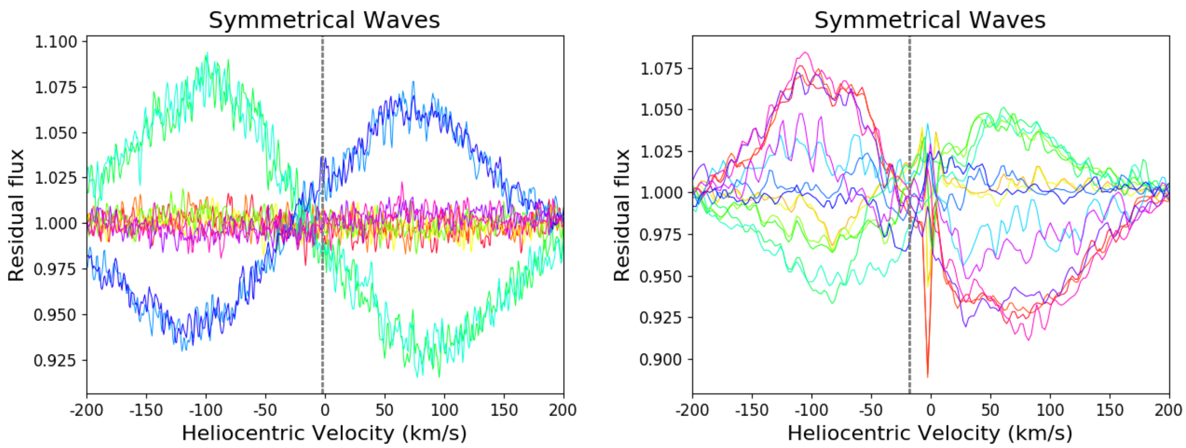

Figure 5.3: Symmetrical wavy pattern. Two examples where "symmetrical waves" are observed. They show a (relatively) symmetrical variation with respect to the radial velocity of the star. **Left:** symmetrical waves alternated with flat residuals where no variability is observed. **Right:** symmetrical waves combined with narrow emission/absorption features in some epochs.

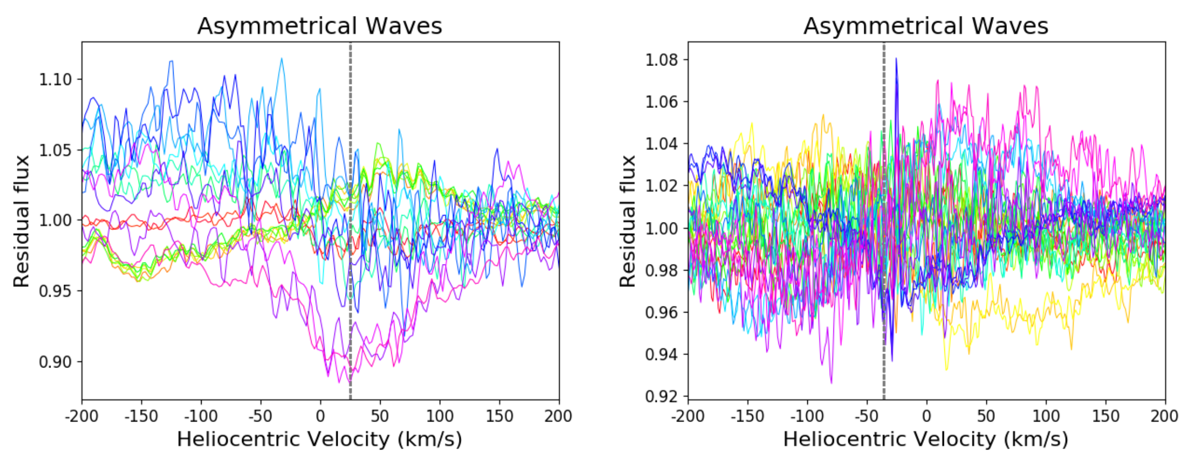

Figure 5.4: Asymmetrical wavy pattern. Two examples of "asymmetrical waves" observed in known variable stars. They show asymmetrical variations with respect to the radial velocity of the star. **Left:** asymmetrical waves observed in all the residual profiles. **Right:** asymmetrical waves combined with narrow emission/absorption features in some epochs (notice, for instance, the emission in blue).

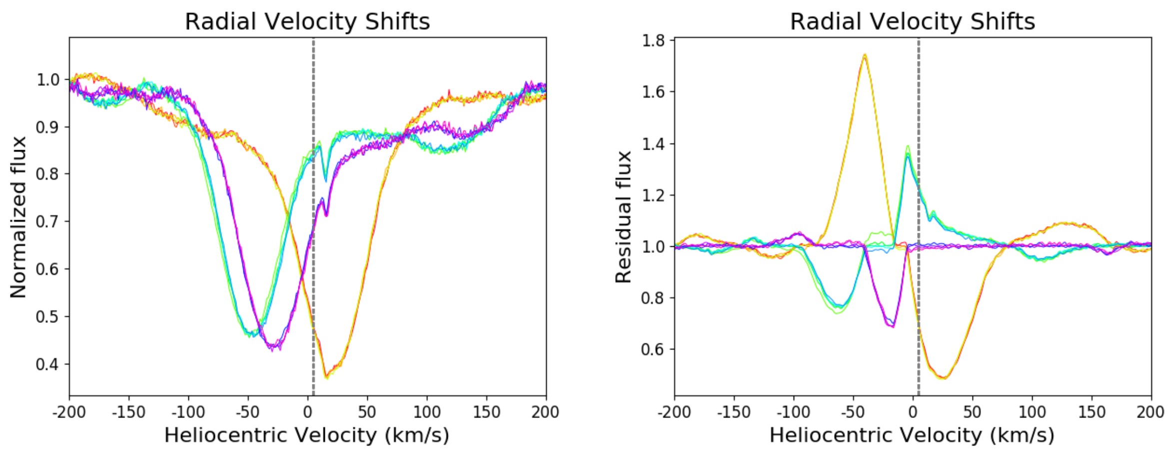

Figure 5.5: Radial velocity shifts observed in a known binary. Close spectra were taken a few minutes apart while shifted spectra were taken five days apart. Notice the insterstellar absorption at $\sim$16 km.s^{-1}. **Left:** normalized flux of the photospheric line. Clear shifts in the radial velocity of the line are shown. **Right:** residual spectrum of the same object, epochs shown in the same color of left figure. Strong P cygni-like profiles are observed.

Table 5.3: Type of variability observed in the residual spectra.

Object	Emission/Absorption at the stellar RV	Emission/Absorption at random RV	Symmetrical Waves	Asymmetrical Waves	RV shifts
HD 1466	✓	✓			
HD 1461	✓	✓			
kap Phe		✓		✓	
lam01 Phe			✓		✓
HD 3670	✓	✓			
nu. Phe	✓	✓			
49 Cet	✓	✓			
q01 Eri	✓	✓			
q02 Eri			✓		
V DK Cet	✓				
HD 13246	✓				
bet Tri	✓				
gam Tri		✓		✓	
alf For	✓	✓			
94 Cet	✓	✓			

Continued on next page

Table 5.3 – continued from previous page

Object	Emission/Absorption at the stellar RV	Emission/Absorption at random RV	Symmetrical Waves	Asymmetrical Waves	RV shifts
HD 21997		✓		✓	
V1229 Tau				✓	✓
28 Tau	✓				
HD 25457	✓	✓			
gam Dor				✓	
V EX Eri		✓		✓	
HD 30447		✓			
pi.01 Ori		✓		✓	
HD 35367		✓			
HD 287861				✓	
HD 290609		✓		✓	
HR 1915	✓	✓			
HD 37306	✓	✓			
HR 1975		✓	✓		
HD 38858	✓	✓			
HD 45184	✓	✓			
HD 46190	✓	✓		✓	
HD 52265	✓	✓			
HD 61005	✓	✓			
HD 69830	✓				
HD 71722		✓		✓	
HD 76151	✓				
HR 3570	✓	✓			
HD 82943	✓	✓			
HR 3927				✓	
HR 4138	✓	✓			
V CE Ant	✓	✓		✓	
HD 95086	✓	✓			
bet UMa	✓	✓		✓	
HD 98363		✓		✓	

Continued on next page

Table 5.3 – continued from previous page

Object	Emission/Absorption at the stellar RV	Emission/Absorption at random RV	Symmetrical Waves	Asymmetrical Waves	RV shifts
HD 101088		✓		✓	
HD 102458		✓			
HD 104231	✓	✓			
CD-54 4621		✓		✓	
HD 106906		✓		✓	
HD 107146	✓	✓			
HD 108857		✓	✓		✓
eta Crv	✓	✓		✓	
HR 4796	✓	✓		✓	
HD 110058		✓			
rho Vir		✓		✓	
V MO Hya		✓	✓		✓
HD 113556	✓	✓			
HD 114082		✓			
iot Cen	✓	✓			
lam Boo		✓		✓	
HD 128311	✓	✓			
HD 131835		✓	✓		
bet Cir	✓	✓			
BD-07 4003		✓			
HD 137057	✓	✓		✓	✓
alf CrB		✓	✓	✓	✓
HD 138813		✓		✓	
HD 140817				✓	
HD 144587		✓		✓	
HR 6051		✓		✓	
HR 6037	✓	✓		✓	
HD 146897	✓	✓			
HR 6507	✓	✓		✓	
HD 159082					✓

Continued on next page

Table 5.3 – continued from previous page

Object	Emission/Absorption at the stellar RV	Emission/Absorption at random RV	Symmetrical Waves	Asymmetrical Waves	RV shifts
HR 6534				✓	
mu. Ara	✓	✓			✓
HD 164249	✓	✓		✓	
eps Sgr	✓	✓		✓	
HR 6948		✓		✓	
rho Tel			✓	✓	
HD 181327	✓	✓			
5 Vul		✓			
c Aql	✓	✓		✓	
HD 190470	✓	✓			
kap01 Sgr		✓	✓		
phi01 Pav				✓	
iot Del					✓
V AU Mic	✓	✓		✓	✓
HR 8013	✓	✓			
alf Oct				✓	✓
HD 202206	✓	✓			
HD 207129	✓				
39 Peg		✓		✓	
tau01 Aqr		✓		✓	
V342 Peg	✓	✓	✓	✓	
HR 8843	✓	✓			

Consequently, given this trend, although at risk to perpetuate a bias, we selected the systems around stars within the range B1-F5 (61 systems) as preliminary candidates to identify possible signs of FEBs. Later spectral types are discarded as variability is more likely to be due to chromospheric or other kind of stellar activity. Main sequence stars start to show evidence of chromospheric lines around middle F-type stars. However, signs of chromospheric emission features have been found also in early F stars (Linsky, 2017). Therefore, from our selection of early-type stars, we visually inspected each F-type stars (16 objects) looking for signs of chromospheric emission lines in order to discard these candidates. Only one of these F-type stars (an F5V star) exhibited chromospheric lines and was thus, discarded from the preliminary group of candidates.

From the remaining preliminary selection of 60 candidates to exocometary activity based on their spectral types, we further discarded objects based on their previously known variable properties. It is important to note that the fact that a star is, for instance, a variable or a binary, does not imply that it is incompatible with exhibiting signs of exocometary activity. Indeed, β Pic is known to be a Delta Scuti variable star and has shown clear evidence of exocometary transits (Zieba et al., 2019). However, we discarded those objects with reported variable-related characteristics that exhibited variability in agreement with their properties. For instances, known multiple stars displaying variability due to evident velocity shifts or variable stars showing wave-like features typical from stellar pulsations. This way, we discarded 14 targets (including e.g. spectroscopic/eclipsing binaries, Delta Scuti and Gamma Doradus variable stars) showing variations in agreement with their respective reported variable properties.

The next step in the selection process is discarding from the remaining 46 objects those showing signs more according to stellar pulsations (symmetric or asymmetric waves) or radial velocity shifts, rather than narrow features. We also discard those objects exhibiting narrow features in emission but not in absorption (as only absorptions should be expected as evidence of FEB-like phenomena). This leave us with a selection of 30 candidates exhibiting narrow absorption features in their residual spectra and that might be originated from exocometary activity. This final selection of candidates is shown in Table 5.5.

Table 5.4: Stellar parameters related to variability.

Name	Variable Type	Period [d]	Multiplicity	Other
HD 1466	–	–	–	High PM
HD 1461	–	–	–	High PM, Substellar companion
kap Phe	–	–	–	High PM
lam01 Phe	–	–	–	High PM
HD 3670	–	–	–	High PM
nu. Phe	–	–	–	High PM
49 Cet	–	–	–	High PM
q01 Eri	–	–	–	High PM, Substellar companion
q02 Eri	–	–	–	High PM
V DK Cet	BY Draconis	3.02	–	Star in Association
HD 13246	–	–	–	High PM
bet Tri	Spectroscopic binary	?	✓	–
gam Tri	–	–	–	High PM
alf For	–	–	✓	–
94 Cet	–	–	–	High PM, Substellar companion
HD 21997	–	–	–	High PM
V1229 Tau	Eclipsing binary of Algol type	?	✓	–
28 Tau	–	–	–	Be Star
HD 25457	T Tauri	?	–	Member of moving group
gam Dor	Gamma Doradus	0.7570[a]	–	–
V EX Eri	Delta Scuti	?	–	Lambda Boötis Star
HD 30447	–	–	–	–
pi.01 Ori	–	–	–	High PM, Lambda Boötis Star
HD 35367	–	–	–	–
HD 287861	–	–	–	–
HD 290609	–	–	–	–
HR 1915	–	–	–	–
HD 37306	–	–	–	–
HR 1975	–	–	–	–
HD 38858	–	–	–	High PM, Substellar companion
HD 45184	–	–	–	High PM, Substellar companion
HD 46190	–	–	–	–
HD 52265	–	–	–	High PM, Substellar companion
HD 61005	–	–	–	High PM
HD 69830	–	–	–	High PM, 3 Substellar companions
HD 71722	–	–	–	–
HD 76151	–	–	–	High PM
HR 3570	–	–	–	High PM

Continued on next page

Table 5.4 – continued from previous page

Name	Variable Type	Period [d]	Multiplicity	Other
HD 82943	–	–	–	High PM, 2 Substellar companions
HR 3927	–	–	–	–
HR 4138	–	–	–	–
V CE Ant	T Tauri	5.00	–	–
HD 95086	–	–	–	Substellar companion
bet UMa	–	–	–	High PM
HD 98363	–	–	–	–
HD 101088	–	–	✓	–
HD 102458	–	–	–	Young Stellar Object
HD 104231	–	–	–	Star in Association
CD-54 4621	–	–	–	Pre-main sequence Star
HD 106906	–	–	–	Star in Association
HD 107146	–	–	–	High PM
HD 108857	–	–	–	–
eta Crv	–	–	–	High PM
HR 4796	–	–	✓	–
HD 110058	–	–	–	–
rho Vir	Delta Scuti	?	–	Lambda Boötis Star
V MO Hya	Delta Scuti	?	–	Lambda Boötis Star
HD 113556	–	–	–	Star in Association
HD 114082	–	–	–	Star in Association
iot Cen	–	–	–	High PM
lam Boo	Delta Scuti	?	–	Lambda Boötis Star
HD 128311	BY Draconis	?	–	2 Substellar companions
HD 131835	–	–	–	–
bet Cir	–	–	–	High PM
BD-07 4003	BY Draconis	?	–	4 or more Substellar companions
HD 137057	–	–	–	–
alf CrB	Eclipsing binary of Algol type	17.36	✓	–
HD 138813	–	–	–	–
HD 140817	–	–	✓	–
HD 144587	–	–	–	–
HR 6051	–	–	–	–
HR 6037	–	–	–	High PM
HD 146897	–	–	–	–
HR 6507	–	–	–	High PM
HD 159082	Spectroscopic binary	?	✓	–
HR 6534	–	–	–	High PM
mu. Ara	–	–	–	High PM, 4 Substellar companions

Continued on next page

Table 5.4 – continued from previous page

Name	Variable Type	Period [d]	Multiplicity	Other
HD 164249	–	–	–	High PM
eps Sgr	–	–	✓	Lambda Boötis Star
HR 6948	–	–	–	High PM
rho Tel	–	–	–	High PM
HD 181327	–	–	–	High PM
5 Vul	–	–	–	–
cAql	Delta Scuti	?	–	Lambda Boötis Star
HD 190470	–	–	–	High PM
kap01 Sgr	–	–	–	High PM
phi01 Pav	–	–	–	High PM
iot Del	Spectroscopic binary	?	✓	–
V AU Mic	BY Draconis	4.85	–	–
HR 8013	–	–	–	High PM
alf Oct	Eclipsing binary of beta Lyr type	?	✓	–
HD 202206	–	–	–	High PM, 2 Substellar companions
HD 207129	–	–	–	High PM
39 Peg	Gamma Doradus	0.75574[a]	–	–
tau01 Aqr	–	–	–	–
V342 Peg	Ellipsoidal, Gamma Doradus	0.5053[a]	–	4 Substellar companions, Lambda Boötis Star
HR 8843	–	–	–	High PM

[a]Henry et al. (2011).

We carefully further inspected each one of these candidates in order to try to assess whether the variable absorption features observed in these candidates are likely attributable to FEBs or not. We evaluated whether the features were observed in consecutive epochs (either during the same night or in consecutive nights, depending on the data available) in matching positions (i.e. found at the same radial velocity within the errors). We also took into account previous reports of FEBs or presence of gas in the literature and examined if the residual feature matched with the location of a stable feature present in the reference spectrum. The presence of "wavy" patterns or p-cygi profiles in addition to the narrow features were also considered.

Taking into consideration the characteristics described above, we classified the origin of the absorption features observed in each object as "likely" if they seem consistent with exocometary activity (i.e. we found consistent absorptions in consecutive epochs and/or there are previous reports of gas of FEBs) or "unclear" if they do not show clear evidence of exocometary activity but cannot be completely ruled out. For instance, in the case of HD 110058, the variable features matched with the position of a stable feature with confirmed circumstellar gas origin (Hales et al. 2017, Iglesias et al. 2018, Rebollido et al. 2018). However, these variations could likely be due to the difference in resolution between FEROS and HARPS observations (e.g. see Fig. 2.2 in Chapter 2), but given the confirmed presence of gas, FEBs cannot be completely ruled out and we will do further quantitative analysis of the variability of this object in the future. These results are summarized in Table 5.5 with notes explaining the observed characteristics that led to the classification. As a final result, we found seven candidates with variability likely attributable to exocometary activity and 23 objects exhibiting signatures of unclear origin that cannot be immediately ruled out from the FEB scenario.

Table 5.5: Selection of candidates of exocometary activity.

ID	Unclear	Likely	Notes
kap Phe	✓		not consistent in consecutive epochs
49 Cet		✓	weak but consistent in consecutive epochs, reported gas
gam Tri		✓	consistent in consecutive epochs
HD 21997		✓	consistent and not in consec. epochs, mixed w. "waves", reported gas
HD 30447	✓		weakly consistent or not consistent in consecutive epochs
pi.01 Ori	✓		not consistent in consecutive epochs, mixed with "waves"
HD 35367	✓		matches with the position of an ISM feature but cannot be discarded
HR 1915	✓		not consistent in consecutive epochs, mixed with "waves"
HD 37306		✓	very strong and consistent in consecutive epochs, reported FEBs
HR 1975	✓		consistent in consecutive epochs but mixed with p-cygni profiles
HD 46190	✓		not consistent in consecutive epochs, mixed with "waves"
HD 71722	✓		not consistent in consecutive epochs
HD 95086		✓	consistent and not in consecutive epochs, reported gas
HD 98363	✓		not consistent in consecutive epochs, mixed with "waves"
HD 106906	✓		not consistent in consecutive epochs, mixed with "waves"
eta Crv	✓		not consistent in consecutive epochs, reported gas
HR 4796		✓	consistent and not in consecutive epochs, reported gas
HD 110058	✓		likely instrumental but reported stable gas, FEBs cannot be discarded
rho Vir	✓		not consistent in consecutive epochs, mixed with "waves"
HD 113556	✓		not consistent in consecutive epochs, a bit noisy
HD 114082	✓		not consistent in consecutive epochs
iot Cen	✓		not consistent in consecutive epochs
HD 131835	✓		not consistent in consecutive epochs, mixed with "waves"
bet Cir	✓		not consistent in consecutive epochs
HD 138813	✓		not consistent in consecutive epochs, mixed with "waves"
HR 6037	✓		not consistent in consecutive epochs, mixed with "waves"
HR 6948	✓		not consistent in consecutive epochs, mixed with "waves"
5 Vul	✓		not consistent in consecutive epochs
c Aql		✓	consistent in consecutive epochs, mixed with "waves", reported FEBs
kap01 Sgr	✓		not consistent in consecutive epochs, mixed with "waves"

5.2.3 Multiple line comparison for the candidates

We performed further analysis of the seven candidates presenting variability likely due to exocometary activity. We did a simultaneous comparison of the observed variability found in the Ca II K line with respect to the Ca II H and Hδ lines aiming to confirm or discard that the variability is attributable to exocomets. Absorption due to gas produced in the Ca II K line should be simultaneously detected also in the Ca II H line. Therefore, we compare simultaneous observations with the Ca II H line in order to confirm a gas detection. However, it is important to notice that for optically thin gas the intensity of the Ca II H absorption should be half as intense as the absorption detected in the Ca II K line (Kiefer et al., 2014c) and thus, for weak detections in Ca II K, simultaneous absorptions in the Ca II H line will be hard to detect.

On the other hand, the Balmer lines are very much used to study stellar activity since they are very sensitive to changes in stellar temperature and pressure (Houdebine et al., 1995). Therefore, we compare the variability with one of these Hydrogen lines in order to observe any possible correlation with stellar activity, which might help to discard the variability in the Ca II K line being of exocometary origin. Besides, no evidence has been found of absorptions attributable to exocometary gas in these lines. Although, it is worth mentioning that they are good tracers for gas accretion or radiative processes in the disk of Herbig Ae/Be stars presented as emission lines at the core of the Balmer series (Silaj et al. 2014, Moura et al. 2020), but this is not the case of our objects of analysis. We chose to perform a simultaneous comparison with the Hδ line given that is close in wavelength to the Ca II doublet and, therefore, simultaneous observations are available for any instrument used in this study (unlike, for instance, the Hα line which is outside of the coverage of the blue arm for UVES and MIKE spectrographs).

Below, we analyse and discuss the simultaneous observations of these lines individually for each candidate.

49 Cet

We detect a weak narrow residual absorption in the Ca II K line of 49 Cet at a consistent radial velocity in three consecutive epochs, as shown in Fig. 5.6. The first two observations were taken during the same night only a few minutes apart and the third one was taken the following night. No simultaneous absorption was observed in the in the Ca II H line, although, given the weak intensity of the detection in K, the according intensity expected for the H line might not reach a level beyond 2σ over the noise. No significant variability was observed in the Hδ line either, likely discarding stellar activity. Both molecular and atomic gas have been detected in 49 Cet. The first report of molecular gas being present in 49 Cet was made by Zuckerman et al. (1995) who revealed the presence of CO in this debris disk. Later, further detections of CO were published (e.g. Hughes et al. 2008, Moór et al. 2019), as well as the detection of molecular Hydrogen (H_2) (Thi et al., 2001a). There are also several detections of atomic gas either in emission (e.g. C II: Roberge et al. 2013, C I: Higuchi et al. 2017) or absorption (e.g. C I, O I, Fe I: Roberge et al. 2014, C IV: Miles et al. 2016) and, in particular, variable absorption features in the Ca II K line of 49 Cet have been reported by Montgomery and Welsh (2012), whereas Rebollido et al. (2018) suggests that the absorption feature observed in Ca II K line of 49 Cet is most likely a blend of interstellar and circumstellar gas. Our detections in the Ca II K line of 49 Cet are consistent with the neard edge-on inclination of the disk estimated to be of 80.6$\pm$0.4 degrees by Hughes et al. (2017), which favours the detection of circumstellar material transiting in front of the star (although this constrain can be less strict for the case of exocomets). Our detections, although weak and thus not detected in the H counterpart of the K line, might be likely consistent with exocometary activity given the confirmed presence of gas in the system, the favourable inclination of the disk, and previous reports of variability attributed to FEBs in the Ca II K line. We cautiously assign a circumstellar gas origin for the variability observed in 49 Cet, however, we will perform further analysis of this particular case to better assess the variability and confirm it is not due to possible artificially induced variations.

gam Tri

gam Tri presents a weak absorption feature in the Ca II K line at consistent radial velocity in consecutive observations. The peak of the absorption seen at $\sim$45 km.s^{-1} reaches 3σ in the two observations taken on the night of 2018-10-20. One observation was taken on the previous night and apparently there is also an absorption at the same velocity, however its peak only reaches 2.9σ, just slightly under our detection constrain. That feature is still marked with a Gaussian fit in Fig. 5.7 in order to show that its velocity is consistent with those of the following night. We

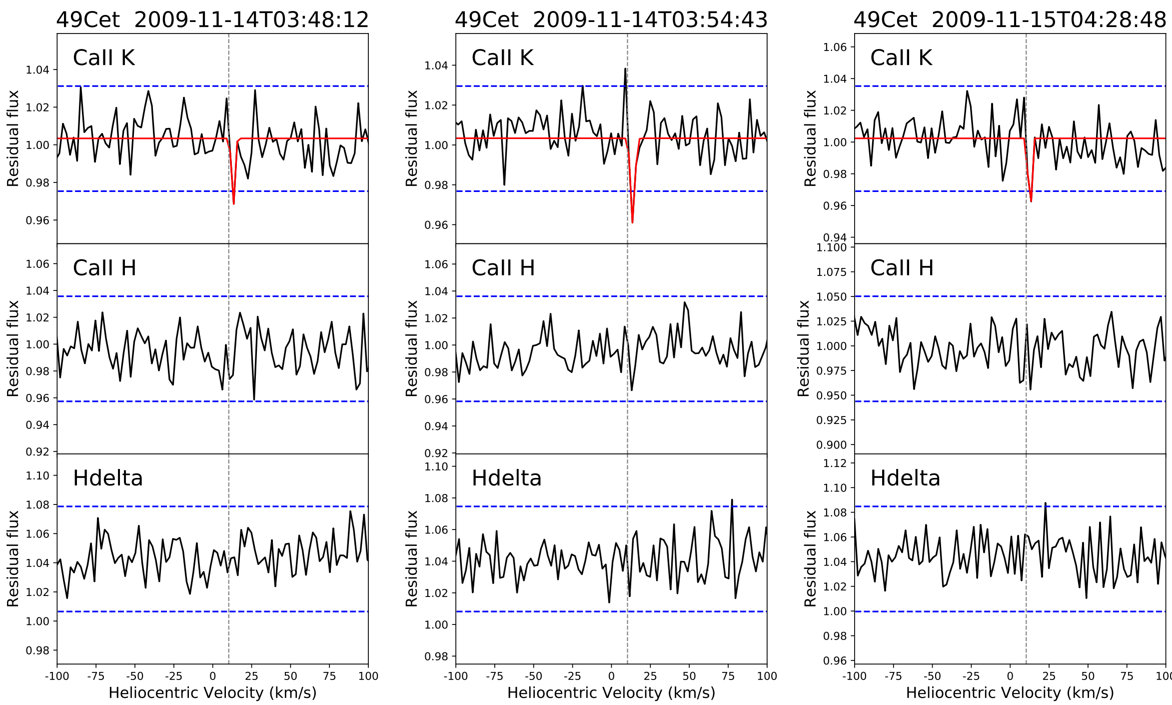

Figure 5.6: Three consecutive observations of 49 Cet presenting a narrow absorption feature in the Ca II K line at $\sim$12 km.s^{-1}. In this and the six following figures the radial velocity of the star is marked with a vertical gray dashed line and the upper and lower 3σ limit are shown in horizontal dashed blue lines.

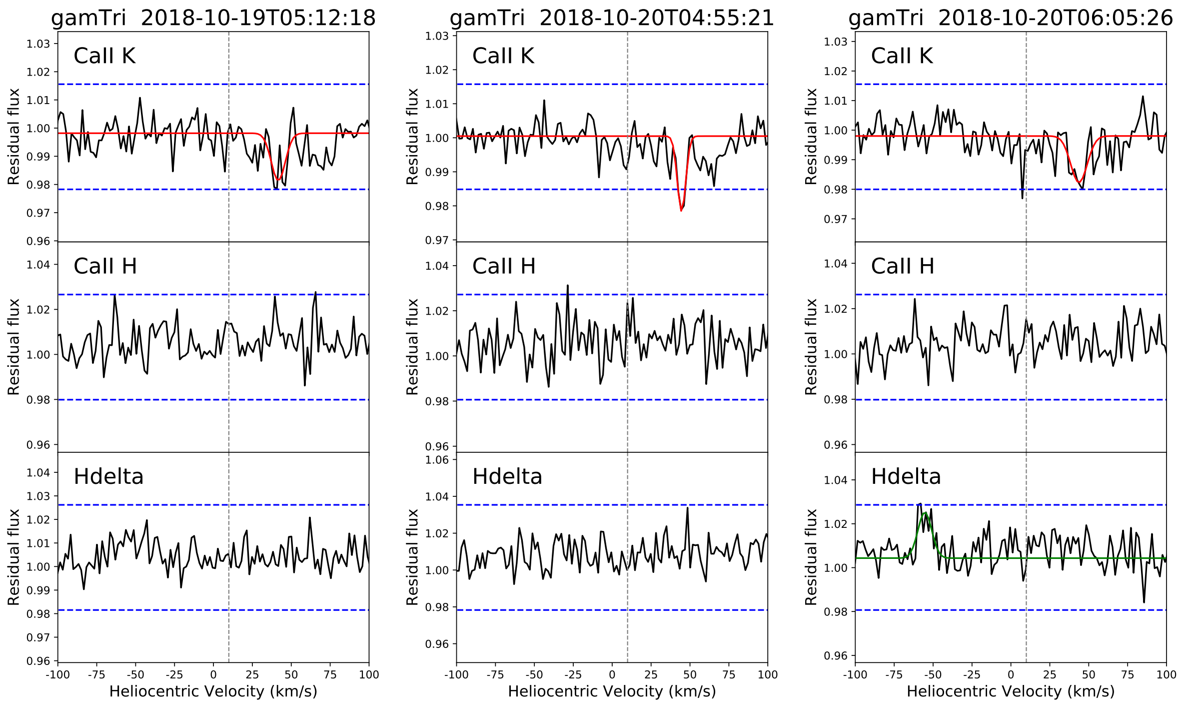

Figure 5.7: Three consecutive observations of gam Tri presenting a weak absorption feature in the Ca II K line at $\sim$45 km.s^{-1}.

do not detect any correlated absorption either in the Ca II H or the Hδ line. This is in agreement with the Ca II H line being likely too weak to be detected and the detection in Ca II K not being correlated with stellar activity. In the case of gam Tri, there are no previous detections of gas or variability attributed to exocomets in the system. The disk has been resolved with Herschel observation and the inclination of the disk was estimated to be $\sim$89°, almost exactly edge-on (Booth et al., 2013). Therefore, considering that the inclination of the disk strongly favours the transit of its material across the line of sight of the star, although the intensity of our detection is weak, is consistent in three epochs and with the detection of the disk, therefore we consider that the absorption features observed in gam Tri are likely due to exocometary activity.

HD 21997

HD 21997 presents absorption features in the Ca II K line in many of its observations. In Fig. 5.8 we show four consecutive observations where absorption features in the Ca II K line are detected over 3σ. However, in most cases these absorptions are not seen at the same radial velocity

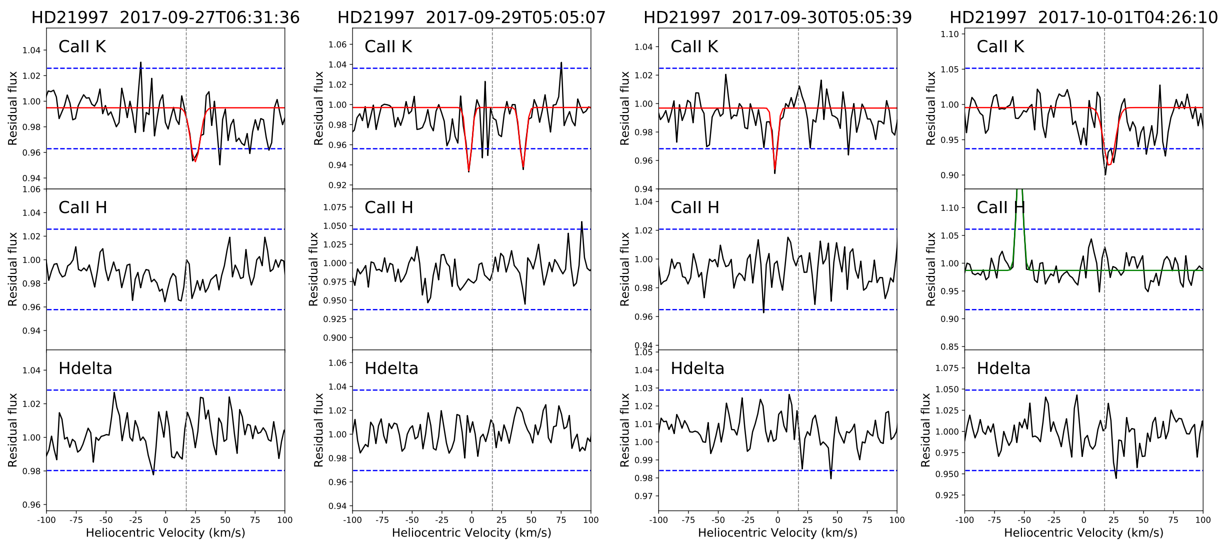

Figure 5.8: Four consecutive observations of HD 21997 presenting narrow absorption features in the Ca II K line at different radial velocities.

in consecutive observations. Only one feature detected at ∼-2km.s^{-1} seems to be consistent in the two consecutive night of 2017-09-29 and 2017-09-30. We do not find correlated absorption features in the Ca II H or the Hδ lines (there is only an emission in the Ca II H line in one of the observations likely due to a poorly removed cosmic ray contamination). This neither confirms exocometary origin or a correlation with stellar activity. Molecular gas has been previosly detected in this system. CO emissions were reported by Moór et al. (2011) and Kóspál et al. (2013), although, given the large amount of gas estimated to be in the system ($6.0\times10^{-2}M_{\oplus}$), it has been attributed to be of primordial origin (Kóspál et al. 2013, Kral et al. 2017b). No signs of exocometary activity has been reported for this object. In Rebollido et al. (2018), the authors searched for non-photospheric absorption features in the Ca II and Na I doublets of HD 21997 and no absorptions were found. The disk around HD 21997 was spatially resolved with an estimated inclination for the disk of 32.9°±2.6° (Moór et al., 2015), thus far from edge-on and not favourable for the transit of exocomets unless their orbits were highly inclined with respect to the disk, which is less likely. Therefore, we will leave HD 21997 only as a possible candidate for exocometary activity that would require further study.

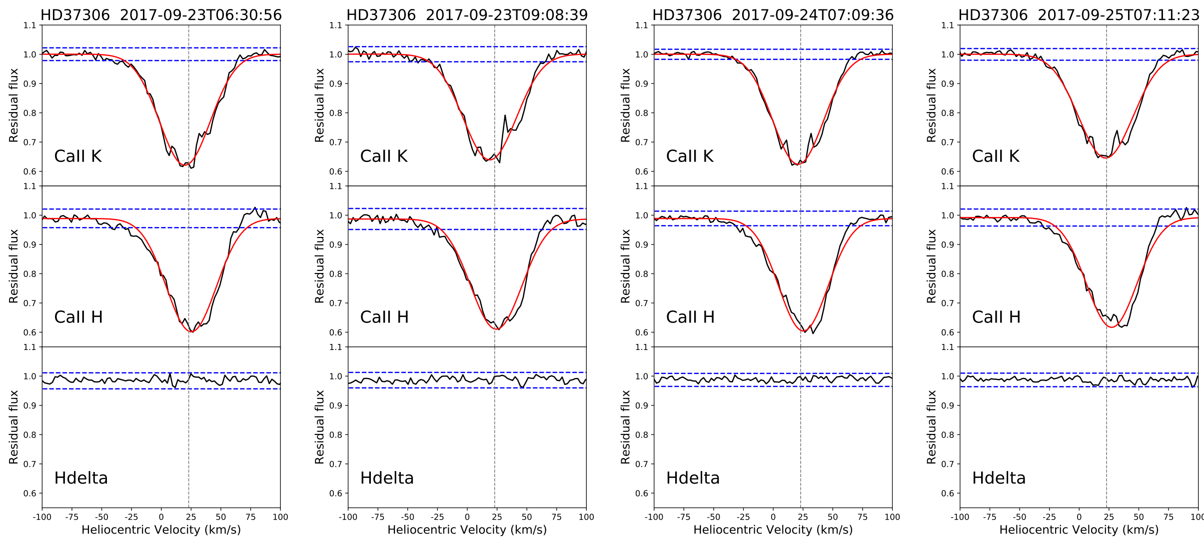

Figure 5.9: Four consecutive observations of HD 37306 presenting deep absorption features in the Ca II H and K lines centered at the radial velocity of the star. We used the same scale for the three lines for better comparison of the intensity of the absorptions.

HD 37306

HD 37306 presents a very significant (>30σ) absorption in the Ca II K line in eight consecutive observations that span a time range of eight nights. In Fig. 5.9 we show four of these consecutive observations. We can clearly see that in all these observations there is also an absorption in the Ca II H line with an intensity, width and radial velocity similar to the Ca II K line, which is (roughly) centered at the radial velocity of the star. The Ca II H and K lines presenting the same intensity are consistent with the presence of optically thick gas in the line of sight of the star. There is no similar absorption in the Hδ line which is in agreement with a lack of stellar activity. This particular object was analyzed in detail in Chapter 4 and the results of this analysis were published in Iglesias et al. (2019). It not only shows consistent atomic gas absorptions in the Ca II doublet, but also in the Ca II triplet and several Fe II and Ti II lines. In Iglesias et al. (2019) we concluded that the variability observed in this object was likely due to an exocometary break-up sublimating very close to the star (at a few stellar radii) and producing a ring-shaped stream of gas. This variability was interpreted as a shell star by Rebollido et al. (2020), but our analysis, as mentioned, was more consistent with the massive disruption of an exocomet.

HD 95086

HD 95086 presents absorption features at random velocities in the Ca II K line in many of its observations. In Fig. 5.10 we show some of the absorption features detected during the night of 2014-01-18. The Ca II K line presents narrow absorptions in consecutive observations but they are not observed at the same radial velocities. The Ca II H line presents absorption features in a few epochs, however these are not consistent with the radial velocity of the feature observed in the simultaneous observation of the K line (e.g. see the second observation in Fig. 5.10). The Hδ line does not show significant features thus the detections in the Ca II doublet are not likely attributable to stellar activity. The presence of CO has been reported by Booth et al. (2019). The authors conclude that the levels of gas detected in the system are consistent with second generation gas. The debris disk around HD 95086 was resolved with ALMA by Su et al. (2017). They estimated an inclination for the disk of 30°±3°, which is far from being edge-on and thus, not favourable for the transit of circumstellar material in front of the star. No traces of gas absorptions in the optical have been reported. A 5±2 M_{Jup} planet (HD 95086b) in the system has been detected by direct imaging at ∼56 AU from the star (Rameau et al. 2013, Galicher et al. 2014. Considering all we know about this system and the characteristics of its observed variability, the inconsistency of the detections in terms of radial velocity and the unfavourable disk inclination, we conclude that the detected variations might be more likely attributable to a relatively low (<100) SNR at the core of the Ca II K line in most observations, producing noisy features. However, given that there is a planet likely stirring the disk and that the CO detections point towards ongoing collisions in the system, we cannot completely rule out exocometary activity in this system. We will keep HD 95086 as an interesting candidate to search for exocomets.

HR 4796

We detected narrow absorption features in the Ca II K line of HR 4796 consistently present during the night of 2007-05-07 at ∼-9km.s^{-1}. We show four consecutive observations during this night presenting these absorptions in Fig. 5.11 (top row). In Iglesias et al. (2018), we reported the detection of two stable absorption features of interstellar origin in the Ca II K line of HR 4796

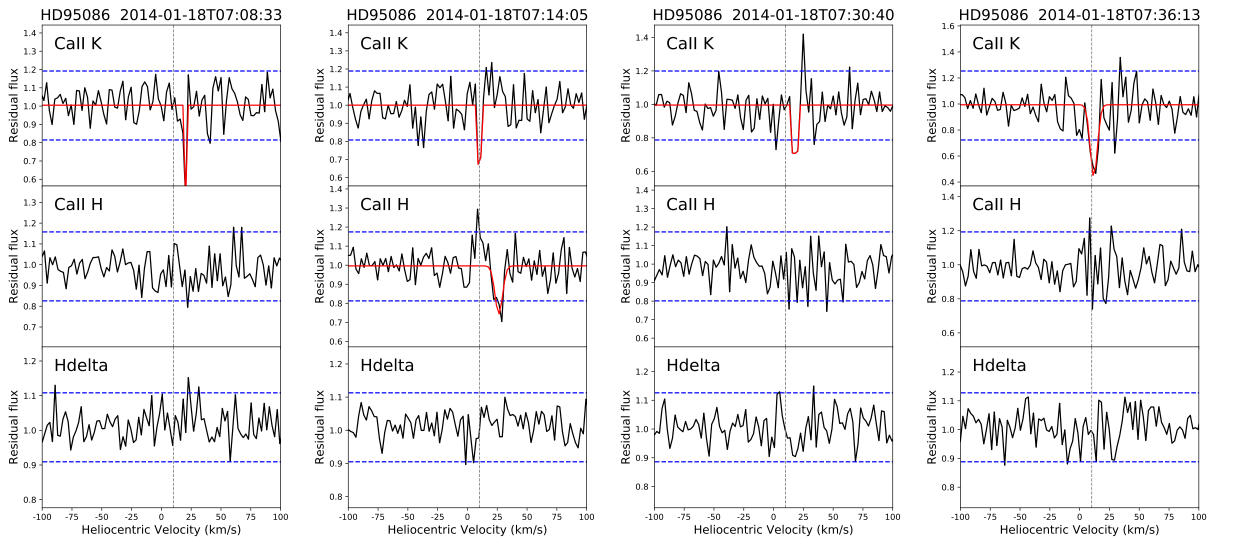

Figure 5.10: Four consecutive observations of HD 95086 presenting narrow absorption features in the Ca II K line at different radial velocities.

having estimated radial velocities of ∼-14km.s^{-1} and ∼-5km.s^{-1}. Thus, the variable absorption feature observed at ∼-9km.s^{-1} does not match with the velocity of any of the interstellar features. Interestingly, we also detected a narrow emission feature consistently present in the Ca II K line of HR 4796 during the night of 2007-05-15 at ∼4.3km.s^{-1}. This matches with our estimated radial velocity of the star of 5.35±2.94km.s^{-1}. No simultaneous absorption or emission features were detected neither in the Ca II H or Hδ line that might confirm the presence of circumstellar gas or stellar activity. No emission of molecular gas has been detected in this system (Kennedy et al., 2018). However, signs of absorption features in the Ca II K line attributable to circumstellar gas have been reported by Iglesias et al. (2018) (as discussed in Chapter 3) and Welsh and Montgomery (2015). Iglesias et al. (2018) also reports a weak stable circumstellar feature in the Ca II K line matching the radial velocity of the star and likely of circumstellar nature. The inclination of the system of 76.5° is fairly close to edge on (Milli et al. 2017; Kennedy et al. 2018), and thus, favourable for the detection of transits of circumstellar gas. Therefore, we estimate that the absorption features in the Ca II K line are likely consistent with exocometary activity or collisions of icy bodies. Regarding the detection of emission features in the center of this line, we discard stellar activity given the lack of emission in the simultaneous observations of other lines. We speculate it might be due to infalling exocometary material getting burned in the hot

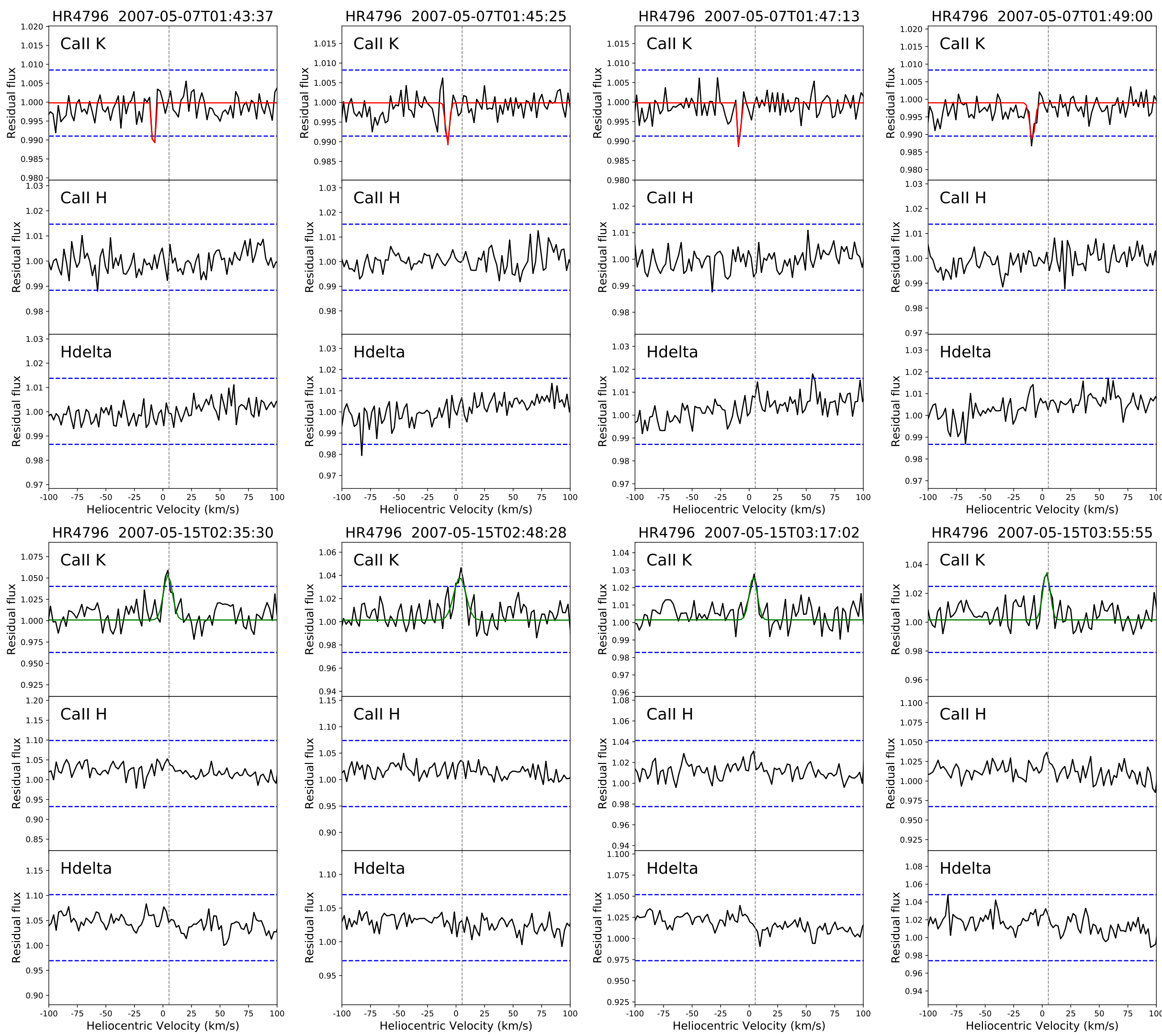

Figure 5.11: Top: Four consecutive observations of HR 4796 during the night of 2007-05-07 presenting narrow absorption features in the Ca II K line at ∼-9km.s^{-1}. **Bottom:** Four consecutive observations of HR 4796 during the night of 2007-05-15 presenting an emission feature in the Ca II K line matching the radial velocity of the star.

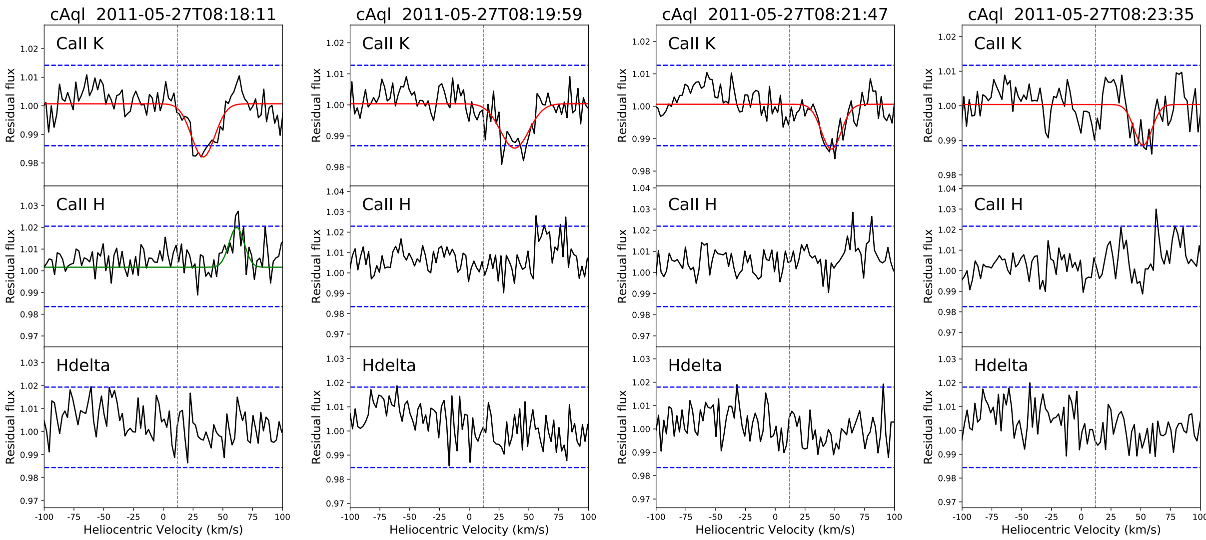

Figure 5.12: Four consecutive observations of c Aql presenting absorption features in the Ca II K line at increasing radial velocities. From left to right, the absorption features are observed at ∼34km.s^{-1}, ∼39km.s^{-1}, ∼48km.s^{-1} and ∼52km.s^{-1}, respectively. Observations are ∼2 minutes apart.

stellar surface, but we will keep investigating other possibilities.

c Aql

c Aql presents variable absorption features in its Ca II K line that are relatively wider than those observed in other objects (FWHM∼0.1–0.2Å), except for the case of HD 37306. Absorption features of similar characteristics are present in consecutive observations, as shown in Fig. 5.12. However, the absorption features are found at increasing radial velocities at a cadence of ∼2 minutes between the observations. The absorptions (shown in Fig. 5.12 from left to right) are found at ∼34km.s^{-1}, ∼39km.s^{-1}, ∼48km.s^{-1} and ∼52km.s^{-1}, respectively. No matching absorption features are found either in the Ca II H or Hδ lines. FEB-like events observed in the Ca II K line of c Aql were previously reported by Montgomery and Welsh (2017) and Iglesias et al. (2018) (as in Chapter 3). No hints of circumstellar gas have been found in other atomic or molecular lines. Although we do not detect simultaneous absorption features in other lines that may point towards a stellar activity origin, given that c Aql is a known δ Scuti variable star (Kuschnig et al., 1994), and that we detect a few emission features in some epochs (e.g. the emission shown in the Ca II H line, the first observation in Fig.5.12), we decided to further analyse a possible correlation with the stellar pulsations.

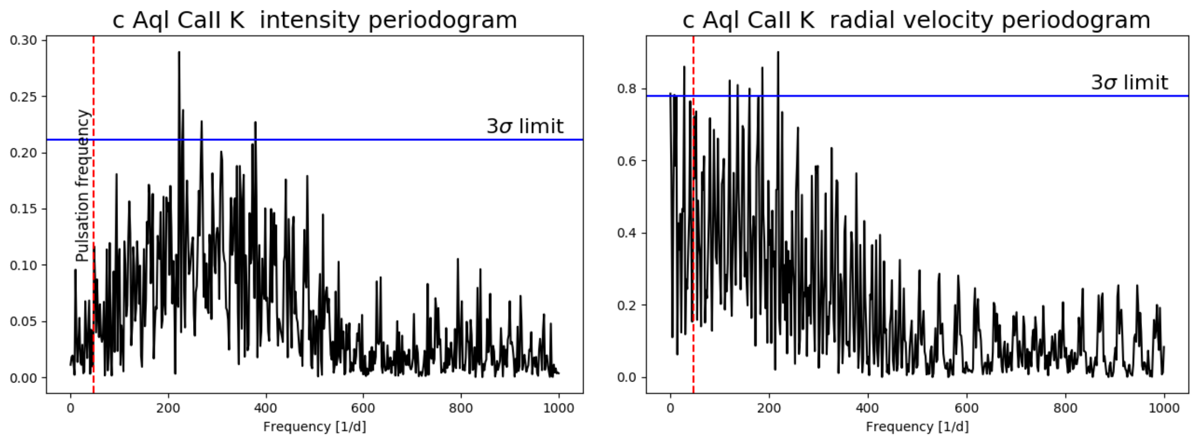

Figure 5.13: Left: Periodogram for the intensity of the absorption feature detected in the Ca II K line of c Aql. **Right:** Periodogram for the radial velocity of the same absorption feature. Vertical red dashed line in both periodograms marks the pulsation frequency of the star.

We computed periodograms for the absorption features observed in the Ca II K line to test whether the intensity and/or radial velocity of these features presented any sign of periodicity that could match with stellar pulsations. c Aql has a pulsation period of 30.39 minutes, which corresponds to a frequency of 47.48 days^{-1} (Kuschnig et al., 1994). We computed two periodograms for the Ca II K absorption feature along all epochs where it is detected; one considering the variation of its intensity and one considering the variation of its radial velocity. These periodograms are shown in Fig. 5.13. We used a frequency range from 1 to 500 days^{-1} with a sampling of 0.5 days^{-1}. We searched for frequency peaks by selecting those having $>3\sigma$ significance. In both periodograms, several peaks reached 3σ and none of them showed a clear, distinctive frequency peak. The intensity periodogram showed peaks $>3\sigma$ at 223.22, 231.23, 269.27, and 379.38 days^{-1}, while the radial velocity periodogram showed peaks at 9.01, 29.03, 121.12, 137.14, 161.16, 187.19, and 219.22 days^{-1}. None of these peaks matched between the two periodograms and none matched with the stellar pulsation period either. Therefore, we concluded there was no correlation between the observed absorption feature in Ca II K and stellar pulsations. The variability detected in c Aql might be likely due to outgassing processes such as exocometary activity in the circumstellar environment. The increasing radial velocity of the absorption feature could be compatible with the detection of the accelerated motion of an infalling sublimating body.

5.3 Conclusions

We found 97 objects within a sample of 269 debris disks having at least three epochs of observations that exhibited any kind of variability in their Ca II K spectral lines. We analyzed the observed variability in order to find in which objects the variations are more likely attributable to exocometary activity. We selected a group of 30 objects with variability that could be compatible with transiting FEBs in the line of sight of the star. From this group, seven of them showed evidence that might suggest that the observed variability could be induced by the presence of exocometary activity. Therefore, we performed a multiple line analysis for these seven object in order to confirm that the variability is indeed likely due to exocometary activity. Among these seven objects, for five of them; 49 Cet, gam Tri, HD 37306, HR 4796 and c Aql, we confirmed, after further analysis, that their variability was consistent with FEBs, while the remaining two objects; HD 21997 and HD 95086 might be good candidates for further observations to possibly confirm FEB-like activity. Two of the confirmed objects, HR 4796 and c Aql were previously found in Iglesias et al. (2018), as described in Chapter 3, and one of them, HD 37306, was found during this analysis and given its unusually strong absorption features it was studied in more detail in Iglesias et al. (2019), as shown in Chapter 4. The remaining 23 objects among the first selection of 30 showed signs of activity that could be attributed to some other mechanism but that cannot be completely ruled out from transits of circumstellar gas, thus their origin remain unclear and further analysis will be necessary in order to determine the cause of the observed residual features. As a by-product, among the objects that were discarded to have features due to transiting circumstellar gas, we found a few objects exhibiting other kinds of interesting behaviour like variability compatible with multiplicity that were not previously reported in the literature, or strong changes in the overall profile of the Ca II K that would require of further analysis in order to understand what is going on in the system.

Chapter 6

Debris disks with stable single absorption features in metallic lines and an update in multiple features: circumstellar or interstellar origin?

This Chapter is based on a paper in preparation (Iglesias et al. in prep.), which is meant to be published under the same title.

6.1 Sub-sample

In Chapter 3 we analyzed a sample of 27 objects exhibiting multiple stable absorption features within a database of observations taken up until December 2016, in order to determine their origin. In this Chapter we analyzed the systems presenting single absorption features and, in addition, further systems with multiple absorption features that were found in more recent observations taken up to March 2019. The purpose of the analysis was the same as in Chapter 3: to determine whether these stable non-photospheric absorption features were of interstellar or circumstellar origin.

We selected those systems presenting stable non-photospheric absorption features in their

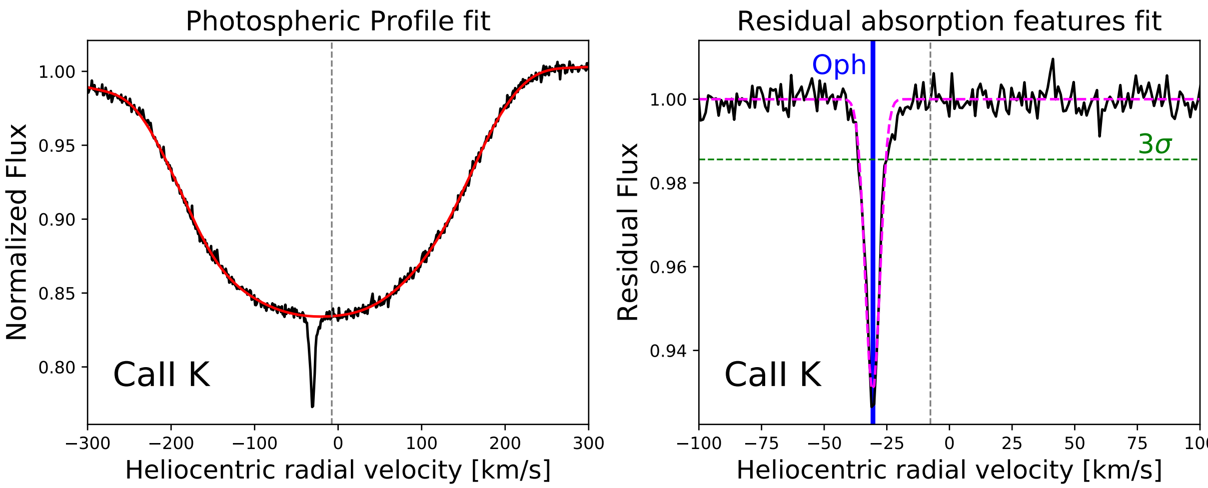

Figure 6.1: Example of profile fits for the object gam Oph. **Left:** Median spectrum of the Ca II K line in black and photospheric profile fit in red. The radial velocity of the star is marked with a vertical gray dashed line in both plots. **Right:** Residual spectrum after normalizing by the photospheric profile in black. Gaussian fit for the absorption feature is shown in a magenta dashed line. The 3σ limit is shown with a horizontal dashed green line. Vertical blue line shows the radial velocity of the Oph cloud, which traverses the line of sight of this star. The width of this line is given by the error of the radial velocity of this cloud.

Ca II K lines having at least a 3σ significance. By "stable", we mean that the features are present in all the observations and their characteristics (such as intensity and radial velocity) remain constant. As a general rule, we selected objects having a minimum of three observations covering the Ca II K line in order to have a reliable stable feature. However, two out of the 107 objects in our selected sample have only one and two observations of this line; 78 Her and tet CrB, respectively. We decided to keep these two objects in this sample since it is more probable that their features are stable rather than variable and being detected by chance in only one or two observations. Therefore, we still performed the same analysis for these two objects, but keeping in mind that there is a chance that they could be variable.

A median spectrum of the Ca II K line was obtained for each object in the sample from all the collected spectra (except for 78 Her, having only one spectrum covering the Ca II K line). Each individual spectrum was previously normalized to unity by fitting the continuum at both sides of the Ca II K line. A spline function was used to fit the photospheric profile of the Ca II K medium spectrum isolating the section where non-photospheric absorption features were observed. An example of this fit is shown in Fig. 6.1 (left). The order of the spline fit was adjusted for each object according to the S/N of its median spectrum in order to obtain a smooth profile of the line (i.e. the noisier the spectra the larger the order, meaning, the larger the distance between points of interpolation). Then, the median spectrum was normalized by the smoothed photospheric profile in order to isolate the non-photospheric components. Gaussian profiles were fit to the non-photospheric absorption features found in the residual spectrum. Those objects presenting features with an amplitude of 3σ above the noise of the residual spectrum were selected (see Fig. 6.1, right panel).

Regarding the former fitting strategy, we are aware that a spline function fit does not rely on physical parameters, however it is a time saving strategy and we will show that it yields consistent estimates for the features. In order to quantify the difference between fitting the photospheric profile with a model based on stellar parameters (such as Kurucz models, Castelli et al. (1997)) versus fitting a spline function, we compared the Kurucz model fit obtained for the object HD 110058 obtained in Chapter 3 with a spline fit. We chose this particular object as this was the only one having both, a circumstellar and an interstellar absorption, this way we can test whether the different fits affect the verdict for the origin of the features. In Fig. 6.2 we show both, the residual absorption features as normalized by the Kurucz model and as normalized by the spline fit of the photospheric profile. We also show the Gaussian fits obtained for each absorption features, as we estimate the properties of the features from the Gaussian parameters. In Chapter 3, we obtained radial velocities for the features of 1.85$\pm$0.99 km.s^{-1} for the interstellar one and 12.50$\pm$0.77 km.s^{-1} for the circumstellar one, and FWHM of 14.77$\pm$1.13 km.s^{-1} and 2.70$\pm$0.70 km.s^{-1}, respectively. On the other hand, when using a spline fit for the photospheric profile we obtained radial velocities of 1.83$\pm$0.94 km.s^{-1} for the interstellar one and 12.50$\pm$0.77 km.s^{-1} for the circumstellar one, and FWHM of 13.27$\pm$1.00 km.s^{-1} and 2.18$\pm$0.65 km.s^{-1}, respectively. In comparison, we obtained almost the same radial velocity for the interstellar feature, with a negligible difference of 0.02 km.s^{-1}, and the exact same value for the radial velocity of the circumstellar feature. Regarding the FWHM, we obtained differences in the order of $\sim$1 km.s^{-1}, thus the values are in agreement within the errors. The interstellar feature still matches with the radial velocity of the nearby stars within the uncertainties, and the circumstellar feature still matches with the estimated radial velocity of the star of 11.20$\pm$0.81 km.s^{-1} within the uncertainties. Therefore, we estimate we will obtain the same results within

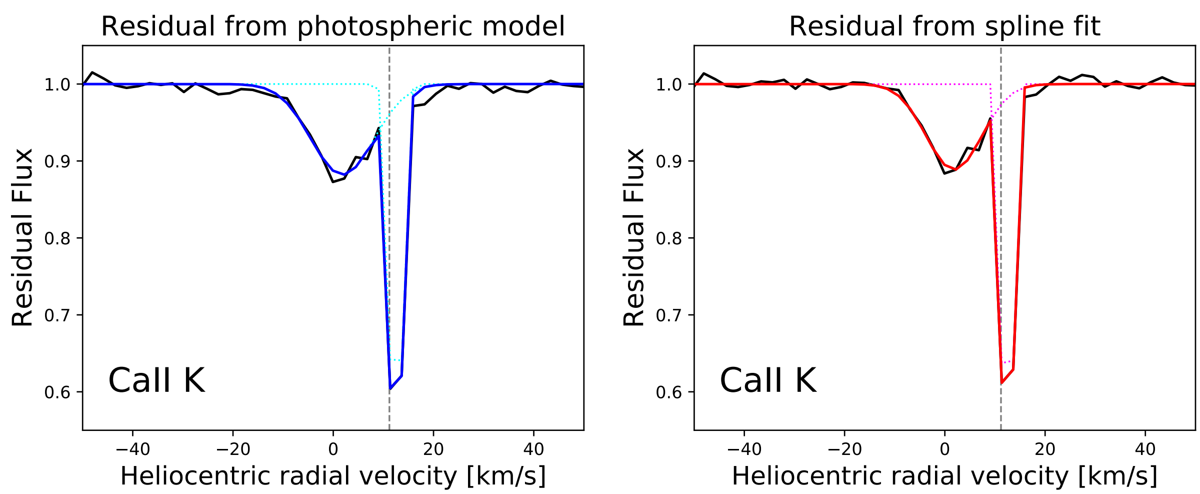

Figure 6.2: Comparison between Kurucz model fitting and spline function fitting for the photospheric profile of HD 110058. Residual absorptions are shown after normalizing by the photospheric fit. The radial velocity of the star computed in Iglesias et al. (2018) is marked with a vertical gray dashed line in both plots. **Left:** Residual spectrum of the median Ca II K line after normalizing by the Kurucz model obtained in Chapter 3. Individual Gaussian fit of the absorptions are shown in cyan dotted line and the combined fit in blue. **Right:** Residual of the same spectrum but normalized by a spline function fit of the photospheric profile. Gaussian fit for each absorption feature are shown in magenta dotted line and the combined Gaussian fit is shown in red.

the uncertainties by using a spline fit compared to using a Kurucz model for the photospheric profile.

We obtained a sub-sample of 107 objects presenting stable non-photospheric absorption features among our full sample of 273 objects having observations of the Ca II K line. This sub-sample excludes those 27 objects already analyzed in Chapter 3. The sub-sample is presented in Table 6.1 and their parameters are given in Table E.1, found in the Appendix. As can be seen in Fig. 6.3 (left) and Table E.1, the selected sample ranges in spectral types from B7 to F6, thus mainly consisting of stellar types having a radiative surface layer. A total of 201 non-photospheric stable absorption features were identified in the spectra of the 107 objects in this sample, ranging from one up to five features per object. The sample ranges in distances between 11 and 504 pc, with the majority of the sample being located within ∼200 pc, as shown in Fig. 6.3 (right) and Table E.1. Regarding the spatial distribution of these systems, they are spread all over the sky that is observable from the telescopes located in Chile (i.e. under ∼35° of declination), most of them being field stars. We observe some clustering in a few regions, for instance, in the Pleiades cluster, but also in other regions of field stars. Their coordinates are

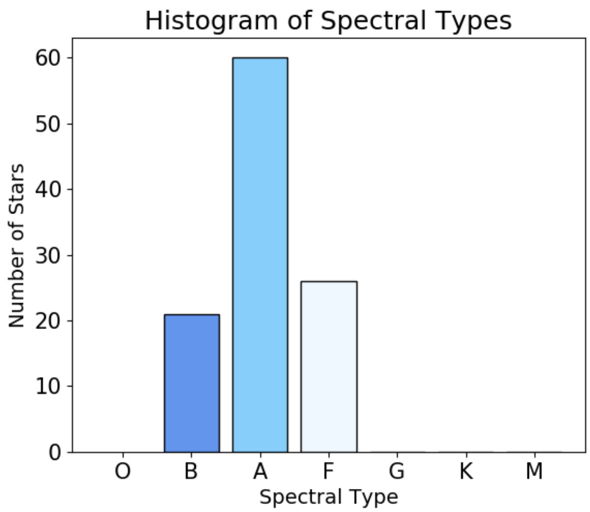

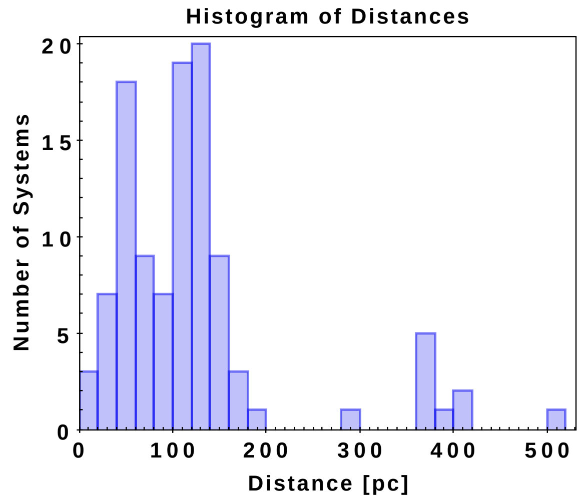

Figure 6.3: Left: Histogram of spectral types of the host stars of this selected sample of debris disks presenting non-photospheric stable absorption features. **Right:** Histogram of the distances for this sample.

shown in Table 6.1.

Table 6.1: Sub-sample of debris discs presenting single or multiple stable absorption features in their Ca II K line.

Name	HD Id	R.A. [J2000]	Dec. [J2000]	Name	HD Id	R.A. [J2000]	Dec. [J2000]
HD 225200	225200	00:04:20.3	-29:16:07.7	V MO Hya	111786	12:51:57.8	-26:44:17.7
lam01 Phe	2834	00:31:24.9	-48:48:12.6	HD 112383	112383	12:57:26.1	-67:57:38.5
HD 3670	3670	00:38:56.7	-52:32:03.4	HD 113457	113457	13:05:02.0	-64:26:29.7
49 Cet	9672	01:34:37.7	-15:40:34.8	HD 113556	113556	13:05:32.6	-58:32:07.9
HD 10472	10472	01:40:24.0	-60:59:56.6	HD 113902	113902	13:07:38.2	-53:27:35.1
q02 Eri	10939	01:46:06.2	-53:31:19.3	iot Cen	115892	13:20:35.8	-36:42:44.2
gam Tri	14055	02:17:18.8	+33:50:49.8	HD 117484	117484	13:31:30.9	-46:44:06.8
phi For	15427	02:28:01.7	-33:48:39.7	HD 117665	117665	13:32:39.2	-44:27:00.9
HD 16743	16743	02:39:07.5	-52:56:05.3	HD 118379	118379	13:37:17.7	-40:53:52.3
HD 17390	17390	02:46:45.1	-21:38:22.2	HD 118588	118588	13:38:42.8	-44:30:58.6
41 Ari	17573	02:49:59.0	+27:15:37.8	tau Vir	122408	14:01:38.7	+01:32:40.3
V V1229 Tau	23642	03:47:29.4	+24:17:18.0	HD 122705	122705	14:04:42.1	-50:04:17.0
HD 23863	23863	03:49:12.1	+23:53:12.4	HD 124619	124619	14:16:16.9	-53:49:01.9
HD 23923	23923	03:49:43.5	+23:42:42.6	HD 127750	127750	14:34:33.4	-46:18:17.2

Continued on next page

Table 6.1 – continued from previous page

Name	HD Id	R.A. [J2000]	Dec. [J2000]	Name	HD Id	R.A. [J2000]	Dec. [J2000]
kap Lep	33949	05:13:13.8	-12:56:28.6	HD 128207	128207	14:36:44.1	-40:12:41.6
HD 34324	34324	05:15:43.9	-22:53:39.7	HD 131835	131835	14:56:54.4	-35:41:43.6
HD 35150	35150	05:22:47.9	+01:43:00.2	HD 132238	132238	14:59:13.9	-37:52:52.4
HD 287787	287787	05:23:06.8	+01:18:23.7	HD 134888	134888	15:13:27.9	-33:08:50.2
HD 35332	35332	05:24:07.8	+01:38:00.1	HD 135454	135454	15:16:37.1	-42:22:12.5
HD 35367	35367	05:24:20.7	+01:35:26.5	HD 136246	136246	15:20:31.4	-28:17:13.5
HD 287850	287850	05:25:39.7	+01:38:18.3	HD 136482	136482	15:22:11.2	-37:38:08.2
HD 287854	287854	05:25:48.6	+01:23:22.0	HD 137015	137015	15:25:06.4	-38:10:09.2
HD 35625	35625	05:26:11.9	+01:53:35.7	HD 137119	137119	15:25:30.1	-36:11:57.9
HD 38056	38056	05:41:26.9	-33:24:02.6	tet CrB	138749	15:32:55.7	+31:21:32.8
HD 46190	46190	06:27:48.6	-62:08:59.7	HD 138813	138813	15:35:16.1	-25:44:03.0
HD 50571	50571	06:50:01.0	-60:14:56.9	HD 138923	138923	15:36:11.3	-33:05:34.0
bet CMi	58715	07:27:09.0	+08:17:21.5	HD 138965	138965	15:40:11.5	-70:13:40.3
HD 60995	60995	07:36:32.7	-14:14:33.4	HD 140840	140840	15:47:06.1	-35:31:04.9
HD 68420	68420	08:10:08.4	-49:00:43.4	HD 141011	141011	15:48:24.7	-42:37:05.0
30 Mon	71155	08:25:39.6	-03:54:23.1	HD 142446	142446	15:56:05.6	-36:53:34.3
HD 71722	71722	08:26:25.2	-52:48:26.9	HD 144587	144587	16:07:29.9	-23:57:02.4
HD 74374	74374	08:41:22.7	-53:38:09.4	HD 145880	145880	16:14:57.7	-39:37:40.1
HD 78702	78702	09:09:04.2	-18:19:42.7	HD 145689	145689	16:17:05.4	-67:56:28.6
HD 79108	79108	09:12:12.8	+03:52:01.1	HD 146606	146606	16:18:16.1	-28:02:30.1
HD 88215	88215	10:10:05.8	-12:48:57.3	HD 146897	146897	16:19:29.2	-21:24:13.2
HD 93738	93738	10:47:53.5	-64:15:46.2	HD 148657	148657	16:31:11.6	-38:22:58.7
HD 98363	98363	11:17:58.1	-64:02:33.3	HD 151109	151109	16:47:01.6	-39:32:01.9
HD 101088	101088	11:37:14.6	-69:40:27.1	HD 153053	153053	17:00:06.2	-54:35:49.8
bet Leo	102647	11:49:03.5	+14:34:19.4	78 Her	159139	17:31:49.5	+28:24:26.9
HD 103234	103234	11:53:08.0	-56:43:38.1	HD 159082	159082	17:32:14.8	+11:55:48.1
HD 103266	103266	11:53:26.8	-35:03:59.9	HD 1591	159170	17:33:29.8	-05:44:41.2
HD 103703	103703	11:56:26.5	-58:49:16.8	gam Oph	161868	17:47:53.5	+02:42:26.2
HD 104231	104231	12:00:09.4	-57:07:01.9	zet CrA	176638	19:03:06.8	-42:05:42.3
HD 104600	104600	12:02:37.6	-69:11:32.2	rho Tel	177171	19:06:19.9	-52:20:27.2

Continued on next page

Table 6.1 – continued from previous page

Name	HD Id	R.A. [J2000]	Dec. [J2000]	Name	HD Id	R.A. [J2000]	Dec. [J2000]
HD 105613	105613	12:09:38.7	-58:20:58.7	alf CrA	178253	19:09:28.3	-37:54:16.1
HD 105857	105857	12:11:05.8	-56:24:04.8	eta Tel	181296	19:22:51.2	-54:25:26.1
HD 105912	105912	12:11:21.7	-03:46:43.9	HD 181327	181327	19:22:58.9	-54:32:16.9
HD 106797	106797	12:17:06.3	-65:41:34.6	5 Vul	182919	19:26:13.2	+20:05:51.8
HD 107301	107301	12:20:28.2	-65:50:33.5	rho Aql	192425	20:14:16.6	+15:11:51.3
HD 107649	107649	12:22:24.8	-51:01:34.3	HD 192758	192758	20:18:15.7	-42:51:36.2
HD 107947	107947	12:24:51.9	-72:36:14.0	phi01 Pav	195627	20:35:34.8	-60:34:54.3
HD 108904	108904	12:31:12.6	-61:54:31.4	3 Peg	205811	21:37:43.6	+06:37:06.2
eta Crv	109085	12:32:04.2	-16:11:45.6	del Scl	223352	23:48:55.5	-28:07:48.9
f Vir	109704	12:36:47.3	-05:49:54.8				

6.2 Methods and Results

6.2.1 Comparison to database of interstellar clouds

In order to discriminate whether the absorption features found in the Ca II K line of each object are of circumstellar or interstellar origin, we compared the radial velocity of such features with the radial velocity of known interstellar clouds from the database of Redfield and Linsky (2008), as we did on Chapter 3. For each object we searched for the clouds traversing the line of sight using Redfield's online tool "Dynamical Model of the Local Interstellar Medium"[1]. For a given coordinate, this tool gives the name and radial velocity of the cloud traversing that sightline among the database of 15 clouds identified in Redfield and Linsky (2008) that are located within 15pc from the Sun. This tools also identifies those clouds located within 20 degrees of angular separation and we have also collected this information as there is a possibility that some of these clouds are actually traversing the line of sight. The clouds in this database have been identified from only 157 sightlines, thus providing a relatively low spatial sampling and opening the possibility for the extension of the clouds to be underestimated. We have observed that,

[1] `http://lism.wesleyan.edu/LISMdynamics.html`

in many cases, those clouds identified in the database as located within 20° but not directly in the line of sight matched exactly with the velocity of some absorption features. To test whether the observed features are possibly attributable to those matching nearby clouds, we have tried slightly changing the coordinates by a few minutes and, often such a cloud have appeared to be directly in the line of sight only a few minutes away. Therefore, we cannot discard those clouds within 20° to be the origin of some absorption features.

As mentioned, we have fit Gaussian profiles to each absorption feature with peak intensity over 3σ, obtained their radial velocity from the center of the profile, and crossmatched their radial velocity with those of the clouds in the database of the local interstellar medium. A "match" in radial velocity was considered to be within the quadratic sum of the FWHM of the absorption feature and the uncertainty of the radial velocity of the cloud (so the cloud falls within the width of the absorption). The interstellar clouds matching the radial velocity of the non-photospheric absorption features are presented in Tables 6.2 (showing the first ten objects) and E.2 (found in the Appendix and showing the remaining objects). We identify those matching clouds traversing the line of sight of the star as well as those matching clouds within 20° of angular distance. In some cases, more than one match was found for either category. For simplicity, we present only the closest match. An example of a cloud (Oph) matching the radial velocity the absorption feature in the object gam Oph is shown above, in Fig. 6.1 (right panel).

Table 6.2: Clouds in the line of sight or at less than 20° of our targets taken from Redfield and Linsky (2008) LISM database. The name of each target, the radial velocity of each non-photospheric absorption feature, the FWHM of each feature, the name of the cloud found in the line of sight of the target that matches with the radial velocity of the feature (within its FWHM), the radial velocity of this cloud, the name of a cloud found within 20° that also matches with the feature and its corresponding radial velocity.

Name	RV feature [km.s^{-1}]	FWHM feat. [km.s^{-1}]	Cloud line of sight	RV Cloud LoS [km.s^{-1}]	Cloud $< 20°$	RV Cloud $< 20°$ [km.s^{-1}]
HD 225200	-0.08±2.31	8.43±1.93	LIC	1.22±1.37	Mic	-3.59±1.14
lam01 Phe	1.76±0.78	4.36±0.33	LIC	0.11±1.38	G	3.37±1.79
	6.73±0.76	1.28±0.10	–	–	Vel	6.55±0.83
HD 3670	2.38±2.59	3.33±0.86	LIC	-0.11±1.38	G	2.93±1.76
	19.55±2.60	6.25±1.62	Dor	22.23±0.66	–	–

Continued on next page

Table 6.2 – continued from previous page

Name	RV feature [km.s^{-1}]	FWHM feat. [km.s^{-1}]	Cloud line of sight	RV Cloud LoS [km.s^{-1}]	Cloud $< 20^{\circ}$	RV Cloud $< 20^{\circ}$ [km.s^{-1}]
49 Cet	12.60±2.30	5.54±1.27	LIC	11.01±1.29	G	16.96±1.64
HD 10472	4.65±0.84	8.22±0.63	Cet	4.24±0.56	LIC	0.92±1.38
q02 Eri	7.87±1.50	7.44±1.09	Vel	8.51±0.85	G	3.89±1.71
	13.51±1.48	5.65±0.83	Vel	8.51±0.85	–	–
gam Tri	16.31±1.78	6.17±1.09	LIC	17.38±1.15	–	–
phi For	12.02±1.47	2.81±0.41	LIC	10.67±1.30	Blue	8.87±1.61
HD 16743	15.72±1.51	8.36±1.22	Cet	15.71±0.74	Vel	18.04±1.07
HD 17390	18.20±1.51	8.48±1.24	G	20.79±1.51	Blue	10.39±1.49

We attribute an interstellar origin to all those features matching with the velocity of an interstellar cloud located directly in the line of sight of the star. From the total of 201 detected absorption features, 101 of them (detected in 83 objects) matched with the velocity of a known cloud in the solar vicinity identified by Redfield and Linsky (2008). Most of these features (35 of them) seem to be attributable to the Galactic (G) cloud and many others (26) are likely due to the Local Interstellar Cloud (LIC). Our Sun is embedded within the LIC cloud, while the G cloud is located right next to the LIC cloud (Redfield, 2006). Therefore, it makes sense that more than half of the observed features are due to the two closest clouds in the interstellar medium as they are likely to cover the line of sight of many stars.

6.2.2 Search and comparison with reference stars

Since the objects in this sample are located at distances up to ~500 pc and the clouds within Redfield and Linsky (2008) database only include those clouds located within 15 pc from the Sun (and have a fairly sparse spatial sampling), it is likely that those absorption features that do not match with any of these known clouds might be due to clouds located at larger distances (or due to underestimation of clouds spatial coverage). Therefore, for the remaining objects with yet unidentified absorption features (besides a few exceptions), we searched for high-Resolution spectra of nearby early-type stars (ranging from B0 to F5) around each object in the ESO archive in order to search for the presence of similar absorption features in them (as we did as part of the analysis of the objects in Chapter 3). We chose the ESO archive as it offers science-ready data from instruments such as FEROS, UVES and HARPS, which count with the needed resolution and spectral coverage. However, we do not discard the use of other archives such as the Keck Observatory Archive (KOA) or the Canada-France-Hawaii Telescope (CFHT) archives in the future. In the present Chapter, this part of the analysis was done in collaboration with the undergraduate student Gabriel Corvalán as a practice project for his Bachellor Thesis. As mentioned, we searched for spectra of reference stars around 54 objects having features not matching any identified cloud and we were able to find useful reference spectra for 39 of these objects. These objects and their nearby reference stars having available spectra in the ESO archive are shown in Tables 6.3 (showing the first ten objects) and E.3 (found in the Appendix, with the remaining objects).

Table 6.3: Comparison stars.

Object of science	Distance [pc]	R_{search} [deg.]	Object of reference	Spectral type	Distance [pc]	θ sep. [deg]
49 Cet	57.07±0.33	3.0	HD 9399	A1V	245.63±6.61	1.32
q02 Eri	60.97±0.48	5.8	HD 12894	F4V	46.28±0.11	3.02
			HD 13418	A7V	252.34±1.68	3.48
			HD 12707	B6V	632.63±17.64	4.70
HD 23863	134.25±1.44	4.4	HR 1183	B8V	133.40±1.21	0.21
HD 23923	133.40±1.21	4.4	None	–	–	–
kap Lep	140.96±6.64	5.5	HD 34282	B9.	311.57±4.60	3.20
			HD 34816	B0.	269.70±26.63	1.56
HD 35150	370.67±8.97	4.3	V346-Ori	A8V	366.54±5.78	0.48
			HD 287787	A2	410.78±8.39	0.42
			HD 34748	B3V	375.69±14.00	3.23

Continued on next page

Table 6.3 – continued from previous page

Object of science	Distance [pc]	R_{search} [deg.]	Object of reference	Spectral type	Distance [pc]	θ sep. [deg]
			HD 35625	A0V	361.96±9.89	0.87
HD 35332	384.19±10.50	4.5	V346-Ori	A8V	366.54±5.78	0.17
			HD 287787	A2	410.78±8.39	0.41
			HD 34748	B3V	375.69±14.00	3.25
			HD 35625	A0V	361.96±9.89	0.58
HD 35625	361.96±9.89	4.1	V346-Ori	A8V	366.54±5.78	0.41
			HD 287787	A2	410.78±8.39	0.97
			HD 34748	B3V	375.69±14.00	3.70
			HD 36646	B3V	398.65±16.90	4.00
			HD36841	B8V	451.15±11.53	3.09
HD 38056	128.31±0.77	4.5	None	–	–	–
HD 60995	504.64±12.91	2.5	None	–	–	–

For the 39 objects having reference stars with available high-resolution spectra, we searched for matching absorption features in the Ca II K line of each of those reference stars. We followed the same procedure as for the objects of science in our sample and fit Gaussian profiles to those absorption features found in the reference stars having at least a 3σ intensity above the noise. After obtaining the radial velocity and FWHM for those features, we compared whether they "match" with those of our objects of science. A "match" was considered when the absolute difference between the radial velocity of the features (the one of the object of science and the one of the reference star) was smaller than the square sum of the FWHM of both features. In other words, they match if their radial velocities are close enough so their FWHM overlap with each other. Two example of matching absorptions are shown in Fig. 6.4. We found matching absorption features in the reference stars for 36 out of the 39 objects analyzed, although for one of the stars, HD 148657, we found a match for only one of its two features. For the three remaining objects, namely bet Leo, HD 104600 and zet CrA, we did not find any matching absorption

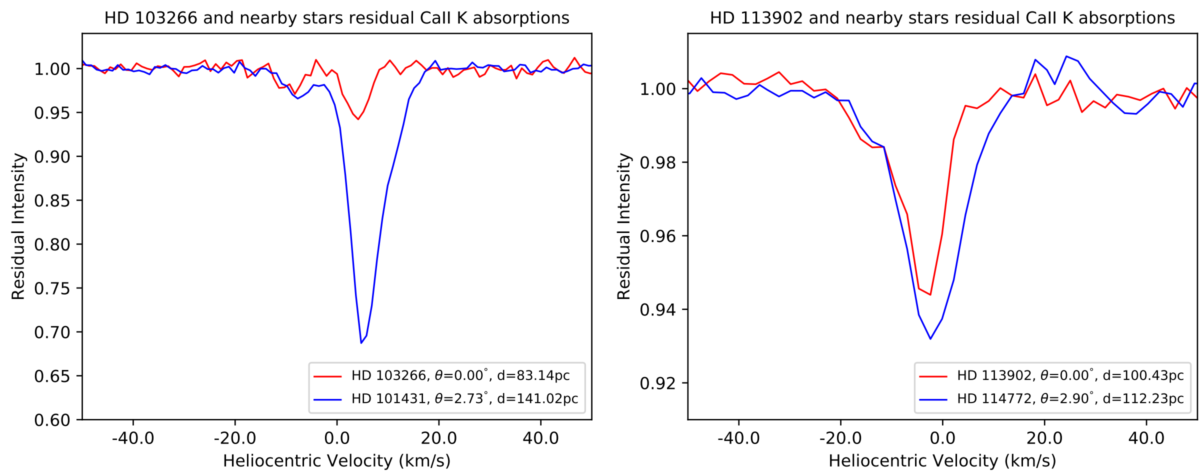

Figure 6.4: Example of comparison of the Ca II K line of our objects of science with reference stars. Residual of the median spectrum of the object of science in red and residual of the reference spectrum in blue. **Left:** The object of science HD 103266 and the reference star HD 101431. **Right:** The object HD 113902 and the star of comparison HD 114772.

features in their stars of reference (Bs. Thesis Corvalán, 2020). These results are shown in Tables 6.4 (the first 10 objects) and E.4 (in the Appendix, showing the remaining objects).

For the three objects for which we did not find any matching absorption features in their reference stars, we performed an exercise of artificially "injecting" the feature from the object of science into the reference star in order to test whether the feature was detectable over a 3σ level or not. We directly added the absorption feature to the spectrum of the reference star at the same position where it is located in the object of science. An example of this exercise is shown in Fig. 6.5 for the case of HD 104600. If we assume that the cloud is homogeneous and that it is actually covering the reference star, then the feature should be detected in this reference star. However, considering that the reference star is located at 3.26° of angular separation (about 6pc of physical distance) it is possible that the cloud was thinner at this distance and harder to detect, or not covering the line of sight of this star. For the case of zet CrA, the feature should have also been detected in its reference star (under the same conditions), but for bet Leo, however, the feature is to weak to be detected over a 3σ level.

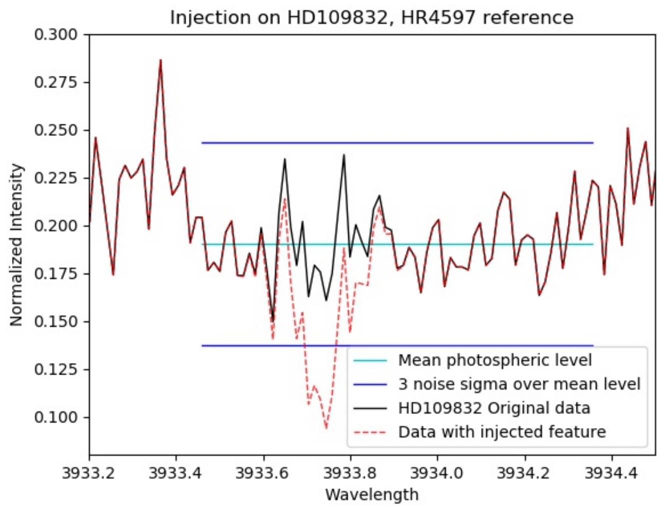

Figure 6.5: Injection of the absorption feature found in HD 104600 (also HR 4597) into the Ca II K line of its reference star HD 109832 (from Bs. Thesis Corvalán, 2020). Notice how the absorption feature (in red) should have been detected if the cloud was homogeneous and covering this star.

Table 6.4: Comparison stars.

Object of science	RV feature $[km.s^{-1}]$	FWHM feat. $[km.s^{-1}]$	Reference star	RV feat. ref. $[km.s^{-1}]$	FWHM feat. ref. $[km.s^{-1}]$
49 Cet	12.60±2.30	5.54±1.27	HD 9399	13.89±2.35	6.98±1.60
q02 Eri	7.87±1.50	7.44±1.09	HD 13418	6.24±0.65	18.10±0.44
	13.51±1.48	5.65±0.83	HD 12707	14.42±0.27	10.42±0.19
HD 23863	16.00±1.48	5.20±0.76	HR1183	15.20±0.13	7.43±0.13
kap Lep	-20.80±1.65	17.67±2.59	HD 34282	-26.03±0.30	6.92±0.32
	2.81±1.48	5.21±0.76	HD 34816	4.95±0.05	10.74±0.06
	16.26±1.51	8.18±1.20	HD 34282	12.85±0.49	9.57±0.51
	23.83±1.48	4.99±0.73	HD 34816	22.15±0.12	12.75±0.13
	32.16±1.51	8.48±1.24	HD 34816	22.15±0.12	12.75±0.13
HD 35150	-2.88±2.37	14.35±3.28	HD34748	-1.28±1.25	22.04±2.82
	11.60±2.32	8.79±2.01	HD35625	9.96±0.09	6.39±0.11
	22.26±2.31	7.88±1.80	V346-Ori	23.64±0.39	7.61±0.41

Continued on next page

Table 6.4 – continued from previous page

Object of science	RV feature [km.s^{-1}]	FWHM feat. [km.s^{-1}]	Reference star	RV feat. ref. [km.s^{-1}]	FWHM feat. ref. [km.s^{-1}]
HD 35332	10.52±2.39	16.71±3.82	HD35625	9.71±0.08	5.49±0.09
	23.08±2.29	4.32±0.99	V346-Ori	23.64±0.39	7.61±0.41
	33.51±2.30	6.16±1.41	HD287787	27.79±0.83	5.10±0.91
HD 35625	10.32±1.50	7.05±1.03	HD 36646	10.48±0.18	9.38±0.21
	18.91±1.82	25.54±3.74	V346-Ori	23.64±0.39	7.61±0.41
HD 98363	3.89±2.31	7.49±1.71	HD308804	2.11±0.25	6.61±0.18
	10.05±2.29	2.51±0.57	HD308804	8.75±0.18	7.57±0.12
	16.37±2.30	4.84±1.11	HD308804	8.75±0.18	7.57±0.12
HD 101088	-4.65±2.30	6.08±1.39	HD95881	2.91±0.29	44.30±0.82
	6.78±2.34	12.13±2.77	HR4597	6.30±0.25	10.08±0.26
bet Leo	2.21±2.29	3.13±0.72	None	–	–
	13.64±2.30	4.95±1.13	None	–	–

6.2.3 Comparison to nearby stars within our own sample

With the previous exercise we realized that some of the reference stars found for each object in this sub-sample were also stars belonging to our sample. Therefore, we decided to perform an additional search of nearby stars among all the early-type stars within our full sample of debris disks. This time, we searched for nearby stars for all the objects in this study, as this additional search not only might help to find missing references but also to confirm the already found references and matching clouds. We selected all the systems in our sample having observations of the Ca II K line and having a spectral type equal or earlier than F6, since this is the latest spectral type for which non-photospheric absorption features are detected. These were a total of 234 stars, including stars that present non-photospheric absorptions (i.e. including the sample analyzed in the present chapter and in chapter 3) and stars that do not. Stars presenting features are potentially useful to confirm an interstellar origin for the features, whereas stars with no features might help to find candidates with circumstellar gas.

Since we do not know the size or the distance of the interstellar clouds that might be crossing the line of sight of our stars, determining the ideal radius of search for nearby stars is challenging. Therefore, we used a rough estimation based on the overall stellar distances and a standard cloud size. We computed a median distance for the early type stars in our sample, which resulted of 86 pc. Then, considering that our Local Interstellar Cloud (where the Sun is embedded) has an extension of $\sim$ pc across, a cloud of a similar size located at a distance of 86 pc (and assuming it has a spherical shape) would cover an area of angular radius $\sim 3^{\circ}$. Thus, we chose 3° as a standard radius to search for nearby stars within our own sample. Then, same as we did for the reference stars found in the ESO archive, we compared whether the features found in the nearby stars matched with those of our objects of science using the same matching criterion (that the features overlapped with each other). We present the results of this search and the matches for each feature of the objects in our sample of study in Tables 6.5 (with the first 20 objects) and E.5 (in the Appendix, with the remaining objects). We found nearby stars within an angular separation of 3° for 51 out of the 107 objects in our sample of study and found matching features for 39 objects among those 51 having comparison stars. Two examples of these matches are shown in Fig. 6.6. Notice how the absorption features share a very similar radial velocity.

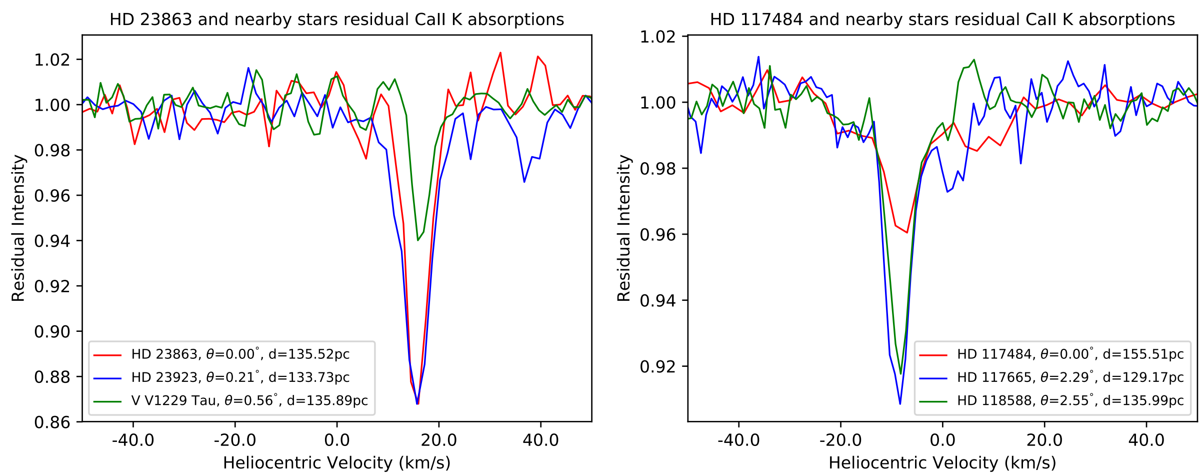

Figure 6.6: Example of comparison of among stars within our sample. Residual spectrum of the Ca II K line showing only the absorption features. The angular separation with respect to the first star (in red) is shown, as well as the distance (from the Earth) for each object. **Left:** HD 23863 as the central object and HD 23923 and V V1229 Tau in comparison. The absorption feature at ∼16 km.s^{-1} matches for the three objects. **Right:** HD 117484 as the central star compared to HD 117665 and HD 118588. The absorption feature at ∼-8 km.s^{-1} matches in radial velocity for the three stars.

Table 6.5: Comparison stars within our own sample. Object of science, number of comparison stars found within 3°, radial velocity of the features of the object of science, number of stars within the sample having features matching each one of those of the object of science, and the list of these stars. Radial velocity of the features for the comparison stars are not given again here as they have been already presented in previous tables.

Object of science	N nearby stars	RV feature [km.s^{-1}]	N matches	Matching stars within our sample
HD 225200	0	-0.08±2.31	–	–
lam01 Phe	0	1.76±0.78	–	–
		6.73±0.76	–	–
HD 3670	0	2.38±2.59	–	–
		19.55±2.60	–	–
49 Cet	0	12.60±2.30	–	–
HD 10472	0	4.65±0.84	–	–
q02 Eri	0	7.87±1.50	–	–
		13.51±1.48	–	–

Continued on next page

Table 6.5 – continued from previous page

Object of science	N nearby stars	RV feature [km.s^{-1}]	N matches	Matching stars within our sample
gam Tri	1	16.31±1.78	0	–
phi For	0	12.02±1.47	–	–
HD 16743	0	15.72±1.51	–	–
HD 17390	0	18.20±1.51	–	–
41 Ari	0	16.13±1.17	–	–
V V1229 Tau	3	16.64±1.14	2	HD 23863, HD 23923
HD 23863	3	16.00±1.48	2	HD 23923, V V1229 Tau
HD 23923	3	15.74±1.49	2	HD 23863, V V1229 Tau
		37.39±1.48	0	–
kap Lep	0	-20.80±1.65	–	–
		2.81±1.48	–	–
		16.26±1.51	–	–
		23.83±1.48	–	–
		32.16±1.51	–	–
HD 34324	1	9.07±2.30	0	–
HD 35150	7	-2.88±2.37	6	HD 287787, HD 287850, HD 287854, HD 35332, HD 35367, HD 35625
		11.60±2.32	5	HD 287850, HD 287854, HD 35332, HD 35367, HD 35625
		22.26±2.31	6	HD 287787, HD 287850, HD 287854, HD 35332, HD 35367, HD 35625
HD 287787	7	-14.11±1.48	1	HD 35150
		0.73±1.48	4	HD 287850, HD 35150, HD 35332, HD 35625
		24.70±1.48	6	HD 287850, HD 287854, HD 35150, HD 35332, HD 35367, HD 35625
		31.56±1.47	4	HD 287850, HD 35332, HD 35367, HD 35625

Continued on next page

Table 6.5 – continued from previous page

Object of science	N nearby stars	RV feature [km.s^{-1}]	N matches	Matching stars within our sample
HD 35332	7	10.52±2.39	6	HD 287787, HD 287850, HD 287854, HD 35150, HD 35367, HD 35625
		23.08±2.29	6	HD 287787, HD 287850, HD 287854, HD 35150, HD 35367, HD 35625
		33.51±2.30	4	HD 287787, HD 287850, HD 35367, HD 35625
HD 35367	7	9.89±1.47	5	HD 287850, HD 287854, HD 35150, HD 35332, HD 35625
		22.23±1.48	6	HD 287787, HD 287850, HD 287854, HD 35150, HD 35332, HD 35625
		34.45±1.47	4	HD 287787, HD 287850, HD 35332, HD 35625

6.3 Results, Discussion and Conclusions

6.3.1 Results and Discussion

After comparing the radial velocity of the features with known interstellar clouds in the line of sight of the stars, searching for matching features in nearby stars found in the ESO archive and comparing the features with those in other nearby stars from our own sample, we gathered all this information together in order to assess the origin of the absorption features. We compiled all this information in Tables 6.6 and E.6 (showing 20 objects and the rest, respectively) along with the radial velocity of the star, and present here our verdict on the origin of the absorptions. Our criteria to discern the origin of each absorption are that if its radial velocity matches with that of a known cloud in the line of sight, and/or with that of features in reference stars, and/or with that of features in other stars from the sample located within 3°, we conclude the feature is likely of interstellar origin (ISM). In addition, given that stable circumstellar gas should have the same radial velocity of the star (as it should move along with the system), in case we do not find any match with clouds or nearby stars, if the radial velocity of the feature does not match with the radial velocity of the star (within its FWHM), then it does not likely belong to the system and thus, it is more probably of interstellar origin. On the other hand, in case there are no matches with interstellar clouds or nearby star and the feature matches with the radial velocity of the star, then the feature could be of circumstellar (CS) origin. For instance, for the case of HD 110058 found in Chapter 3, which we confirmed to have one feature of interstellar origin and one feature of circumstellar nature, the circumstellar feature matched with the radial velocity of the star within a difference of 1.30 km.s^{-1}, within a FWHM of 1.98 km.s^{-1} (see Fig. 6.2). Other examples outside our sample are the cases of β Pic and HD 172555, although the authors do not give numbers in the case of β Pic, it is shown that a stable circumstellar component is found at the radial velocity of the star (Kiefer, 2014). For the case of HD 172555, Rebollido et al. (2018) shows that a stable circumstellar feature is found at 2.3 km.s^{-1} with a FWHM of 9.7 km.s^{-1} matching very closely with the radial velocity of the star of 2.6 km.s^{-1}.

We confirmed an interstellar origin for the absorption features of 102 objects out of our sample of 107 under the criteria described above, one of them, 49 Cet, having a "shared" origin part interstellar and part circumstellar (see discussion below). For five objects, however, we were not able to confirm an interstellar origin for one of their features, and thus, they are good candidates for circumstellar gas. These particular features of these five objects are marked as inconclusive ("?") in Tables 6.6 and E.6. Following, we proceed to further analyse each of these candidates aiming to confirm or discard an interstellar origin for their absorption features and we also discuss the case of 49 Cet having a "shared" ISM/CS origin.

Table 6.6: Summary of all the analysis performed and conclusions for the origin of the features. This Table shows the science object, its radial velocity (when available), the radial velocity of each absorption feature, whether the radial velocity of the feature matches with: the radial velocity of the star, a known cloud in the line of sight of the star, a feature in a reference star found in the ESO archive, a feature in another star of our own sample. Finally, a verdict on the most likely origin of the feature. A match is indicated with a ✓, a non match with an ✗, and "–" when no information is available.

Object of science	RV star [km.s^{-1}]	RV feature [km.s^{-1}]	Match RV star	Match Cloud	Match reference	Match within sample	Origin
49 Cet	10.3	12.60	✓	✓	✓	–	ISM/CS
q02 Eri	9.5	7.87	✓	✓	✓	–	ISM
		13.51	✓	✓	✓	–	ISM
phi For	19.0	12.02	✗	✓	–	–	ISM
HD 16743	–	15.72	–	✓	–	–	ISM
HD 17390	7.2	18.20	✗	✓	–	–	ISM
41 Ari	4.0	16.13	✗	✓	–	–	ISM
V V1229 Tau	5.0	16.64	✗	✗	–	✓	ISM
HD 23863	5.0	16.00	✗	✗	✓	✓	ISM
HD 23923	9.5	15.74	✓	✓	–	✓	ISM
		37.39	✗	✗	–	✗	ISM
kap Lep	20.8	-20.80	✗	✗	✓	–	ISM
		2.81	✗	✗	✓	–	ISM
		16.26	✓	✓	✓	–	ISM
		23.83	✓	✓	✓	–	ISM
		32.16	✗	✗	✓	–	ISM
HD 34324	–	9.07	–	✓	–	✗	ISM
HD 35150	–	-2.88	–	✗	✓	✓	ISM
		11.60	–	✗	✓	✓	ISM
		22.26	–	✓	✓	✓	ISM
HD 287787	–	-14.11	–	✗	–	✓	ISM
		0.73	–	✗	–	✓	ISM

Continued on next page

Table 6.6 – continued from previous page

Object of science	RV star [km.s^{-1}]	RV feature [km.s^{-1}]	Match RV star	Match Cloud	Match reference	Match within sample	Origin
		24.70	–	✓	–	✓	ISM
		31.56	–	✗	–	✓	ISM
HD 35332	–	10.52	–	✓	✓	✓	ISM
		23.08	–	✓	✓	✓	ISM
		33.51	–	✗	✓	✓	ISM
HD 35367	–	9.89	–	✗	–	✓	ISM
		22.23	–	✓	–	✓	ISM
		34.45	–	✗	–	✓	ISM
HD 38056	28.1	6.07	✗	✓	–	–	ISM
		12.86	✗	✓	–	–	ISM
		22.68	✓	✗	–	–	?
HD 68420	–	0.83	–	✗	–	–	?
		12.39	–	✗	–	–	?
		25.55	–	✗	–	–	?
HD 78702	16.9	11.38	✓	✓	–	–	ISM
		18.13	✓	✗	–	–	?
tau Vir	-6.7	-10.92	✓	✗	–	–	?
del Scl	8.7	-2.36	✗	✓	–	–	ISM
		6.78	✓	✗	–	–	?

6.3.2 Discussion and further analysis on the persisting candidates

HD 38056: This object presents three absorption features, two of them match with a cloud in the line of sight of the star and do not match with the stellar radial velocity, while the third one does not match with any cloud in the line of sight and matches (within its FWHM) with the radial velocity of the star. This third feature, with a radial velocity of 22.68±1.51 km.s^{-1}, might (in principle) be of circumstellar origin. We did not, however, find any nearby star within our sample or the archive to compare and confirm or discard a circumstellar origin. The radial velocity of the star of 28.10$\pm$1.70 km.s^{-1} matches within the FWHM of 8.45$\pm$1.24 km.s^{-1}. Although it is not a close match, it falls within the errors. This features matches with clouds located within 20°, thus there is a possibility that they might cross the line of sight of the star. However, this cannot be confirmed or discarded. We analyzed the Na I lines and the three features appear completely blended into a single wider one having a weaker intensity, therefore it is not clear whether the third feature is detected or not as it is not resolved and it has the weakest intensity out of the three. We also extended our search of nearby stars within the sample up to 5° not finding any matching features in two stars separated by 4.8°. These two stars are located at $\sim$59 pc, closer than HD 38056 being at 128 pc, thus there is a possibility that there could be clouds in between those distances. Since neither an interstellar or a circumstellar origin can be confirmed for this feature its origin remains inconclusive. We will obtain spectra of nearby stars around this object in order to confirm its origin in the future.

HD 68420: This object also presents three non-photospheric absorption features. However, we did not find any radial velocity measurement for this object thus we were not able to confirm whether they matched with the radial velocity of the star. Although, they do appear well centered in the photospheric Ca II K line (the middle one in particular) thus it is likely that one of them is found close to the stellar radial velocity. In order to confirm this, we performed a rough measurement of the radial velocity of the star by fitting a Gaussian profile to the photospheric Ca II K line. We obtained an estimate for the radial velocity of 9.77$\pm$4.56 km.s^{-1} following the procedure we used in Section 3.2. This radial velocity would match within the FWHM of the feature located at 12.39 km.s^{-1}. We did not find any cloud in the line of sight of this star, and although we do find clouds within 20° matching with the radial velocities of each feature, we are not able to confirm they are indeed in the line of sight of the star. Nevertheless, this star is located at a distance of 411 pc (being one of the most distant objects in the sample), therefore, the probability that there are clouds in the line of sight of this star is larger. We did not find any nearby star to compare with, thus we were not able to confirm or discard the presence of matching absorptions in other stars. Therefore, we further extended our search within our sample up to 5° and, in this case, we found matching absorption features in two stars: HD 71722, with an angular separation of 4.58°, and HD 71043, with a separation of 3.71°, being their features, however, much weaker than those in HD 68420. These two stars are located at ∼70 pc, much closer than HD 68420, therefore, it makes sense that the line of sight of this star traverses a larger amount of interstellar material. The three features are also present in the Na I lines, with an even larger intensity than the Ca I K line, which is typical for the ISM at more distant lines of sight (Welsh et al., 2010). Although the criterium regarding the intensity of the Na I lines versus the Ca I lines is not free of exceptions, the fact that we also observe features at similar velocities in two other stars help us to confirm an interstellar origin for the absorptions found in HD 68420.

HD 78702: This system presents two (blended) absorption features that are close to the radial velocity of the star. One of them matches with the velocity of a cloud in the line of sight of the system while the other (located at 18.13 km.s^{-1} and matching closer with the radial velocity of the star) does not. Similar to the previous cases, it matched with the radial velocity of clouds located within 20°, but we did not find any nearby star to confirm or discard clouds in the line of sight of this star being the origin of this feature. We extended our search for nearby stars to 5°, still not finding any references. We analyzed the Na I lines and, in this case, we observe three absorption features, the third one being redshifted with respect to the other two, which have a similar intensity to those detected in the Ca I K line. We also observe a weak third feature in the Ca I K line, but it is only detected with a $\sim 2\sigma$ peak intensity and, therefore, it was not considered as a significant detection. The origin of feature matching the radial velocity of the star remains inconclusive and will be a candidate to search for comparison stars in the future with the aim of assessing its origin.

tau Vir: This object presents a small single feature near the center of its photospheric Ca II K line, matching (within the criteria) with the radial velocity of the star. Just like in the previous cases, it does not match with a cloud in the line of sight of the star but it does match with a cloud located within 20°, and we did not find reference stars for comparison of the spectra. Extending the search within our sample up to 5° did not give us any comparison stars either. We observed that the feature is also present in the Na I lines, although slightly less intense. This object will remain as a candidate for circumstellar origin and the origin of its feature will be classified as inconclusive until we obtain the necessary data to confirm its origin.

del Scl: This object presents two tiny absorption features more or less centered in the photospheric Ca II K line. One of them matches with a cloud in the line of sight (and with other nearby clouds as well) and does not match with the stellar radial velocity, while the other one does match with the radial velocity of the star and does not match with any interstellar cloud. When extending our search within our sample up to 5°, we found a matching feature in HD 225200 at an angular separation of 3.57°, although much more intense and wider. We have observed that, typically, those features observed towards more distant stars are much larger in comparison to those observed in less distant stars, and this is also the case, being del Scl at ∼44 pc and HD 225200 at ∼134 pc. The feature is not detected in the Na I lines of del Scl, which is often (but not always) the case for circumstellar gas. However, abundances in the ISM for shorter distances are also observed to be richer in Ca II rather than Na I (Murga et al., 2015), and considering that the Ca II K detection is weak (only slightly over 3σ) it is possible that Na I falls under the detection level. Since we find an absorption matching within its FWHM with the feature in del Scl, we tentatively assign an interstellar origin for the feature. However, we would like to further confirm this by searching for closer reference stars in the future.

49 Cet: The case of 49 Cet is particular. It presents a single, narrow non-photospheric absorption feature in its Ca II K line matching both, the radial velocity of the star (10.3 km.s^{-1}) and the radial velocity of the LIC cloud (11.01 km.s^{-1}) which traverses the line of sight of the star. For this exceptional case, although its feature already matched with a cloud, we also searched for a nearby reference star in the ESO archive, as we considered it was worthy of further study. We found a matching absorption feature in the star HD 9399 at 1.32° of angular separation. The feature in 49 Cet is also detected in its Na I lines, with a stronger intensity. All this information points towards an interstellar origin of the feature. However, in Chapter 5 we demonstrated that we found variability in 49 Cet in the form of narrow absorption features at the radial velocity of the star and we attributed it to circumstellar gas considering the characteristics of the absorptions and the background of the system (the disk being near edge-on and having gas emissions). This variability is additional to the stable feature of interstellar origin. Therefore, we conclude that the origin of this feature is part interstellar and part circumstellar. This conclusion is in agreement with Rebollido et al. (2018), who also determined that the feature is likely a blend of interstellar and circumstellar gas absorptions.

6.3.3 Discussion regarding objects having a different verdict in the literature

For the case of 49 Cet, our conclusion was in agreement with previous studies. However, in other cases, the results of our study challenge previous attributions of circumstellar origin for the non-photospheric features in some of the objects. Following, we discuss these cases.

HD 145689: This object presents a very small absorption feature in its Ca II K line matching both, the radial velocity of the star and the radial velocity of the G cloud. We attributed an ISM origin for the feature since it matches with this interstellar cloud in the line of sight of the system. We did not find any reference star for this object. In Rebollido et al. (2020), the authors also found the feature near both, the radial velocity of the star and the radial velocity of the G cloud. In addition, they analyzed a nearby star (HD 147787) having an angular separation of $\sim 4^{\circ}$ and located at 40 pc. They did not find any absorption feature in this object, and therefore, they assigned a circumstellar origin for the feature. Considering this, we further searched for comparison stars within our sample up to a radius of 5° of angular separation in order to better assess the nature of the feature. We found the star HD 138965 at a separation of 4.0° and a distance of 78 pc, having an absorption feature at the exact same radial velocity of that in HD 145689 (-11.51 km.s^{-1}). This confirms our verdict of interstellar origin for the absorption.

eta Tel (HD 181296): This systems presents a narrow absorption feature at -22.94 km.s^{-1}, not matching with the radial velocity of the star (13.0 km.s^{-1}) nor with any known cloud in the line of sight of the star. We found that this feature matches exactly with the radial velocity of the feature detected in HD 181327, which is separated by only 0.12° from eta Tel and is located almost at the same distance ($\sim$48 pc). Rebollido et al. (2018) analyzed eta Tel, finding the feature at the same radial velocity. However, they also analyzed HD 181327, not finding any absorption feature. Therefore, they suggest a circumstellar origin of the feature (despite the fact that it far blueshifted with respect to the radial velocity of the star). Our matching detection in HD 181327 clearly confirms an interstellar origin for the feature. Furthermore, we also tried extending a bit our search and we found another matching absorption feature in rho Tel, which has an angular separation of 3.23° from eta Tel and has a similar distance. This, of course, strengthen our verdict of interstellar origin.

6.3.4 Conclusions

We analysed 107 debris disks in our sample presenting stable non-photospheric absorption features in their Ca II K line aiming to determine whether these features were of circumstellar or interstellar origin. For this purpose, we compared the radial velocities of these absorption features with those of: 1) known interstellar clouds from Redfield and Linsky (2008)'s database, 2) nearby stars retrieved from the ESO archive, and 3) nearby stars within our own sample. For 102 objects we initially concluded that their absorption features were more likely of interstellar origin given that their features matched with a cloud located directly in the line of sight of the star, and/or it matches with a feature present in a nearby star (either from the ESO archive or from our sample), and/or the feature did not coincide with the radial velocity of the star. For one of these objects (49 Cet), however, we determined that the feature was part interstellar and part circumstellar. For the five remaining objects (discussed above) we were not able to confirm or discard a circumstellar or interstellar origin for their features with the information we obtained. Therefore, we performed further analysis of these five objects and were able to determine an interstellar origin for two of them. For the three remaining objects, we leave their origin as inconclusive in the meantime, and we will obtain high-resolution spectra of early-type stars near these candidates in order to better assess the cause of their absorptions.

With this study, we confirmed a (partial) circumstellar origin for only one system, 49 Cet, but we also obtained three possible candidates for circumstellar gas and, as a by product, a considerable amount of information regarding interstellar clouds that will be useful to study the structure of the interstellar medium, and thus, useful for future research prospects. In addition, we provided evidence strongly favouring an interstellar origin for the features in HD 145689 and eta Tel, which were reported as circumstellar in the literature.

Chapter 7

Summary and Conclusions

We have studied a database of 301 debris disks with the aim of determining how frequent the presence of gas is. By construction, this database is unbiased with respect to disk inclination and contains only main sequence stars, ranging in spectral types from B to M. Most of them are field stars and the majority of them are located within 200 pc. Given the considerable size of the sample, we considered the most efficient way of assessing the presence of gas for hundreds of objects was via high-resolution optical spectroscopy. This method has the advantage of allowing us to obtain spectra for dozens of objects per night and even perform monitoring observations, it is sensitive enough to detect small traces of gas, but has the limitation of being able to detect gas only when it crosses the line of sight of the star. In addition, since many of our targets have been searched for planets via radial velocity monitoring, there are plenty of available data in the observatories archives that can be recycled for our science case.

During the course of this Thesis, we gathered spectra from our own observations, from the ESO archive and from data shared among collaborators. As detailed in Chapter 2, we were able to collect high resolution optical spectra for 273 objects in our sample, missing mainly the northern targets. The total amount of spectra collected and analyzed during this Thesis is close to ∼17500 spectra. We were awarded a total of 11 observing proposals concerning the research of this Thesis with Iglesias as a principal investigator, plus two additional proposals in line with her future projects (described in the next Chapter).

Our study mainly focused in the analysis of the Ca II K line at 3933.7Å, since it is the most sensitive gas tracer in the near-UV/optical range, but it also included the analysis of other sensitive tracers such as the Ca II H line at 3968.5Å , the Na I D1 and D2 lines at 5895.9Å and 5889.9Å, the Ca II triplet at ∼8.550Å, several Fe II and Ti II lines, and other important spectral lines such as the Balmer lines, to name some of them.

At the beginning of this Thesis, in 2015, gas had been detected in about 18 debris disks, 15 of them detected with the same method we used. During the course of this research, ∼26 new gaseous debris disks have been detected, 16 of them via absorption spectroscopy, increasing the total number to 44 according to our records (with an overlap with some of those detected in emission, as discussed in Section 1.2). These numbers must be taken with caution though, as they come from a compilation of the reports of circumstellar gas detections in the literature, but during this research we have demonstrated that some of these detections might be dubious. Nevertheless, the evidence shows that these detections are increasing exponentially and will likely keep increasing in the future along with the variety of species detected since the sensitivity of the instruments is always improving. Throughout the course of this Thesis, we detected a total of six gaseous debris disks, two of them with no previous reports of gas detections in the literature.

In Chapter 3, our preliminary analysis of the sub-sample of objects with multiple absorption features with the data gathered during the first ∼three years of research, already showed evidence of gas in debris disks being a common phenomenon (Iglesias et al., 2018). We detected the presence of circumstellar gas in three out of 27 objects, two presenting variable absorptions and one presenting a stable circumstellar component. Considering that only ∼10% of the disks (assuming a uniform distribution of inclinations) would be near edge-on, these numbers would imply a high detection rate. One has to keep in mind, however, that the most plausible cause of the variable detections are exocomets that could follow orbits that are non-coplanar with the main planetesimal belt, and therefore those disks "would not need to be edge on" for their exocomets to be detected.

In Chapter 4 we analyzed in detail the very exceptional detection of circumstellar gas in the object HD 37306 (HR 1919). We detected for the first time an unusually large absorption observed in several ionized lines such as Ca II, Fe II and Ti II. This phenomenon lasted for at least eight days, being exceptionally long compared to previous detections. Given its peculiarity, we analyzed many different possibilities that might have explained this phenomenon and we determined that the most plausible explanation would be a massive exocometary break-up producing a long stream of gas that remained in orbit around the star for several days (Iglesias et al., 2019). We are yet unable to determine the frequency of this kind of events and neither are able to confirm it at the moment. This is, to the best of our knowledge, the first one detected via absorption spectroscopy, perhaps comparable to the case of the Tabby star detected in photometry (Boyajian et al., 2016). We obtained time with ALMA to perform follow-up observations of this object to try to detect traces of residual gas that may have remained in the disk as a product of the possible exocometary break-up, and we aim to obtain monitoring spectroscopic observations in the future, hoping to spot another event.

The research presented in Chapter 5 was devoted to the study of variability in the spectral lines of our sample of debris disks with the aim to find signs of exocometary activity. We found 97 objects presenting some variability in their Ca II K line. We classified the different kinds of variability observed and selected those consistent with exocometary activity. We found five candidates presenting variable absorption features likely attributable to exocomets sublimating across the line of sight of the star. Considering:

- the challenge of detecting these kind of events in later spectral types given their narrow spectral lines and chromospheric activity
- that the observations have a scattered temporal sampling and in many cases they are too few to confirm a reliable detection of exocomets
- and of course, the bias of the detections being limited to a small range of inclinations with respect to the observer where the exocomets must cross the line of sight of the star to be detectable via absorption spectroscopy

then these results are in agreement with our preliminary results of exocomets being a common phenomenon among debris disks.

Finally, in Chapter 6 we studied all the objects with stable single absorption features not included in Chapter 3 and additional objects with multiple absorption features found within our updated database of observations. We found 107 objects presenting stable absorption features in addition to those 27 already analyzed in Chapter 3. We confirmed a likely interstellar origin for the features observed in the Ca II K line of 104 objects, one of them being (that of 49 Cet) a blend of both interstellar and circumstellar gas. Three objects remain as candidates for circumstellar gas and we will obtain the needed data to be able to confirm the origin of their absorptions.

Gathering together our results, we found five objects with variable absorption features likely attributable to exocometary activity: c Aql, HR 4796, HD 37306, 49 Cet and gam Tri, and one object with a stable component at the radial velocity of the star likely due to the presence of circumstellar gas in the disk: HD 110058, besides other three candidates yet to be confirmed. Regarding the case of 49 Cet, we include it in the variable group rather than in the stable group since we are not able to quantify what fraction of its stable absorption feature is of circumstellar origin given that it is blended with an interstellar absorption. All of these debris disks are surrounding A-type stars, ranging from A0 to A2. This follows the trend of the majority of the gas detections being in A-type stars (see Section 1.2). Their ages range between $\sim$10 and $\sim$450 Myr. Similarly to the general demographics of gas detections shown in Table 1.1, there is no strong correlation with age. This is in agreement with the results found by Rebollido et al. (2020), the authors found exocometary activity in debris disks with a wide range of ages. Out of these six debris disks, five of them have been spatially resolved or at least partially resolved. c Aql was partially resolved in Herschel observations and Morales et al. (2016) reported an inclination of $21^\circ \pm 42^\circ$. HR 4796 was spatially resolved by Schneider et al. (1999) among others, estimating an inclination of $73.1^\circ \pm 1.2^\circ$, which is close to more recent estimations of $\sim 76^\circ$ (e.g. Wahhaj et al. 2014, Milli et al. 2017, Kennedy et al. 2018). 49 Cet too has been spatially resolved, with an inclination of the disk estimated to be of $80.6^\circ \pm 0.4^\circ$ by Hughes et al. (2017), in agreement with Moór et al. (2015). gam Tri's inclination of the disk was estimated to be $\sim 89^\circ$ by Booth et al. (2013) who spatially resolved the disk, and although they did not obtain an accurate estimate for the inclination they show the disk is likely edge-on. Finally, the debris disc around HD 110058 has been resolved by Kasper et al. (2015), who determined an inclination for the disk of $\sim 90^\circ$. The disk around HD 37306 has not been spatially resolved yet.

With the exception of c Aql, which disk has only been marginally resolved and thus there is a large uncertainty in the estimation of its inclination, there is a clear correlation between the detection of gas and the inclination of the disk being near edge-on, which was expected, and is in agreement with the study by Rebollido et al. (2020). Now, if we compare variable versus stable gas detections, although we only have one stable case, we see that in the stable case the disk is exactly edge-on, whereas in the variable cases they are near edge-on. The case of β Pic, not part of our sample but the most studied gaseous debris disk, which happen to have both a stable component and variable absorption features, also has an edge-on inclination of $\sim 90^{\circ}$ (Dent et al. 2014, Kiefer et al. 2014b). This is also in agreement with what we expected since, in the case of the stable detection, we are detecting gas that is likely co-located with the dust disk (Wyatt et al. 2015, Marino et al. 2020) and therefore its detection in absorption is the most favourable when the disk is crossing the line of sight of the star. Regarding the variable cases, these are attributable to the transit of exocomets or collisions of icy bodies and thus their inclinations may differ to that of the disk allowing their detection even when the disk may not cross directly the line of sight of the star. Since exocomets are not yet directly observable with the current observing instrumentation, we cannot really give values for the typical inclinations of exocomets' orbits in debris disks, but if we compare with the Solar System, misalignments in cometary orbits with respect to the system are very common (Nesvorný et al., 2017) and we assume these misalignments may also be common in debris disks.

Regarding other objects in our sample that have known inclinations, 70 of them have been spatially resolved and if we consider those with inclinations $> 70^{\circ}$ as near edge-on, then there are 37 debris disks in our sample with known near edge-on inclinations. If we consider other gas detections via absorption spectroscopy reported in the literature among this group of 37 debris disks with known near edge-on inclinations, there are only two additional objects: eta Tel (Welsh and Montgomery 2018, Rebollido et al. 2018, Smith et al. 2009) and rho Vir (Welsh and Montgomery 2018, Morales et al. 2016) besides our four edge-on gaseous debris disks (HR 4796, HD 110058, 49 Cet and gam Tri). Regarding other detections of circumstellar gas absorptions in debris disks within our sample reported in the literature, none of them have been resolved, thus their inclinations are yet unknown.

Now, why we did not detect gas in all these near edge-on disks? The reasons could be many. For instance, some of them are later spectral types (e.g. AU Mic; Schneider et al. 2014, 61 Vir; Greaves et al. 2014) making the detection challenging, as discussed in Sec. 1.2. Some of them are variable stars, as the case of gam Dor, the canonical case of γ Doradus variable stars (Broekhoven-Fiene et al. 2013, Kaye et al. 1999) which spectral lines display pulsation modes, making it difficult to disentangle from exocometary activity, as discussed in Chapter 5 (see Fig. 5.4, left panel). But most importantly, variable gas absorptions due to exocomets are serendipitous detections, exocometary transits are sporadical events and regular monitoring would be necessary in order to improve our chances of detections. Our observations, however, are scattered in frequency, ranging from seconds to years of temporal separation, and in most cases, unfortunately too scarce to reliably conclude that the variations are likely due exocometary activity. Regarding the detection of stable gas components, given the abundance of interstellar clouds in the line of sight of the stars, often matching with the radial velocity of the star, a stable circumstellar gas feature might be completely blended with another of interstellar origin, limiting our possibilities to detect it.

Taking into account all the detection challenges, observational limitations and serendipitous nature of variable gas detections, we speculate that the presence of gas in debris disk is a common phenomenon. Evidence has shown that the number of detections of gaseous debris disks has rapidly increased in the last few years, and if we consider that today the idea that most stars probably have planets has been accepted given their increasing detection rate (e.g. Borucki, Bonavita and Desidera 2020), the idea that probably most debris disks have some gas, contrary of what has been assumed for years, makes sense.

The paradigm-changing idea that maybe most debris disks have moderate amounts of gas has deep implications on planet forming processes, as discussed in Section 1.2. For instance, it can affect the dynamics of the system inducing planet migration (Wyatt 2008, Morbidelli 2018) or cause the formation of a secondary atmosphere on rocky planets (Kral et al., 2020). It can also serve as a possible explanation for the formation of gaps in some debris disks and the observed overheated dust temperatures in some disks (Lyra and Kuchner 2013, Wyatt et al. 2018). Therefore, from now on, planet formation studies may need to take into account the impact of the presence of gas during the debris disks stage and, in particular, how exocometary activity in the inner region of the disk may affect the evolution of terrestrial planets.

Chapter 8

Future Prospects

Motivated by my great interest in exoplanets and the idea of exploiting archival data, besides my experience working with high-resolution spectroscopy, I developed a future project where I could combine all that. I found a paper by Johnson et al. (2015) that inspired me for this project. Johnson et al. (2015) studied the ISM in the Kepler search volume by analysing absorptions toward 17 early-type stars. From these absorptions, they identified 11 interstellar clouds within the Kepler field and estimated astrosphere sizes for 11 systems with confirmed exoplanets that could lie within these clouds.

8.1 Main idea of the project

My main research goal as a postdoctoral investigator in the future would be to assess the habitability of planetary systems by studying the properties of their surrounding interstellar medium (ISM). For this purpose, I would estimate astrosphere sizes of planetary systems by constraining the surrounding interstellar clouds sizes, compositions and densities. Astrospheres are cavities carved out by the stellar wind in the surrounding ISM and their characterization can result crucial to assess exoplanetary habitability since they act as a shield against cosmic rays. So far, planetary habitability has been studied focusing mainly on temperature; the habitable zone has been defined as the region where liquid water can exist. Of course, the question of what makes a planet habitable is much more complex than having a planet located at the right distance from its host star so that water can be liquid: various geophysical and geodynamical aspects, the radiation, magnetic fields, and the host star's plasma environment can influence the evolution of planets and life. Liquid water is a necessary but not sufficient condition for life as we know it, as habitability is a function of a multitude of environmental parameters. With this project, I would add a new habitability criterion which has not been frequently taken into consideration: cosmic rays flux, and I would study a very under-exploited topic: astrospheres. This project would be the largest statistical study of planetary systems' astrospheres and aims to provide the best "habitable" candidates to look for life signatures, the best candidates for direct astrosphere detection, and to determine the surrounding ISM conditions in which these planetary systems formed, which could be linked to the planet and its atmosphere composition.

8.2 Observational aspects of the project

The ISM can be studied by analysing absorption lines that are most easily detected in the spectra of early-type stars, as they have few photospheric absorption lines which are typically rotationally broadened. ISM absorptions are very narrow, with FWHM in the order of 0.01-0.1Å. The more distant the star, the more interstellar clouds are likely to be detected in the stellar spectrum. These clouds can have similar radial velocities, thus usually their absorptions can be separated by only a few km.s^{-1}. In order to be able to detect and resolve these different absorption features, it is necessary to use high-resolution spectrographs, with at least R>10'000.

Most atoms and molecules found in the ISM (elements such as C, N, O, Mg, Si, S, and Fe) produce absorption lines at ultraviolet (UV) wavelengths Savage and Sembach (1996). Their detection through spectroscopy requires instrumentation above the Earth's atmosphere. Many interstellar studies have been performed with the Space Telescope Imaging Spectrograph (STIS) and the Goddard High- Resolution Spectrograph (GHRS), both aboard the Hubble Space Telescope (HST), and the International Ultraviolet Explorer (IUE) satellite, and the data from these missions are publicly available. The ISM can also be studied from the ground at UV-optical wavelengths. The main elements detectable in the optical are Ca II, K I, Ti II and Na I, besides certain Diffuse Interstellar Bands (DIBs), which are caused by largely unidentified molecules. A large amount of science-ready UV-optical high-resolution spectra of early-type stars (from instruments such as HARPS, UVES and FEROS) is available in the ESO archive and can be used to study the ISM. Ground-based observations have the significant advantage of providing easier access to further observations. Indeed, I have been awarded two proposals (with UVES and MIKE spectrographs) to obtain observations that will further complete the needed database for this project. I already obtained 69 targets during my observing run with MIKE and other 65 targets were observed with UVES. However, considering that the optical line of Ca II is not the primary ionisation state and both Na I and Ca II can be heavily depleted onto dust, the UV lines visible only from space can add significant additional information on the ISM conditions, thus both ground-based and space-based observations will complement this study.

8.3 Effects of the ISM on planetary systems and their habitability

Stellar winds carve out a cavity in the surrounding ISM known as the astrosphere, the stellar analogue to the heliosphere (see Fig. 8.1). Planetary surfaces can be protected from cosmic rays by three major shields: the magnetic field carried by the stellar wind within the astrosphere, the planetary magnetic field and the planetary atmosphere. Astrospheres are not spherical, they have a cometary shape given by the stars motion through the ISM, and their sizes are determined by a momentum balance between the outgoing stellar wind and the streaming ISM (Johnson et al., 2015). The higher the ISM density or the higher the velocity of the star relative to the ISM, the smaller the astrosphere size, and thus, the less effective it is as a shield against cosmic rays. The cosmic ray flux can have several effects on the climate and habitability of planets. Lightning may be affected by cosmic rays inducing atmospheric ionization, increasing the production of NO_x compounds which affect the formation of ozone. Cosmic rays may also induce cloud nucleation, which would change the planets albedo and thus its surface temperature. For life-bearing planets, cosmic rays could also produce radiation damage and increase mutation rates (Scherer et al., 2006). Interstellar dust can also affect the climate of planets. If sufficient amounts of dust are swept up into a planetary atmosphere, it can cause a "reverse greenhouse" effect, radiating efficiently in the infrared and cooling the planet (Pavlov et al., 2005). The most extreme events occur inside dense interstellar clouds, where the increased pressure may compress an astrosphere to a size smaller than the liquid-water habitable-zone distance. Habitable planets

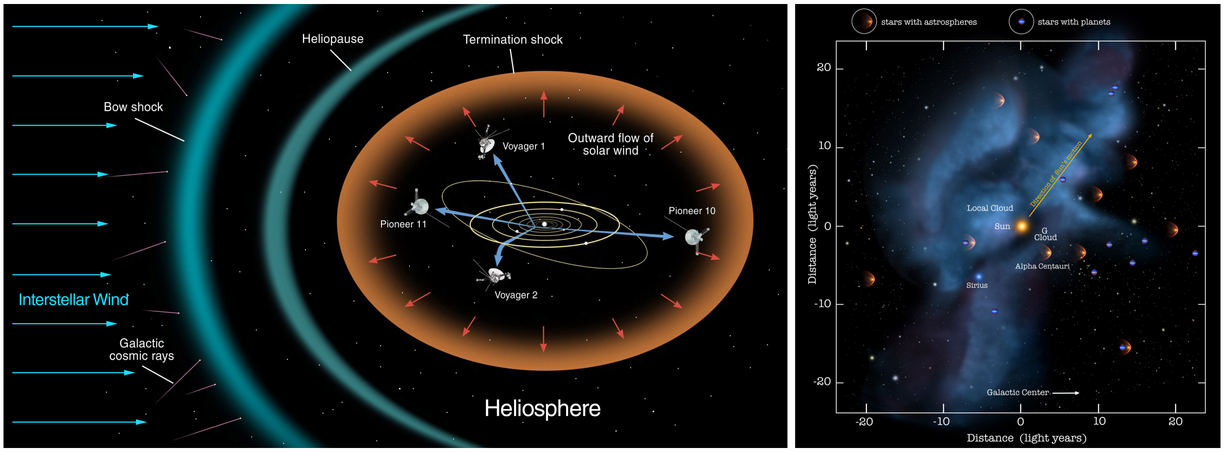

Figure 8.1: An astrosphere is analogous to the Sun's heliosphere, and marks the interface between the outward flow of the stellar wind and the inward pressure of the surrounding ISM. Knowledge of the LISM environment around a star is essential for a complete understanding of its astrosphere. They provide a protective shielding of dangerous galactic cosmic rays, thus these structures are important for the planets that orbit the respective stars. **Left:** A diagram of the Sun's heliosphere. The outermost edge of the heliosphere is the heliopause. Credit: www.jcgonzalez.org/ (edited). **Right:** Graphic of the most immediate environment around the Sun. The locations of known astrospheres and exoplanets are indicated. The Sun is located within the Local Cloud, very close to the G cloud. Credit: NASA/Goddard/Adler/U. Chicago/Wesleyan

then enjoy no astrospheric buffering from exposure to the full flux of galactic cosmic rays and interstellar dust and gas, a situation called "descreening" or "astrospheric collapse". Under such conditions the ionization fraction in the atmosphere and contribution to radiation damage of putative coding organisms at the surface would increase significantly (Smith and Scalo, 2009). Therefore, the goal of my project is to find the best suitable systems to look for life signatures based on their astrosphere sizes and properties of the surrounding ISM and, as a by-product, the candidates for direct astrosphere detection. Astrospheres can be detected by the spectral signature of its "hydrogen wall" (Edelman et al., 2019). The astrospheric absorption can be derived from fitting the (often saturated) HI Lyα profile. A prerequisite for astrospheric Lyα emission or absorption to be detectable is that the star must be surrounded by ISM that is at least partially neutral and with a high streaming velocity so the astrosphere is compact (Wood et al., 2003).

8.4 Feasibility of the project

In order to test the feasibility of this project, from the total of 4'084[1] confirmed planets to date, I have selected the ones located within the Local ISM (LISM) (i.e. within 100 pc): a total of 546 systems and 784 planets. The LISM, is the closest and simplest sample of interstellar gas to study, with the significant advantage of having a small number of traversing clouds (and therefore, a small number of absorptions) to evaluate interstellar structures (Redfield and Linsky, 2015). Considering that the size of our local interstellar cloud (LIC) is roughly 10 pc across, a cloud of a similar size located at 100 pc would cover an area of approximately 5° of width (and larger angular areas for closer distances). With this in mind, I performed a cone search around each planetary system looking for the available spectra of early-type stars in the ESO, IUE, STIS and GHRS archives within a radius of 5°, as shown in Fig. 8.2, to have an idea of the amount of data available that could be useful for this project. The idea is to analyse several lines of sight surrounding a planetary system and identify those absorptions belonging to the same cloud to estimate if the system lies within such a cloud. I will identify LISM clouds based on the radial velocity of the absorptions and use the same assumptions as other works mapping the ISM; the clouds move approximately as solid bodies and the upper limit to the distance of each cloud from the Sun is the distance to the nearest star having a component with a velocity consistent with such a cloud. For this work, it is important to use reliable distance measurements to have good estimates on the proximity of a cloud to a planetary system, and to have good measurements of radial velocities and proper motions in order to estimate the relative velocities between the planetary systems and the clouds. Gaia provides parallaxes and proper motions of unprecedented precision, thus I will rely on these measurements, and I will either use radial velocity measurements from the literature (which are likely available for planetary systems) or estimate them myself. For the clouds, I will fit Voigt profiles to the ISM absorptions to estimate their radial velocity and other parameters such as equivalent width, column density and Doppler broadening parameter (b-value).

The "astrosphere size" refers to the distance from the star to the astropause (analogue to the heliopause), the contact interface between the stellar wind and the ISM. The size of an

[1]`https://exoplanetarchive.ipac.caltech.edu/index.html`

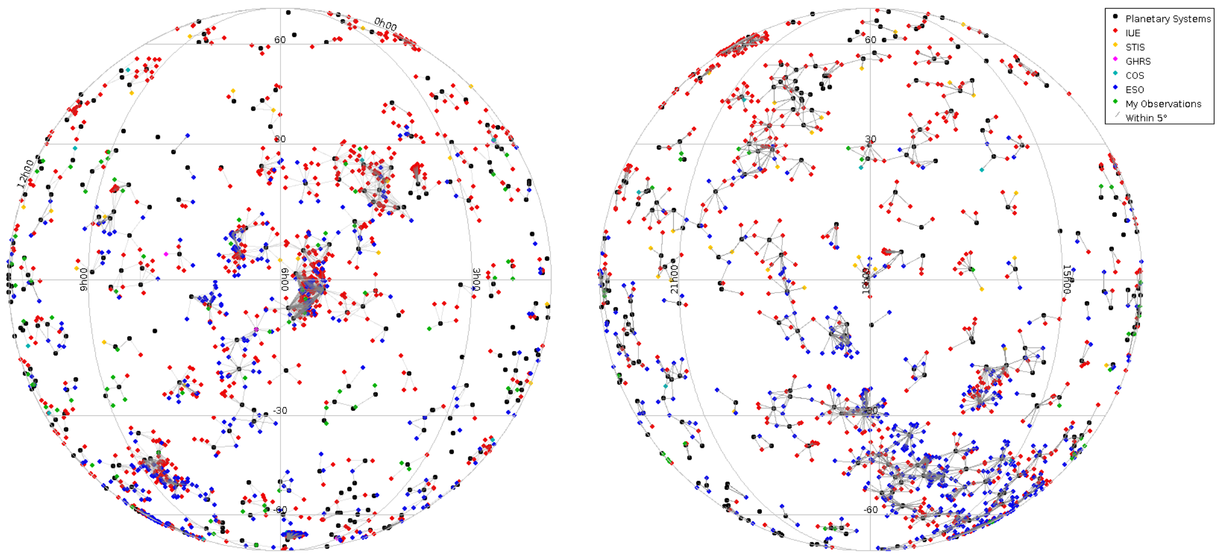

Figure 8.2: Equatorial view of the available data coordinates. Coordinates of the selected planetary systems within 100 pc in black circles and available spectra of early-type stars from ESO, my observations, IUE, STIS, GHRS and COS in blue, green, red, yellow, pink and cyan diamonds, respectively. Grey lines connect each system with the available data within an angular separation of 5°. 526 systems out of 546 (i.e. 96% of the systems) have at least one data within this angular separation that could be useful for this project. **Left:** View of RA between 00h and 12h. **Right:** View of RA between 12h and 24h.

astrosphere is given as a function of the surrounding ISM density, ISM streaming velocity, and the outflowing stellar wind density and velocity. To estimate the stellar wind parameters I will follow the assumptions by Smith and Scalo (2009). They assume that the wind within astrospheres of stars of different spectral types is analogue to the solar wind. The wind speed is assumed to be independent of distance from the star, but the wind density and velocity depend on stellar mass and age.

The main difference of this project with previous work is that they map the ISM at a large scale using somewhat low spatial sampling and my project will focus on smaller areas surrounding planetary systems using a denser sampling to be able to obtain well constrained astrospheres limits. I have taken into consideration that I would need several lines of sights around each system to be able to constrain its surroundings; if the same cloud is detected in different stars surrounding the system, that would indicate that the system is likely embedded within that cloud, thus I could estimate its astrosphere size based on the cloud (and stellar) parameters. Therefore, I would also use estimates from previous works mapping the ISM to complement the available data (such as Lallement et al. 2003, 2014 and 2019, Smoker et al. 2011 and 2015, Redfield and

Linsky 2008 and 2015, Welsh et al. 2010, Murga et al. 2015, Hunter et al. 2006, Edelman et al. 2019, Savage and Sembach 1996) and crossmatch them with Gaia distances to obtain improved constrains. With all the available data, catalogs, and my own observations, I estimate it would be possible to constrain the astrosphere sizes for a statistically significant sample of planetary systems and thus, add a new factor to consider when analyzing the habitability of exoplanets.

Given the growing number of known exoplanets in the solar vicinity, assessing their local ISM characteristics and understanding the structure of their astrospheres will be important in evaluating how the incident cosmic ray flux and the strength of the winds of the host star affect habitability and long-term planetary atmosphere evolution.

Bibliography

(1997). *The HIPPARCOS and TYCHO catalogues. Astrometric and photometric star catalogues derived from the ESA HIPPARCOS Space Astrometry Mission*, volume 1200.

Abt, H. A. (2008). New Data on A-Type Disk Stars. , 174(2):499–503.

Abt, H. A. (2015). Hot Gaseous Stellar Disks Avoid Regions of Low Interstellar Densities. , 127(958):1218.

Abt, H. A. and Moyd, K. I. (1973). Rotation and shell spectra among A-type dwarfs. , 182:809.

Abt, H. A., Tan, H., and Zhou, H. (1997). Hot Inner Disks that Appear and Disappear Around Rapidly Rotating A-Type Dwarfs. , 487(1):365–369.

Alexander, R. D. and Armitage, P. J. (2007). Dust dynamics during protoplanetary disc clearing. , 375(2):500–512.

Alexander, R. D., Clarke, C. J., and Pringle, J. E. (2006). Photoevaporation of protoplanetary discs - I. Hydrodynamic models. , 369:216–228.

Andrews, J. J., Chanamé, J., and Agüeros, M. A. (2017). Wide binaries in Tycho-Gaia: search method and the distribution of orbital separations. , 472(1):675–699.

Apai, D., Schneider, G., Grady, C. A., Wyatt, M. C., Lagrange, A.-M., Kuchner, M. J., Stark, C. J., and Lubow, S. H. (2015). The Inner Disk Structure, Disk-Planet Interactions, and Temporal Evolution in the β Pictoris System: A Two-epoch HST/STIS Coronagraphic Study. , 800(2):136.

Aumann, H. H., Gillett, F. C., Beichman, C. A., de Jong, T., Houck, J. R., Low, F. J., Neugebauer, G., Walker, R. G., and Wesselius, P. R. (1984). Discovery of a shell around alpha Lyrae. , 278:L23–L27.

Ballering, N. P., Rieke, G. H., Su, K. Y. L., and Montiel, E. (2013). A Trend between Cold Debris Disk Temperature and Stellar Type: Implications for the Formation and Evolution of Wide-orbit Planets. , 775:55.

Baraffe, I., Chabrier, G., Allard, F., and Hauschildt, P. H. (1998). Evolutionary models for solar metallicity low-mass stars: mass-magnitude relationships and color-magnitude diagrams. , 337:403–412.

Barnes, S. I., Tobin, W., and Pollard, K. R. (2000). The Variable Ca II Absorption in β Pictoris during 1998. , 17:241–243.

Barucci, M. A., Brown, M. E., Emery, J. P., and Merlin, F. (2008). *Composition and Surface Properties of Transneptunian Objects and Centaurs*, page 143.

Baruteau, C. and Masset, F. (2008). Type I Planetary Migration in a Self-Gravitating Disk. , 678:483–497.

Bayo, A., Rodrigo, C., Barrado Y Navascués, D., Solano, E., Gutiérrez, R., Morales-Calderón, M., and Allard, F. (2008). VOSA: virtual observatory SED analyzer. An application to the Collinder 69 open cluster. , 492:277–287.

Bell, C. P. M., Mamajek, E. E., and Naylor, T. (2015). A self-consistent, absolute isochronal age scale for young moving groups in the solar neighbourhood. , 454(1):593–614.

Bernstein, R., Shectman, S. A., Gunnels, S. M., Mochnacki, S., and Athey, A. E. (2003). MIKE: A Double Echelle Spectrograph for the Magellan Telescopes at Las Campanas Observatory. In Iye, M. and Moorwood, A. F. M., editors, *Instrument Design and Performance for Optical/Infrared Ground-based Telescopes*, volume 4841 of , pages 1694–1704.

Bertin, P., Lallement, R., Ferlet, R., and Vidal-Madjar, A. (1993). The NA I/Ca II ratio in the local interstellar medium. , 278:549–560.

Beust, H., Augereau, J. C., Bonsor, A., Graham, J. R., Kalas, P., Lebreton, J., Lagrange, A. M., Ertel, S., Faramaz, V., and Thébault, P. (2014). An independent determination of Fomalhaut b's orbit and the dynamical effects on the outer dust belt. , 561:A43.

Beust, H., Karmann, C., and Lagrange, A.-M. (2001). Falling Evaporating Bodies around Herbig stars. A theoretical study. , 366:945–964.

Beust, H., Lagrange, A.-M., Crawford, I. A., Goudard, C., Spyromilio, J., and Vidal-Madjar, A. (1998). The beta Pictoris circumstellar disk. XXV. The Ca Ii absorption lines and the Falling Evaporating Bodies model revisited using UHRF observations. , 338:1015–1030.

Beust, H., Madjar, A. V., Lagrange-Henri, A. M., and Ferlet, R. (1991). The beta Pictoris circumstellar disk. XI. New CA II absorption features reproduced numerically. , 241:488.

Beust, H. and Morbidelli, A. (2000). Falling Evaporating Bodies as a Clue to Outline the Structure of the β Pictoris Young Planetary System. , 143(1):170–188.

Beust, H. and Tagger, M. (1993). A Hydrodynamical Model for Infalling Evaporating Bodies in the β Pictoris Circumstellar Disk. , 106(1):42–58.

Beuzit, J. L., Vigan, A., Mouillet, D., Dohlen, K., Gratton, R., Boccaletti, A., Sauvage, J. F., Schmid, H. M., Langlois, M., Petit, C., Baruffolo, A., Feldt, M., Milli, J., Wahhaj, Z., Abe, L., Anselmi, U., Antichi, J., Barette, R., Baudrand, J., Baudoz, P., Bazzon, A., Bernardi, P., Blanchard, P., Brast, R., Bruno, P., Buey, T., Carbillet, M., Carle, M., Cascone, E., Chapron, F., Chauvin, G., Charton, J., Claudi, R., Costille, A., De Caprio, V., Delboulbé, A., Desidera, S., Dominik, C., Downing, M., Dupuis, O., Fabron, C., Fantinel, D., Farisato, G., Feautrier, P., Fedrigo, E., Fusco, T., Gigan, P., Ginski, C., Girard, J., Giro, E., Gisler, D., Gluck, L., Gry, C., Henning, T., Hubin, N., Hugot, E., Incorvaia, S., Jaquet, M., Kasper, M., Lagadec, E., Lagrange, A. M., Le Coroller, H., Le Mignant, D., Le Ruyet, B., Lessio, G., Lizon, J. L., Llored, M., Lundin, L., Madec, F., Magnard, Y., Marteaud, M., Martinez, P., Maurel, D., Ménard, F., Mesa, D., Möller-Nilsson, O., Moulin, T., Moutou, C., Origné, A., Parisot, J., Pavlov, A., Perret, D., Pragt, J., Puget, P., Rabou, P., Ramos, J., Reess, J. M., Rigal, F., Rochat, S., Roelfsema, R., Rousset, G., Roux, A., Saisse, M., Salasnich, B., Santambrogio, E., Scuderi, S., Segransan, D., Sevin, A., Siebenmorgen, R., Soenke, C., Stadler, E., Suarez, M., Tiphène, D., Turatto, M., Udry, S., Vakili, F., Waters, L. B. F. M., Weber, L., Wildi, F., Zins, G., and Zurlo, A. (2019). SPHERE: the exoplanet imager for the Very Large Telescope. *arXiv e-prints*, page arXiv:1902.04080.

Boccaletti, A., Sezestre, E., Lagrange, A. M., Thébault, P., Gratton, R., Langlois, M., Thalmann, C., Janson, M., Delorme, P., Augereau, J. C., Schneider, G., Milli, J., Grady, C., Debes, J., Kral, Q., Olofsson, J., Carson, J., Maire, A. L., Henning, T., Wisniewski, J., Schlieder, J., Dominik, C., Desidera, S., Ginski, C., Hines, D., Ménard, F., Mouillet, D., Pawellek, N., Vigan, A., Lagadec, E., Avenhaus, H., Beuzit, J. L., Biller, B., Bonavita, M., Bonnefoy, M., Brandner, W., Cantalloube, F., Chauvin, G., Cheetham, A., Cudel, M., Gry, C., Daemgen, S., Feldt, M., Galicher, R., Girard, J., Hagelberg, J., Janin-Potiron, P., Kasper, M., Le Coroller, H., Mesa, D., Peretti, S., Perrot, C., Samland, M., Sissa, E., Wildi, F., Zurlo, A., Rochat, S., Stadler, E., Gluck, L., Origné, A., Llored, M., Baudoz, P., Rousset, G., Martinez, P., and Rigal, F. (2018). Observations of fast-moving features in the debris disk of AU Mic on a three-year timescale: Confirmation and new discoveries. , 614:A52.

Bohlin, R. C., Savage, B. D., and Drake, J. F. (1978). A survey of interstellar H I from L-alpha absorption measurements. II. , 224:132–142.

Bonavita, M. and Desidera, S. (2020). Frequency of Planets in Binaries. *Galaxies*, 8(1):16.

Booth, M., Kennedy, G., Sibthorpe, B., Matthews, B. C., Wyatt, M. C., Duchêne, G., Kavelaars, J. J., Rodriguez, D., Greaves, J. S., Koning, A., Vican, L., Rieke, G. H., Su, K. Y. L., Moro-Martín, A., and Kalas, P. (2013). Resolved debris discs around A stars in the Herschel DEBRIS survey. , 428(2):1263–1280.

Booth, M., Matrà, L., Su, K. Y. L., Kral, Q., Hales, A. S., Dent, W. R. F., Hughes, A. M., MacGregor, M. A., Löhne, T., and Wilner, D. J. (2019). Deep ALMA search for CO gas in the HD 95086 debris disc. , 482(3):3443–3452.

Borucki, W. J. (2016). KEPLER Mission: development and overview. *Reports on Progress in Physics*, 79(3):036901.

Bouvier, A. and Wadhwa, M. (2010). The age of the Solar System redefined by the oldest Pb-Pb age of a meteoritic inclusion. *Nature Geoscience*, 3(9):637–641.

Boyajian, T. S., LaCourse, D. M., Rappaport, S. A., Fabrycky, D., Fischer, D. A., Gandolfi, D., Kennedy, G. M., Korhonen, H., Liu, M. C., and Moor, A. (2016). Planet Hunters IX. KIC 8462852 - where's the flux? , 457(4):3988–4004.

Brahm, R., Jordán, A., and Espinoza, N. (2017). CERES: A Set of Automated Routines for Echelle Spectra. , 129(973):034002.

Brandeker, A., Cataldi, G., Olofsson, G., Vand enbussche, B., Acke, B., Barlow, M. J., Blommaert, J. A. D. L., Cohen, M., Dent, W. R. F., Dominik, C., Di Francesco, J., Fridlund, M., Gear, W. K., Glauser, A. M., Greaves, J. S., Harvey, P. M., Heras, A. M., Hogerheijde, M. R., Holland , W. S., Huygen, R., Ivison, R. J., Leeks, S. J., Lim, T. L., Liseau, R., Matthews, B. C., Pantin, E., Pilbratt, G. L., Royer, P., Sibthorpe, B., Waelkens, C., and Walker, H. J. (2016). Herschel detects oxygen in the β Pictoris debris disk. , 591:A27.

Brandeker, A., Liseau, R., Olofsson, G., and Fridlund, M. (2004). The spatial structure of the β Pictoris gas disk. , 413:681–691.

Breger, M., Stich, J., Garrido, R., Martin, B., Jiang, S. Y., Li, Z. P., Hube, D. P., Ostermann, W., Paparo, M., and Scheck, M. (1993). Nonradial pulsation of the delta Scuti star BU CANCRI in the Praesepe cluster. , 271:482–486.

Broekhoven-Fiene, H., Matthews, B. C., Kennedy, G. M., Booth, M., Sibthorpe, B., Lawler, S. M., Kavelaars, J. J., Wyatt, M. C., Qi, C., Koning, A., Su, K. Y. L., Rieke, G. H., Wilner, D. J., and Greaves, J. S. (2013). The Debris Disk around γ Doradus Resolved with Herschel. , 762(1):52.

Brown, A. G. A., de Geus, E. J., and de Zeeuw, P. T. (1994). The Orion OB1 association. 1: Stellar content. , 289:101–120.

Cannon, A. J. and Pickering, E. C. (1918). The Henry Draper catalogue 0h, 1h, 2h, and 3h. *Annals of Harvard College Observatory*, 91:1–290.

Canovas, H., Montesinos, B., Schreiber, M. R., Cieza, L. A., Eiroa, C., Meeus, G., de Boer, J., Ménard, F., Wahhaj, Z., Riviere-Marichalar, P., Olofsson, J., Garufi, A., Rebollido, I., van Holstein, R. G., Caceres, C., Hardy, A., and Villaver, E. (2017). DZ Cha: a bona fide photoevaporating disc. *ArXiv e-prints*.

Carmona, A., van der Plas, G., van den Ancker, M. E., Audard, M., Waters, L. B. F. M., Fedele, D., Acke, B., and Pantin, E. (2011). A survey for near-infrared H_2 emission in Herbig Ae/Be stars: emission from the outer disks of HD 97048 and HD 100546. , 533:A39.

Carpenter, J. M., Ricci, L., and Isella, A. (2014). An ALMA Continuum Survey of Circumstellar Disks in the Upper Scorpius OB Association. , 787(1):42.

Castelli, F., Gratton, R. G., and Kurucz, R. L. (1997). Notes on the convection in the ATLAS9 model atmospheres. , 318:841–869.

Cataldi, G., Brandeker, A., Olofsson, G., Chen, C. H., Dent, W. R. F., Kamp, I., Roberge, A., and Vand enbussche, B. (2015). Constraints on the gas content of the Fomalhaut debris belt. Can gas-dust interactions explain the belt's morphology? , 574:L1.

Cataldi, G., Wu, Y., Brandeker, A., Ohashi, N., Moór, A., Olofsson, G., Ábrahám, P., Asensio-Torres, R., Cavallius, M., Dent, W. R. F., Grady, C., Henning, T., Higuchi, A. E., Hughes, A. M., Janson, M., Kamp, I., Kóspál, Á., Redfield, S., Roberge, A., Weinberger, A., and Welsh, B. (2020). The Surprisingly Low Carbon Mass in the Debris Disk around HD 32297. , 892(2):99.

Chen, C. H. and Jura, M. (2003). The Low-Velocity Wind from the Circumstellar Matter around the B9 V Star σ Herculis. , 582:443–448.

Claudi, R. U., Turatto, M., Gratton, R. G., Antichi, J., Bonavita, M., Bruno, P., Cascone, E., De Caprio, V., Desidera, S., Giro, E., Mesa, D., Scuderi, S., Dohlen, K., Beuzit, J. L., and Puget, P. (2008). SPHERE IFS: the spectro differential imager of the VLT for exoplanets search. In , volume 7014 of *Society of Photo-Optical Instrumentation Engineers (SPIE) Conference Series*, page 70143E.

Cleeves, L. I., Öberg, K. I., Wilner, D. J., Huang, J., Loomis, R. A., Andrews, S. M., and Czekala, I. (2016). The Coupled Physical Structure of Gas and Dust in the IM Lup Protoplanetary Disk. , 832:110.

Cuello, N., Montesinos, M., Stammler, S. M., Louvet, F., and Cuadra, J. (2019). Dusty spirals triggered by shadows in transition discs. , 622:A43.

Cunha, M. S., Antoci, V., Holdsworth, D. L., Kurtz, D. W., Balona, L. A., Bognár, Z., Bowman, D. M., Guo, Z., Kołaczek-Szymański, P. A., Lares-Martiz, M., Paunzen, E., Skarka, M., Smalley, B., Sódor, Á., Kochukhov, O., Pepper, J., Richey-Yowell, T., Ricker, G. R., Seager, S., Buzasi, D. L., Fox-Machado, L., Hasanzadeh, A., Niemczura, E., Quitral-Manosalva, P., Monteiro, M. J. P. F. G., Stateva, I., De Cat, P., García Hernández, A., Ghasemi, H., Handler, G., Hey, D., Matthews, J. M., Nemec, J. M., Pascual-Granado, J., Safari, H., Suárez, J. C., Szabó, R., Tkachenko, A., and Weiss, W. W. (2019). Rotation and pulsation in Ap stars: first light results from TESS sectors 1 and 2. , 487(3):3523–3549.

Currie, T., Guyon, O., Tamura, M., Kudo, T., Jovanovic, N., Lozi, J., Schlieder, J. E., Brandt, T. D., Kuhn, J., Serabyn, E., Janson, M., Carson, J., Groff, T., Kasdin, N. J., McElwain, M. W., Singh, G., Uyama, T., Kuzuhara, M., Akiyama, E., Grady, C., Hayashi, S., Knapp, G., Kwon, J.-m., Oh, D., Wisniewski, J., Sitko, M., and Yang, Y. (2017). Subaru/SCExAO First-light Direct Imaging of a Young Debris Disk around HD 36546. , 836(1):L15.

Czesla, S., Schröter, S., Schneider, C. P., Huber, K. F., Pfeifer, F., Andreasen, D. T., and Zechmeister, M. (2019). PyA: Python astronomy-related packages.

David, T. J. and Hillenbrand, L. A. (2015). The Ages of Early-type Stars: Strömgren Photometric Methods Calibrated, Validated, Tested, and Applied to Hosts and Prospective Hosts of Directly Imaged Exoplanets. , 804:146.

De Rosa, R. J., Patience, J., Wilson, P. A., Schneider, A., Wiktorowicz, S. J., Vigan, A., Marois, C., Song, I., Macintosh, B., Graham, J. R., Doyon, R., Bessell, M. S., Thomas, S., and Lai, O. (2014). VizieR Online Data Catalog: VAST Survey. A-type stars multiplicity (De Rosa+, 2014). *VizieR Online Data Catalog*, 743.

Debes, J. H., Kilic, M., Faedi, F., Shkolnik, E. L., Lopez-Morales, M., Weinberger, A. J., Slesnick, C., and West, R. G. (2012). Detection of Weak Circumstellar Gas around the DAZ White Dwarf WD 1124-293: Evidence for the Accretion of Multiple Asteroids. , 754(1):59.

Debes, J. H., Weinberger, A. J., and Kuchner, M. J. (2009). Interstellar Medium Sculpting of the HD 32297 Debris Disk. , 702(1):318–326.

Dekker, H., D'Odorico, S., Kaufer, A., Delabre, B., and Kotzlowski, H. (2000). Design, construction, and performance of UVES, the echelle spectrograph for the UT2 Kueyen Telescope at the ESO Paranal Observatory. In Iye, M. and Moorwood, A. F., editors, *Optical and IR Telescope Instrumentation and Detectors*, volume 4008 of , pages 534–545.

Dent, W. R. F., Wyatt, M. C., Roberge, A., Augereau, J. C., Casassus, S., Corder, S., Greaves, J. S., de Gregorio-Monsalvo, I., Hales, A., Jackson, A. P., Hughes, A. M., Lagrange, A. M., Matthews, B., and Wilner, D. (2014). Molecular Gas Clumps from the Destruction of Icy Bodies in the β Pictoris Debris Disk. *Science*, 343(6178):1490–1492.

Díaz-Luis, J. J., García-Hernández, D. A., Kameswara Rao, N., Manchado, A., and Cataldo, F. (2015). A search for diffuse bands in fullerene planetary nebulae: evidence of diffuse circumstellar bands. , 573:A97.

Docobo, J. A. and Ling, J. F. (2007). Orbits and System Masses of 14 Visual Double Stars with Early-Type Components. , 133:1209–1216.

Dohlen, K., Langlois, M., Saisse, M., Hill, L., Origne, A., Jacquet, M., Fabron, C., Blanc, J.-C., Llored, M., Carle, M., Moutou, C., Vigan, A., Boccaletti, A., Carbillet, M., Mouillet, D., and Beuzit, J.-L. (2008). The infra-red dual imaging and spectrograph for SPHERE: design and performance. In , volume 7014 of *Society of Photo-Optical Instrumentation Engineers (SPIE) Conference Series*, page 70143L.

Dommanget, J. and Nys, O. (2002). VizieR Online Data Catalog: CCDM (Catalog of Components of Double Multiple stars) (Dommanget+ 2002). *VizieR Online Data Catalog*, 1274.

Donaldson, J. K., Lebreton, J., Roberge, A., Augereau, J. C., and Krivov, A. V. (2013). Modeling the HD 32297 Debris Disk with Far-infrared Herschel Data. , 772(1):17.

Dvorak, R., Loibnegger, B., and Cuntz, M. (2020). *On the dynamics of comets in extrasolar planetary systems*, pages 331–350.

Edelman, E., Redfield, S., Linsky, J. L., Wood, B. E., and Müller, H. (2019). Properties of the Interstellar Medium along Sight Lines to Nearby Planet-hosting Stars. , 880(2):117.

Eiroa, C., Fedele, D., Maldonado, J., González-García, B. M., Rodmann, J., Heras, A. M., Pilbratt, G. L., Augereau, J. C., Mora, A., Montesinos, B., Ardila, D., Bryden, G., Liseau, R., Stapelfeldt, K., Launhardt, R., Solano, E., Bayo, A., Absil, O., Arévalo, M., Barrado, D., Beichmann, C., Danchi, W., Del Burgo, C., Ertel, S., Fridlund, M., Fukagawa, M., Gutiérrez, R., Grün, E., Kamp, I., Krivov, A., Lebreton, J., Löhne, T., Lorente, R., Marshall, J., Martínez-Arnáiz, R., Meeus, G., Montes, D., Morbidelli, A., Müller, S., Mutschke, H., Nakagawa, T., Olofsson, G., Ribas, I., Roberge, A., Sanz-Forcada, J., Thébault, P., Walker, H., White, G. J., and Wolf, S. (2010). Cold DUst around NEarby Stars (DUNES). First results. A resolved exo-Kuiper belt around the solar-like star ζ^2 Ret. , 518:L131.

Eiroa, C., Marshall, J. P., Mora, A., Montesinos, B., Absil, O., Augereau, J. C., Bayo, A., Bryden, G., Danchi, W., del Burgo, C., Ertel, S., Fridlund, M., Heras, A. M., Krivov, A. V., Launhardt, R., Liseau, R., Löhne, T., Maldonado, J., Pilbratt, G. L., Roberge, A., Rodmann, J., Sanz-Forcada, J., Solano, E., Stapelfeldt, K., Thébault, P., Wolf, S., Ardila, D., Arévalo, M., Beichmann, C., Faramaz, V., González-García, B. M., Gutiérrez, R., Lebreton, J., Martínez-Arnáiz, R., Meeus, G., Montes, D., Olofsson, G., Su, K. Y. L., White, G. J., Barrado, D., Fukagawa, M., Grün, E., Kamp, I., Lorente, R., Morbidelli, A., Müller, S., Mutschke, H., Nakagawa, T., Ribas, I., and Walker, H. (2013). DUst around NEarby Stars. The survey observational results. , 555:A11.

Eiroa, C., Rebollido, I., Montesinos, B., Villaver, E., Absil, O., Henning, T., Bayo, A., Canovas, H., Carmona, A., Chen, C., Ertel, S., Iglesias, D. P., Launhardt, R., Maldonado, J., Meeus, G., Moór, A., Mora, A., Mustill, A. J., Olofsson, J., Riviere-Marichalar, P., and Roberge, A. (2016). Exocomet signatures around the A-shell star Leonis? , 594:L1.

Esposito, T. M., Fitzgerald, M. P., Graham, J. R., Kalas, P., Lee, E. J., Chiang, E., Duchêne, G., Wang, J., Millar-Blanchaer, M. A., Nielsen, E., Ammons, S. M., Bruzzone, S., De Rosa,

R. J., Draper, Z. H., Macintosh, B., Marchis, F., Metchev, S. A., Perrin, M., Pueyo, L., Rajan, A., Rantakyrö, F. T., Vega, D., and Wolff, S. (2016). Bringing "The Moth" to Light: A Planet-sculpting Scenario for the HD 61005 Debris Disk. , 152(4):85.

Facchini, S., van Dishoeck, E. F., Manara, C. F., Tazzari, M., Maud, L., Cazzoletti, P., Rosotti, G., van der Marel, N., Pinilla, P., and Clarke, C. J. (2019). High gas-to-dust size ratio indicating efficient radial drift in the mm-faint CX Tauri disk. , 626:L2.

Farhang, A., van Loon, J. T., Khosroshahi, H. G., Javadi, A., and Bailey, M. (2019). A three-dimensional map of the hot Local Bubble using diffuse interstellar bands. *Nature Astronomy*, 3:922–927.

Fedele, D., van den Ancker, M. E., Henning, T., Jayawardhana, R., and Oliveira, J. M. (2010). Timescale of mass accretion in pre-main-sequence stars. , 510:A72.

Ferlet, R., Hobbs, L. M., and Madjar, A. V. (1987). The beta Pictoris circumstellar disk. V. Time variations of the CA II-K line. , 185:267–270.

Fernández, R., Brandeker, A., and Wu, Y. (2006). Braking the Gas in the β Pictoris Disk. , 643:509–522.

Feroz, F., Hobson, M. P., and Bridges, M. (2009). MULTINEST: an efficient and robust Bayesian inference tool for cosmology and particle physics. , 398(4):1601–1614.

Figueira, P. (2013). Stellar Noise in Exoplanet Searches. In Chavez, M., Bertone, E., Vega, O., and De la Luz, V., editors, *New Quests in Stellar Astrophysics III: A Panchromatic View of Solar-Like Stars, With and Without Planets*, volume 472 of *Astronomical Society of the Pacific Conference Series*, page 137.

Foreman-Mackey, D. (2016). corner.py: Scatterplot matrices in python. *The Journal of Open Source Software*, 1(2):24.

Foreman-Mackey, D., Hogg, D. W., Lang, D., and Goodman, J. (2013). emcee: The MCMC Hammer. , 125:306.

France, K., Roberge, A., Lupu, R. E., Redfield, S., and Feldman, P. D. (2007). A Low-Mass H_2 Component to the AU Microscopii Circumstellar Disk. , 668(2):1174–1181.

Gagné, J., Mamajek, E. E., Malo, L., Riedel, A., Rodriguez, D., Lafrenière, D., Faherty, J. K., Roy-Loubier, O., Pueyo, L., Robin, A. C., and Doyon, R. (2018). BANYAN. XI. The BANYAN Σ Multivariate Bayesian Algorithm to Identify Members of Young Associations with 150 pc. , 856(1):23.

Gaia Collaboration (2018). VizieR Online Data Catalog: Gaia DR2 (Gaia Collaboration, 2018). *VizieR Online Data Catalog*, page I/345.

Gaia Collaboration, Brown, A. G. A., Vallenari, A., Prusti, T., de Bruijne, J. H. J., Mignard, F., Drimmel, R., Babusiaux, C., Bailer-Jones, C. A. L., Bastian, U., and et al. (2016). Gaia Data Release 1. Summary of the astrometric, photometric, and survey properties. , 595:A2.

Galicher, R., Rameau, J., Bonnefoy, M., Baudino, J. L., Currie, T., Boccaletti, A., Chauvin, G., Lagrange, A. M., and Marois, C. (2014). Near-infrared detection and characterization of the exoplanet HD 95086 b with the Gemini Planet Imager. , 565:L4.

Galván-Madrid, R., Liu, H. B., Izquierdo, A. F., Miotello, A., Zhao, B., Carrasco-González, C., Lizano, S., and Rodríguez, L. F. (2018). On the Effects of Self-obscuration in the (Sub)Millimeter Spectral Indices and the Appearance of Protostellar Disks. , 868(1):39.

Golimowski, D. A., Ardila, D. R., Krist, J. E., Clampin, M., Ford, H. C., Illingworth, G. D., Bartko, F., Benítez, N., Blakeslee, J. P., Bouwens, R. J., Bradley, L. D., Broadhurst, T. J., Brown, R. A., Burrows, C. J., Cheng, E. S., Cross, N. J. G., Demarco, R., Feldman, P. D., Franx, M., Goto, T., Gronwall, C., Hartig, G. F., Holden, B. P., Homeier, N. L., Infante, L., Jee, M. J., Kimble, R. A., Lesser, M. P., Martel, A. R., Mei, S., Menanteau, F., Meurer, G. R., Miley, G. K., Motta, V., Postman, M., Rosati, P., Sirianni, M., Sparks, W. B., Tran, H. D., Tsvetanov, Z. I., White, R. L., Zheng, W., and Zirm, A. W. (2006). Hubble Space Telescope ACS Multiband Coronagraphic Imaging of the Debris Disk around β Pictoris. , 131(6):3109–3130.

Gomez Gonzalez, C. A., Wertz, O., Absil, O., Christiaens, V., Defrère, D., Mawet, D., Milli, J., Absil, P.-A., Van Droogenbroeck, M., Cantalloube, F., Hinz, P. M., Skemer, A. J., Karlsson, M., and Surdej, J. (2017). VIP: Vortex Image Processing Package for High-contrast Direct Imaging. , 154(1):7.

Gontcharov, G. A. (2006). Pulkovo Compilation of Radial Velocities for 35 495 Hipparcos stars in a common system. *Astronomy Letters*, 32(11):759–771.

Gontcharov, G. A. (2012). Spatial distribution and kinematics of OB stars. *Astronomy Letters*, 38:694–706.

Grady, C. A., Brown, A., Welsh, B., Roberge, A., Kamp, I., and Rivière Marichalar, P. (2018). The Star-grazing Bodies in the HD 172555 System. , 155(6):242.

Graham, J. R., Kalas, P. G., and Matthews, B. C. (2007). The Signature of Primordial Grain Growth in the Polarized Light of the AU Microscopii Debris Disk. , 654(1):595–605.

Gray, R. O. and Corbally, J., C. (2009). *Stellar Spectral Classification*. Princeton University Press.

Greaves, J. S., Holland, W. S., Matthews, B. C., Marshall, J. P., Dent, W. R. F., Woitke, P., Wyatt, M. C., Matrà, L., and Jackson, A. (2016). Gas and dust around A-type stars at tens of Myr: signatures of cometary breakup. , 461:3910–3917.

Greaves, J. S., Kennedy, G. M., Thureau, N., Eiroa, C., Marshall, J. P., Maldonado, J., Matthews, B. C., Olofsson, G., Barlow, M. J., Moro-Martín, A., Sibthorpe, B., Absil, O., Ardila, D. R., Booth, M., Broekhoven-Fiene, H., Brown, D. J. A., Cameron, A. C., del Burgo, C., Di Francesco, J., Eislöffel, J., Duchêne, G., Ertel, S., Holland, W. S., Horner, J., Kalas, P., Kavelaars, J. J., Lestrade, J. F., Vican, L., Wilner, D. J., Wolf, S., and Wyatt, M. C. (2014). Alignment in star-debris disc systems seen by Herschel. , 438(1):L31–L35.

Gvaramadze, V. V., Kniazev, A. Y., Maryeva, O. V., and Berdnikov, L. N. (2018). Optical spectroscopy of the blue supergiant Sk-69° 279 and its circumstellar shell with SALT. , 474(1):1412–1425.

Hales, A. S., Barlow, M. J., Crawford, I. A., and Casassus, S. (2017). Atomic gas in debris discs. , 466:3582–3593.

Hales, A. S., De Gregorio-Monsalvo, I., Montesinos, B., Casassus, S., Dent, W. F. R., Dougados, C., Eiroa, C., Hughes, A. M., Garay, G., Mardones, D., Ménard, F., Palau, A., Pérez, S., Phillips, N., Torrelles, J. M., and Wilner, D. (2014). A CO Survey in Planet-forming Disks: Characterizing the Gas Content in the Epoch of Planet Formation. , 148:47.

Harmanec, P., Koubský, P., Krpata, J., and Ždárský, F. (1976). Properties and Nature of Shell Stars. 6. The Shell Star 4 Herculis as an Interacting Binary. *Bulletin of the Astronomical Institutes of Czechoslovakia*, 27:47.

Hauck, B. and Jaschek, C. (2000). A-shell stars in the Geneva system. , 354:157–162.

Heap, S. R., Lindler, D. J., Lanz, T. M., Cornett, R. H., Hubeny, I., Maran, S. P., and Woodgate, B. (2000). Space Telescope Imaging Spectrograph Coronagraphic Observations of β Pictoris. , 539(1):435–444.

Henry, G. W., Fekel, F. C., and Henry, S. M. (2011). A Volume-limited Photometric Survey of 114 γ Doradus Candidates. , 142(2):39.

Henyey, L. G. and Greenstein, J. L. (1941). Diffuse radiation in the Galaxy. , 93:70–83.

Herbig, G. H. (1995). The Diffuse Interstellar Bands. , 33:19–74.

Hernández, J., Briceño, C., Calvet, N., Hartmann, L., Muzerolle, J., and Quintero, A. (2006). Spitzer Observations of the Orion OB1 Association: Second-Generation Dust Disks at 5-10 Myr. , 652:472–481.

Hernández, J., Hartmann, L., Megeath, T., Gutermuth, R., Muzerolle, J., Calvet, N., Vivas, A. K., Briceño, C., Allen, L., Stauffer, J., Young, E., and Fazio, G. (2007). A Spitzer Space Telescope Study of Disks in the Young σ Orionis Cluster. , 662:1067–1081.

Higuchi, A. E., Sato, A., Tsukagoshi, T., Sakai, N., Iwasaki, K., Momose, M., Kobayashi, H., Ishihara, D., Watanabe, S., Kaneda, H., and Yamamoto, S. (2017). Detection of Submillimeter-wave [C I] Emission in Gaseous Debris Disks of 49 Ceti and β Pictoris. , 839:L14.

Hoffleit, D. (1964). *Catalogue of Bright Stars*.

Houck, J. R., Roellig, T. L., van Cleve, J., Forrest, W. J., Herter, T., Lawrence, C. R., Matthews, K., Reitsema, H. J., Soifer, B. T., Watson, D. M., Weedman, D., Huisjen, M., Troeltzsch, J., Barry, D. J., Bernard-Salas, J., Blacken, C. E., Brandl, B. R., Charmandaris, V., Devost, D., Gull, G. E., Hall, P., Henderson, C. P., Higdon, S. J. U., Pirger, B. E., Schoenwald, J., Sloan, G. C., Uchida, K. I., Appleton, P. N., Armus, L., Burgdorf, M. J., Fajardo-Acosta, S. B., Grillmair, C. J., Ingalls, J. G., Morris, P. W., and Teplitz, H. I. (2004). The Infrared Spectrograph (IRS) on the Spitzer Space Telescope. , 154:18–24.

Houdebine, E. R., Doyle, J. G., and Koscielecki, M. (1995). Observation and modelling of main sequence star chromospheres. III. Differential analysis of hydrogen lines versus activity level in M dwarfs. , 294:773–791.

Howarth, I. D., Price, R. J., Crawford, I. A., and Hawkins, I. (2002). A VAPID analysis of interstellar lithium in the ζ Oph sightline. , 335:267–274.

Huang, J., Andrews, S. M., Dullemond, C. P., Isella, A., Pérez, L. M., Guzmán, V. V., Öberg, K. I., Zhu, Z., Zhang, S., Bai, X.-N., Benisty, M., Birnstiel, T., Carpenter, J. M., Hughes, A. M., Ricci, L., Weaver, E., and Wilner, D. J. (2018). The Disk Substructures at High Angular Resolution Project (DSHARP). II. Characteristics of Annular Substructures. , 869(2):L42.

Hughes, A. M., Duchene, G., and Matthews, B. (2018). Debris Disks: Structure, Composition, and Variability. *ArXiv e-prints*.

Hughes, A. M., Lieman-Sifry, J., Flaherty, K. M., Daley, C. M., Roberge, A., Kóspál, Á., Moór, A., Kamp, I., Wilner, D. J., Andrews, S. M., Kastner, J. H., and Ábrahám, P. (2017). Radial Surface Density Profiles of Gas and Dust in the Debris Disk around 49 Ceti. , 839(2):86.

Hughes, A. M., Wilner, D. J., Kamp, I., and Hogerheijde, M. R. (2008). A Resolved Molecular Gas Disk around the Nearby A Star 49 Ceti. , 681(1):626–635.

Hunter, I., Smoker, J. V., Keenan, F. P., Ledoux, C., Jehin, E., Cabanac, R., Melo, C., and Bagnulo, S. (2006). Early-type stars observed in the ESO UVES Paranal Observatory Project - I. Interstellar NaI UV, TiII and CaII K observations*. , 367(4):1478–1514.

Husser, T. O., Wende-von Berg, S., Dreizler, S., Homeier, D., Reiners, A., Barman, T., and Hauschildt, P. H. (2013). A new extensive library of PHOENIX stellar atmospheres and synthetic spectra. , 553:A6.

Iglesias, D., Bayo, A., Olofsson, J., Wahhaj, Z., Eiroa, C., Montesinos, B., Rebollido, I., Smoker, J., Sbordone, L., Schreiber, M. R., and Henning, T. (2018). Debris discs with multiple absorption features in metallic lines: circumstellar or interstellar origin? , 480(1):488–520.

Iglesias, D. P., Olofsson, J., Bayo, A., Zieba, S., Montesinos, M., Smoker, J., Kennedy, G. M., Godoy, N., Pantoja, B., Talens, G. J., Wahhaj, Z., and Zamora, C. (2019). An unusually large gaseous transit in a debris disc. , 490(4):5218–5227.

Jaschek, C. and Andrillat, Y. (1998). AE and A type shell stars. , 130:507–512.

Jaschek, M., Jaschek, C., and Andrillat, Y. (1988). A survey of AE and A-type shell stars in the photographic region. , 72:505–513.

Jaschek, M., Jaschek, C., and Andrillat, Y. (1991). AE and A-type shell stars in the near infrared. , 250:127–133.

Jaschek, M., Jaschek, C., and Malaroda, S. (1969). The spectra of some Be stars. , 3:485.

Jenkins, J. M. (2017). Kepler Data Processing Handbook: Overview of the Science Operations Center. Technical report, NASA Ames Research Center.

Jenkins, J. M., Caldwell, D. A., Chandrasekaran, H., Twicken, J. D., Bryson, S. T., Quintana, E. V., Clarke, B. D., Li, J., Allen, C., Tenenbaum, P., Wu, H., Klaus, T. C., Middour, C. K., Cote, M. T., McCauliff, S., Girouard, F. R., Gunter, J. P., Wohler, B., Sommers, J., Hall, J. R., Uddin, A. K., Wu, M. S., Bhavsar, P. A., Van Cleve, J., Pletcher, D. L., Dotson, J. A., Haas, M. R., Gilliland, R. L., Koch, D. G., and Borucki, W. J. (2010). Overview of the Kepler Science Processing Pipeline. , 713:L87–L91.

Jenkins, J. M., Twicken, J. D., McCauliff, S., Campbell, J., Sanderfer, D., Lung, D., Mansouri-Samani, M., Girouard, F., Tenenbaum, P., Klaus, T., Smith, J. C., Caldwell, D. A., Chacon,

A. D., Henze, C., Heiges, C., Latham, D. W., Morgan, E., Swade, D., Rinehart, S., and Vanderspek, R. (2016). The TESS science processing operations center. In *Software and Cyberinfrastructure for Astronomy IV*, volume 9913 of *Society of Photo-Optical Instrumentation Engineers (SPIE) Conference Series*, page 99133E.

Johnson, M. C., Redfield, S., and Jensen, A. G. (2015). The Interstellar Medium in the Kepler Search Volume. , 807(2):162.

Jura, M., Zuckerman, B., Becklin, E. E., and Smith, R. C. (1993). Constraints on the Evolution of Remnant Protostellar Dust Debris around HR 4796. , 418:L37.

Kalas, P., Graham, J. R., and Clampin, M. (2005). A planetary system as the origin of structure in Fomalhaut's dust belt. , 435(7045):1067–1070.

Kalas, P. and Jewitt, D. (1995). Asymmetries in the Beta Pictoris Dust Disk. , 110:794.

Kalas, P., Liu, M. C., and Matthews, B. C. (2004). Discovery of a Large Dust Disk Around the Nearby Star AU Microscopii. *Science*, 303(5666):1990–1992.

Kalas, P. G., Rajan, A., Wang, J. J., Millar-Blanchaer, M. A., Duchene, G., Chen, C., Fitzgerald, M. P., Dong, R., Graham, J. R., Patience, J., Macintosh, B., Murray-Clay, R., Matthews, B., Rameau, J., Marois, C., Chilcote, J., De Rosa, R. J., Doyon, R., Draper, Z. H., Lawler, S., Ammons, S. M., Arriaga, P., Bulger, J., Cotten, T., Follette, K. B., Goodsell, S., Greenbaum, A., Hibon, P., Hinkley, S., Hung, L.-W., Ingraham, P., Konapacky, Q., Lafreniere, D., Larkin, J. E., Long, D., Maire, J., Marchis, F., Metchev, S., Morzinski, K. M., Nielsen, E. L., Oppenheimer, R., Perrin, M. D., Pueyo, L., Rantakyrö, F. T., Ruffio, J.-B., Saddlemyer, L., Savransky, D., Schneider, A. C., Sivaramakrishnan, A., Soummer, R., Song, I., Thomas, S., Vasisht, G., Ward-Duong, K., Wiktorowicz, S. J., and Wolff, S. G. (2015). Direct Imaging of an Asymmetric Debris Disk in the HD 106906 Planetary System. , 814(1):32.

Karoff, C., Metcalfe, T. S., Montet, B. T., Jannsen, N. E., Santos, A. R. G., Nielsen, M. B., and Chaplin, W. J. (2019). Sounding stellar cycles with Kepler - III. Comparative analysis of chromospheric, photometric, and asteroseismic variability. , 485(4):5096–5104.

Kasper, M., Apai, D., Wagner, K., and Robberto, M. (2015). Discovery of an Edge-on Debris Disk with a Dust Ring and an Outer Disk Wing-tilt Asymmetry. , 812:L33.

Kaufer, A., Stahl, O., Tubbesing, S., Nørregaard, P., Avila, G., Francois, P., Pasquini, L., and Pizzella, A. (1999). Commissioning FEROS, the new high-resolution spectrograph at La-Silla. *The Messenger*, 95:8–12.

Kausch, W., Noll, S., Smette, A., Kimeswenger, S., Barden, M., Szyszka, C., Jones, A. M., Sana, H., Horst, H., and Kerber, F. (2015). Molecfit: A general tool for telluric absorption correction. II. Quantitative evaluation on ESO-VLT/X-Shooterspectra. , 576:A78.

Kaye, A. B., Handler, G., Krisciunas, K., Poretti, E., and Zerbi, F. M. (1999). Gamma Doradus Stars: Defining a New Class of Pulsating Variables. , 111(761):840–844.

Kelson, D. D. (2003). Optimal Techniques in Two-dimensional Spectroscopy: Background Subtraction for the 21st Century. , 115(808):688–699.

Kelson, D. D., Illingworth, G. D., van Dokkum, P. G., and Franx, M. (2000). The Evolution of Early-Type Galaxies in Distant Clusters. III. M/L_V Ratios in the z=0.33 Cluster CL 1358+62. , 531(1):184–199.

Kennedy, G. M., Marino, S., Matrá, L., Panić, O., Wilner, D., Wyatt, M. C., and Yelverton, B. (2018). ALMA observations of the narrow HR 4796A debris ring. .

Kennedy, G. M. and Wyatt, M. C. (2013). The bright end of the exo-Zodi luminosity function: disc evolution and implications for exo-Earth detectability. , 433(3):2334–2356.

Kennedy, G. M. and Wyatt, M. C. (2014). Do two-temperature debris discs have multiple belts? , 444(4):3164–3182.

Kenyon, S. J. and Bromley, B. C. (2002). Dusty Rings: Signposts of Recent Planet Formation. , 577(1):L35–L38.

Kenyon, S. J., Najita, J. R., and Bromley, B. C. (2016). Rocky Planet Formation: Quick and Neat. , 831:8.

Kharchenko, N. V. (2001). All-sky compiled catalogue of 2.5 million stars. *Kinematika i Fizika Nebesnykh Tel*, 17:409–423.

Kiefer, F. (2014). Two families of exocomets in the circumstellar disk of Beta Pictoris. In *Thirty years of Beta Pic and Debris Disks Studies*.

Kiefer, F., Lecavelier des Etangs, A., Augereau, J.-C., Vidal-Madjar, A., Lagrange, A.-M., and Beust, H. (2014a). Exocomets in the circumstellar gas disk of HD 172555. , 561:L10.

Kiefer, F., Lecavelier des Etangs, A., Boissier, J., Vidal-Madjar, A., Beust, H., Lagrange, A.-M., Hébrard, G., and Ferlet, R. (2014b). Two families of exocomets in the β Pictoris system. , 514:462–464.

Kiefer, F., Lecavelier des Etangs, A., and Vidal-Madjar, A. (2014c). Exocomets in the disk of two young A-type stars. In Ballet, J., Martins, F., Bournaud, F., Monier, R., and Reylé, C., editors, *SF2A-2014: Proceedings of the Annual meeting of the French Society of Astronomy and Astrophysics*, pages 39–43.

Kochanek, C. S., Shappee, B. J., Stanek, K. Z., Holoien, T. W.-S., Thompson, T. A., Prieto, J. L., Dong, S., Shields, J. V., Will, D., Britt, C., Perzanowski, D., and Pojmański, G. (2017). The All-Sky Automated Survey for Supernovae (ASAS-SN) Light Curve Server v1.0. , 129(10):104502.

Kóspál, Á. and Moór, A. (2016). Debris Disks in Nearby Young Moving Groups in the ALMA Era. In Kastner, J. H., Stelzer, B., and Metchev, S. A., editors, *Young Stars & Planets Near the Sun*, volume 314 of *IAU Symposium*, pages 183–188.

Kóspál, Á., Moór, A., Juhász, A., Ábrahám, P., Apai, D., Csengeri, T., Grady, C. A., Henning, T., Hughes, A. M., Kiss, C., Pascucci, I., and Schmalzl, M. (2013). ALMA Observations of the Molecular Gas in the Debris Disk of the 30 Myr Old Star HD 21997. , 776:77.

Koubsky, P., Horn, J., Harmanec, P., Hubert, A. M., Hubert, H., and Floquet, M. (1993). Coming shell phase of the Be star 4 Herculis. , 277:521–523.

Kourniotis, M., Kraus, M., Arias, M. L., Cidale, L., and Torres, A. F. (2018). On the evolutionary state of massive stars in transition phases in M33. , 480(3):3706–3717.

Kral, Q., Clarke, C., and Wyatt, M. (2017a). Circumstellar discs: What will be next? *ArXiv e-prints*.

Kral, Q., Davoult, J., and Charnay, B. (2020). Formation of secondary atmospheres on terrestrial planets by late disk accretion. *arXiv e-prints*, page arXiv:2004.02496.

Kral, Q., Marino, S., Wyatt, M. C., Kama, M., and Matrà, L. (2019). Imaging [CI] around HD 131835: reinterpreting young debris discs with protoplanetary disc levels of CO gas as shielded secondary discs. , 489(4):3670–3691.

Kral, Q., Matrà, L., Wyatt, M. C., and Kennedy, G. M. (2017b). Predictions for the secondary CO, C and O gas content of debris discs from the destruction of volatile-rich planetesimals. , 469:521–550.

Kuchner, M. J. and Stark, C. C. (2010). Collisional Grooming Models of the Kuiper Belt Dust Cloud. , 140(4):1007–1019.

Kuschnig, R., Paunzen, E., and Weiss, W. W. (1994). HD183324, A Pulsating lambda Boo Star? *Information Bulletin on Variable Stars*, 4070:1.

Lagrange, A. M., Gratadour, D., Chauvin, G., Fusco, T., Ehrenreich, D., Mouillet, D., Rousset, G., Rouan, D., Allard, F., Gendron, É., Charton, J., Mugnier, L., Rabou, P., Montri, J., and Lacombe, F. (2009). A probable giant planet imaged in the β Pictoris disk. VLT/NaCo deep L'-band imaging. , 493(2):L21–L25.

Lagrange-Henri, A. M., Beust, H., Ferlet, R., Hobbs, L. M., and Madjar, A. V. (1990a). HR 10 : a new beta Pictoris-like star ? , 227:L13–L16.

Lagrange-Henri, A. M., Ferlet, R., Vidal-Madjar, A., Beust, H., Gry, C., and Lallement, R. (1990b). Search for beta Pictoris-like star. , 85:1089.

Lagrange-Henri, A. M., Vidal-Madjar, A., and Ferlet, R. (1988). The beta Pictoris circumstellar disk. VI. Evidence for material falling on to the star. , 190:275–282.

Lallement, R., Babusiaux, C., Vergely, J. L., Katz, D., Arenou, F., Valette, B., Hottier, C., and

Capitanio, L. (2019). Gaia-2MASS 3D maps of Galactic interstellar dust within 3 kpc. , 625:A135.

Lallement, R., Vergely, J. L., Valette, B., Puspitarini, L., Eyer, L., and Casagrande, L. (2014). 3D maps of the local ISM from inversion of individual color excess measurements. , 561:A91.

Lallement, R., Welsh, B. Y., Vergely, J. L., Crifo, F., and Sfeir, D. (2003). 3D mapping of the dense interstellar gas around the Local Bubble. , 411:447–464.

Lee, E. J. and Chiang, E. (2016). A Primer on Unifying Debris Disk Morphologies. , 827(2):125.

Lenz, P. and Breger, M. (2005). Period04 User Guide. *Communications in Asteroseismology*, 146:53–136.

Lieman-Sifry, J., Hughes, A. M., Carpenter, J. M., Gorti, U., Hales, A., and Flaherty, K. M. (2016). Debris Disks in the Scorpius-Centaurus OB Association Resolved by ALMA. , 828(1):25.

Lin, J. W. and Chiang, E. (2019). Sculpting eccentric debris disks with eccentric gas rings. *arXiv e-prints*, page arXiv:1907.10640.

Linsky, J. L. (2017). Stellar Model Chromospheres and Spectroscopic Diagnostics. , 55(1):159–211.

Liou, J.-C. and Zook, H. A. (1999). Signatures of the Giant Planets Imprinted on the Edgeworth-Kuiper Belt Dust Disk. , 118(1):580–590.

Löhne, T., Augereau, J. C., Ertel, S., Marshall, J. P., Eiroa, C., Mora, A., Absil, O., Stapelfeldt, K., Thébault, P., Bayo, A., Del Burgo, C., Danchi, W., Krivov, A. V., Lebreton, J., Letawe, G., Magain, P., Maldonado, J., Montesinos, B., Pilbratt, G. L., White, G. J., and Wolf, S. (2012). Modelling the huge, Herschel-resolved debris ring around HD 207129. , 537:A110.

Lovis, C., Dumusque, X., Santos, N. C., Bouchy, F., Mayor, M., Pepe, F., Queloz, D., Ségransan, D., and Udry, S. (2011). The HARPS search for southern extra-solar planets. XXXI. Magnetic activity cycles in solar-type stars: statistics and impact on precise radial velocities. *arXiv e-prints*, page arXiv:1107.5325.

Lyra, W., Johansen, A., Klahr, H., and Piskunov, N. (2009). Standing on the shoulders of giants. Trojan Earths and vortex trapping in low mass self-gravitating protoplanetary disks of gas and solids. , 493(3):1125–1139.

Lyra, W. and Kuchner, M. (2013). Formation of sharp eccentric rings in debris disks with gas but without planets. , 499:184–187.

MacGregor, M. A., Matrà, L., Kalas, P., Wilner, D. J., Pan, M., Kennedy, G. M., Wyatt, M. C., Duchene, G., Hughes, A. M., Rieke, G. H., Clampin, M., Fitzgerald, M. P., Graham, J. R., Holland, W. S., Panić, O., Shannon, A., and Su, K. (2017). A Complete ALMA Map of the Fomalhaut Debris Disk. , 842(1):8.

MacGregor, M. A., Weinberger, A. J., Hughes, A. M., Wilner, D. J., Currie, T., Debes, J. H., Donaldson, J. K., Redfield, S., Roberge, A., and Schneider, G. (2018). ALMA Detection of Extended Millimeter Halos in the HD 32297 and HD 61005 Debris Disks. , 869(1):75.

MacGregor, M. A., Wilner, D. J., Rosenfeld, K. A., Andrews, S. M., Matthews, B., Hughes, A. M., Booth, M., Chiang, E., Graham, J. R., Kalas, P., Kennedy, G., and Sibthorpe, B. (2013). Millimeter Emission Structure in the First ALMA Image of the AU Mic Debris Disk. , 762(2):L21.

Malamut, C., Redfield, S., Linsky, J. L., Wood, B. E., and Ayres, T. R. (2014). The Structure of the Local Interstellar Medium. VI. New Mg II, Fe II, and Mn II Observations toward Stars within 100 pc. , 787(1):75.

Mamajek, E. E. and Bell, C. P. M. (2014). On the age of the β Pictoris moving group. , 445(3):2169–2180.

Maness, H. L., Kalas, P., Peek, K. M. G., Chiang, E. I., Scherer, K., Fitzgerald, M. P., Graham, J. R., Hines, D. C., Schneider, G., and Metchev, S. A. (2009). Hubble Space Telescope Optical Imaging of the Eroding Debris Disk HD 61005. , 707(2):1098–1114.

Manser, C. J., Gänsicke, B. T., Gentile Fusillo, N. P., Ashley, R., Breedt, E., Hollands, M., Izquierdo, P., and Pelisoli, I. (2020). The frequency of gaseous debris discs around white dwarfs. , 493(2):2127–2139.

Marino, S., Carpenter, J., Wyatt, M. C., Booth, M., Casassus, S., Faramaz, V., Guzman, V., Hughes, A. M., Isella, A., Kennedy, G. M., Matrà, L., Ricci, L., and Corder, S. (2018). A gap in the planetesimal disc around HD 107146 and asymmetric warm dust emission revealed by ALMA. , 479(4):5423–5439.

Marino, S., Flock, M., Henning, T., Kral, Q., Matrà, L., and Wyatt, M. C. (2020). Population synthesis of exocometary gas around A stars. , 492(3):4409–4429.

Marino, S., Matrà, L., Stark, C., Wyatt, M. C., Casassus, S., Kennedy, G., Rodriguez, D., Zuckerman, B., Perez, S., Dent, W. R. F., Kuchner, M., Hughes, A. M., Schneider, G., Steele, A., Roberge, A., Donaldson, J., and Nesvold, E. (2016). Exocometary gas in the HD 181327 debris ring. , 460:2933–2944.

Marino, S., Wyatt, M. C., Panić, O., Matrà, L., Kennedy, G. M., Bonsor, A., Kral, Q., Dent, W. R. F., Duchene, G., Wilner, D., Lisse, C. M., Lestrade, J.-F., and Matthews, B. (2017). ALMA observations of the η Corvi debris disc: inward scattering of CO-rich exocomets by a chain of 3-30 M planets? , 465:2595–2615.

Marois, C., Lafrenière, D., Doyon, R., Macintosh, B., and Nadeau, D. (2006). Angular Differential Imaging: A Powerful High-Contrast Imaging Technique. , 641(1):556–564.

Mashonkina, L. I., Shimanskiĭ, V. V., and Sakhibullin, N. A. (2000). Non-LTE Effects in Na I Spectral Lines in Stellar Atmospheres. *Astronomy Reports*, 44:790–803.

Matrà, L., Dent, W. R. F., Wyatt, M. C., Kral, Q., Wilner, D. J., Panić, O., Hughes, A. M., de Gregorio-Monsalvo, I., Hales, A., Augereau, J. C., Greaves, J., and Roberge, A. (2017a). Exocometary gas structure, origin and physical properties around β Pictoris through ALMA CO multitransition observations. , 464(2):1415–1433.

Matra, L., Kral, Q., Su, K., Brand eker, A., Dent, W., Gaspar, A., Kennedy, G., Marino, S., Oberg, K., Roberge, A., Wilner, D., Wilson, P., Wyatt, M., Cataldi, G., Higuchi, A., Hughes, M., Kiefer, F., Lecavelier des Etangs, A., Lyra, W., Matthews, B., Moor, A., Welsh, B., and Zuckerman, B. (2019). Exocometary Science. , 51(3):391.

Matrà, L., MacGregor, M. A., Kalas, P., Wyatt, M. C., Kennedy, G. M., Wilner, D. J., Duchene, G., Hughes, A. M., Pan, M., Shannon, A., Clampin, M., Fitzgerald, M. P., Graham, J. R., Holland , W. S., Panić, O., and Su, K. Y. L. (2017b). Detection of Exocometary CO within the 440 Myr Old Fomalhaut Belt: A Similar CO+CO_2 Ice Abundance in Exocomets and Solar System Comets. , 842(1):9.

Matrà, L., Öberg, K. I., Wilner, D. J., Olofsson, J., and Bayo, A. (2019). On the Ubiquity and Stellar Luminosity Dependence of Exocometary CO Gas: Detection around M Dwarf TWA 7. , 157(3):117.

Matthews, B. C., Krivov, A. V., Wyatt, M. C., Bryden, G., and Eiroa, C. (2014). Observations, Modeling, and Theory of Debris Disks. *Protostars and Planets VI*, pages 521–544.

Mayor, M., Pepe, F., Queloz, D., Bouchy, F., Rupprecht, G., Lo Curto, G., Avila, G., Benz, W., Bertaux, J.-L., Bonfils, X., Dall, T., Dekker, H., Delabre, B., Eckert, W., Fleury, M., Gilliotte, A., Gojak, D., Guzman, J. C., Kohler, D., Lizon, J.-L., Longinotti, A., Lovis, C., Megevand, D., Pasquini, L., Reyes, J., Sivan, J.-P., Sosnowska, D., Soto, R., Udry, S., van Kesteren, A., Weber, L., and Weilenmann, U. (2003). Setting New Standards with HARPS. *The Messenger*, 114:20–24.

Mazoyer, J., Boccaletti, A., Augereau, J. C., Lagrange, A. M., Galicher, R., and Baudoz, P. (2014). Is the HD 15115 inner disk really asymmetrical? , 569:A29.

McEvoy, C. M., Smoker, J. V., Dufton, P. L., Smith, K. T., Kennedy, M. B., Keenan, F. P., Lambert, D. L., Welty, D. E., and Lauroesch, J. T. (2015). Early-type stars observed in the ESO UVES Paranal Observatory Project - V. Time-variable interstellar absorption. , 451:1396–1412.

Melis, C., Dufour, P., Farihi, J., Bochanski, J., Burgasser, A. J., Parsons, S. G., Gänsicke, B. T., Koester, D., and Swift, B. J. (2012). Gaseous Material Orbiting the Polluted, Dusty White Dwarf HE 1349-2305. , 751(1):L4.

Miles, B. E., Roberge, A., and Welsh, B. (2016). UV Spectroscopy of Star-grazing Comets Within the 49 Ceti Debris Disk. , 824(2):126.

Milli, J., Mouillet, D., Lagrange, A. M., Boccaletti, A., Mawet, D., Chauvin, G., and Bonnefoy, M. (2012). Impact of angular differential imaging on circumstellar disk images. , 545:A111.

Milli, J., Vigan, A., Mouillet, D., Lagrange, A.-M., Augereau, J.-C., Pinte, C., Mawet, D., Schmid, H. M., Boccaletti, A., Matrà, L., Kral, Q., Ertel, S., Chauvin, G., Bazzon, A., Ménard, F., Beuzit, J.-L., Thalmann, C., Dominik, C., Feldt, M., Henning, T., Min, M., Girard, J. H., Galicher, R., Bonnefoy, M., Fusco, T., de Boer, J., Janson, M., Maire, A.-L., Mesa, D., Schlieder, J. E., and SPHERE Consortium (2017). Near-infrared scattered light properties of the HR 4796 A dust ring. A measured scattering phase function from $13.6\mathrm{deg}\, to 166.6\mathrm{deg}., 599 : A108$.

Mittal, T., Chen, C. H., Jang-Condell, H., Manoj, P., Sargent, B. A., Watson, D. M., and Lisse, C. M. (2015). The Spitzer Infrared Spectrograph Debris Disk Catalog. II. Silicate Feature Analysis of Unresolved Targets. , 798:87.

Montesinos, B., Eiroa, C., Krivov, A. V., Marshall, J. P., Pilbratt, G. L., Liseau, R., Mora, A., Maldonado, J., Wolf, S., Ertel, S., Bayo, A., Augereau, J. C., Heras, A. M., Fridlund, M., Danchi, W. C., Solano, E., Kirchschlager, F., del Burgo, C., and Montes, D. (2016). Incidence of debris discs around FGK stars in the solar neighbourhood. , 593:A51.

Montesinos, B., Eiroa, C., Lillo-Box, J., Rebollido, I., Djupvik, A. A., Absil, O., Ertel, S., Marion, L., Kajava, J. J. E., Redfield, S., Isaacson, H., Cánovas, H., Meeus, G., Mendigutía, I., Mora, A., Rivière-Marichalar, P., Villaver, E., Maldonado, J., and Henning, T. (2019). HR 10: a main-sequence binary with circumstellar envelopes around both components. Discovery and analysis. , 629:A19.

Montesinos, B., Eiroa, C., Mora, A., and Merín, B. (2009). Parameters of Herbig Ae/Be and Vega-type stars. , 495(3):901–917.

Montesinos, M., Cuadra, J., Perez, S., Baruteau, C., and Casassus, S. (2015). Protoplanetary Disks Including Radiative Feedback from Accreting Planets. , 806:253.

Montgomery, S. L. and Welsh, B. Y. (2012). Detection of Variable Gaseous Absorption Features in the Debris Disks Around Young A-type Stars. , 124(920):1042.

Montgomery, S. L. and Welsh, B. Y. (2017). Unusually high circumstellar absorption variability around the δ Scuti /λ Boötis star HD 183324. , 468:L55–L58.

Moór, A., Ábrahám, P., Derekas, A., Kiss, C., Kiss, L. L., Apai, D., Grady, C., and Henning, T. (2006). Nearby Debris Disk Systems with High Fractional Luminosity Reconsidered. , 644(1):525–542.

Moór, A., Ábrahám, P., Juhász, A., Kiss, C., Pascucci, I., Kóspál, Á., Apai, D., Henning, T., Csengeri, T., and Grady, C. (2011). Molecular Gas in Young Debris Disks. , 740:L7.

Moór, A., Curé, M., Kóspál, Á., Ábrahám, P., Csengeri, T., Eiroa, C., Gunawan, D., Henning, T., Hughes, A. M., Juhász, A., Pawellek, N., and Wyatt, M. (2017). Molecular Gas in Debris Disks around Young A-type Stars. , 849(2):123.

Moór, A., Juhász, A., Kóspál, Á., Ábrahám, P., Apai, D., Csengeri, T., Grady, C., Henning, T., Hughes, A. M., Kiss, C., Pascucci, I., Schmalzl, M., and Gabányi, K. (2013). ALMA Continuum Observations of a 30 Myr Old Gaseous Debris Disk around HD 21997. , 777(2):L25.

Moór, A., Kóspál, Á., Ábrahám, P., Apai, D., Balog, Z., Grady, C., Henning, T., Juhász, A., Kiss, C., Krivov, A. V., Pawellek, N., and Szabó, G. M. (2015). Stirring in massive, young debris discs from spatially resolved Herschel images. , 447:577–597.

Moór, A., Kral, Q., Ábrahám, P., Kóspál, Á., Dutrey, A., Di Folco, E., Hughes, A. M., Juhász, A., Pascucci, I., and Pawellek, N. (2019). New Millimeter CO Observations of the Gas-rich Debris Disks 49 Cet and HD 32297. , 884(2):108.

Morales, F. Y., Bryden, G., Werner, M. W., and Stapelfeldt, K. R. (2016). Herschel-resolved Outer Belts of Two-belt Debris DisksEvidence of Icy Grains. , 831:97.

Morales, F. Y., Rieke, G. H., Werner, M. W., Bryden, G., Stapelfeldt, K. R., and Su, K. Y. L. (2011). Common Warm Dust Temperatures Around Main-sequence Stars. , 730(2):L29.

Morales, F. Y., Werner, M. W., Bryden, G., Plavchan, P., Stapelfeldt, K. R., Rieke, G. H., Su, K. Y. L., Beichman, C. A., Chen, C. H., Grogan, K., Kenyon, S. J., Moro-Martin, A., and Wolf, S. (2009). Spitzer Mid-IR Spectra of Dust Debris Around A and Late B Type Stars: Asteroid Belt Analogs and Power-Law Dust Distributions. , 699(2):1067–1086.

Morbidelli, A. (2018). *Dynamical Evolution of Planetary Systems*, page 145.

Mordasini, C., Alibert, Y., Klahr, H., and Henning, T. (2012). Characterization of exoplanets from their formation. I. Models of combined planet formation and evolution. , 547:A111.

Morey, É. and Lestrade, J.-F. (2014). On the steady state collisional evolution of debris disks around M dwarfs. , 565:A58.

Morton, D. C. (1991). Atomic data for resonance absorption lines. I - Wavelengths longward of the Lyman limit. , 77:119–202.

Mouillet, D., Larwood, J. D., Papaloizou, J. C. B., and Lagrange, A. M. (1997). A planet on an inclined orbit as an explanation of the warp in the beta Pictoris disc. , 292(4):896–904.

Moura, T., Alencar, S. H. P., Sousa, A. P., Alecian, E., and Lebreton, Y. (2020). Spectroscopic analysis of accretion/ejection signatures in the Herbig Ae/Be stars HD 261941 and V590 Mon. .

Murga, M., Zhu, G., Ménard, B., and Lan, T.-W. (2015). Calcium HK and sodium D absorption induced by the interstellar and circumgalactic media of the Milky Way. , 452:511–519.

Nazé, Y., Pigulski, A., Rauw, G., and Smith, M. (2020). Let there be more variability in two γ Cas stars. .

Nesvold, E. R. and Kuchner, M. J. (2015). A SMACK Model of Colliding Planetesimals in the β Pictoris Debris Disk. , 815(1):61.

Nesvorný, D., Vokrouhlický, D., Dones, L., Levison, H. F., Kaib, N., and Morbidelli, A. (2017). Origin and Evolution of Short-period Comets. , 845:27.

Nielsen, E. L., De Rosa, R. J., Macintosh, B., Wang, J. J., Ruffio, J.-B., Chiang, E., Marley, M. S., Saumon, D., Savransky, D., Ammons, S. M., Bailey, V. P., Barman, T., Blain, C., Bulger, J., Burrows, A., Chilcote, J., Cotten, T., Czekala, I., Doyon, R., Duchêne, G., Esposito, T. M., Fabrycky, D., Fitzgerald, M. P., Follette, K. B., Fortney, J. J., Gerard, B. L., Goodsell, S. J., Graham, J. R., Greenbaum, A. Z., Hibon, P., Hinkley, S., Hirsch, L. A., Hom, J., Hung, L.-W., Dawson, R. I., Ingraham, P., Kalas, P., Konopacky, Q., Larkin, J. E., Lee, E. J., Lin, J. W., Maire, J., Marchis, F., Marois, C., Metchev, S., Millar-Blanchaer, M. A., Morzinski, K. M., Oppenheimer, R., Palmer, D., Patience, J., Perrin, M., Poyneer, L., Pueyo, L., Rafikov, R. R., Rajan, A., Rameau, J., Rantakyrö, F. T., Ren, B., Schneider, A. C., Sivaramakrishnan, A., Song, I., Soummer, R., Tallis, M., Thomas, S., Ward-Duong, K., and Wolff, S. (2019). The Gemini Planet Imager Exoplanet Survey: Giant Planet and Brown Dwarf Demographics from 10 to 100 au. , 158(1):13.

Olofsson, J., Juhász, A., Henning, T., Mutschke, H., Tamanai, A., Moór, A., and Ábrahám, P. (2012). Transient dust in warm debris disks. Detection of Fe-rich olivine grains. , 542:A90.

Olofsson, J., Milli, J., Thébault, P., Kral, Q., Ménard, F., Janson, M., Augereau, J. C., Bayo, A., Beamín, J. C., Henning, T., Iglesias, D., Kennedy, G. M., Montesinos, M., Pawellek, N., Schreiber, M. R., Zamora, C., Carbillet, M., Feautrier, P., Fusco, T., Madec, F., Rabou, P., Sevin, A., Szulágyi, J., and Zurlo, A. (2019). Dust production in the debris disk around HR 4796 A. *arXiv e-prints*, page arXiv:1908.10378.

Olofsson, J., Samland, M., Avenhaus, H., Caceres, C., Henning, T., Moór, A., Milli, J., Canovas, H., Quanz, S. P., Schreiber, M. R., Augereau, J. C., Bayo, A., Bazzon, A., Beuzit, J. L., Boccaletti, A., Buenzli, E., Casassus, S., Chauvin, G., Dominik, C., Desidera, S., Feldt, M., Gratton, R., Janson, M., Lagrange, A. M., Langlois, M., Lannier, J., Maire, A. L., Mesa, D., Pinte, C., Rouan, D., Salter, G., Thalmann, C., and Vigan, A. (2016). Azimuthal asymmetries in the debris disk around HD 61005. A massive collision of planetesimals? , 591:A108.

Olofsson, J., van Holstein, R. G., Boccaletti, A., Janson, M., Thébault, P., Gratton, R., Lazzoni, C., Kral, Q., Bayo, A., Canovas, H., Caceres, C., Ginski, C., Pinte, C., Asensio-Torres, R., Chauvin, G., Desidera, S., Henning, T., Langlois, M., Milli, J., Schlieder, J. E., Schreiber, M. R., Augereau, J. C., Bonnefoy, M., Buenzli, E., Brandner, W., Durkan, S., Engler, N., Feldt, M., Godoy, N., Grady, C., Hagelberg, J., Lagrange, A. M., Lannier, J., Ligi, R., Maire, A. L., Mawet, D., Ménard, F., Mesa, D., Mouillet, D., Peretti, S., Perrot, C., Salter, G., Schmidt, T., Sissa, E., Thalmann, C., Vigan, A., Abe, L., Feautrier, P., Le Mignant, D., Moulin, T., Pavlov, A., Rabou, P., Rousset, G., and Roux, A. (2018). Resolving faint structures in the debris disk around TWA 7. Tentative detections of an outer belt, a spiral arm, and a dusty cloud. , 617:A109.

Ozernoy, L. M., Gorkavyi, N. N., Mather, J. C., and Taidakova, T. A. (2000). Signatures of Exosolar Planets in Dust Debris Disks. , 537(2):L147–L151.

Panić, O., Holland, W. S., Wyatt, M. C., Kennedy, G. M., Matthews, B. C., Lestrade, J. F., Sibthorpe, B., Greaves, J. S., Marshall, J. P., Phillips, N. M., and Tottle, J. (2013). First results of the SONS survey: submillimetre detections of debris discs. , 435(2):1037–1046.

Pavlov, A., Möller-Nilsson, O., Feldt, M., Henning, T., Beuzit, J.-L., and Mouillet, D. (2008). SPHERE data reduction and handling system: overview, project status, and development. In , volume 7019 of *Society of Photo-Optical Instrumentation Engineers (SPIE) Conference Series*, page 701939.

Pavlov, A. A., Toon, O. B., Pavlov, A. K., Bally, J., and Pollard, D. (2005). Passing through a giant molecular cloud: “Snowball” glaciations produced by interstellar dust. , 32(3):L03705.

Pawellek, N., Moór, A., Milli, J., Kóspál, Á., Olofsson, J., Ábrahám, P., Keppler, M., Kral, Q., Pohl, A., Augereau, J.-C., Boccaletti, A., Chauvin, G., Choquet, É., Engler, N., Henning, T., Langlois, M., Lee, E. J., Ménard, F., Thébault, P., and Zurlo, A. (2019). A multiwavelength study of the debris disc around 49 Cet. , 488(3):3507–3525.

Pearce, T. D. and Wyatt, M. C. (2014). Dynamical evolution of an eccentric planet and a less massive debris disc. , 443(3):2541–2560.

Pecaut, M. J. and Mamajek, E. E. (2013). Intrinsic Colors, Temperatures, and Bolometric Corrections of Pre-main-sequence Stars. , 208:9.

Pecaut, M. J. and Mamajek, E. E. (2016). The star formation history and accretion-disc fraction among the K-type members of the Scorpius-Centaurus OB association. , 461(1):794–815.

Pecaut, M. J., Mamajek, E. E., and Bubar, E. J. (2012). A Revised Age for Upper Scorpius and the Star Formation History among the F-type Members of the Scorpius-Centaurus OB Association. , 746(2):154.

Perrin, M. D., Duchene, G., Millar-Blanchaer, M., Fitzgerald, M. P., Graham, J. R., Wiktorowicz, S. J., Kalas, P. G., Macintosh, B., Bauman, B., Cardwell, A., Chilcote, J., De Rosa, R. J., Dillon, D., Doyon, R., Dunn, J., Erikson, D., Gavel, D., Goodsell, S., Hartung, M., Hibon, P., Ingraham, P., Kerley, D., Konapacky, Q., Larkin, J. E., Maire, J., Marchis, F., Marois, C., Mittal, T., Morzinski, K. M., Oppenheimer, B. R., Palmer, D. W., Patience, J., Poyneer, L., Pueyo, L., Rantakyrö, F. T., Sadakuni, N., Saddlemyer, L., Savransky, D., Soummer, R., Sivaramakrishnan, A., Song, I., Thomas, S., Wallace, J. K., Wang, J. J., and Wolff, S. G. (2015). Polarimetry with the Gemini Planet Imager: Methods, Performance at First Light, and the Circumstellar Ring around HR 4796A. , 799(2):182.

Plez, B. (2013). Model atmospheres and fundamental stellar parameters. In Cambresy, L., Martins, F., Nuss, E., and Palacios, A., editors, *SF2A-2013: Proceedings of the Annual meeting of the French Society of Astronomy and Astrophysics*, pages 141–146.

Pontoppidan, K. M., Salyk, C., Bergin, E. A., Brittain, S., Marty, B., Mousis, O., and Öberg, K. I. (2014). Volatiles in Protoplanetary Disks. *Protostars and Planets VI*, pages 363–385.

Poppe, A. R., Lisse, C. M., Piquette, M., Zemcov, M., Horányi, M., James, D., Szalay, J. R., Bernardoni, E., and Stern, S. A. (2019). Constraining the Solar System's Debris Disk with In Situ New Horizons Measurements from the EdgeworthâŤĂKuiper Belt. , 881(1):L12.

Przybilla, N., Nieva, M.-F., and Butler, K. (2011). Testing common classical LTE and NLTE model atmosphere and line-formation codes for quantitative spectroscopy of early-type stars. In *Journal of Physics Conference Series*, volume 328 of *Journal of Physics Conference Series*, page 012015.

Quillen, A. C., Morbidelli, A., and Moore, A. (2007). Planetary embryos and planetesimals residing in thin debris discs. , 380(4):1642–1648.

Rameau, J., Chauvin, G., Lagrange, A. M., Boccaletti, A., Quanz, S. P., Bonnefoy, M., Girard, J. H., Delorme, P., Desidera, S., Klahr, H., Mordasini, C., Dumas, C., and Bonavita, M. (2013). Discovery of a Probable 4-5 Jupiter-mass Exoplanet to HD 95086 by Direct Imaging. , 772(2):L15.

Raskin, G., van Winckel, H., Hensberge, H., Jorissen, A., Lehmann, H., Waelkens, C., Avila, G., de Cuyper, J. P., Degroote, P., Dubosson, R., Dumortier, L., Frémat, Y., Laux, U., Michaud, B., Morren, J., Perez Padilla, J., Pessemier, W., Prins, S., Smolders, K., van Eck, S., and Winkler, J. (2011). HERMES: a high-resolution fibre-fed spectrograph for the Mercator telescope. , 526:A69.

Raymond, S. N., Armitage, P. J., Moro-Martín, A., Booth, M., Wyatt, M. C., Armstrong, J. C., Mand ell, A. M., Selsis, F., and West, A. A. (2012). Debris disks as signposts of terrestrial planet formation. II. Dependence of exoplanet architectures on giant planet and disk properties. , 541:A11.

Rebollido, I., Eiroa, C., Montesinos, B., Maldonado, J., Villaver, E., Absil, O., Bayo, A., Canovas, H., Carmona, A., Chen, C., Ertel, S., Garufi, A., Henning, T., Iglesias, D. P., Launhardt, R., Liseau, R., Meeus, G., Moór, A., Mora, A., Olofsson, J., Rauw, G., and Riviere-Marichalar, P. (2018). The co-existence of hot and cold gas in debris discs. , 614:A3.

Rebollido, I., Eiroa, C., Montesinos, B., Maldonado, J., Villaver, E., Absil, O., Bayo, A., Canovas, H., Carmona, A., Chen, C., Ertel, S., Henning, T., Iglesias, D. P., Launhardt, R., Liseau, R., Meeus, G., Moór, A., Mora, A., Olofsson, J., Rauw, G., and Riviere-Marichalar, P. (2020). Exocomets: A spectroscopic survey. *arXiv e-prints*, page arXiv:2003.11084.

Redfield, S. (2006). *The Local Interstellar Medium*, volume 352 of *Astronomical Society of the Pacific Conference Series*, page 79.

Redfield, S. (2007). Gas Absorption Detected from the Edge-on Debris Disk Surrounding HD 32297. , 656:L97–L100.

Redfield, S. and Linsky, J. L. (2008). The Structure of the Local Interstellar Medium. IV. Dynamics, Morphology, Physical Properties, and Implications of Cloud-Cloud Interactions. , 673:283–314.

Redfield, S. and Linsky, J. L. (2015). Evaluating the Morphology of the Local Interstellar Medium: Using New Data to Distinguish between Multiple Discrete Clouds and a Continuous Medium. , 812(2):125.

Ren, B., Pueyo, L., Zhu, G. B., Debes, J., and Duchêne, G. (2018). Non-negative Matrix Factorization: Robust Extraction of Extended Structures. , 852(2):104.

Rhee, J. H., Song, I., Zuckerman, B., and McElwain, M. (2007). Characterization of Dusty Debris Disks: The IRAS and Hipparcos Catalogs. , 660:1556–1571.

Ricci, L., Carpenter, J. M., Fu, B., Hughes, A. M., Corder, S., and Isella, A. (2015). ALMA Observations of the Debris Disk around the Young Solar Analog HD 107146. , 798(2):124.

Ricker, G. R. (2015). The Transiting Exoplanet Survey Satellite (TESS): Discovering New Earths and Super-Earths in the Solar Neighborhood. In *AAS/Division for Extreme Solar Systems Abstracts*, volume 47, page 503.01.

Riviere-Marichalar, P., Barrado, D., Augereau, J.-C., Thi, W. F., Roberge, A., Eiroa, C., Montesinos, B., Meeus, G., Howard, C., Sandell, G., Duchêne, G., Dent, W. R. F., Lebreton, J., Mendigutía, I., Huélamo, N., Ménard, F., and Pinte, C. (2012). HD 172555: detection of 63 μm [OI] emission in a debris disc. , 546:L8.

Riviere-Marichalar, P., Barrado, D., Montesinos, B., Duchêne, G., Bouy, H., Pinte, C., Menard, F., Donaldson, J., Eiroa, C., Krivov, A. V., Kamp, I., Mendigutía, I., Dent, W. R. F., and Lillo-Box, J. (2014). Gas and dust in the beta Pictoris moving group as seen by the Herschel Space Observatory. , 565:A68.

Roberge, A., Feldman, P. D., Weinberger, A. J., Deleuil, M., and Bouret, J.-C. (2006). Stabilization of the disk around βPictoris by extremely carbon-rich gas. , 441:724–726.

Roberge, A., Kamp, I., Montesinos, B., Dent, W. R. F., Meeus, G., Donaldson, J. K., Olofsson, J., Moór, A., Augereau, J. C., Howard, C., Eiroa, C., Thi, W. F., Ardila, D. R., Sandell, G., and Woitke, P. (2013). Herschel Observations of Gas and Dust in the Unusual 49 Ceti Debris Disk. , 771(1):69.

Roberge, A. and Weinberger, A. J. (2008). Debris Disks around Nearby Stars with Circumstellar Gas. , 676(1):509–517.

Roberge, A., Welsh, B. Y., Kamp, I., Weinberger, A. J., and Grady, C. A. (2014). Volatile-rich Circumstellar Gas in the Unusual 49 Ceti Debris Disk. , 796:L11.

Rodigas, T. J., Malhotra, R., and Hinz, P. M. (2014). Predictions for Shepherding Planets in Scattered Light Images of Debris Disks. , 780(1):65.

Sai, S., Itoh, Y., Fukagawa, M., Shibai, H., and Sumi, T. (2015). Near-infrared image of the debris disk around HD 15115. , 67(2):20.

Savage, B. D. and Sembach, K. R. (1991). The analysis of apparent optical depth profiles for interstellar absorption lines. , 379:245–259.

Savage, B. D. and Sembach, K. R. (1996). Interstellar Abundances from Absorption-Line Observations with the Hubble Space Telescope. , 34:279–330.

Sbordone, L., Bonifacio, P., Castelli, F., and Kurucz, R. L. (2004). ATLAS and SYNTHE under Linux. *Memorie della Societa Astronomica Italiana Supplementi*, 5:93.

Scherer, K., Fichtner, H., Borrmann, T., Beer, J., Desorgher, L., Flükiger, E., Fahr, H. J., Ferreira, S. E. S., Langner, U. W., Potgieter, M. S., Heber, B., Masarik, J., Shaviv, N., and Veizer, J. (2006). Interstellar-Terrestrial Relations: Variable Cosmic Environments, The Dynamic Heliosphere, and Their Imprints on Terrestrial Archives and Climate. , 127(1-4):327–465.

Schneider, G., Grady, C. A., Hines, D. C., Stark, C. C., Debes, J. H., Carson, J., Kuchner, M. J., Perrin, M. D., Weinberger, A. J., Wisniewski, J. P., Silverstone, M. D., Jang-Condell, H., Henning, T., Woodgate, B. E., Serabyn, E., Moro-Martin, A., Tamura, M., Hinz, P. M., and Rodigas, T. J. (2014). Probing for Exoplanets Hiding in Dusty Debris Disks: Disk Imaging, Characterization, and Exploration with HST/STIS Multi-roll Coronagraphy. , 148(4):59.

Schneider, G., Smith, B. A., Becklin, E. E., Koerner, D. W., Meier, R., Hines, D. C., Lowrance, P. J., Terrile, R. J., Thompson, R. I., and Rieke, M. (1999). NICMOS Imaging of the HR 4796A Circumstellar Disk. , 513(2):L127–L130.

Schüppler, C., Krivov, A. V., Löhne, T., Booth, M., Kirchschlager, F., and Wolf, S. (2016). Origin and evolution of two-component debris discs and an application to the q^1 Eridani system. , 461(2):2146–2154.

Shakura, N. I. and Sunyaev, R. A. (1973). Black holes in binary systems. Observational appearance. , 24:337–355.

Shappee, B. J., Prieto, J. L., Grupe, D., Kochanek, C. S., Stanek, K. Z., De Rosa, G., Mathur, S., Zu, Y., Peterson, B. M., Pogge, R. W., Komossa, S., Im, M., Jencson, J., Holoien, T. W.-S., Basu, U., Beacom, J. F., Szczygieł, D. M., Brimacombe, J., Adams, S., Campillay, A., Choi, C., Contreras, C., Dietrich, M., Dubberley, M., Elphick, M., Foale, S., Giustini, M., Gonzalez, C., Hawkins, E., Howell, D. A., Hsiao, E. Y., Koss, M., Leighly, K. M., Morrell, N., Mudd, D., Mullins, D., Nugent, J. M., Parrent, J., Phillips, M. M., Pojmanski, G., Rosing, W., Ross, R., Sand, D., Terndrup, D. M., Valenti, S., Walker, Z., and Yoon, Y. (2014). The Man behind the Curtain: X-Rays Drive the UV through NIR Variability in the 2013 Active Galactic Nucleus Outburst in NGC 2617. , 788:48.

Sibthorpe, B., Kennedy, G. M., Wyatt, M. C., Lestrade, J. F., Greaves, J. S., Matthews, B. C., and Duchêne, G. (2018). Analysis of the Herschel DEBRIS Sun-like star sample. , 475(3):3046–3064.

Siess, L., Dufour, E., and Forestini, M. (2000). An internet server for pre-main sequence tracks of low- and intermediate-mass stars. , 358:593–599.

Silaj, J., Jones, C. E., Sigut, T. A. A., and Tycner, C. (2014). The Hα Profiles of Be Shell Stars. , 795(1):82.

Siluk, R. S. and Silk, J. (1974). On the velocity dependence of the interstellar Na I/Ca II ratio. , 192:51–57.

Sissa, E., Olofsson, J., Vigan, A., Augereau, J. C., D'Orazi, V., Desidera, S., Gratton, R., Langlois, M., Rigliaco, E., Boccaletti, A., Kral, Q., Lazzoni, C., Mesa, D., Messina, S., Sezestre, E., Thébault, P., Zurlo, A., Bhowmik, T., Bonnefoy, M., Chauvin, G., Feldt, M., Hagelberg, J., Lagrange, A. M., Janson, M., Maire, A. L., Ménard, F., Schlieder, J., Schmidt, T., Szulágyi, J., Stadler, E., Maurel, D., Delboulbé, A., Feautrier, P., Ramos, J., and Rigal, F. (2018). New disk discovered with VLT/SPHERE around the M star GSC 07396-00759. , 613:L6.

Sitnova, T., Ryabchikova, T., Alexeeva, S., and Mashonkina, L. (2017). NLTE abundances of C, O, Ca, Ti, and Fe in the reference BAF-type stars. *ArXiv e-prints*.

Slettebak, A. (1975). Some interesting bright southern stars of early type. , 197:137–138.

Slettebak, A. (1982). Spectral types and rotational velocities of the brighter Be stars and A-F type shell stars. , 50:55–83.

Slettebak, A. (1986). H-alpha and near-infrared spectra of late-type Be and A-F-type shell stars. , 98:867–871.

Smette, A., Sana, H., Noll, S., Horst, H., Kausch, W., Kimeswenger, S., Barden, M., Szyszka, C., Jones, A. M., Gallenne, A., Vinther, J., Ballester, P., and Taylor, J. (2015). Molecfit: A general tool for telluric absorption correction. I. Method and application to ESO instruments. , 576:A77.

Smith, D. S. and Scalo, J. M. (2009). Habitable Zones Exposed: Astrosphere Collapse Frequency as a Function of Stellar Mass. *Astrobiology*, 9(7):673–681.

Smith, K. T., Fossey, S. J., Cordiner, M. A., Sarre, P. J., Smith, A. M., Bell, T. A., and Viti, S. (2013). Small-scale structure in the interstellar medium: time-varying interstellar absorption towards κ Velorum. , 429(2):939–953.

Smith, R., Churcher, L. J., Wyatt, M. C., Moerchen, M. M., and Telesco, C. M. (2009). Resolved debris disc emission around η Telescopii: a young solar system or ongoing planet formation? , 493(1):299–308.

Smith, R., Wyatt, M. C., and Haniff, C. A. (2012). Resolving the terrestrial planet forming regions of HD 113766 and HD 172555 with MIDI. , 422(3):2560–2580.

Smoker, J. V., Bagnulo, S., Cabanac, R., Keenan, F. P., Fossati, L., Ledoux, C., Jehin, E., and Melo, C. (2011). Early-type stars observed in the ESO UVES Paranal Observatory Project - III. Sub-parsec and au-scale structure in the interstellar medium*. , 414(1):59–75.

Smoker, J. V., Keenan, F. P., and Fox, A. J. (2015). The large- and small-scale Ca II K structure of the Milky Way from observations of Galactic and Magellanic sightlines$\star$. , 582:A59.

Strubbe, L. E. and Chiang, E. I. (2006). Dust Dynamics, Surface Brightness Profiles, and Thermal Spectra of Debris Disks: The Case of AU Microscopii. , 648(1):652–665.

Stumpe, M. C., Smith, J. C., Van Cleve, J. E., Twicken, J. D., Barclay, T. S., Fanelli, M. N., Girouard, F. R., Jenkins, J. M., Kolodziejczak, J. J., McCauliff, S. D., and Morris, R. L. (2012). Kepler Presearch Data Conditioning I—Architecture and Algorithms for Error Correction in Kepler Light Curves. *Publications of the Astronomical Society of the Pacific*, 124:985.

Su, K. Y. L., MacGregor, M. A., Booth, M., Wilner, D. J., Flaherty, K., Hughes, A. M., Phillips, N. M., Malhotra, R., Hales, A. S., Morrison, S., Ertel, S., Matthews, B. C., Dent, W. R. F., and Casassus, S. (2017). ALMA 1.3 mm Map of the HD 95086 System. , 154(6):225.

Su, K. Y. L., Rieke, G. H., Stansberry, J. A., Bryden, G., Stapelfeldt, K. R., Trilling, D. E., Muzerolle, J., Beichman, C. A., Moro-Martin, A., Hines, D. C., and Werner, M. W. (2006). Debris Disk Evolution around A Stars. , 653:675–689.

Takeuchi, T. and Artymowicz, P. (2001). Dust Migration and Morphology in Optically Thin Circumstellar Gas Disks. , 557(2):990–1006.

Talens, G. J. J., Deul, E. R., Stuik, R., Burggraaff, O., Lesage, A. L., Spronck, J. F. P., Mellon, S. N., Bailey, J. I., Mamajek, E. E., Kenworthy, M. A., and Snellen, I. A. G. (2018). Data calibration for the MASCARA and bRing instruments. , 619:A154.

Talens, G. J. J., Spronck, J. F. P., Lesage, A. L., Otten, G. P. P. L., Stuik, R., Pollacco, D., and Snellen, I. A. G. (2017). The Multi-site All-Sky CAmeRA (MASCARA). Finding transiting exoplanets around bright (m_V < 8) stars. , 601:A11.

Telesco, C. M., Fisher, R. S., Wyatt, M. C., Dermott, S. F., Kehoe, T. J. J., Novotny, S., Mariñas, N., Radomski, J. T., Packham, C., De Buizer, J., and Hayward, T. L. (2005). Mid-infrared images of β Pictoris and the possible role of planetesimal collisions in the central disk. , 433(7022):133–136.

Telting, J. H., Avila, G., Buchhave, L., Frandsen, S., Gandolfi, D., Lindberg, B., Stempels, H. C., Prins, S., and NOT staff (2014). FIES: The high-resolution Fiber-fed Echelle Spectrograph at the Nordic Optical Telescope. *Astronomische Nachrichten*, 335(1):41.

Thébault, P. (2009). Vertical structure of debris discs. , 505(3):1269–1276.

Thébault, P. and Augereau, J. C. (2007). Collisional processes and size distribution in spatially extended debris discs. , 472(1):169–185.

Thébault, P. and Beust, H. (2001). Falling evaporating bodies in the β Pictoris system. Resonance refilling and long term duration of the phenomenon. , 376:621–640.

Thi, W. F., Blake, G. A., van Dishoeck, E. F., van Zadelhoff, G. J., Horn, J. M. M., Becklin, E. E., Mannings, V., Sargent, A. I., van den Ancker, M. E., and Natta, A. (2001a). Substantial reservoirs of molecular hydrogen in the debris disks around young stars. , 409(6816):60–63.

Thi, W. F., Pinte, C., Pantin, E., Augereau, J. C., Meeus, G., Ménard, F., Martin-Zaïdi, C., Woitke, P., Riviere-Marichalar, P., Kamp, I., Carmona, A., Sandell, G., Eiroa, C., Dent, W., Montesinos, B., Aresu, G., Meijerink, R., Spaans, M., White, G., Ardila, D., Lebreton, J., Mendigutía, I., and Brittain, S. (2014). Gas lines from the 5-Myr old optically thin disk around HD 141569A . Herschel observations and modeling. , 561:A50.

Thi, W. F., van Dishoeck, E. F., Blake, G. A., van Zadelhoff, G. J., Horn, J., Becklin, E. E., Mannings, V., Sargent, A. I., van den Ancker, M. E., Natta, A., and Kessler, J. (2001b). H_2 and CO Emission from Disks around T Tauri and Herbig Ae Pre-Main-Sequence Stars and from Debris Disks around Young Stars: Warm and Cold Circumstellar Gas. , 561(2):1074–1094.

Tobin, W., Barnes, S. I., Persson, S., and Pollard, K. R. (2019). β Pictoris: observations of the Ca II H&K absorptions in 1997 and 1998. , 489(1):574–593.

Torres, C. A. O., Quast, G. R., da Silva, L., de La, R. R., Melo, C. H. F., and Sterzik, M. (2006). VizieR Online Data Catalog: Search for Associations Containing Young stars (Torres+, 2006). *VizieR Online Data Catalog*, 346.

Vallerga, J. V., Vedder, P. W., Craig, N., and Welsh, B. Y. (1993). High-Resolution CA II Observations of the Local Interstellar Medium. , 411:729.

van Leeuwen, F. (2007). Validation of the new Hipparcos reduction. , 474:653–664.

Vican, L. (2012). Age Determination for 346 Nearby Stars in the Herschel DEBRIS Survey. , 143(6):135.

Vidal-Madjar, A., Kiefer, F., Lecavelier des Etangs, A., Bourrier, V., Ehrenreich, D., Ferlet, R., Hébrard, G., and Wilson, P. A. (2017). Fe I in the β Pictoris circumstellar gas disk. I. Physical properties of the neutral iron gas. , 607:A25.

Vigan, A., Moutou, C., Langlois, M., Allard, F., Boccaletti, A., Carbillet, M., Mouillet, D., and Smith, I. (2010). Photometric characterization of exoplanets using angular and spectral differential imaging. , 407(1):71–82.

Visser, R., van Dishoeck, E. F., and Black, J. H. (2009). The photodissociation and chemistry of CO isotopologues: applications to interstellar clouds and circumstellar disks. , 503(2):323–343.

Wahhaj, Z., Liu, M. C., Biller, B. A., Nielsen, E. L., Hayward, T. L., Kuchner, M., Close, L. M., Chun, M., Ftaclas, C., and Toomey, D. W. (2014). The Gemini NICI planet-finding campaign: The offset ring of HR 4796 A. , 567:A34.

Wang, J. J., Graham, J. R., Pueyo, L., Nielsen, E. L., Millar-Blanchaer, M., De Rosa, R. J., Kalas, P., Ammons, S. M., Bulger, J., Cardwell, A., Chen, C., Chiang, E., Chilcote, J. K., Doyon, R., Draper, Z. H., Duchêne, G., Esposito, T. M., Fitzgerald, M. P., Goodsell, S. J., Greenbaum, A. Z., Hartung, M., Hibon, P., Hinkley, S., Hung, L.-W., Ingraham, P., Larkin, J. E., Macintosh, B., Maire, J., Marchis, F., Marois, C., Matthews, B. C., Morzinski, K. M., Oppenheimer, R., Patience, J., Perrin, M. D., Rajan, A., Rantakyrö, F. T., Sadakuni, N., Serio, A., Sivaramakrishnan, A., Soummer, R., Thomas, S. r., Ward-Duong, K., Wiktorowicz, S. J., and Wolff, S. G. (2015). Gemini Planet Imager Observations of the AU Microscopii Debris Disk: Asymmetries within One Arcsecond. , 811(2):L19.

Welsh, B. Y., Craig, N., Crawford, I. A., and Price, R. J. (1998). Beta Pic-like circumstellar disk gas surrounding HR 10 and HD 85905. , 338:674–682.

Welsh, B. Y., Lallement, R., Vergely, J.-L., and Raimond, S. (2010). New 3D gas density maps of NaI and CaII interstellar absorption within 300 pc. , 510:A54.

Welsh, B. Y. and Montgomery, S. (2013). Circumstellar Gas-Disk Variability Around A-Type Stars: The Detection of Exocomets? , 125:759–774.

Welsh, B. Y. and Montgomery, S. L. (2015). The Appearance and Disappearance of Exocomet Gas Absorption. *Advances in Astronomy*, 2015:980323.

Welsh, B. Y. and Montgomery, S. L. (2018). Further detections of exocomet absorbing gas around Southern hemisphere A-type stars with known debris discs. , 474:1515–1525.

Welsh, B. Y. and Montgomery, S. L. (2019). Warm Circumstellar Disk Gas Surrounding the 1.4 Gyr Old F2V Star HD 109085? *Research Notes of the American Astronomical Society*, 3(1):25.

Welty, D. E., Morton, D. C., and Hobbs, L. M. (1996). A High-Resolution Survey of Interstellar Ca II Absorption. , 106:533.

Wenger, M., Ochsenbein, F., Egret, D., Dubois, P., Bonnarel, F., Borde, S., Genova, F., Jasniewicz, G., Laloë, S., Lesteven, S., and Monier, R. (2000). The SIMBAD astronomical database. The CDS reference database for astronomical objects. , 143:9–22.

Werner, M. W., Roellig, T. L., Low, F. J., Rieke, G. H., Rieke, M., Hoffmann, W. F., Young, E., Houck, J. R., Brandl, B., Fazio, G. G., Hora, J. L., Gehrz, R. D., Helou, G., Soifer, B. T., Stauffer, J., Keene, J., Eisenhardt, P., Gallagher, D., Gautier, T. N., Irace, W., Lawrence, C. R., Simmons, L., Van Cleve, J. E., Jura, M., Wright, E. L., and Cruikshank, D. P. (2004). The Spitzer Space Telescope Mission. , 154:1–9.

Williams, J. P. and Best, W. M. J. (2014). A Parametric Modeling Approach to Measuring the Gas Masses of Circumstellar Disks. , 788:59.

Williams, J. P. and Cieza, L. A. (2011). Protoplanetary Disks and Their Evolution. , 49:67–117.

Wilson, R. E. (1953). General catalogue of stellar radial velocities. *Carnegie Institute Washington D.C. Publication*.

Wise, A. W., Dodson-Robinson, S. E., Bevenour, K., and Provini, A. (2018). New Methods for Finding Activity-sensitive Spectral Lines: Combined Visual Identification and an Automated Pipeline Find a Set of 40 Activity Indicators. , 156(4):180.

Wisniewski, J. P., Kowalski, A. F., Davenport, J. R. A., Schneider, G., Grady, C. A., Hebb, L., Lawson, K. D., Augereau, J.-C., Boccaletti, A., Brown, A., Debes, J. H., Gaspar, A., Henning, T. K., Hines, D. C., Kuchner, M. J., Lagrange, A.-M., Milli, J., Sezestre, E., Stark, C. C., and Thalmann, C. (2019). High-fidelity Imaging of the Inner AU Mic Debris Disk: Evidence of Differential Wind Sculpting? , 883(1):L8.

Wood, B. E., Linsky, J. L., Müller, H.-R., and Zank, G. P. (2003). A Search for Lyα Emission from the Astrosphere of 40 Eridani A. , 591(2):1210–1219.

Wyatt, M. (2020). *Extrasolar Kuiper belts*, pages 351–376.

Wyatt, M. C. (2005). Spiral structure when setting up pericentre glow: possible giant planets at hundreds of AU in the HD 141569 disk. , 440(3):937–948.

Wyatt, M. C. (2006). Dust in Resonant Extrasolar Kuiper Belts: Grain Size and Wavelength Dependence of Disk Structure. , 639(2):1153–1165.

Wyatt, M. C. (2008). Evolution of Debris Disks. , 46:339–383.

Wyatt, M. C. (2018). *Debris Disks: Probing Planet Formation*, page 146.

Wyatt, M. C., Dermott, S. F., Telesco, C. M., Fisher, R. S., Grogan, K., Holmes, E. K., and Piña, R. K. (1999). How Observations of Circumstellar Disk Asymmetries Can Reveal Hidden Planets: Pericenter Glow and Its Application to the HR 4796 Disk. , 527(2):918–944.

Wyatt, M. C., Panić, O., Kennedy, G. M., and Matrà, L. (2015). Five steps in the evolution from protoplanetary to debris disk. , 357:103.

Wyatt, M. C., Smith, R., Greaves, J. S., Beichman, C. A., Bryden, G., and Lisse, C. M. (2007). Transience of Hot Dust around Sun-like Stars. , 658(1):569–583.

Wyatt, M. C., van Lieshout, R., Kennedy, G. M., and Boyajian, T. S. (2018). Modelling the KIC8462852 light curves: compatibility of the dips and secular dimming with an exocomet interpretation. , 473(4):5286–5307.

Zhu, Z., Nelson, R. P., Dong, R., Espaillat, C., and Hartmann, L. (2012). Dust Filtration by Planet-induced Gap Edges: Implications for Transitional Disks. , 755(1):6.

Zieba, S., Zwintz, K., Kenworthy, M. A., and Kennedy, G. M. (2019). Transiting exocomets detected in broadband light by tess in the toris system. *A&A*, 625:L13.

Zorec, J., Frémat, Y., and Cidale, L. (2005). On the evolutionary status of Be stars. I. Field Be stars near the Sun. , 441(1):235–248.

Zorec, J. and Royer, F. (2012). Rotational velocities of A-type stars. IV. Evolution of rotational velocities. , 537:A120.

Zuckerman, B., Forveille, T., and Kastner, J. H. (1995). Inhibition of giant-planet formation by rapid gas depletion around young stars. , 373(6514):494–496.

Zuckerman, B. and Song, I. (2012). A 40 Myr Old Gaseous Circumstellar Disk at 49 Ceti: Massive CO-rich Comet Clouds at Young A-type Stars. , 758(2):77.

Appendix A

Sample

A.1 Identifiers and coordinates of the full sample

Table A.1: Identifiers and coordinates of the sample.

Simbad	HD	HR	HIP	My ID	RA	DEC
HD 225200	225200	9102	345	HR9102	00:04:20.31	-29:16:07.75
HD 166	166	8	544	HD166	00:06:36.78	+29:01:17.40
HD 203	203	9	560	HR9	00:06:50.08	-23:06:27.14
HD 870	870		1031	HD870	00:12:50.24	-57:54:45.39
*sig And	1404	68	1473	sigAnd	00:18:19.65	+36:47:06.81
HD 1466	1466		1481	HD1466	00:18:26.12	-63:28:38.98
HD 1461	1461	72	1499	HD1461	00:18:41.86	-08:03:10.80
*kap Phe	2262	100	2072	kapPhe	00:26:12.20	-43:40:47.39
*lam01 Phe	2834	125	2472	lam01Phe	00:31:24.98	-48:48:12.65
*lam Cas	2772	123	2505	lamCas	00:31:46.35	+54:31:20.22
*bet03 Tuc	3003	136	2578	bet03Tuc	00:32:43.90	-63:01:53.40
HD 3670	3670			HD3670	00:38:56.70	-52:32:03.42

Continued on next page

Table A.1 – continued from previous page

Simbad	HD	HR	HIP	My ID	RA	DEC
*66 Psc	5267	254	4267	66Psc	00:54:35.22	+19:11:18.30
HD 6798	6798	333	5626	HR333	01:12:16.81	+79:40:26.26
*nu. Phe	7570	370	5862	nuPhe	01:15:11.12	-45:31:53.99
*49 Cet	9672	451	7345	49Cet	01:34:37.77	-15:40:34.89
HD 10472	10472		7805	HD10472	01:40:24.06	-60:59:56.62
*q01 Eri	10647	506	7978	q01Eri	01:42:29.31	-53:44:27.00
HD 10638	10638		8122	HD10638	01:44:22.81	+32:30:57.16
*q02 Eri	10939	520	8241	q02Eri	01:46:06.26	-53:31:19.32
V* DK Cet	12039		9141	VDK_Cet	01:57:48.97	-21:54:05.34
*50 Cas	12216	580	9598	50Cas	02:03:26.10	+72:25:16.65
HD 13246	13246		9902	HD13246	02:07:26.12	-59:40:45.94
HD 12467	12467	597	10054	HR597	02:09:25.31	+81:17:45.39
*bet Tri	13161	622	10064	betTri	02:09:32.62	+34:59:14.26
*gam Tri	14055	664	10670	gamTri	02:17:18.86	+33:50:49.89
HD 15115	15115		11360	HD15115	02:26:16.24	+06:17:33.18
*phi For	15427	724	11477	phiFor	02:28:01.70	-33:48:39.74
*12 Tri	15257	717	11486	12Tri	02:28:09.98	+29:40:09.58
HD 15745	15745		11847	HD15745	02:32:55.81	+37:20:01.04
HD 16743	16743		12361	HD16743	02:39:07.56	-52:56:05.30
HD 17390	17390	826	12964	HR826	02:46:45.10	-21:38:22.27
*nu. Hor	17848	852	13141	nuHor	02:49:01.48	-62:48:23.47
*41 Ari	17573	838	13209	41Ari	02:49:59.03	+27:15:37.82
*alf For	20010	963	14879	alfFor	03:12:04.52	-28:59:15.43
*94 Cet	19994	962	14954	94Cet	03:12:46.43	-01:11:45.96
HD 21997	21997	1082	16449	HD21997	03:31:53.64	-25:36:50.93
HD 23267	23267		17549	HD23267	03:45:31.06	+42:00:24.92
V* V1229 Tau	23642		17704	VV1229Tau	03:47:29.45	+24:17:18.03

Continued on next page

Table A.1 – continued from previous page

Simbad	HD	HR	HIP	My ID	RA	DEC
HD 24636	24636		17764	HD24636	03:48:11.47	-74:41:38.81
*28 Tau	23862	1180	17851	28Tau	03:49:11.21	+24:08:12.15
HD 23863	23863			HD23863	03:49:12.18	+23:53:12.45
HD 23923	23923	1183	17900	HR1183	03:49:43.53	+23:42:42.67
HD 24141	24141	1192	18217	HR1192	03:53:43.28	+57:58:30.51
HD 24966	24966		18437	HD24966	03:56:29.37	-38:57:43.80
HD 24817	24817	1224	18481	HR1224	03:57:01.71	+06:02:23.89
HD 25457	25457	1249	18859	HD25457	04:02:36.74	-00:16:08.12
HD 25570	25570	1254	18975	HR1254	04:03:56.60	+08:11:50.15
*gam Dor	27290	1338	19893	gamDor	04:16:01.58	-51:29:11.94
*b Tau	28355	1414	20901	bTau	04:28:50.16	+13:02:51.36
V* EX Eri	30422	1525	22192	VEX_Eri	04:46:25.74	-28:05:14.80
HD 30447	30447		22226	HD30447	04:46:49.52	-26:18:08.84
HD 32195	32195		22295	HD32195	04:48:05.17	-80:46:45.25
*pi.01 Ori	31295	1570	22845	pi01Ori	04:54:53.72	+10:09:02.99
*l Tau	32977	1658	23871	lTau	05:07:48.39	+20:25:06.16
*kap Lep	33949	1705	24327	kapLep	05:13:13.87	-12:56:28.64
HD 34324	34324		24528	HD34324	05:15:43.90	-22:53:39.70
HD 35150	35150			HD35150	05:22:47.95	+01:43:00.29
HD 287787	287787			HD287787	05:23:06.87	+01:18:23.76
HD 35332	35332			HD35332	05:24:07.85	+01:38:00.14
HD 35367	35367			HD35367	05:24:20.74	+01:35:26.59
HD 287861	287861			HD287861	05:25:10.29	+01:15:31.37
HD 287850	287850			HD287850	05:25:39.79	+01:38:18.35
HD 287854	287854			HD287854	05:25:48.65	+01:23:22.05
HD 35625	35625			HD35625	05:26:11.98	+01:53:35.73
HD 35841	35841			HD35841	05:26:36.58	-22:29:23.72

Continued on next page

Table A.1 – continued from previous page

Simbad	HD	HR	HIP	My ID	RA	DEC
HD 290540	290540			HD290540	05:31:31.35	-01:49:33.27
HD 36444	36444			HD36444	05:31:40.48	-01:07:33.29
HD 290609	290609			HD290609	05:33:05.58	-01:43:15.50
HD 36968	36968			HD36968	05:33:24.06	-39:27:04.63
HD 37286	37286	1915	26309	HR1915	05:36:10.29	-28:42:28.84
HD 37306	37306	1919	26395	HR1919	05:37:08.77	-11:46:31.85
HD 37484	37484		26453	HD37484	05:37:39.62	-28:37:34.66
HD 38056	38056	1966	26796	HR1966	05:41:26.92	-33:24:02.66
HD 38207	38207			HD38207	05:43:20.95	-20:11:21.46
HD 38206	38206	1975	26966	HR1975	05:43:21.67	-18:33:26.91
*zet Lep	38678	1998	27288	zetLep	05:46:57.34	-14:49:19.01
HD 38858	38858	2007	27435	HD38858	05:48:34.93	-04:05:40.71
*eta Lep	40136	2085	28103	etaLep	05:56:24.29	-14:10:03.71
HD 40540	40540		28230	HD40540	05:57:52.59	-34:28:34.01
HD 45184	45184	2318	30503	HD45184	06:24:43.87	-28:46:48.41
HD 46190	46190		30760	HD46190	06:27:48.61	-62:08:59.72
HD 53842	53842		32435	HD53842	06:46:13.54	-83:59:29.52
*psi05 Aur	48682A	2483	32480	psi05Aur	06:46:44.33	+43:34:38.72
HD 50571	50571	2562	32775	HR2562	06:50:01.01	-60:14:56.91
HD 53143	53143		33690	HD53143	06:59:59.65	-61:20:10.25
HD 52265	52265	2622	33719	HD52265	07:00:18.03	-05:22:01.78
HD 54341	54341		34276	HD54341	07:06:20.93	-43:36:38.69
*bet CMi	58715	2845	36188	betCMi	07:27:09.04	+08:17:21.53
HD 61005	61005		36948	HD61005	07:35:47.46	-32:12:14.04
HD 60856	60856		36967	HD60856	07:35:56.95	-14:42:39.01
HD 60995	60995			HD60995	07:36:32.77	-14:14:33.44
*rho Pup	67523	3185	39757	rhoPup	08:07:32.64	-24:18:15.56

Continued on next page

Table A.1 – continued from previous page

Simbad	HD	HR	HIP	My ID	RA	DEC
HD 68420	68420			HD68420	08:10:08.41	-49:00:43.41
HD 69830	69830	3259	40693	HD69830	08:18:23.94	-12:37:55.81
HD 71043	71043	3300	41081	HR3300	08:22:55.15	-52:07:25.42
HD 70313	70313	3277	41152	HR3277	08:23:48.50	+53:13:10.96
*30 Mon	71155	3314	41307	30Mon	08:25:39.63	-03:54:23.11
HD 71722	71722	3341	41373	HD71722	08:26:25.20	-52:48:26.99
V* pi.01 UMa	72905	3391	42438	Vpi01UMa	08:39:11.70	+65:01:15.26
HD 74340	74340			HD74340	08:41:09.98	-52:54:10.5
*eta Cha	75416	3502	42637	etaCha	08:41:19.51	-78:57:48.09
HD 74374	74374			HD74374	08:41:22.76	-53:38:09.46
*50 Cnc	74873	3481	43121	50Cnc	08:46:56.01	+12:06:35.82
HD 76151	76151	3538	43726	HD76151	08:54:17.94	-05:26:04.05
HD 76653	76653	3570	43797	HR3570	08:55:11.78	-54:57:56.76
*omi01 Cnc	76543	3561	43970	omi01Cnc	08:57:14.95	+15:19:21.95
*omi02 Cnc	76582	3565	44001	omi02Cnc	08:57:35.20	+15:34:52.61
HD 78702	78702	3638	44923	HR3638	09:09:04.20	-18:19:42.78
HD 79108	79108	3651	45167	HR3651	09:12:12.88	+03:52:01.11
*tet Hya	79469	3665	45336	tetHya	09:14:21.86	+02:18:51.34
HD 80950	80950	3721	45585	HD80950	09:17:27.56	-74:44:04.52
HD 82943	82943		47007	HD82943	09:34:50.73	-12:07:46.37
HD 84075	84075		47135	HD84075	09:36:17.81	-78:20:41.57
HD 84870	84870		48164	HD84870	09:49:02.84	+34:05:07.42
HD 86087	86087	3927	48613	HR3927	09:54:51.23	-50:14:38.25
*21 LMi	87696	3974	49593	21LMi	10:07:25.76	+35:14:40.89
HD 88215	88215	3991	49809	HR3991	10:10:05.88	-12:48:57.32
HD 90874	90874	4115	51194	HD90874	10:27:25.28	-65:42:16.78
HD 91375	91375	4138	51438	HR4138	10:30:20.12	-71:59:34.06

Continued on next page

Table A.1 – continued from previous page

Simbad	HD	HR	HIP	My ID	RA	DEC
HD 92536	92536		52160	HD92536	10:39:22.83	-64:06:42.43
V* CE Ant				VCE_Ant	10:42:30.06	-33:40:16.62
HD 93738	93738		52815	HD93738	10:47:53.53	-64:15:46.22
HD 95086	95086		53524	HD95086	10:57:03.02	-68:40:02.45
*bet UMa	95418	4295	53910	betUMa	11:01:50.47	+56:22:56.73
*b Leo	95608	4300	53954	bLeo	11:02:19.77	+20:10:47.42
HD 95698	95698	4302	53963	HD95698	11:02:24.45	-26:49:53.42
*tet Leo	97633	4359	54879	tetLeo	11:14:14.40	+15:25:46.45
HD 98363	98363		55188	HD98363	11:17:58.13	-64:02:33.34
HD 98673	98673	4388	55485	HR4388	11:21:49.28	+57:04:29.48
HD 101088	101088		56673	HD101088	11:37:14.65	-69:40:27.17
*pi. Cha	101132	4479	56675	piCha	11:37:15.63	-75:53:47.56
HD 102458	102458A		57524	HD102458	11:47:24.54	-49:53:03.01
*bet Leo	102647	4534	57632	betLeo	11:49:03.57	+14:34:19.40
HD 103234	103234		57950	HD103234	11:53:08.00	-56:43:38.10
HD 103266	103266	4553	57971	HD103266	11:53:26.80	-35:03:59.91
HD 103703	103703		58220	HD103703	11:56:26.56	-58:49:16.83
HD 104231	104231		58528	HD104231	12:00:09.40	-57:07:01.99
HD 104600	104600	4597	58720	HR4597	12:02:37.69	-69:11:32.23
*eta Cru	105211B	4616	59072	etaCru	12:06:52.89	-64:36:49.42
HD 105613	105613		59282	HD105613	12:09:38.78	-58:20:58.75
*3 Crv	105850	4635	59394	3Crv	12:11:03.83	-23:36:08.72
HD 105857	105857		59397	HD105857	12:11:05.87	-56:24:04.89
HD 105912	105912		59422	HD105912	12:11:21.79	-03:46:43.93
HD 106036	106036		59502	HD106036	12:12:10.27	-63:27:14.81
CD-54 4621				CD54_4621	12:12:35.75	-55:20:27.29
HD 106389	106389		59693	HD106389	12:14:28.64	-47:36:46.08

Continued on next page

Table A.1 – continued from previous page

Simbad	HD	HR	HIP	My ID	RA	DEC
HD 106797	106797	4669	59898	HD106797	12:17:06.30	-65:41:34.65
HD 106906	106906		59960	HD106906	12:17:53.19	-55:58:31.88
HD 107146	107146		60074	HD107146	12:19:06.50	+16:32:53.86
HD 107301	107301	4692	60183	HR4692	12:20:28.22	-65:50:33.56
HD 107649	107649		60348	HD107649	12:22:24.85	-51:01:34.34
HD 107947	107947		60561	HD107947	12:24:51.91	-72:36:14.02
HD 108857	108857		61049	HD108857	12:30:46.27	-58:11:16.76
HD 108904	108904		61087	HD108904	12:31:12.64	-61:54:31.46
*eta Crv	109085	4775	61174	etaCrv	12:32:04.22	-16:11:45.61
HD 109573	109573	4796	61498	HD109573	12:36:01.03	-39:52:10.22
*f Vir	109704	4799	61558	fVir	12:36:47.35	-05:49:54.84
HD 109832	109832		61684	HD109832	12:38:42.77	-68:45:49.12
HD 110058	110058		61782	HD110058	12:39:46.19	-49:11:55.54
*rho Vir	110411	4828	61960	rhoVir	12:41:53.05	+10:14:08.25
HD 111520	111520		62657	HD111520	12:50:19.71	-49:51:48.95
V* MO Hya	111786	4881	62788	VMO_Hya	12:51:57.89	-26:44:17.78
HD 112383	112383		63236	HD112383	12:57:26.18	-67:57:38.53
HD 112810	112810		63439	HD112810	12:59:59.88	-50:23:22.48
HD 113337	113337	4934	63584	HD113337	13:01:46.92	+63:36:36.80
CPD-52 6110				CPD52_6110	13:01:50.69	-53:04:58.22
HD 113457	113457		63839	HD113457	13:05:02.04	-64:26:29.70
HD 113556	113556		63886	HD113556	13:05:32.60	-58:32:07.95
HD 113902	113902	4951	64053	HR4951	13:07:38.28	-53:27:35.14
HD 114082	114082		64184	HD114082	13:09:16.19	-60:18:30.05
HD 115361	115361		64877	HD115361	13:17:55.41	-61:00:38.82
*61 Vir	115617	5019	64924	61Vir	13:18:24.31	-18:18:40.30
HD 115600	115600		64995	HD115600	13:19:19.53	-59:28:20.43

Continued on next page

Table A.1 – continued from previous page

Simbad	HD	HR	HIP	My ID	RA	DEC
*iot Cen	115892	5028	65109	iotCen	13:20:35.81	-36:42:44.24
HD 117376	117376	5085	65728	HR5085	13:28:27.08	+59:56:44.83
HD 117214	117214		65875	HD117214	13:30:08.97	-58:29:04.34
HD 117484	117484		65965	HD117484	13:31:30.96	-46:44:06.84
HD 117665	117665		66068	HD117665	13:32:39.24	-44:27:00.91
*24 CVn	118232	5112	66234	24CVn	13:34:27.25	+49:00:57.50
V* BH CVn	118216	5110	66257	VBH_CVn	13:34:47.80	+37:10:56.69
HD 118379	118379		66447	HD118379	13:37:17.77	-40:53:52.35
HD 118588	118588		66566	HD118588	13:38:42.87	-44:30:58.63
HD 119124	119124	5148	66704	HD119124	13:40:23.23	+50:31:09.90
HD 119511	119511		67068	HD119511	13:44:43.94	-49:17:57.74
HD 119718	119718		67230	HD119718	13:46:35.39	-62:04:09.75
HD 120326	120326		67497	HD120326	13:49:54.50	-50:14:23.87
HD 121189	121189		67970	HD121189	13:55:09.99	-50:44:42.93
*tau Vir	122408	5264	68520	tauVir	14:01:38.79	+01:32:40.31
HD 122705	122705		68781	HD122705	14:04:42.14	-50:04:17.06
HD 124619	124619		69720	HD124619	14:16:16.99	-53:49:01.94
*lam Boo	125162	5351	69732	lamBoo	14:16:23.01	+46:05:17.90
HD 126062	126062		70441	HD126062	14:24:36.99	-47:10:39.85
HD 126135	126135		70455	HD126135	14:24:43.91	-40:45:18.58
HD 127821	127821	5436	70952	HD127821	14:30:46.06	+63:11:08.83
*gam Boo	127762	5435	71075	gamBoo	14:32:04.67	+38:18:29.70
HD 127750	127750		71271	HD127750	14:34:33.44	-46:18:17.24
HD 128311	128311		71395	HD128311	14:36:00.56	+09:44:47.46
HD 128207	128207	5449	71453	HR5449	14:36:44.13	-40:12:41.69
HD 129590	129590		72070	HD129590	14:44:30.96	-39:59:20.61
HD 132254	132254	5581	73100	HD132254	14:56:23.04	+49:37:42.42

Continued on next page

Table A.1 – continued from previous page

Simbad	HD	HR	HIP	My ID	RA	DEC
HD 131835	131835		73145	HD131835	14:56:54.46	-35:41:43.65
HD 132238	132238	5579	73341	HR5579	14:59:13.92	-37:52:52.42
HD 134888	134888		74499	HD134888	15:13:27.96	-33:08:50.20
HD 135599	135599		74702	HD135599	15:15:59.16	+00:47:46.89
HD 135454	135454		74752	HD135454	15:16:37.15	-42:22:12.55
*bet Cir	135379	5670	74824	betCir	15:17:30.85	-58:48:04.33
HD 135953	135953		74959	HD135953	15:19:05.41	-36:21:44.20
BD-07 4003			74995	BD07_4003	15:19:26.82	-07:43:20.21
HD 136246	136246		75077	HD136246	15:20:31.41	-28:17:13.58
HD 136482	136482		75210	HD136482	15:22:11.25	-37:38:08.25
HD 137015	137015	5722	75476	HD137015	15:25:06.43	-38:10:09.25
HD 137057	137057		75491	HD137057	15:25:16.05	-38:09:28.43
HD 137119	137119		75509	HD137119	15:25:30.17	-36:11:57.94
*tet CrB	138749	5778	76127	tetCrB	15:32:55.78	+31:21:32.87
*alf CrB	139006	5793	76267	alfCrB	15:34:41.26	+26:42:52.89
HD 138813	138813		76310	HD138813	15:35:16.10	-25:44:03.00
HD 138923	138923	5790	76395	HR5790	15:36:11.36	-33:05:34.09
HD 138965	138965	5792	76736	HR5792	15:40:11.55	-70:13:40.38
*g Lup	139664	5825	76829	gLup	15:41:11.37	-44:39:40.34
HD 140817	140817		77315	HD140817	15:47:04.45	-35:30:37.25
HD 140840	140840		77317	HD140840	15:47:06.16	-35:31:04.94
HD 141011	141011		77432	HD141011	15:48:24.78	-42:37:05.01
HD 141378	141378	5875	77464	HD141378	15:48:56.79	-03:49:06.63
HD 141327	141327		77523	HD141327	15:49:43.10	-32:48:29.82
*4 Her	142926	5938	77986	4Her	15:55:30.59	+42:33:58.29
HD 142446	142446		78043	HD142446	15:56:05.62	-36:53:34.31
HD 142139	142139	5905	78045	HR5905	15:56:05.91	-60:28:56.95

Continued on next page

Table A.1 – continued from previous page

Simbad	HD	HR	HIP	My ID	RA	DEC
HD 143675	143675		78641	HD143675	16:03:13.54	-35:17:14.96
V* LM Lup	143939		78756	VLM_Lup	16:04:44.48	-39:26:04.77
HD 144587	144587		78996	HD144587	16:07:29.92	-23:57:02.44
HD 144981	144981		79156	HD144981	16:09:20.88	-19:27:25.94
HD 145554	145554		79410	HD145554	16:12:21.83	-19:34:44.56
HD 145631	145631		79439	HD145631	16:12:44.10	-19:30:10.33
HD 145560	145560		79516	HD145560	16:13:34.33	-45:49:03.66
HD 145964	145964	6051	79599	HR6051	16:14:28.88	-21:06:27.48
HD 145880	145880		79631	HD145880	16:14:57.76	-39:37:40.12
HD 145972	145972		79710	HD145972	16:16:03.83	-49:04:29.39
HD 145689	145689	6037	79797	HR6037	16:17:05.41	-67:56:28.62
HD 146606	146606		79878	HD146606	16:18:16.16	-28:02:30.15
*d Sco	146624	6070	79881	dSco	16:18:17.90	-28:36:50.47
HD 146897	146897		79977	HD146897	16:19:29.24	-21:24:13.27
V* V933 Sco	147010		80024	VV933Sco	16:20:05.49	-20:03:23.02
HD 147594	147594		80320	HD147594	16:23:53.85	-29:46:40.11
HD 148657	148657		80897	HD148657	16:31:11.67	-38:22:58.74
HD 151044	151044		81800	HD151044	16:42:27.81	+49:56:11.19
HD 151109	151109		82154	HD151109	16:47:01.67	-39:32:01.94
*53 Her	152598	6279	82587	53Her	16:52:58.05	+31:42:06.02
HD 153053	153053	6297	83187	HD153053	17:00:06.27	-54:35:49.83
*73 Her	157728	6480	85157	73Her	17:24:06.58	+22:57:37.01
HD 158633	158633	6518	85235	HD158633	17:25:00.09	+67:18:24.14
*b Oph	157792	6486	85340	bOph	17:26:22.21	-24:10:31.11
HD 158352	158352	6507	85537	HR6507	17:28:49.65	+00:19:50.25
*78 Her	159139	6533	85790	78Her	17:31:49.57	+28:24:26.99
HD 159082	159082	6532	85826	HD159082	17:32:14.88	+11:55:48.18

Continued on next page

Table A.1 – continued from previous page

Simbad	HD	HR	HIP	My ID	RA	DEC
HD 1591	159170	6534	85922	HR6534	17:33:29.84	-05:44:41.29
*pi. Ara	159492	6549	86305	piAra	17:38:05.51	-54:30:01.56
*mu. Ara	160691	6585	86796	muAra	17:44:08.70	-51:50:02.58
*gam Oph	161868	6629	87108	gamOph	17:47:53.55	+02:42:26.20
HD 162917	162917	6670	87558	HR6670	17:53:14.18	+06:06:05.11
HD 164249	164249		88399	HD164249	18:03:03.41	-51:38:56.43
HD 169666	169666		89770	HD169666	18:19:08.24	+71:31:04.28
*eps Sgr	169022	6879	90185	epsSgr	18:24:10.31	-34:23:04.61
HD 170773	170773	6948	90936	HR6948	18:33:00.91	-39:53:31.27
*110 Her	173667	7061	92043	110Her	18:45:39.72	+20:32:46.71
*zet CrA	176638	7188	93542	zetCrA	19:03:06.87	-42:05:42.38
*rho Tel	177171	7213	93815	rhoTel	19:06:19.95	-52:20:27.27
*alf CrA	178253	7254	94114	alfCrA	19:09:28.34	-37:54:16.10
*eta Tel	181296	7329	95261	etaTel	19:22:51.20	-54:25:26.14
HD 181327	181327		95270	HD181327	19:22:58.94	-54:32:16.97
*5 Vul	182919	7390	95560	5Vul	19:26:13.24	+20:05:51.84
*c Aql	183324	7400	95793	cAql	19:29:00.98	+01:57:01.61
HD 190470	190470		98828	HD190470	20:04:10.04	+25:47:24.82
HD 191174	191174	7695	98872	HD191174	20:04:44.51	+63:53:24.74
HD 191089	191089		99273	HD191089	20:09:05.21	-26:13:26.52
*tet Aql	191692	7710	99473	tetAql	20:11:18.26	-00:49:17.31
HD 191849	191849		99701	HD191849	20:13:53.39	-45:09:50.47
*rho Aql	192425	7724	99742	rhoAql	20:14:16.61	+15:11:51.39
HD 192758	192758			HD192758	20:18:15.79	-42:51:36.29
*kap01 Sgr	193571	7779	100469	kap01Sgr	20:22:27.50	-42:02:58.36
*phi01 Pav	195627	7848	101612	phi01Pav	20:35:34.85	-60:34:54.30
*bet Del	196524	7882	101769	betDel	20:37:32.94	+14:35:42.31

Continued on next page

Table A.1 – continued from previous page

Simbad	HD	HR	HIP	My ID	RA	DEC
*iot Del	196544	7883	101800	iotDel	20:37:49.11	+11:22:39.63
V* AU Mic	197481		102409	VAU_Mic	20:45:09.53	-31:20:27.24
HD 199260	199260	8013	103389	HR8013	20:56:47.33	-26:17:46.95
*alf Oct	199532	8021	104043	alfOct	21:04:43.06	-77:01:25.56
HD 200800	200800		104411	HD200800	21:09:05.49	-65:47:56.12
HD 202206	202206		104903	HD202206	21:14:57.76	-20:47:21.15
HD 202917	202917		105388	HD202917	21:20:49.95	-53:02:03.14
HD 205674	205674		106741	HD205674	21:37:21.11	-18:26:28.24
*3 Peg	205811	8265	106783	3Peg	21:37:43.64	+06:37:06.21
HD 206893	206893		107412	HD206893	21:45:21.90	-12:47:00.06
HD 207129	207129	8323	107649	HD207129	21:48:15.75	-47:18:13.01
*39 Peg	213617	8586	111278	39Peg	22:32:35.48	+20:13:48.06
*tau01 Aqr	215766	8673	112542	tau01Aqr	22:47:42.76	-14:03:23.14
V* V342 Peg	218396	8799A	114189	VV342Peg	23:07:28.71	+21:08:03.30
HD 219623	219623	8853	114924	HD219623	23:16:42.30	+53:12:48.51
HD 219482	219482	8843	114948	HR8843	23:16:57.68	-62:00:04.32
*kap Psc	220825	8911	115738	kapPsc	23:26:55.95	+01:15:20.19
HD 221853	221853		116431	HD221853	23:35:36.15	+08:22:57.42
*del Scl	223352	9016	117452	delScl	23:48:55.54	-28:07:48.97

A.2 Parameters of the full sample

Table A.2: Main parameters of the sample. Spectral type, heliocentric radial velocity, projected rotational velocity, luminosity ratio L_{disk}/L_{star}, distance and age flag, where "O" stands for older than 100 Myr and "Y" stands for younger than 100 Myr.

Simbad ID	Spectral type	RV [km.s^{-1}]	$v$sin$i$ [km.s^{-1}]	$L_{\rm disk}/L_\star$	Distance [pc]	Age flag
HD 225200	A1V	18.40	341.00	6.14 x10^{-5}	134.46	O
HD 166	G8	-6.59	6.20	6.29 x10^{-5}	13.77	O
HD 203	F3V	6.50	170.00	1.41 x10^{-4}	39.96	Y
HD 870	K0V	1.30	0.79	2.49 x10^{-5}	20.62	O
* sig And	A2V	-8.20	123.00	1.83 x10^{-5}	41.32	O
HD 1466	F8V	6.32	21.00	1.05 x10^{-4}	42.97	Y
HD 1461	G3VFe0.5	-10.09	4.80	4.23 x10^{-5}	23.46	O
* kap Phe	A5IVn	11.30	194.00	1.10 x10^{-5}	23.80	O
* lam01 Phe	A1Va	-2.00	–	1.38 x10^{-5}	56.12	O
* lam Cas	B8Vn	-12.20	220.00	3.14 x10^{-6}	115.74	O
* bet03 Tuc	A0V	7.70	93.00	1.36 x10^{-4}	45.90	Y
HD 3670	F5V	8.92	–	5.15 x10^{-4}	77.59	O
* 66 Psc	A1Vn	8.50	144.00	3.21 x10^{-5}	108.10	O
HD 6798	A3V	10.00	207.00	9.78 x10^{-5}	80.70	O
* nu. Phe	F9VFe+0.4	11.82	–	3.03 x10^{-5}	15.17	O
* 49 Cet	A1V	10.30	196.00	6.93 x10^{-4}	57.06	Y
HD 10472	F2IV/V	12.41	78.20	3.40 x10^{-4}	71.15	O
* q01 Eri	F9V	27.82	3.84	3.18 x10^{-4}	17.34	O
HD 10638	A3	-0.40	–	3.14 x10^{-4}	68.69	O
* q02 Eri	A1V	9.50	–	7.36 x10^{-5}	60.96	O
V* DK Cet	G4V	6.12	15.20	6.34 x10^{-5}	41.41	Y
* 50 Cas	A2V	-18.20	91.00	1.77 x10^{-5}	48.16	O
HD 13246	F7V	10.68	35.60	1.72 x10^{-4}	45.61	Y

Continued on next page

Table A.2 – continued from previous page

Simbad ID	Spectral type	RV [km.s^{-1}]	$v\sin i$ [km.s^{-1}]	$L_{disk}/L_\star$	Distance [pc]	Age flag
HD 12467	A1.5V	-9.00	130.00	8.58 x10^{-5}	70.86	O
* bet Tri	A5III	12.30	70.00	2.70 x10^{-5}	38.89	O
* gam Tri	A1Vnn	9.90	254.00	6.76 x10^{-5}	34.43	Y
HD 15115	F4IV	0.81	89.80	4.76 x10^{-4}	49.00	Y
* phi For	A2.5V	19.00	116.80	4.15 x10^{-5}	47.25	O
* 12 Tri	F0III	-24.80	79.80	3.57 x10^{-5}	49.93	O
HD 15745	F0	5.68	–	2.22 x10^{-3}	71.99	O
HD 16743	F0/2III/IV	–	112.20	3.79 x10^{-4}	57.93	O
HD 17390	F3IV/V	7.20	–	2.08 x10^{-4}	48.19	O
* nu. Hor	A2V	30.90	143.70	4.70 x10^{-5}	51.71	O
* 41 Ari	B8Vn	4.00	175.00	1.57 x10^{-5}	50.78	Y
* alf For	F6V+G7V	-17.14	4.41	5.88 x10^{-4}	14.23	O
* 94 Cet	F8.5V	18.96	7.70	3.94 x10^{-6}	22.53	O
HD 21997	A3IV/V	17.30	69.80	4.79 x10^{-4}	69.64	Y
HD 23267	A0	7.60	–	6.60 x10^{-5}	149.83	O
V* V1229 Tau	A0VpSi+Am	5.00	40.00	2.00 x10^{-4}	139.54	Y
HD 24636	F3IV/V	14.55	–	1.38 x10^{-4}	57.05	Y
* 28 Tau	B8Vne	5.10	220.00	1.49 x10^{-4}	129.48	O
HD 23863	A7Vn	5.00	165.00	5.77 x10^{-5}	134.25	Y
HD 23923	B8V	9.50	290.00	4.95 x10^{-5}	133.40	Y
HD 24141	kA3hF0mF0	-0.20	63.00	3.56 x10^{-5}	54.21	O
HD 24966	A0V	–	–	2.67 x10^{-4}	114.85	Y
HD 24817	A0Vn	12.00	285.00	4.15 x10^{-5}	77.65	O
HD 25457	F7V	17.62	20.24	1.23 x10^{-4}	18.77	Y
HD 25570	F2Vs	38.20	34.40	4.36 x10^{-5}	34.84	O
* gam Dor	F1V	25.20	59.50	1.72 x10^{-5}	20.45	O

Continued on next page

Table A.2 – continued from previous page

Simbad ID	Spectral type	RV [km.s^{-1}]	$v\sin i$ [km.s^{-1}]	$L_{disk}/L_\star$	Distance [pc]	Age flag
* b Tau	kA5hF0VmF0	37.30	105.00	4.84 x10^{-5}	48.57	Y
V* EX Eri	A7VkA3mA3	14.40	130.00	4.37 x10^{-5}	57.47	Y
HD 30447	F3V	24.65	–	9.38 x10^{-4}	80.53	Y
HD 32195	F7V	11.40	–	1.06 x10^{-4}	62.78	Y
* pi.01 Ori	A0Va_lB	11.10	120.00	5.86 x10^{-5}	35.66	O
* l Tau	A5IV	-1.70	112.00	2.84 x10^{-5}	61.97	O
* kap Lep	B7V	20.80	120.00	4.83 x10^{-6}	223.21	O
HD 34324	A3V	–	–	8.98 x10^{-5}	82.04	O
HD 35150	A0V	–	–	3.74 x10^{-4}	370.67	O
HD 287787	A2	–	–	2.23 x10^{-4}	410.77	O
HD 35332	A0V	–	–	3.44 x10^{-4}	384.18	O
HD 35367	A1IV/V	–	–	1.66 x10^{-4}	365.79	O
HD 287861	A0	–	–	3.02 x10^{-4}	363.62	O
HD 287850	A5	–	–	1.30 x10^{-4}	377.57	O
HD 287854	F0	–	–	2.92 x10^{-4}	362.52	O
HD 35625	A0V	–	–	8.51 x10^{-5}	361.96	O
HD 35841	F3V	25.45	–	1.38 x10^{-3}	103.67	Y
HD 290540	A2	–	–	1.12 x10^{-4}	448.75	O
HD 36444	B9V	–	–	2.85 x10^{-3}	443.63	O
HD 290609	B8	–	–	1.60 x10^{-4}	847.45	O
HD 36968	F2V	16.51	–	1.27 x10^{-3}	150.10	Y
HD 37286	A2III/IV	22.40	70.00	7.82 x10^{-5}	58.89	Y
HD 37306	A1V	23.00	148.10	8.68 x10^{-5}	70.46	Y
HD 37484	F4V	26.05	54.51	3.14 x10^{-4}	59.11	Y
HD 38056	B9.5V	28.10	195.00	4.41 x10^{-5}	128.31	O
HD 38207	F2V	24.77	69.88	9.08 x10^{-4}	110.96	Y

Continued on next page

Table A.2 – continued from previous page

Simbad ID	Spectral type	RV [km.s^{-1}]	$v$sin$i$ [km.s^{-1}]	$L_{\rm disk}/L_\star$	Distance [pc]	Age flag
HD 38206	A0V	25.30	35.00	1.47 x10^{-4}	71.40	Y
* zet Lep	A2IV-V(n)	24.70	258.70	8.74 x10^{-5}	21.60	O
HD 38858	G2V	31.61	1.00	5.81 x10^{-5}	15.25	O
* eta Lep	F2V	-2.14	16.99	4.03 x10^{-5}	14.87	O
HD 40540	A8IV(m)	32.59	–	3.91 x10^{-4}	88.29	O
HD 45184	G2Va	-3.73	5.40	8.82 x10^{-5}	21.96	O
HD 46190	A0V	–	–	1.10 x10^{-5}	84.51	O
HD 53842	F5V	12.20	–	3.01 x10^{-4}	57.87	Y
* psi05 Aur	F9V	-23.9	6.50	4.92 x10^{-5}	16.64	O
HD 50571	F5VFe+0.4	26.69	–	1.25 x10^{-4}	34.04	O
HD 53143	G9V	22.04	4.10	2.65 x10^{-4}	18.36	O
HD 52265	G0V	53.92	6.70	1.81 x10^{-5}	30.00	O
HD 54341	A0V	–	–	2.19 x10^{-4}	101.16	Y
* bet CMi	B8Ve	22.00	210.00	8.61 x10^{-5}	49.57	O
HD 61005	G8Vk	22.64	8.20	2.67 x10^{-3}	36.48	Y
HD 60856	B5V	31.20	44.00	1.52 x10^{-5}	471.96	O
HD 60995	B8/9V	29.00	316.00	2.72 x10^{-5}	504.64	O
* rho Pup	F5IIkF2IImF5II	45.80	8.00	1.04 x10^{-5}	19.48	O
HD 68420	A3V	–	–	1.17 x10^{-4}	411.57	O
HD 69830	G8:V	30.29	5.20	1.84 x10^{-4}	12.56	O
HD 71043	A0V	22.50	224.00	5.87 x10^{-5}	73.24	O
HD 70313	A3Va	21.30	112.00	6.93 x10^{-5}	52.09	O
* 30 Mon	A0Va	10.00	134.00	2.71 x10^{-5}	37.50	O
HD 71722	A0V	30.20	–	1.00 x10^{-4}	69.33	O
V* pi.01 UMa	G0.5V	-13.03	11.21	1.64 x10^{-5}	14.45	O
HD 74340	F5V	-30.00	48.80	1.31 x10^{-4}	152.07	O

Continued on next page

Table A.2 – continued from previous page

Simbad ID	Spectral type	RV [km.s^{-1}]	$v$sin$i$ [km.s^{-1}]	$L_{\rm disk}/L_{\star}$	Distance [pc]	Age flag
* eta Cha	B8V	14.00	–	6.27 x10^{-5}	99.56	Y
HD 74374	F3V	16.51	–	1.28 x10^{-4}	153.24	Y
* 50 Cnc	A1Vp	23.30	18.00	3.76 x10^{-5}	56.19	O
HD 76151	G2V	32.08	3.58	2.34 x10^{-5}	16.85	O
HD 76653	F6V	-6.88	10.30	1.68 x10^{-5}	24.26	O
* omi01 Cnc	A5III	-4.60	102.00	3.00 x10^{-5}	48.40	O
* omi02 Cnc	F0IV	-4.00	107.00	1.42 x10^{-4}	48.80	O
HD 78702	A0/1V	16.90	222.00	2.42 x10^{-4}	104.71	O
HD 79108	A0V	22.60	172.00	5.85 x10^{-5}	115.74	O
* tet Hya	B9.5V+DA1.6	-10.70	97.00	4.33 x10^{-6}	35.20	O
HD 80950	A0V	11.20	40.00	1.19 x10^{-4}	77.34	O
HD 82943	F9VFe+0.5	8.220	6.50	1.51 x10^{-4}	27.61	O
HD 84075	G2V	5.040	–	1.83 x10^{-4}	64.09	Y
HD 84870	A3	–	–	3.43 x10^{-4}	89.85	O
HD 86087	A0V	13.90	–	1.35 x10^{-4}	99.33	O
* 21 LMi	A7V(n)	-11.40	165.00	1.85 x10^{-5}	28.24	O
HD 88215	F3V	23.60	148.00	3.57 x10^{-5}	27.81	O
HD 90874	A2V	7.10	65.70	9.51 x10^{-6}	67.73	O
HD 91375	A1V	7.50	10.00	1.05 x10^{-5}	79.87	O
HD 92536	B8V	10.00	–	6.11 x10^{-5}	158.00	O
V* CE Ant	M2Ve	11.40	4.40	1.19 x10^{-3}	34.03	Y
HD 93738	B9.5V	4.00	–	1.71 x10^{-5}	154.85	O
HD 95086	A8III	10.10	–	1.22 x10^{-3}	86.44	Y
* bet UMa	A1IVps	-13.10	46.00	1.11 x10^{-5}	24.44	O
* b Leo	kA1VmA3V	-11.10	21.00	2.02 x10^{-5}	38.86	O
HD 95698	A9III/IV	0.84	42.00	6.86 x10^{-5}	57.38	O

Continued on next page

Table A.2 – continued from previous page

Simbad ID	Spectral type	RV [km.s^{-1}]	$v$sin$i$ [km.s^{-1}]	$L_{\rm disk}/L_\star$	Distance [pc]	Age flag
* tet Leo	A2IV	7.30	23.00	1.16 x10^{-5}	50.60	O
HD 98363	A2V	9.60	–	7.28 x10^{-4}	138.59	O
HD 98673	A7Vn	-10.00	259.00	5.28 x10^{-5}	86.28	O
HD 101088	F5IV	19.70	152.00	2.73 x10^{-5}	101.24	O
* pi. Cha	A9IV	-15.27	–	1.78 x10^{-5}	41.51	O
HD 102458	G4V	14.40	31.00	1.00 x10^{-4}	113.40	O
* bet Leo	A3Va	-0.20	128.00	2.27 x10^{-5}	10.99	O
HD 103234	F2IV/V	13.36	57.00	9.80 x10^{-5}	102.12	O
HD 103266	A1V	-7.50	165.10	3.92 x10^{-5}	83.14	O
HD 103703	F3V	16.01	66.00	4.06 x10^{-4}	107.42	O
HD 104231	F5V	13.51	36.00	1.46 x10^{-4}	102.73	O
HD 104600	B9V	7.60	214.00	1.26 x10^{-4}	104.85	Y
* eta Cru	F2V	10.40	46.10	3.75 x10^{-5}	19.75	O
HD 105613	A3V	7.40	–	1.16 x10^{-4}	104.60	O
* 3 Crv	A1V	11.00	126.80	2.83 x10^{-5}	58.81	O
HD 105857	A2V	7.20	–	1.16 x10^{-4}	112.44	O
HD 105912	F5V	0.40	42.30	7.30 x10^{-5}	48.24	O
HD 106036	A2V	7.70	–	2.94 x10^{-4}	100.60	Y
CD-54 4621	K0Ve	14.70	29.70	3.13 x10^{-4}	113.28	Y
HD 106389	F6IV	15.60	10.00	3.41 x10^{-4}	145.20	O
HD 106797	A0V	21.00	172.00	1.68 x10^{-4}	105.94	Y
HD 106906	F5V	10.20	55.00	1.33 x10^{-3}	103.33	Y
HD 107146	G2V	1.68	13.83	9.67 x10^{-4}	27.47	Y
HD 107301	B9V	-8.30	–	1.12 x10^{-4}	97.36	O
HD 107649	F5V	6.10	72.00	1.21 x10^{-4}	108.32	O
HD 107947	A0V	7.90	–	8.25 x10^{-5}	99.13	O

Continued on next page

Table A.2 – continued from previous page

Simbad ID	Spectral type	RV [km.s^{-1}]	$v$sin$i$ [km.s^{-1}]	$L_{\rm disk}/L_\star$	Distance [pc]	Age flag
HD 108857	F7V	6.50	8.00	4.94 x10^{-4}	104.51	O
HD 108904	F6V	12.45	64.00	5.33 x10^{-4}	108.02	Y
* eta Crv	F2V	0.69	92.00	1.98 x10^{-4}	18.28	O
HD 109573	A0V	7.10	152.00	4.45 x10^{-3}	71.90	Y
* f Vir	A3V	-6.00	155.40	4.73 x10^{-5}	71.44	O
HD 109832	A9V	7.20	–	4.60 x10^{-4}	108.31	O
HD 110058	A0V	5.00	–	1.78 x10^{-3}	129.98	Y
* rho Vir	A0Va_lB	1.60	154.00	5.57 x10^{-5}	38.16	O
HD 111520	F5/6V	11.82	42.00	2.03 x10^{-3}	108.93	Y
V* MO Hya	F0VkA1mA1_lB	-18.10	138.00	6.55 x10^{-5}	62.57	O
HD 112383	A2IV/V	6.60	–	1.28 x10^{-4}	101.64	O
HD 112810	F3/5IV/V	4.20	82.00	7.92 x10^{-4}	132.92	Y
HD 113337	F6V	-15.70	6.00	9.81 x10^{-5}	36.21	O
CPD-52 6110	K3V(e)	10.19	–	3.20 x10^{-4}	117.86	Y
HD 113457	A0V	15.00	–	1.78 x10^{-4}	105.86	Y
HD 113556	F2V	12.75	49.00	6.50 x10^{-4}	101.54	Y
HD 113902	B8/9V	22.00	–	4.25 x10^{-5}	100.42	Y
HD 114082	F3V	11.76	43.00	3.21 x10^{-3}	95.65	Y
HD 115361	F5V	10.76	74.00	2.01 x10^{-4}	96.35	O
* 61 Vir	G6.5V	-8.13	3.90	2.54 x10^{-5}	8.55	O
HD 115600	F2IV/V	12.08	61.00	1.63 x10^{-3}	109.61	Y
* iot Cen	kA1.5hA3mA3Va	0.10	90.30	2.24 x10^{-5}	18.02	O
HD 117376	A1Vn	-11.10	154.00	3.26 x10^{-5}	73.14	O
HD 117214	F6V	10.20	40.00	2.40 x10^{-3}	107.61	Y
HD 117484	B9.5V	2.00	–	1.99 x10^{-4}	155.50	O
HD 117665	A1/2V	1.50	–	1.69 x10^{-4}	129.17	O

Continued on next page

Table A.2 – continued from previous page

Simbad ID	Spectral type	RV [km.s^{-1}]	$v\sin i$ [km.s^{-1}]	$L_{\rm disk}/L_\star$	Distance [pc]	Age flag
* 24 CVn	A4V	-18.30	159.00	1.11 x10^{-5}	55.27	O
V* BH CVn	A6m	6.43	16.00	7.02 x10^{-5}	46.14	O
HD 118379	A3IV/V	6.10	–	1.35 x10^{-4}	111.87	O
HD 118588	A1V	1.20	–	5.62 x10^{-4}	135.98	O
HD 119124	F7.7V	-12.44	12.00	4.85 x10^{-5}	25.48	O
HD 119511	F3V	1.80	124.00	6.22 x10^{-5}	119.37	O
HD 119718	F5V	11.98	98.00	3.40 x10^{-4}	116.66	O
HD 120326	F0V	7.30	70.00	1.63 x10^{-3}	113.93	O
HD 121189	F3V	9.84	50.00	4.11 x10^{-4}	129.18	O
* tau Vir	A2IV/V	-6.70	186.00	1.06 x10^{-5}	68.96	O
HD 122705	A2V	6.60	–	6.11 x10^{-5}	122.58	O
HD 124619	F0V	6.90	115.00	8.60 x10^{-5}	131.85	O
* lam Boo	A0Va_lB	-7.90	110.00	5.39 x10^{-5}	30.35	O
HD 126062	A1V	5.10	–	2.81 x10^{-4}	132.48	O
HD 126135	B8V	12.00	–	4.57 x10^{-5}	182.41	Y
HD 127821	F4IV	-11.80	55.60	2.03 x10^{-4}	31.71	O
* gam Boo	A7IV+(n)	-32.40	115.00	9.93 x10^{-6}	26.60	O
HD 127750	A0V	4.40	–	1.59 x10^{-4}	143.43	O
HD 128311	K3V	-9.58	5.60	7.03 x10^{-5}	16.33	O
HD 128207	B8V	2.00	–	6.49 x10^{-6}	142.77	Y
HD 129590	G3V	2.30	32.00	6.08 x10^{-3}	136.03	Y
HD 132254	F8-V	-15.53	7.70	2.81 x10^{-6}	25.22	O
HD 131835	A2IV	0.50	–	2.03 x10^{-3}	133.65	Y
HD 132238	B7V	15.00	–	4.41 x10^{-5}	161.67	Y
HD 134888	F3/5V	2.95	37.00	8.73 x10^{-4}	112.31	Y
HD 135599	K0V	-3.08	3.80	9.75 x10^{-5}	15.81	O

Continued on next page

Table A.2 – continued from previous page

Simbad ID	Spectral type	RV [km.s^{-1}]	$v$sin$i$ [km.s^{-1}]	$L_{\text{disk}}/L_{\star}$	Distance [pc]	Age flag
HD 135454	B9.5V	1.40	–	2.36 x10^{-5}	134.15	O
* bet Cir	A3Va	9.60	68.50	4.77 x10^{-5}	30.55	O
HD 135953	F5V	3.36	33.00	6.55 x10^{-4}	130.47	Y
BD-07 4003	M3V	-9.21	–	5.41 x10^{-4}	6.29	O
HD 136246	A1V	-2.70	–	4.03 x10^{-5}	114.18	O
HD 136482	B8/9V	-0.20	–	8.12 x10^{-5}	148.27	O
HD 137015	A1/2V	3.20	119.60	2.05 x10^{-5}	296.42	Y
HD 137057	F3V	-0.20	55.00	2.58 x10^{-4}	143.77	O
HD 137119	A2V	-0.70	–	1.53 x10^{-4}	128.34	O
* tet CrB	B6Vnne	-25.70	310.00	1.00 x10^{-5}	115.07	O
* alf CrB	A1IV	1.70	138.00	1.41 x10^{-5}	23.00	O
HD 138813	A0V	-2.54	97.90	9.60 x10^{-4}	137.41	Y
HD 138923	B8V	-3.60	–	1.05 x10^{-4}	134.24	Y
HD 138965	A1V	-2.00	102.70	3.74 x10^{-4}	78.08	O
* g Lup	F3/5V	-7.08	71.60	7.85 x10^{-5}	17.43	O
HD 140817	A0V	–	–	1.26 x10^{-4}	142.46	O
HD 140840	B9/A0V	–	–	1.65 x10^{-4}	148.16	O
HD 141011	F5V	0.20	83.00	1.44 x10^{-4}	128.60	O
HD 141378	A5IV-V	-16.40	107.00	6.93 x10^{-5}	53.54	O
HD 141327	B9V	-5.10	–	4.35 x10^{-5}	217.38	O
* 4 Her	B9pe	-20.20	275.00	1.15 x10^{-4}	169.74	O
HD 142446	F3V	-1.90	66.00	6.29 x10^{-4}	137.54	Y
HD 142139	A1IV/V	-16.70	89.20	3.52 x10^{-5}	69.76	O
HD 143675	A5IV/V	-2.70	–	4.89 x10^{-4}	139.20	O
V* LM Lup	ApSiCr	1.60	–	2.78 x10^{-5}	143.51	Y
HD 144587	A9V	0.00	112.10	3.03 x10^{-4}	144.01	O

Continued on next page

Table A.2 – continued from previous page

Simbad ID	Spectral type	RV [km.s^{-1}]	$v$sin$i$ [km.s^{-1}]	$L_{\rm disk}/L_\star$	Distance [pc]	Age flag
HD 144981	A0V	-1.30	155.20	1.09 x10^{-4}	150.59	O
HD 145554	B9V	-6.15	340.00	1.31 x10^{-4}	136.83	Y
HD 145631	B9V	-5.56	287.00	4.16 x10^{-5}	140.72	Y
HD 145560	F5V	4.38	43.00	3.03 x10^{-3}	120.43	Y
HD 145964	B9V	-7.80	306.00	9.19 x10^{-6}	112.18	Y
HD 145880	B9.5V	-1.80	–	3.65 x10^{-4}	125.62	O
HD 145972	F0V	1.20	61.00	2.07 x10^{-4}	125.88	O
HD 145689	A3V	-9.00	106.40	2.77 x10^{-5}	55.55	O
HD 146606	A0V	-3.43	137.00	7.90 x10^{-5}	137.27	Y
* d Sco	A1Va	-13.00	39.00	1.67 x10^{-5}	41.28	O
HD 146897	F2/3V	-1.60	55.00	5.39 x10^{-3}	131.49	Y
V* V933 Sco	B9II/III	-3.96	15.00	7.30 x10^{-5}	130.76	Y
HD 147594	G3IV	1.10	33.00	1.04 x10^{-4}	134.26	O
HD 148657	A0V	-2.70	–	3.01 x10^{-4}	189.92	O
HD 151044	F8V	-13.22	–	7.04 x10^{-5}	29.33	O
HD 151109	B9IV/V	-2.90	–	1.03 x10^{-4}	174.45	O
* 53 Her	F0V	-21.80	84.00	4.07 x10^{-5}	29.67	Y
HD 153053	A5IV/V	-20.20	102.80	5.82 x10^{-5}	53.25	O
* 73 Her	A7V	-19.70	73.00	3.34 x10^{-4}	42.74	O
HD 158633	K0	-38.49	3.40	2.73 x10^{-5}	12.79	O
* b Oph	kA5hA9mF1III	-37.20	78.00	2.59 x10^{-5}	25.49	O
HD 158352	A8Vp	-36.10	180.00	7.46 x10^{-5}	63.46	O
* 78 Her	A1V	-25.70	–	1.90 x10^{-5}	83.39	O
HD 159082	B9.5V	-11.80	22.00	4.21 x10^{-5}	145.61	O
HD 159170	A5V	-26.00	243.00	3.96 x10^{-5}	46.82	O
* pi. Ara	A5IV/V	-3.30	54.10	1.19 x10^{-4}	41.34	O

Continued on next page

Table A.2 – continued from previous page

Simbad ID	Spectral type	RV [km.s^{-1}]	$v$sin$i$ [km.s^{-1}]	$L_{\rm disk}/L_\star$	Distance [pc]	Age flag
* mu. Ara	G3IV-V	-9.29	1.33	1.48 x10^{-5}	15.60	O
* gam Oph	A1VnkA0mA0	-7.60	210.00	6.63 x10^{-5}	31.51	O
HD 162917	F4IV-V	-26.23	28.40	2.93 x10^{-5}	30.80	O
HD 164249	F6V	-0.09	20.00	9.73 x10^{-4}	49.61	Y
HD 169666	F2V	-43.05	–	1.71 x10^{-4}	52.99	O
* eps Sgr	B9.5III	-15.00	236.00	9.13 x10^{-6}	43.93	O
HD 170773	F5V	-16.55	–	4.27 x10^{-4}	37.05	O
* 110 Her	F5.5IV-V	23.37	14.08	7.33 x10^{-7}	19.20	O
* zet CrA	B9.5Vann	-13.00	–	5.89 x10^{-5}	59.20	O
* rho Tel	F6V	0.30	–	2.56 x10^{-5}	58.85	O
* alf CrA	A2Va	-18.40	203.20	2.00 x10^{-5}	38.43	O
* eta Tel	A0V+M7/8V	13.00	–	1.95 x10^{-4}	48.21	Y
HD 181327	F6V	-0.25	16.00	2.98 x10^{-3}	48.21	Y
* 5 Vul	A0V	-21.20	154.00	3.12 x10^{-5}	71.98	O
* c Aql	A0IVp	12.00	90.00	1.28 x10^{-5}	60.67	O
HD 190470	K3V	-7.38	1.40	1.07 x10^{-4}	22.15	O
HD 191174	A3V	-19.20	41.00	4.22 x10^{-5}	83.56	O
HD 191089	F5V	-5.39	37.70	1.51 x10^{-3}	50.13	Y
* tet Aql	B9.5III	-28.02	45.00	7.64 x10^{-6}	87.79	O
HD 191849	M0V	-33.29	1.00	1.63 x10^{-5}	6.16	O
* rho Aql	A1Va	-23.00	180.00	4.57 x10^{-5}	47.96	O
HD 192758	F0V	-14.36	–	5.33 x10^{-4}	66.52	O
* kap01 Sgr	A0V	-3.40	79.00	2.27 x10^{-5}	68.45	O
* phi01 Pav	F0V	-20.00	–	9.21 x10^{-5}	28.29	O
* bet Del	F5IV	-32.57	39.80	1.54 x10^{-5}	30.93	O
* iot Del	A1IV	-3.90	41.00	3.44 x10^{-5}	59.46	O

Continued on next page

Table A.2 – continued from previous page

Simbad ID	Spectral type	RV [km.s^{-1}]	$v$sin$i$ [km.s^{-1}]	$L_{\rm disk}/L_\star$	Distance [pc]	Age flag
V* AU Mic	M1VeBa1	-4.50	9.68	4.19 x10^{-4}	9.72	Y
HD 199260	F6V	-15.91	13.70	1.75 x10^{-5}	21.28	O
* alf Oct	F6(m)pec	85.90	–	2.20 x10^{-5}	44.40	O
HD 200800	A3V(m)	–	–	4.60 x10^{-5}	126.85	O
HD 202206	G6V	14.68	5.70	9.89 x10^{-5}	46.02	O
HD 202917	G7V	-1.31	15.40	2.21 x10^{-4}	46.84	Y
HD 205674	F3/5IV	-0.38	31.10	3.57 x10^{-4}	56.40	O
* 3 Peg	A2V	3.00	102.60	2.56 x10^{-5}	88.29	O
HD 206893	F5V	-12.45	–	2.54 x10^{-4}	40.80	O
HD 207129	G2V	-7.62	0.56	7.79 x10^{-5}	15.56	O
* 39 Peg	F1V	-18.90	94.00	9.14 x10^{-5}	53.57	O
* tau01 Aqr	B9V	15.00	–	3.09 x10^{-5}	108.87	O
HD 218396	F0+VkA5mA5	-12.60	49.00	2.53 x10^{-4}	41.29	Y
HD 219623	F8V	-27.05	3.00	2.39 x10^{-5}	20.55	O
HD 219482	F6V	0.46	–	3.31 x10^{-5}	20.45	O
* kap Psc	A2VpSrCrSi	-4.40	39.00	2.08 x10^{-5}	48.92	Y
HD 221853	F0	–	–	8.27 x10^{-4}	65.41	O
* del Scl	A0VankB9((_lB))	8.70	299.00	2.78 x10^{-5}	42.14	Y

Appendix B

Spectroscopic Data

Table B.1: Number of observations per instrument and total amounts of observations obtained for our sample of debris disks. Proprietary observations are flagged with a *.

Object	HARPS	UVES	FEROS	MIKE	HERMES	FIES	Total
*110 Her	–	4*	–	1*	21*	–	26*
*12 Tri	–	3*	–	5*	–	2*	10*
*28 Tau	–	2*	1*	4*	–	–	7*
*30 Mon	276	–	–	–	–	–	276
*39 Peg	–	3*	–	3*	–	–	6*
*3 Crv	36	–	2	–	–	–	38
*3 Peg	–	1* + 2	–	3*	–	–	6
*41 Ari	–	4* + 1	–	3*	–	–	8
*49 Cet	37	22	5	–	29*	4*	97
*50 Cnc	25	–	3	–	13*	–	41
*5 Vul	–	3*	2	–	14*	–	19
*61 Vir	1154	9	–	–	–	–	1163
*66 Psc	–	3*	7	4*	–	2*	16
*73 Her	–	–	–	1*	–	2*	3*
*78 Her	–	–	–	1*	–	–	1*

Continued on next page

Table B.1 – continued from previous page

Object	HARPS	UVES	FEROS	MIKE	HERMES	FIES	Total
*94 Cet	1704	5	–	–	–	–	1709
*alf CrA	–	3*	–	2*	–	–	5*
*alf CrB	3	–	–	–	–	4*	7
*alf For	200	2	–	–	–	–	202
*alf Oct	–	–	30	1*	–	–	31
BD-07 4003	249	–	–	–	–	–	249
*bet03 Tuc	36	–	2	–	–	–	38
*bet Cir	42	–	50	–	–	–	92
*bet CMi	–	36	–	–	–	–	36
*bet Del	–	1*	–	4*	–	–	5*
*bet Leo	157	–	4	–	3*	–	164
*bet Tri	–	3*	–	8*	–	–	11*
*bet UMa	–	–	–	–	10*	4*	14*
*b Leo	–	1*	01* + 1	–	–	–	3
*b Oph	–	3*	3	–	–	–	6
*b Tau	1	1*	1*	–	1*	–	4
*c Aql	–	14	10	144*	11*	9*	188
CD-54 4621	–	3*	14* + 3	–	–	–	20
CPD-52 6110	–	–	3	–	–	–	3
*del Scl	10	–	8	–	–	–	18
*d Sco	402	–	4	–	–	–	406
*eps Sgr	–	4*	7	–	–	–	11
*eta Cha	11	–	31	–	–	–	42
*eta Cru	–	2	6	–	–	–	8
*eta Crv	43	1	5	–	3*	–	52
*eta Lep	36	7	017* + 2	–	1*	–	63
*eta Tel	31	–	29	–	–	–	60

Continued on next page

Table B.1 – continued from previous page

Object	HARPS	UVES	FEROS	MIKE	HERMES	FIES	Total
*f Vir	–	3*	1	–	–	–	4
*gam Dor	–	8	10	–	–	–	18
*gam Oph	10	1	–	–	–	–	11
*gam Tri	–	3* + 1	–	–	6*	4*	14
*g Lup	8	1	038* + 3	–	–	–	50
HD 101088	–	10*	3	–	–	–	13
HD 102458	29	–	14* + 4	–	–	–	47
HD 103234	–	3*	3	–	–	–	6
HD 103266	–	3*	–	–	–	–	3*
HD 103703	–	3*	8	–	–	–	11
HD 104231	–	3*	18* + 6	–	–	–	27
HD 10472	12	–	–	–	–	–	12
HD 105613	–	4*	–	–	–	–	4*
HD 105857	–	3*	–	–	–	–	3*
HD 105912	–	3*	16*	–	–	–	19*
HD 106036	–	3*	–	–	–	–	3*
HD 10638	–	4*	–	6*	–	–	10*
HD 106389	–	3*	–	–	–	–	3*
HD 106797	–	3*	–	–	–	–	3*
HD 106906	76	–	18	–	–	–	94
HD 107146	–	3*	13* + 4	–	–	–	20
HD 107649	–	4*	15*	–	–	–	19*
HD 107947	–	3*	–	–	–	–	3*
HD 108857	–	4*	8* + 4	–	–	–	16
HD 108904	–	3*	6	–	–	–	9
HD 109573	10	206	29	–	–	–	245
HD 109832	–	3*	24*	–	–	–	27*

Continued on next page

Table B.1 – continued from previous page

Object	HARPS	UVES	FEROS	MIKE	HERMES	FIES	Total
HD 110058	12	–	11	–	–	–	23
HD 111520	–	3*	23*	–	–	–	26*
HD 112383	–	3*	–	–	–	–	3*
HD 112810	–	3*	–	–	–	–	3*
HD 113457	–	3*	–	–	–	–	3*
HD 113556	–	3*	3	–	–	–	6
HD 114082	–	3*	22* + 3	–	–	–	28
HD 115361	–	3*	–	1*	–	–	4*
HD 115600	–	–	3	–	–	–	3
HD 117214	–	3*	14*	–	–	–	17*
HD 117484	–	2*	4	–	–	–	6
HD 117665	–	3*	–	–	–	–	3*
HD 118379	–	3*	–	–	–	–	3*
HD 118588	–	3*	–	–	–	–	3*
HD 119511	–	3*	6	–	–	–	9
HD 119718	–	3*	3	–	–	–	6
HD 120326	–	3*	–	–	–	–	3*
HD 121189	–	3*	–	–	–	–	3*
HD 122705	–	3*	–	–	–	–	3*
HD 124619	–	3*	–	–	–	–	3*
HD 126062	–	3*	–	–	–	–	3*
HD 126135	4	–	–	–	–	–	4
HD 127750	–	3*	2	–	–	–	5
HD 128311	–	3*	4	–	–	–	7
HD 129590	–	3*	14*	–	–	–	17*
HD 131835	1	2*	15	–	–	–	18
HD 13246	–	1* + 1	12* + 1	2*	–	–	17

Continued on next page

Table B.1 – continued from previous page

Object	HARPS	UVES	FEROS	MIKE	HERMES	FIES	Total
HD 134888	–	3*	–	–	–	–	3*
HD 135454	1	2*	6	–	–	–	9
HD 135599	–	3*	–	–	–	–	3*
HD 135953	–	3*	15*	–	–	–	18*
HD 136246	1	1*	7	–	–	–	9
HD 136482	1	2*	–	2*	–	–	5
HD 137015	1	1*	–	2*	–	–	4
HD 137057	–	3*	3	2*	–	–	8
HD 137119	–	3*	–	2*	–	–	5*
HD 138813	–	6*	13	2*	7*	–	28
HD 140817	–	3*	2	2*	–	–	7
HD 140840	–	1*	2	2*	–	–	5
HD 141011	–	4*	24*	2*	–	–	30*
HD 141327	–	–	4	2*	–	–	6
HD 141378	–	2*	1	3*	–	–	6
HD 142446	–	3*	–	2*	–	–	5*
HD 143675	4	–	–	2*	–	–	6
HD 144587	–	–	3	2*	–	–	5
HD 144981	–	–	2	2*	–	–	4
HD 145554	–	–	1	2*	–	–	3
HD 145560	–	–	23* + 2	2*	–	–	27
HD 145631	–	–	2	2*	–	–	4
HD 145880	–	–	2	2*	–	–	4
HD 145972	–	–	13* + 3	2*	–	–	18
HD 1461	452	10	–	–	–	–	462
HD 1466	22	4	16* + 11	–	–	–	53
HD 146606	–	1*	5	2*	–	–	8

Continued on next page

Table B.1 – continued from previous page

Object	HARPS	UVES	FEROS	MIKE	HERMES	FIES	Total
HD 146897	–	–	8	2*	–	–	10
HD 147594	–	–	8*	2*	–	–	10*
HD 148657	–	1*	–	2*	–	–	3*
HD 151109	–	2*	2	2*	–	–	6
HD 15115	8	–	10	–	–	2*	20
HD 153053	28	–	–	–	–	–	28
HD 159082	–	–	3	1*	–	–	4
HD 164249	44	4	4	–	–	–	52
HD 166	–	3*	–	–	–	–	3*
HD 16743	–	3*	–	5*	–	–	8*
HD 181327	64	3	10	–	–	–	77
HD 190470	–	3*	7*	3*	–	–	13*
HD 191089	30	3	22* + 4	–	–	–	59
HD 191849	40	–	17*	–	–	–	57
HD 192758	–	3*	–	4*	–	–	7*
HD 200800	–	3*	–	5*	–	–	8*
HD 202206	66	–	–	–	–	–	66
HD 202917	23	1	7* + 5	–	–	–	36
HD 205674	3	–	–	3*	–	–	6
HD 206893	16	2*	21* + 1	3*	–	–	43
HD 207129	344	–	–	–	–	–	344
HD 21997	4	3	19	–	13*	–	39
HD 221853	–	3*	–	3*	–	–	6*
HD 23863	–	5*	–	4*	–	–	9*
HD 24636	1	3	–	1*	–	–	5
HD 24966	3	3*	1*	3*	–	–	10
HD 25457	83	6	41	–	–	–	130

Continued on next page

Table B.1 – continued from previous page

Object	HARPS	UVES	FEROS	MIKE	HERMES	FIES	Total
HD 287787	–	3*	–	2*	–	–	5*
HD 287850	–	5*	1*	1*	–	–	7*
HD 287854	–	2*	1*	1*	–	–	4*
HD 287861	–	2*	1*	2*	–	–	5*
HD 290540	–	1*	2*	–	–	–	3*
HD 290609	–	2*	1*	1*	–	–	4*
HD 30447	19	4	2	–	–	–	25
HD 32195	–	4	1	–	–	–	5
HD 34324	5	3*	1*	–	–	–	9
HD 35150	–	1*	2*	2*	–	–	5*
HD 35332	–	2*	1*	2*	–	–	5*
HD 35367	–	4*	–	2*	–	–	6*
HD 35625	–	3*	–	2*	–	–	5*
HD 35841	–	3	–	1*	–	–	4
HD 36444	–	2*	1*	1*	–	–	4*
HD 3670	–	3*	19*	5*	–	–	27*
HD 36968	–	3*	–	2*	–	–	5*
HD 37484	–	2	–	–	–	–	2
HD 38207	–	1	1	1*	–	–	3
HD 38858	203	–	–	–	–	–	203
HD 40540	–	2*	1*	2*	–	–	5*
HD 45184	306	2	–	–	–	–	308
HD 46190	12	–	1	–	–	–	13
HD 52265	11	–	2	–	–	–	13
HD 53143	25	–	3	–	–	–	28
HD 53842	–	1*	3	–	–	–	4
HD 54341	4	–	–	–	–	–	4

Continued on next page

Table B.1 – continued from previous page

Object	HARPS	UVES	FEROS	MIKE	HERMES	FIES	Total
HD 60856	–	3*	1*	–	2*	–	6*
HD 60995	–	3*	–	1*	–	–	4*
HD 61005	33	2	43	–	–	–	78
HD 68420	–	3*	1*	–	–	–	4*
HD 69830	685	–	–	–	–	–	685
HD 71722	5	–	12	–	–	–	17
HD 74340	–	2*	1* + 2	–	–	–	5
HD 74374	–	3*	1*	–	–	–	4*
HD 76151	9	8	33* + 5	–	–	–	55
HD 80950	28	–	–	–	–	–	28
HD 82943	197	–	–	–	–	–	197
HD 84075	12	1	16*	–	–	–	29
HD 84870	–	3*	–	–	–	–	3*
HD 870	4	–	1	–	–	–	5
HD 90874	–	2*	1*	–	–	–	3*
HD 92536	10	–	–	–	–	–	10
HD 93738	4	1*	2*	–	–	–	7
HD 95086	125	–	16	–	–	–	141
HD 95698	–	2*	1*	–	–	–	3*
HD 98363	–	3*	8	–	–	–	11
HD 23923	–	4*	–	4*	–	–	8*
HD 24817	–	3*	–	4*	–	–	7*
HD 25570	1	2*	1*	1*	–	–	5
HD 37286	5	1*	3	–	–	–	9
HD 37306	22	–	12	1*	9*	–	44
HD 38056	5	3*	–	2*	–	–	10
HD 38206	15	–	7	–	11*	–	33

Continued on next page

Table B.1 – continued from previous page

Object	HARPS	UVES	FEROS	MIKE	HERMES	FIES	Total
HD 50571	–	2*	16* + 2	–	–	–	20
HD 71043	10	–	15	–	–	–	25
HD 76653	44	–	16* + 5	–	–	–	65
HD 78702	6	3*	1*	–	–	–	10
HD 79108	–	–	3* + 9	–	–	–	12
HD 86087	–	1*	2* + 1	–	–	–	4
HD 88215	–	3* + 1	–	–	–	–	4
HD 91375	41	1	5	–	–	–	47
HD 104600	–	3*	–	–	–	–	3*
HD 107301	–	3*	–	–	–	–	3*
HD 113902	–	3*	6	–	–	–	9
HD 128207	7	–	1	–	–	–	8
HD 132238	1	2*	–	–	–	–	3
HD 138923	–	3*	2	2*	–	–	7
HD 138965	1	2*	2	1*	–	–	6
HD 142139	26	–	24	–	–	–	50
HD 145689	28	3	7	–	–	–	38
HD 145964	–	–	14	2*	5*	–	21
HD 158352	21	3	–	–	–	–	24
HD 1591	10	–	–	–	–	–	10
HD 162917	–	2*	–	2*	–	–	4*
HD 170773	–	3*	7* + 2	3*	–	–	15
HD 199260	51	–	17* + 5	–	–	–	73
HD 17390	–	18*	–	130*	–	–	148*
HD 219482	34	–	4	–	–	–	38
HD 203	–	4*	8	–	–	–	12
HD 225200	9	–	1	–	–	–	10

Continued on next page

Table B.1 – continued from previous page

Object	HARPS	UVES	FEROS	MIKE	HERMES	FIES	Total
*iot Cen	34	–	28	–	–	–	62
*iot Del	–	3*	–	6*	–	–	9*
*kap01 Sgr	–	3*	11	–	–	–	14
*kap Lep	–	3*	–	3*	–	–	6*
*kap Phe	6	2*	65	–	–	–	73
*kap Psc	–	3*	–	5*	–	–	8*
*lam01 Phe	10	–	–	–	–	–	10
*lam Boo	–	–	–	–	2*	2*	4*
*l Tau	38	–	–	–	–	–	38
*mu. Ara	2979	6	–	–	–	–	2985
*nu. Hor	24	–	–	–	–	–	24
*nu. Phe	69	7	17*	–	–	–	93
*omi01 Cnc	–	1*	5	–	–	–	6
*omi02 Cnc	–	–	5	–	–	–	5
*phi01 Pav	–	4*	–	6*	–	–	10*
*phi For	–	3*	–	6*	–	–	9*
*pi.01 Ori	–	3*	11	3*	5*	–	22
*pi. Ara	224	–	–	–	–	–	224
*pi. Cha	–	3*	–	–	–	–	3*
*q01 Eri	142	9	–	–	–	–	151
*q02 Eri	6	3*	–	4*	–	–	13
*rho Aql	20	–	–	–	–	–	20
*rho Pup	447	2	–	–	–	–	449
*rho Tel	39	–	–	–	–	–	39
*rho Vir	14	1	14	–	30*	2*	61
*tau01 Aqr	–	4*	–	2*	–	–	6*
*tau Vir	–	3*	–	–	–	–	3*

Continued on next page

Table B.1 – continued from previous page

Object	HARPS	UVES	FEROS	MIKE	HERMES	FIES	Total
*tet Aql	–	3*	–	3*	–	–	6*
*tet CrB	–	2	–	–	–	–	2
*tet Hya	6	1* + 2	4	–	–	–	13
*tet Leo	–	1* + 2	–	–	–	–	3
V* AU Mic	48	5	3	–	–	–	56
V* CE Ant	29	3	24	–	–	–	56
V* DK Cet	60	2	34	–	–	–	96
V* EX Eri	4	6*	10	4*	–	–	24
V* LM Lup	–	1*	–	2*	–	–	3*
V* MO Hya	–	6	9	–	–	–	15
V* V1229 Tau	–	13	–	–	–	–	13
V* V342 Peg	155	2	150	–	–	–	307
V* V933 Sco	–	–	–	2*	–	–	2*
*zet CrA	10	–	2	–	–	–	12
*zet Lep	23	–	–	–	–	–	23
Total	12275	432* + 453	607* + 1157	503*	196*	37*	15660

Appendix C

Figures and Tables of Chapter 3

C.1 Photospheric line fits

In this appendix we provide the figures illustrating the Kurucz models that best reproduce each one of the lines of the reference spectrum for each star in the sample presented in Chapter 3. In all cases the reference spectrum is displayed in black and the best-fitting model in red. Please note that the parameters are allowed to vary between different lines for the same object (as these models do not include non-LTE effects).

C.2 Residual components

Here we provide the figures showing every isolated component and the multi-Gaussian fit obtained to reproduce and characterize the absorption features in the objects presented in Chapter 3.

C.3 Neighbouring stars

In this appendix we show the analysis performed with neighbouring stars looking for features of similar characteristics to those detected in each 'science' target in Chapter 3 (paying particular attention to the velocity). The detection of the same feature in several stars does automatically support an ISM origin of the feature.

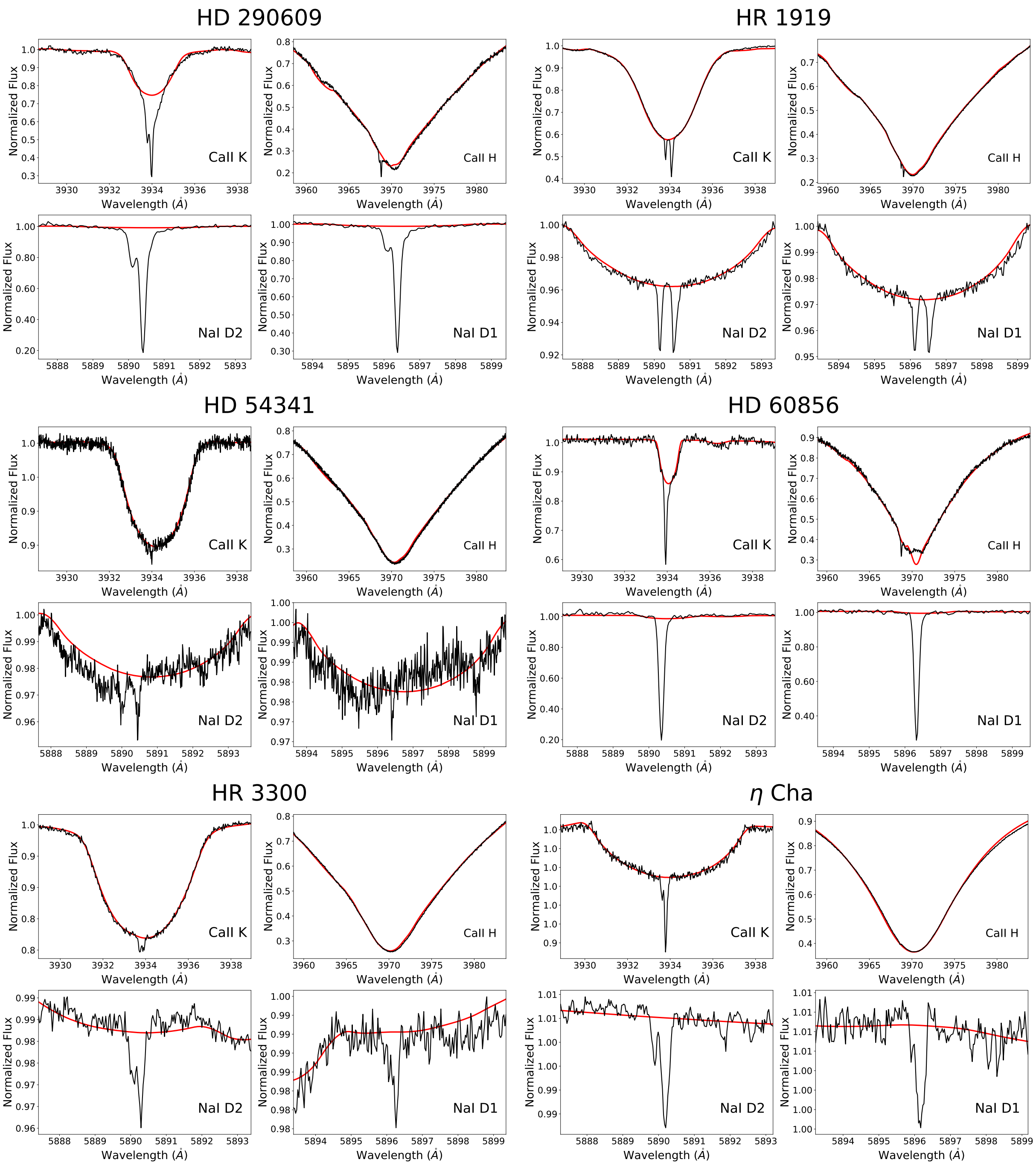

Figure C.1: Best-fit models for HD 290609's, HR 1919's, HD 54341's, HD 60856's, HR 3300's and η Cha's Ca II H&K and Na I D1&D2 lines. Median from the real spectra in black, synthetic spectrum in red.

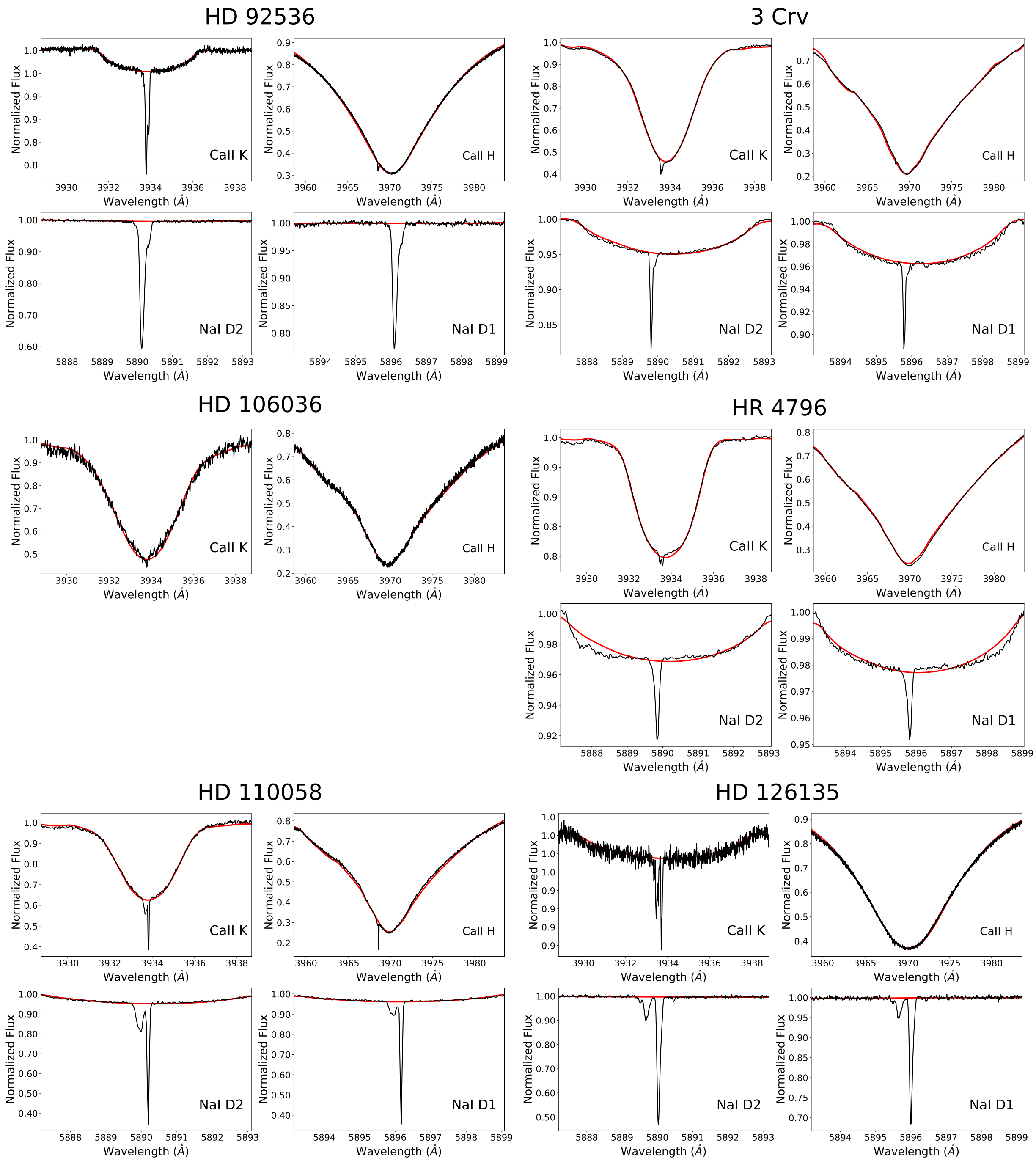

Figure C.2: Best-fit models for HD 92536's, 3 Crv's, HD 106036's, HR 4796's, HD 110058's and HD 126235's Ca II H&K and Na I D1&D2 lines. Median from the real spectra in black, synthetic spectrum in red.

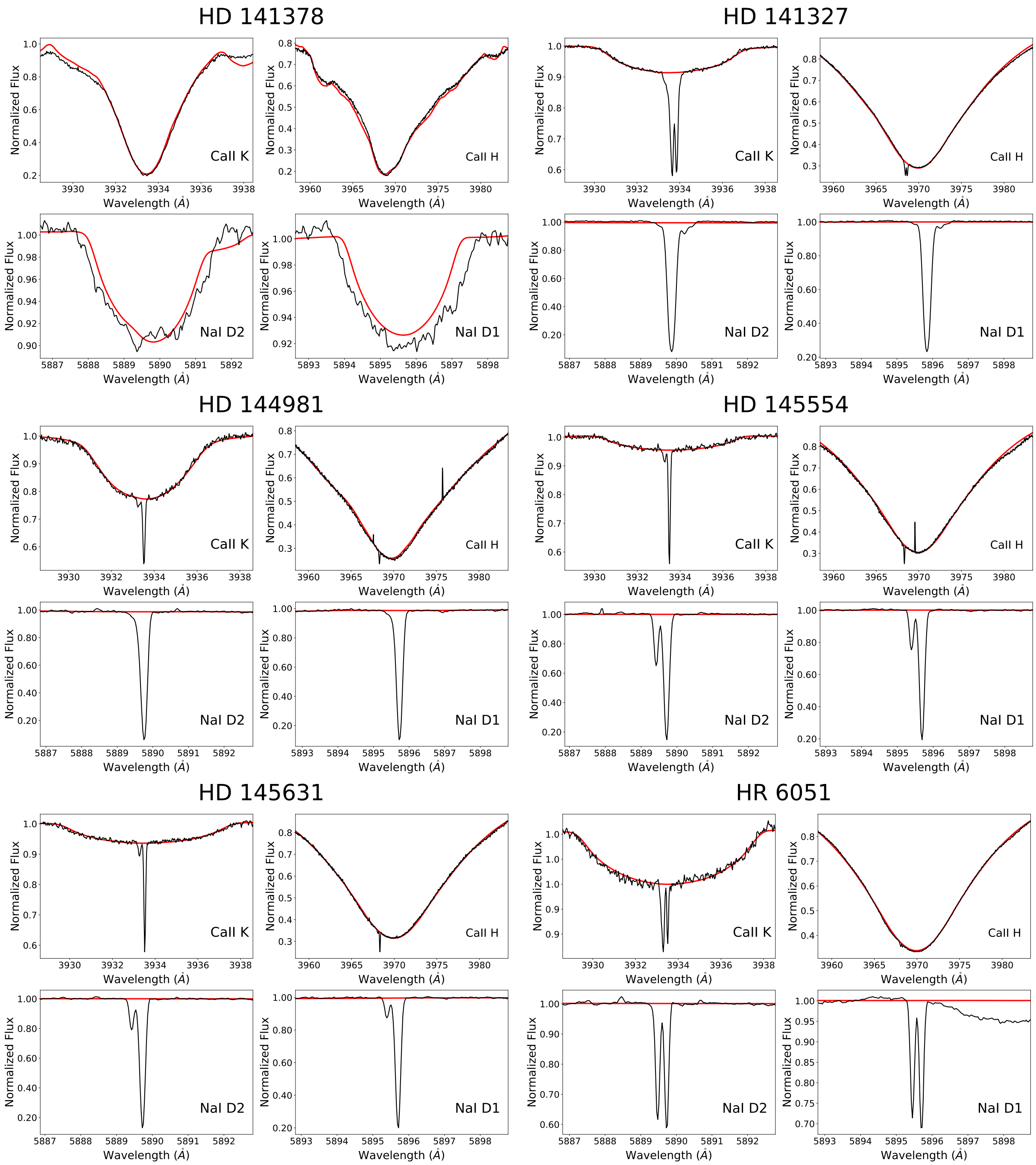

Figure C.3: Best-fit models for HD 141378's, HD 141327's, HD 1444981's, HD 145554's, HD 145631's and HR 6051's Ca II H&K and Na I D1&D2 lines. Median from the real spectra in black, synthetic spectrum in red.

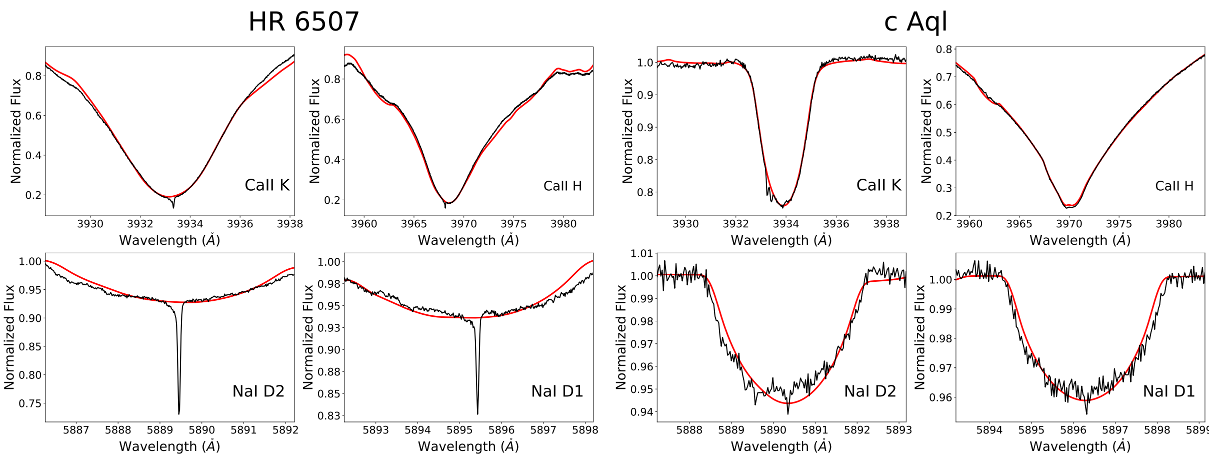

Figure C.4: Best-fit models for HR 6507's and c Aql's Ca II H&K and Na I D1&D2 lines. Median from the real spectra in black, synthetic spectrum in red.

Table C.1: All nearby stars used in the analysis per each object of science, their number of spectra, instrument and ESO program ID. Note that HD 290540, HD 36444 and HD 290609 are each other's nearby stars and in addition have three other common nearby stars, as well as HD 145554, HD 144981 and HD 145631 which also have another common nearby star.

Object	Nearby star	Number of Spectra	Instrument	Program ID
β03 Tuc	β01 Tuc	6	HARPS	073.C-0733(E)
		2	HARPS	075.C-0689(A)
		2	HARPS	077.C-0295(A)
		2	HARPS	077.C-0295(B)
		3	FEROS	094.A-9012(A)
ν Hor	HR 798	1	FEROS	179.C-0197(B)
	HR 762	4	FEROS	088.C-0498(A)
HD 290540, HD 36444 and HD 290609	HR 1861	1	FEROS	074.B-0455(A)
	HR 1863	12	UVES	266.D-5655(A)
	VVV Ori	98	UVES	194.C-0833(C)
		6	FEROS	096.A-9030(A)
		2	FEROS	096.A-9024(A)
HR 1919	VV350 Ori	2	UVES	082.C-0831(A)

Continued on next page

Table C.1 – continued from previous page

Object	Nearby star	Number of Spectra	Instrument	Program ID
	HD 38735	79	FEROS	084.C-1008(A)
		24	FEROS	084.A-9004(B)
		4	FEROS	091.D-0414(B)
HD 54341	L01 Pup	1	FEROS	088.A-9003(A)
HD 60856	HD 61045	8	UVES	072.D-0410(A)
	HD 60995	6	UVES	098.C-0463(A)
HR 3300	HD 70731	7	UVES	093.D-0852(A)
	HD 71722	5	HARPS	094.C-0946(A)
		12	FEROS	094.A-9012(A)
η Cha	HD 75505	7	FEROS	084.A-9003(A)
		1	FEROS	086.A-9006(A)
	9 Cha	310	FEROS	078.D-0549(A)
		3	FEROS	084.A-9003(A)
HD 92536	tet Car	1	FEROS	073.D-0291(A)
		1	FEROS	074.D-0300(A)
		15	UVES	076.C-0503(A)
		80	UVES	077.C-0547(A)
		1	FEROS	078.D-0080(A)
		125	UVES	194.C-0833(A)
	VV407 Car	9	FEROS	086.D-0449(A)
	HD 93738	2	FEROS	096.A-9018(A)
	VV364 Car	6	FEROS	086.D-0449(A)
3 Crv	zet Crv	1	FEROS	179.C-0197(D)
HD 106036	zet Cru	1	FEROS	090.D-0358(A)
HR 4796	u Cen	30	FEROS	60.A-9700(A)
		121	HARPS	60.A-9036(A)

Continued on next page

Table C.1 – continued from previous page

Object	Nearby star	Number of Spectra	Instrument	Program ID
		120	HARPS	60.A-9700(G)
HD 110058	tau Cen	8	HARPS	076.C-0279(A)
		4	HARPS	076.C-0279(C)
		1	FEROS	078.D-0080(A)
		20	UVES	087.D-0010(A)
	HD 110484	3	FEROS	083.C-0139(A)
	HR 4871	1	FEROS	078.D-0080(A)
		1	FEROS	087.C-0227(C)
		13	HARPS	088.C-0353(A)
		13	HARPS	089.C-0006(A)
	sig Cen	1	FEROS	082.B-0484(A)
		40	FEROS	084.B-0029(A)
HD 112810	H Cen	10	UVES	266.D-5655(A)
		2	HARPS	185.D-0056(A)
		1	HARPS	185.D-0056(C)
HD 126135	a Cen	14	UVES	266.D-5655(A)
		64	UVES	073.D-0504(A)
		3	HARPS	075.C-0234(A)
		3	HARPS	079.C-0170(A)
		18	UVES	081.C-0475(A)
		4	UVES	097.D-0035(A)
	HD 124961	2	FEROS	072.D-0021(A)
		2	FEROS	073.D-0049(A)
		2	FEROS	082.D-0061(A)
HD 141378	HD 141569	1	UVES	075.C-0637(A)
		109	UVES	079.C-0789(A)

Continued on next page

Table C.1 – continued from previous page

Object	Nearby star	Number of Spectra	Instrument	Program ID
		1	FEROS	083.A-9003(A)
		7	FEROS	085.A-9027(B)
	b Ser	10	UVES	076.B-0055(A)
		8	HARPS	077.C-0295(A)
		2	HARPS	077.C-0295(C)
		2	FEROS	083.A-9014(A)
		2	FEROS	083.A-9011(B)
		1	FEROS	083.A-9014(B)
		3	FEROS	084.A-9011(B)
		3	FEROS	085.A-9027(G)
HD 141327	HD 142426	6	FEROS	089.D-0097(B)
		2	FEROS	090.D-0061(B)
		2	FEROS	091.D-0145(A)
	HD 140037	1	FEROS	179.C-0197(C)
		1	FEROS	091.C-0713(A)
	ksi01 Lup	11	FEROS	075.D-0342(A)
		6	HARPS	075.C-0689(A)
		2	HARPS	075.C-0689(B)
		2	HARPS	077.C-0295(D)
	ksi02 Lup	2	HARPS	075.C-0689(B)
		2	HARPS	077.C-0295(D)
		2	HARPS	077.C-0295(C)
		12	HARPS	184.C-0815(F)
HD 145554, HD 144981 and HD 145631	HD 145501	2	FEROS	086.D-0449(A)
HR 6051	HD 146029	1	FEROS	179.C-0197(A)
	HD 144822	1	FEROS	077.C-0138(A)

Continued on next page

Table C.1 – continued from previous page

Object	Nearby star	Number of Spectra	Instrument	Program ID
HR 6507	V2373 Oph	9	FEROS	091.D-0122(A)
	HD 156208	8	FEROS	081.D-2002(A)
c Aql	BD+01 3992	10	UVES	293.D-5036(A)
	HD 183735	1	FEROS	083.D-0034(A)

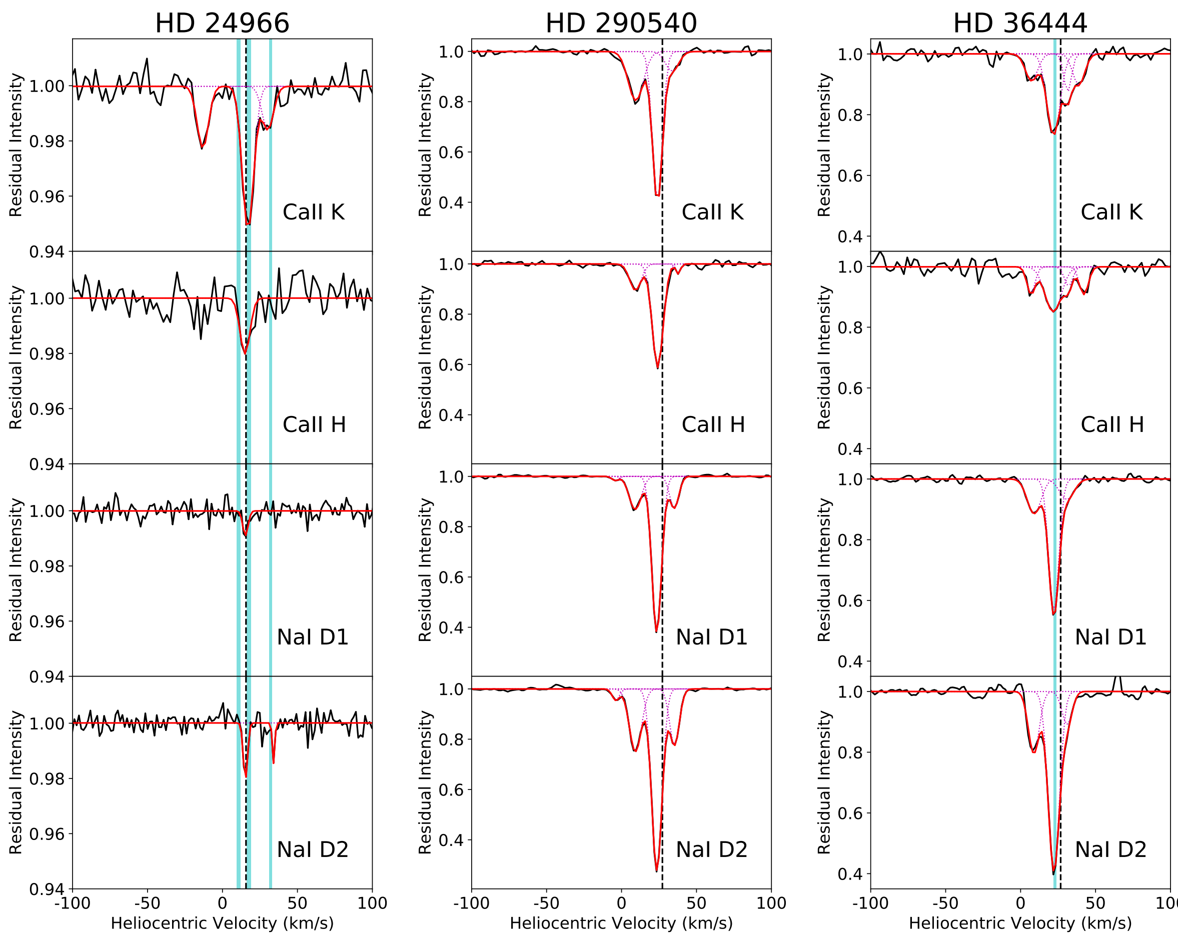

Figure C.5: Absorption profiles of the Ca II H & K and Na I D1 & D2 lines for HD 24966, HD 290540 and HD 36444. Photospheric absorptions have been subtracted and the remaining extra components have been modelled by gaussian profiles. Individual gaussian fits are shown in dotted magenta lines and the combined profile is shown in red. Dashed black line marks the estimated radial velocity of the star and cyan lines mark the velocity of the traversing clouds in the line of sight with their respective errors as their line widths.

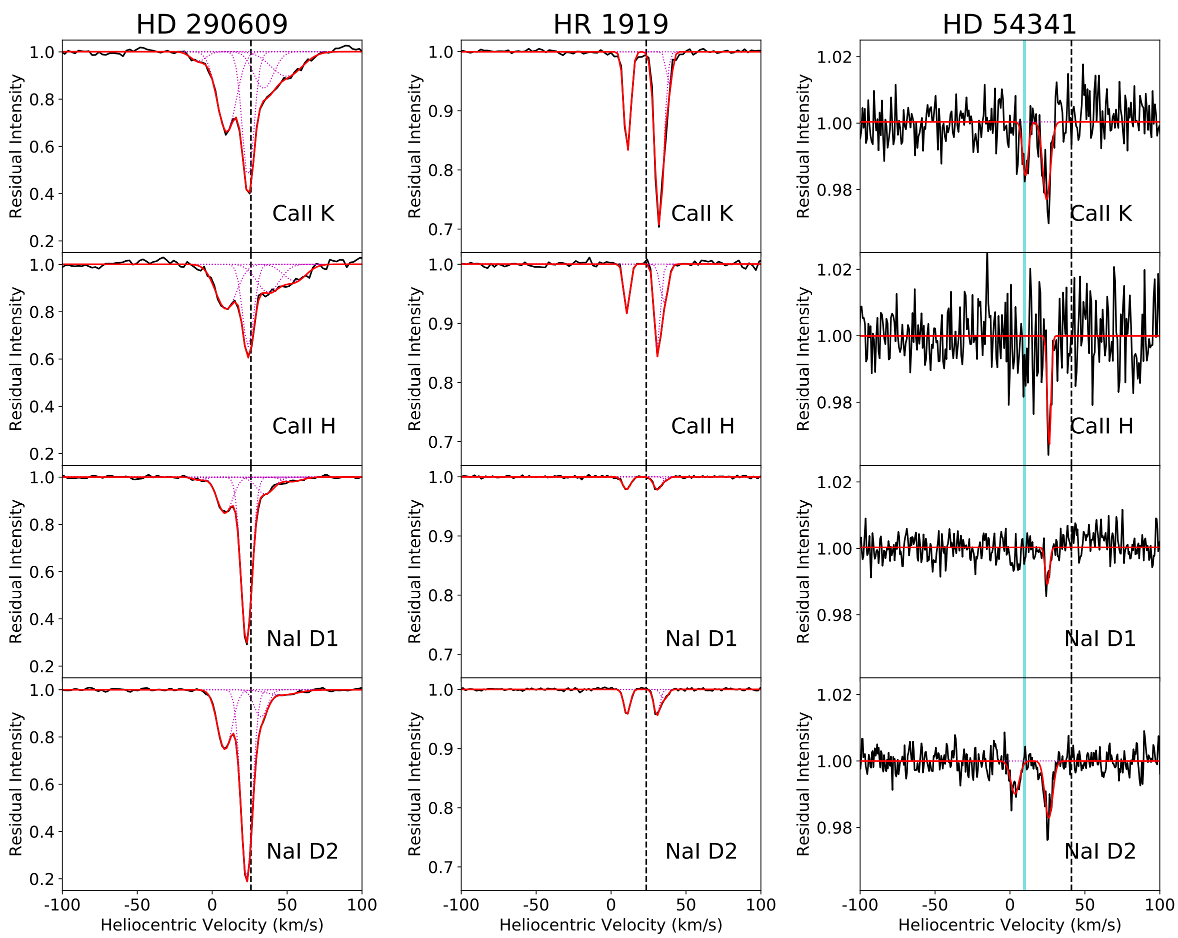

Figure C.6: Absorption profiles of the Ca II H & K and Na I D1 & D2 lines for HD 290609, HR 1919 and HD 54341. Same specifications as in Fig. C.5.

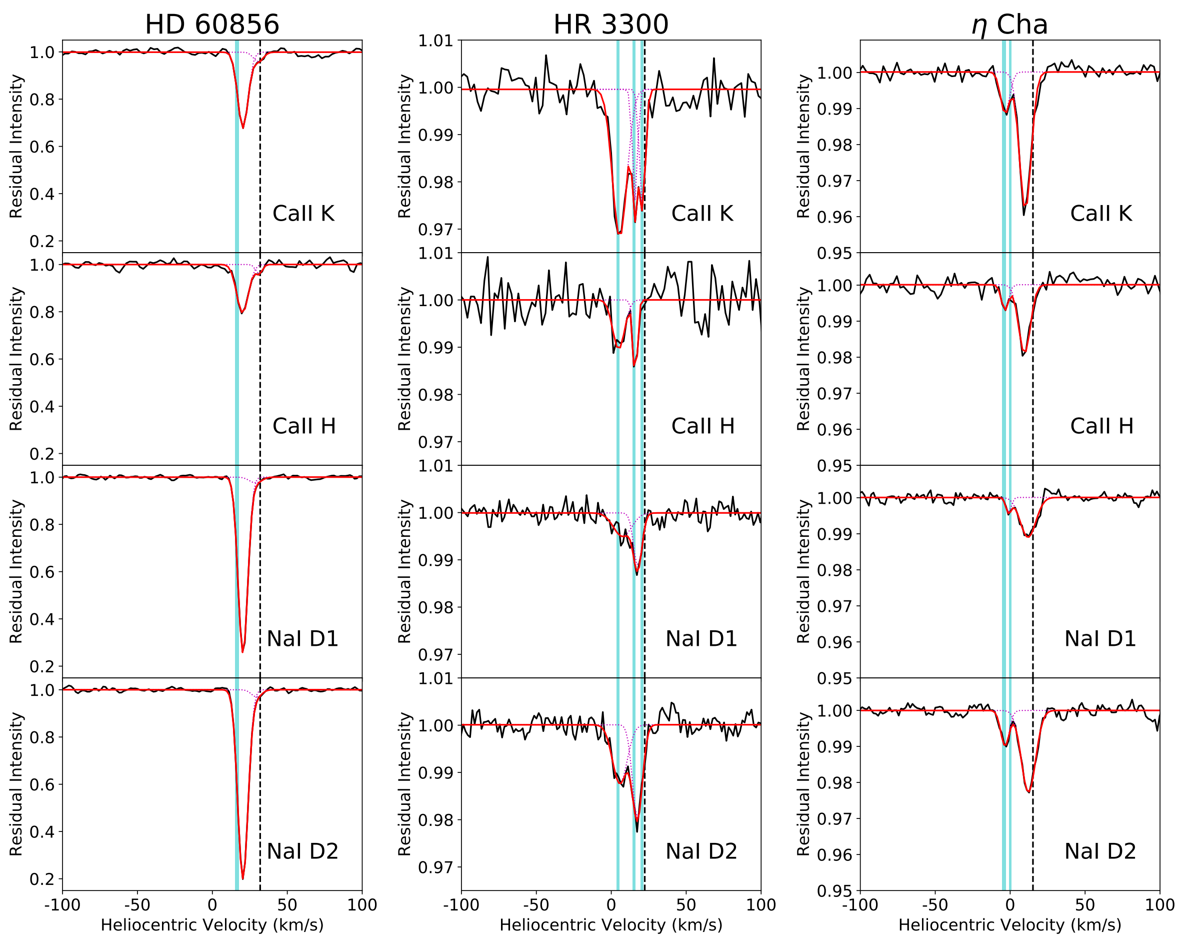

Figure C.7: Absorption profiles of the Ca II H & K and Na I D1 & D2 lines for HD 60856, HR 3300 and η Cha. Same specifications as in Fig. C.5.

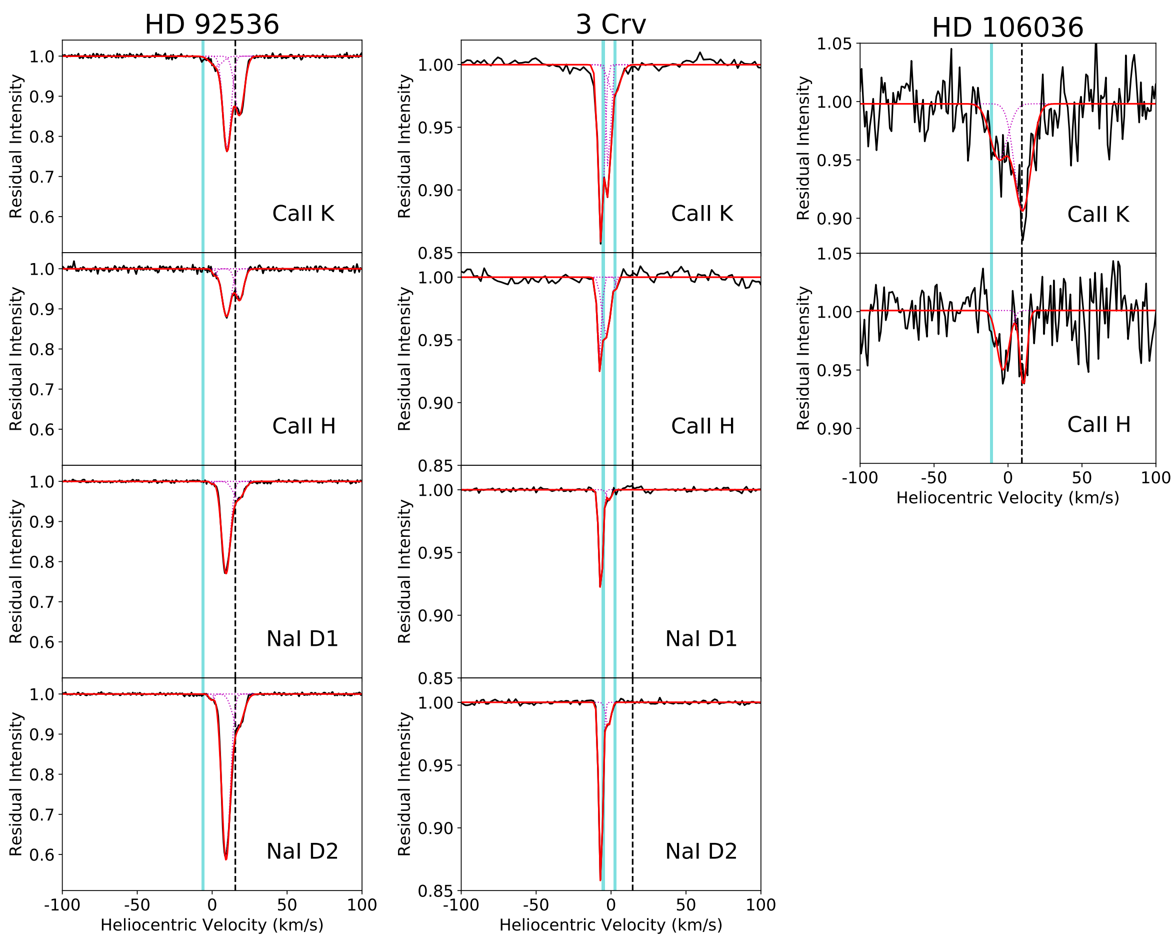

Figure C.8: Absorption profiles of the Ca II H & K and Na I D1 & D2 lines for HD 92536, 3 Crv and HD 106036. Same specifications as in Fig. C.5.

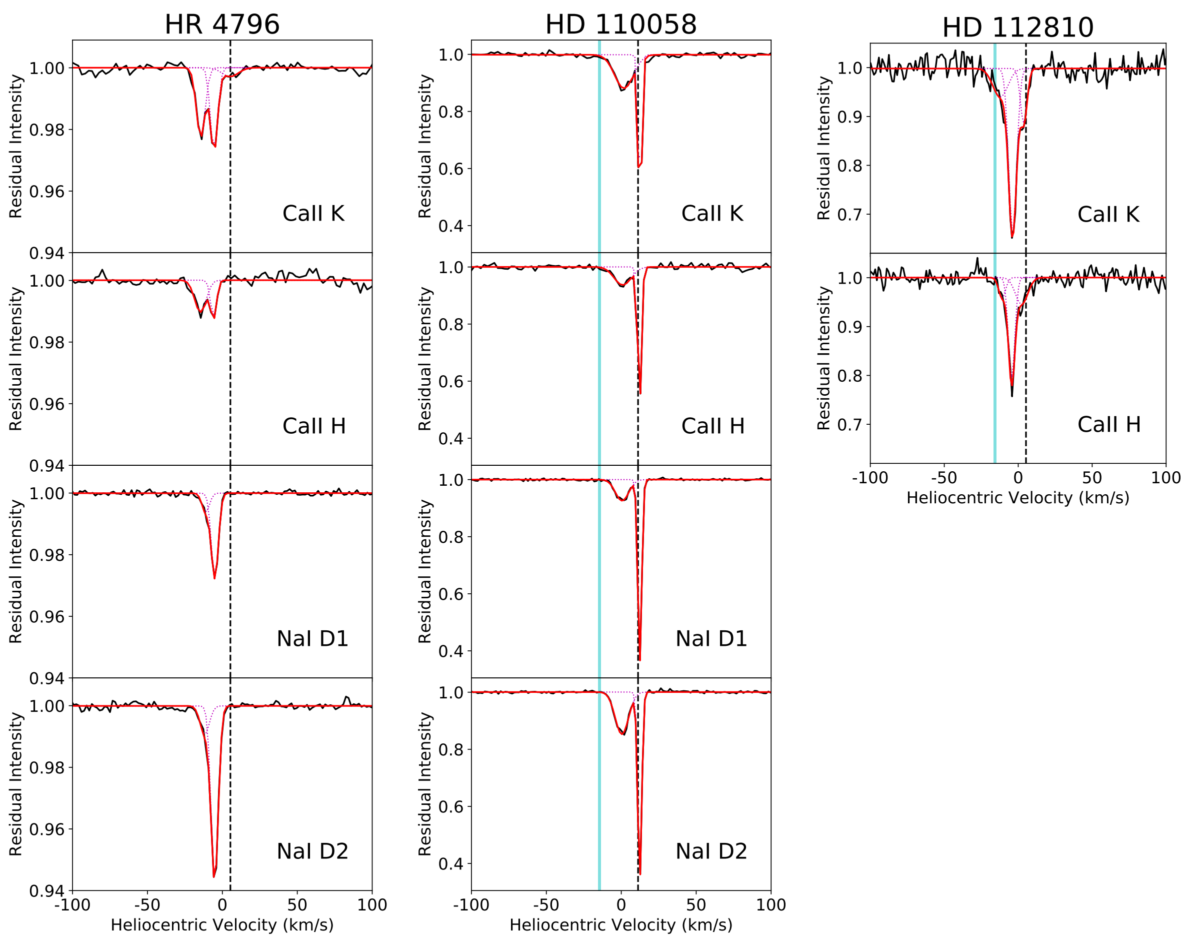

Figure C.9: Absorption profiles of the Ca II H & K and Na I D1 & D2 lines for HR 4796, HD 110058 and HD 112810. Same specifications as in Fig. C.5.

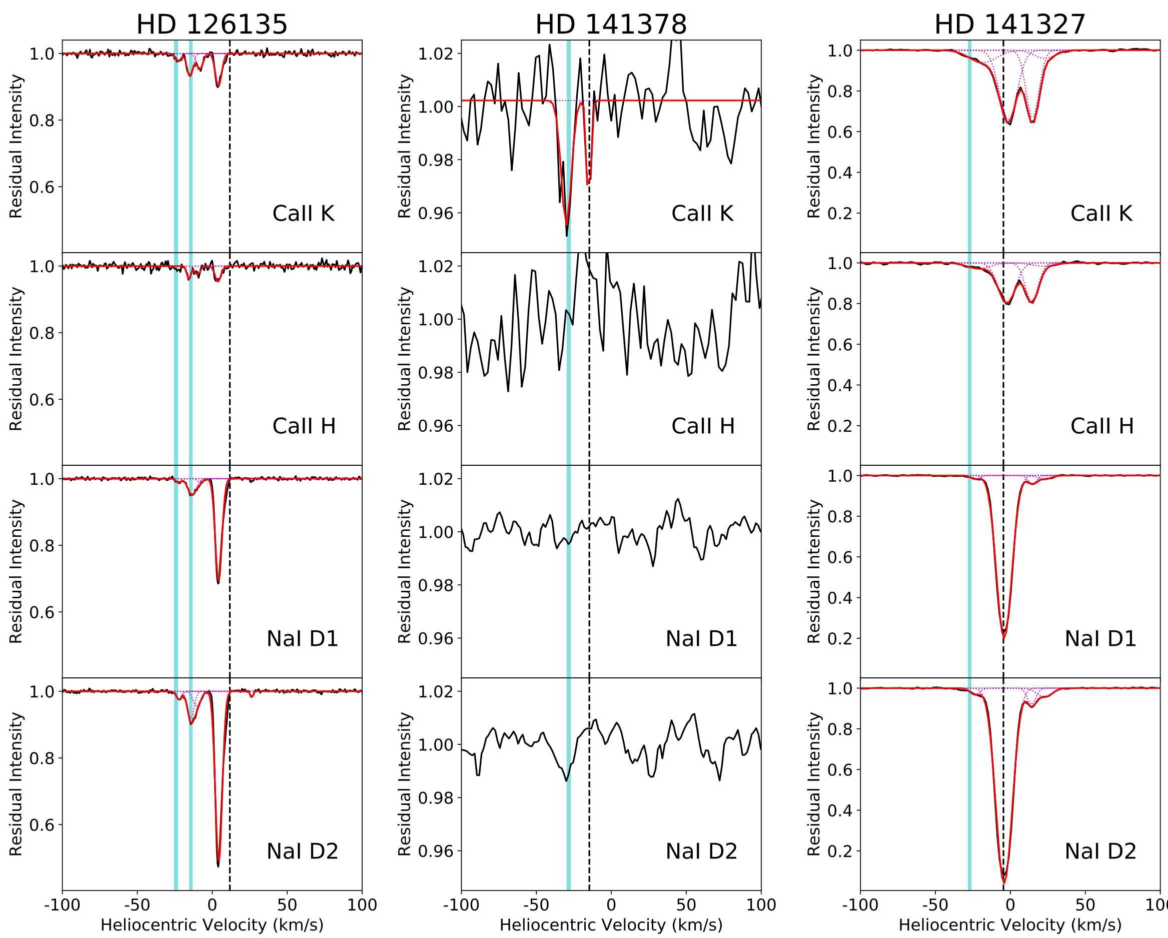

Figure C.10: Absorption profiles of the Ca II H & K and Na I D1 & D2 lines for HD 126135, HD 141378 and HD 141327. Same specifications as in Fig. C.5.

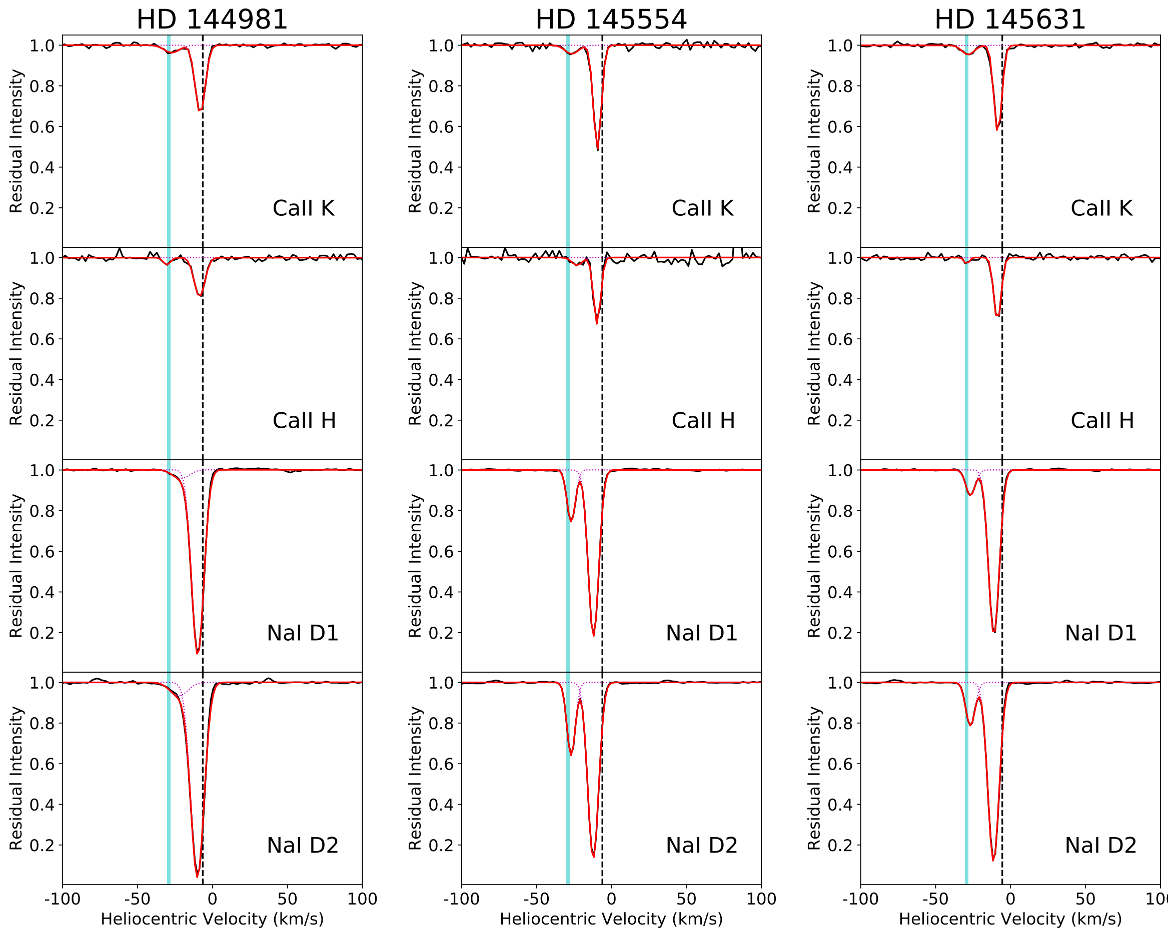

Figure C.11: Absorption profiles of the Ca II H & K and Na I D1 & D2 lines for HD 144981, HD 145554 and HD 145631. Same specifications as in Fig. C.5.

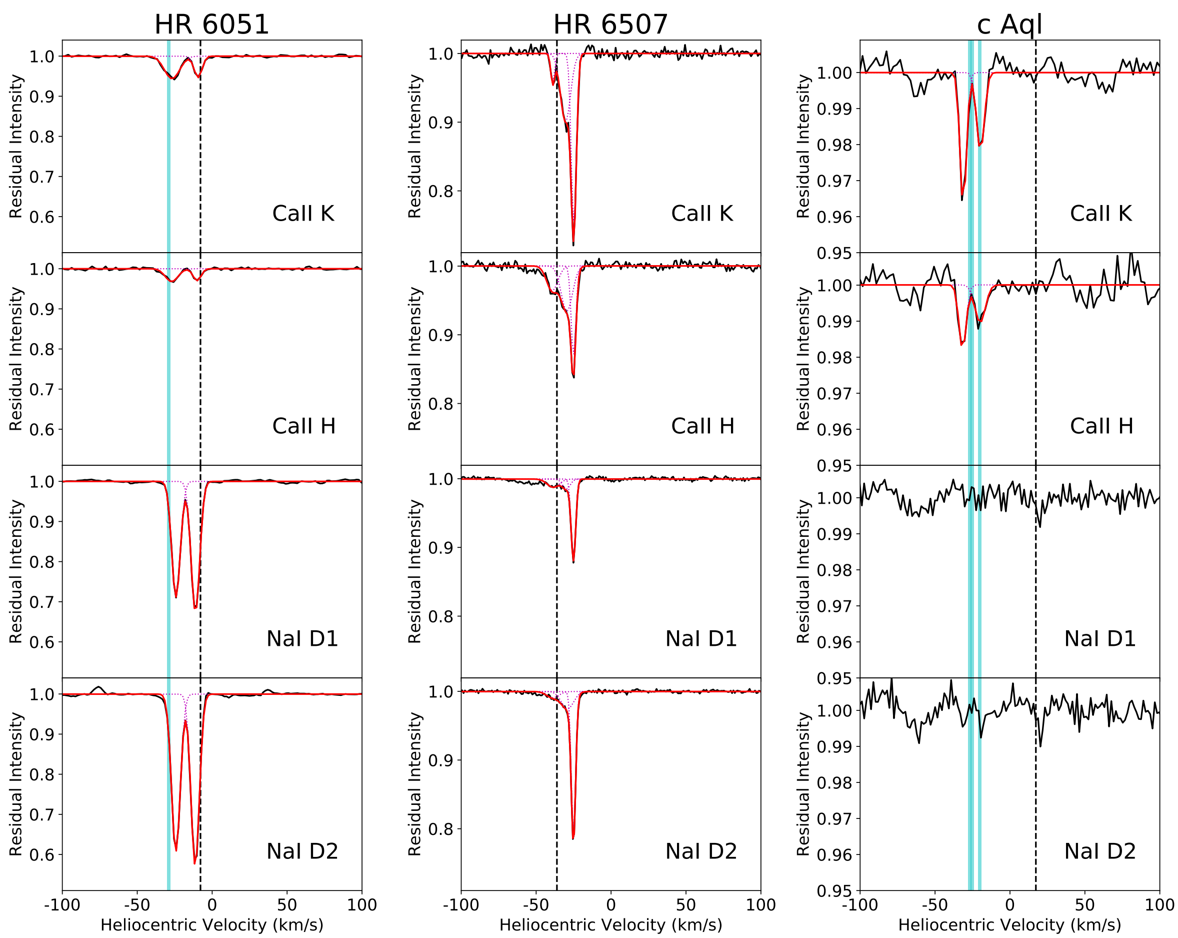

Figure C.12: Absorption profiles of the Ca II H & K and Na I D1 & D2 lines for HR 6051, HR 6507 and c Aql. Same specifications as in Fig. C.5.

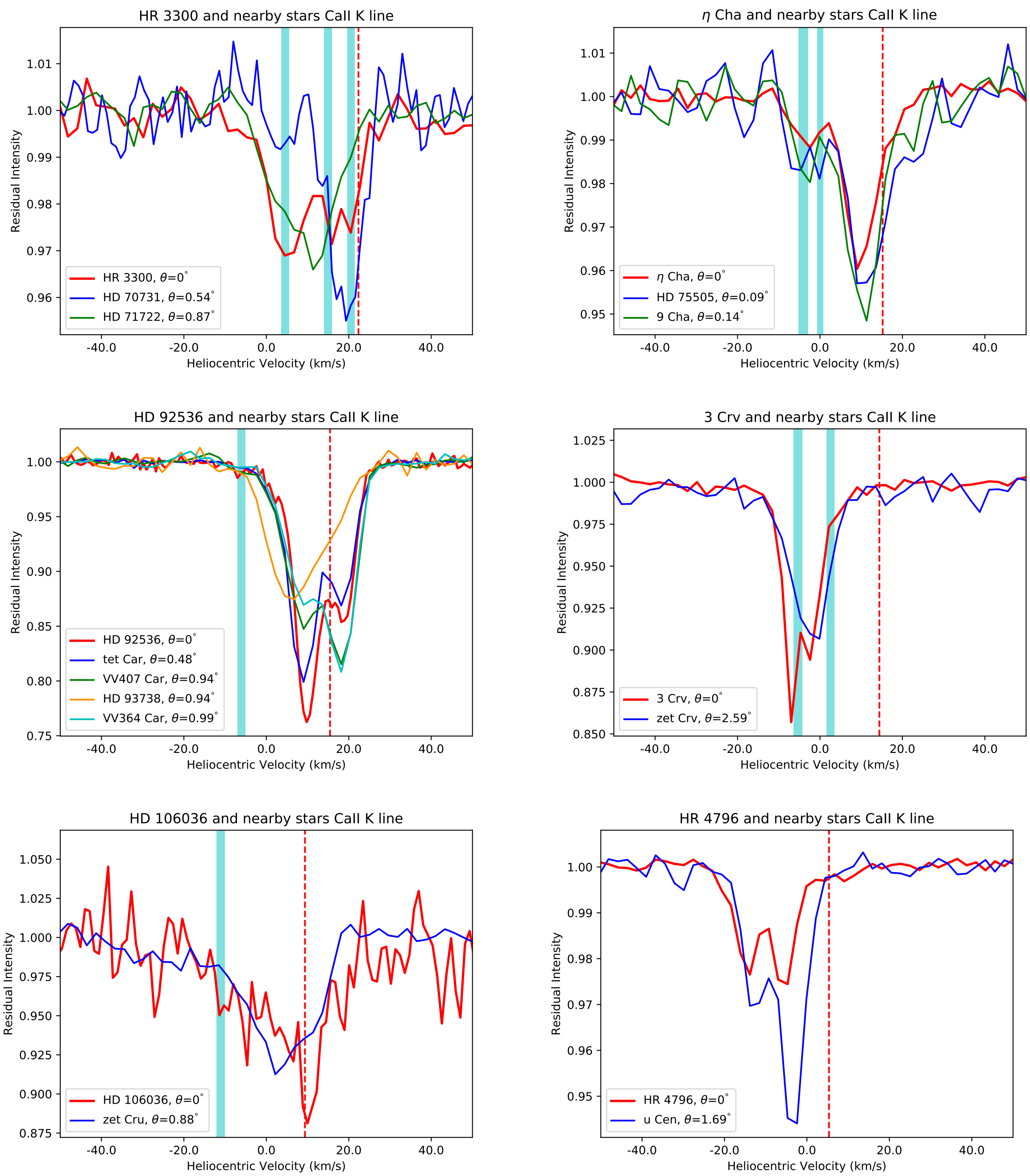

Figure C.13: Nearby stars around HR 3300, η Cha, HD 92536, 3 Crv, HD 106036 and HR 4796. Dashed line marks the estimated radial velocity of the star and cyan lines mark the velocity of the traversing clouds in the line of sight with their respective errors as their line widths.

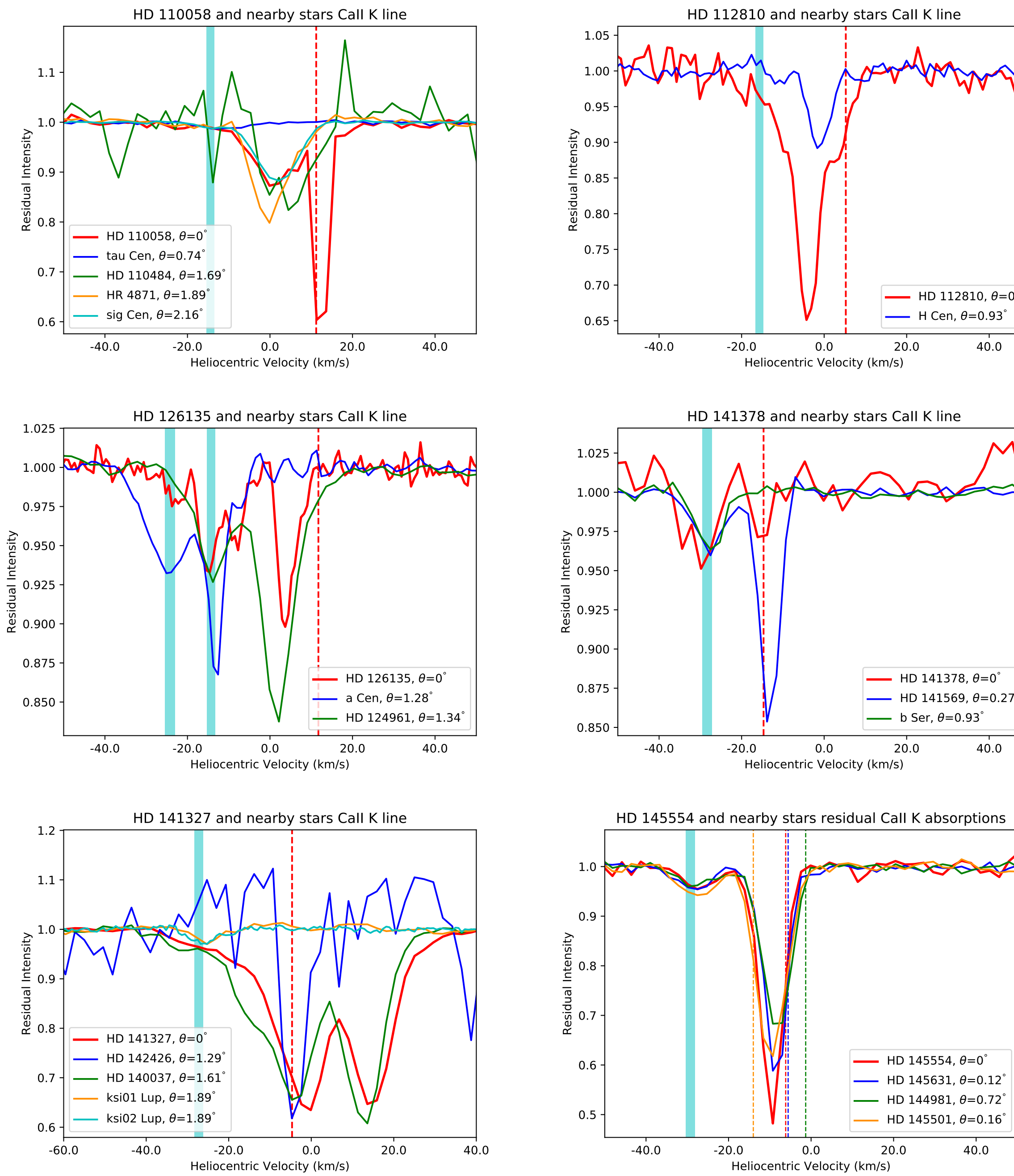

Figure C.14: Nearby stars around HD 110058, HD 112810, HD 126135, HD 141378, HD 141327 and HD 145554 (along with HD 144981 and HD 145631). Dashed line marks the estimated radial velocity of the star and cyan lines mark the velocity of the traversing clouds in the line of sight with their respective errors as their line widths.

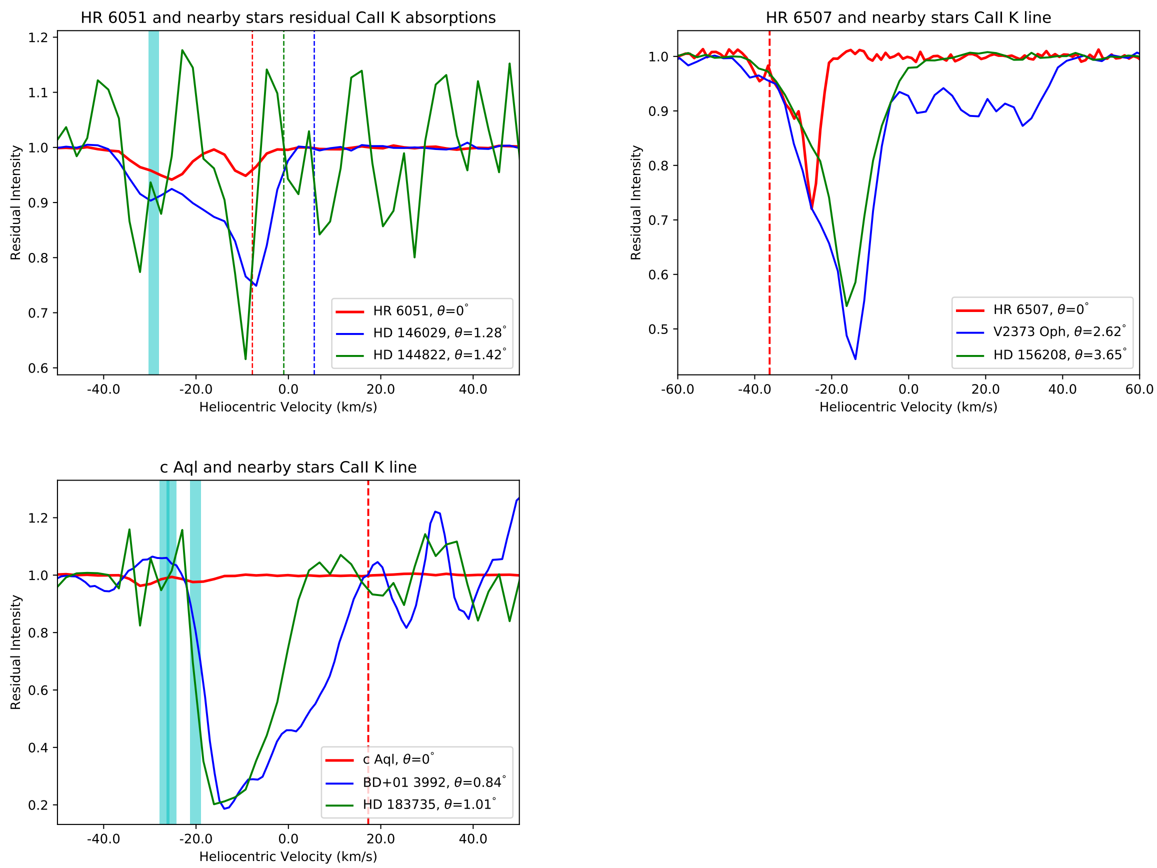

Figure C.15: Nearby stars around HR 6051, HR 6507 and c Aql. Dashed line marks the estimated radial velocity of the star and cyan lines mark the velocity of the traversing clouds in the line of sight with their respective errors as their line widths.

Appendix D

Tables of Chapter 5

D.1 Parameters of the sample

Table D.1: Main parameters of the sample. Spectral type, heliocentric radial velocity, projected rotational velocity, luminosity ratio L_{disk}/L_{star}, distance and age flag, where "O" stands for older than 100 Myr and "Y" stands for younger than 100 Myr.

Simbad ID	Spectral type	RV [km.s^{-1}]	$v$sin$i$ [km.s^{-1}]	$L_{\rm disk}/L_\star$	Distance [pc]	Age flag
HD 1466	F8V	6.32	21.00	1.05 x10^{-4}	42.97	Y
HD 1461	G3VFe0.5	-10.09	4.80	4.23 x10^{-5}	23.46	O
kap Phe	A5IVn	11.30	194.00	1.10 x10^{-5}	23.8	O
lam01 Phe	A1Va	-2.00	–	1.38 x10^{-5}	56.12	O
HD 3670	F5V	8.92	–	5.15 x10^{-4}	77.59	O
nu. Phe	F9VFe+0.4	11.82	–	3.03 x10^{-5}	15.17	O
49 Cet	A1V	10.30	196.00	6.93 x10^{-4}	57.06	Y
q01 Eri	F9V	27.82	3.84	3.18 x10^{-4}	17.34	O
q02 Eri	A1V	9.50	–	7.36 x10^{-5}	60.96	O
V DK Cet	G4V	6.12	15.20	6.34 x10^{-5}	41.41	Y
HD 13246	F7V	10.68	35.60	1.72 x10^{-4}	45.61	Y
bet Tri	A5III	12.30	70.00	2.70 x10^{-5}	38.89	O
gam Tri	A1Vnn	9.90	254.00	6.76 x10^{-5}	34.43	Y
alf For	F6V+G7V	-17.14	4.41	5.88 x10^{-4}	14.23	O
94 Cet	F8.5V	18.96	7.70	3.94 x10^{-6}	22.53	O
HD 21997	A3IV/V	17.30	69.80	4.79 x10^{-4}	69.64	Y
V1229 Tau	A0VpSi+Am	5.00	40.00	2.00 x10^{-4}	139.54	Y
28 Tau	B8Vne	5.10	220.00	1.49 x10^{-4}	129.48	O
HD 25457	F7V	17.62	20.24	1.23 x10^{-4}	18.77	Y
gam Dor	F1V	25.20	59.50	1.72 x10^{-5}	20.45	O
V EX Eri	A7VkA3mA3	14.40	130.00	4.37 x10^{-5}	57.47	Y
HD 30447	F3V	24.65	–	9.38 x10^{-4}	80.53	Y
pi.01 Ori	A0Va_lB	11.10	120.00	5.86 x10^{-5}	35.66	O
HD 35367	A1IV/V	–	–	1.66 x10^{-4}	365.79	O

Continued on next page

Table D.1 – continued from previous page

Simbad ID	Spectral type	RV [km.s^{-1}]	$v$sin$i$ [km.s^{-1}]	$L_{\rm disk}/L_{\star}$	Distance [pc]	Age flag
HD 287861	A0	–	–	3.02 x10^{-4}	363.62	O
HD 290609	B8	–	–	1.60 x10^{-4}	847.45	O
HR 1915	A2III/IV	22.40	70.00	7.82 x10^{-5}	58.89	Y
HD 37306	A1V	23.00	148.10	8.68 x10^{-5}	70.46	Y
HR 1975	A0V	25.30	35.00	1.47 x10^{-4}	71.4	Y
HD 38858	G2V	31.61	1.00	5.81 x10^{-5}	15.25	O
HD 45184	G2Va	-3.73	5.40	8.82 x10^{-5}	21.96	O
HD 46190	A0V	–	–	1.10 x10^{-5}	84.51	O
HD 52265	G0V	53.92	6.70	1.81 x10^{-5}	30.0	O
HD 61005	G8Vk	22.64	8.20	2.67 x10^{-3}	36.48	Y
HD 69830	G8:V	30.29	5.20	1.84 x10^{-4}	12.56	O
HD 71722	A0V	30.20	–	1.00 x10^{-4}	69.33	O
HD 76151	G2V	32.08	3.58	2.34 x10^{-5}	16.85	O
HR 3570	F6V	-6.88	10.30	1.68 x10^{-5}	24.26	O
HD 82943	F9VFe+0.5	8.220	6.50	1.51 x10^{-4}	27.61	O
HR 3927	A0V	13.90	–	1.35 x10^{-4}	99.33	O
HR 4138	A1V	7.50	10.00	1.05 x10^{-5}	79.87	O
V CE Ant	M2Ve	11.40	4.40	1.19 x10^{-3}	34.03	Y
HD 95086	A8III	10.10	–	1.22 x10^{-3}	86.44	Y
bet UMa	A1IVps	-13.10	46.00	1.11 x10^{-5}	24.44	O
HD 98363	A2V	9.60	–	7.28 x10^{-4}	138.59	O
HD 101088	F5IV	19.70	152.00	2.73 x10^{-5}	101.24	O
HD 102458	G4V	14.40	31.00	1.00 x10^{-4}	113.4	O
HD 104231	F5V	13.51	36.00	1.46 x10^{-4}	102.73	O
CD-54 4621	K0Ve	14.70	29.70	3.13 x10^{-4}	113.28	Y
HD 106906	F5V	10.20	55.00	1.33 x10^{-3}	103.33	Y

Continued on next page

Table D.1 – continued from previous page

Simbad ID	Spectral type	RV [km.s^{-1}]	$v$sin$i$ [km.s^{-1}]	$L_{\rm disk}/L_\star$	Distance [pc]	Age flag
HD 107146	G2V	1.68	13.83	9.67 x10^{-4}	27.47	Y
HD 108857	F7V	6.50	8.00	4.94 x10^{-4}	104.51	O
eta Crv	F2V	0.69	92.00	1.98 x10^{-4}	18.28	O
HR 4796	A0V	7.10	152.00	4.45 x10^{-3}	71.9	Y
HD 110058	A0V	5.00	–	1.78 x10^{-3}	129.98	Y
rho Vir	A0Va_lB	1.60	154.00	5.57 x10^{-5}	38.16	O
V MO Hya	F0VkA1mA1_lB	-18.10	138.00	6.55 x10^{-5}	62.57	O
HD 113556	F2V	12.75	49.00	6.50 x10^{-4}	101.54	Y
HD 114082	F3V	11.76	43.00	3.21 x10^{-3}	95.65	Y
iot Cen	kA1.5hA3mA3Va	0.10	90.30	2.24 x10^{-5}	18.02	O
lam Boo	A0Va_lB	-7.90	110.00	5.39 x10^{-5}	30.35	O
HD 128311	K3V	-9.58	5.60	7.03 x10^{-5}	16.33	O
HD 131835	A2IV	0.50	–	2.03 x10^{-3}	133.65	Y
bet Cir	A3Va	9.60	68.50	4.77 x10^{-5}	30.55	O
BD-07 4003	M3V	-9.21	–	5.41 x10^{-4}	6.29	O
HD 137057	F3V	-0.20	55.00	2.58 x10^{-4}	143.77	O
alf CrB	A1IV	1.70	138.00	1.41 x10^{-5}	23.0	O
HD 138813	A0V	-2.54	97.90	9.60 x10^{-4}	137.41	Y
HD 140817	A0V	–	–	1.26 x10^{-4}	142.46	O
HD 144587	A9V	0.00	112.10	3.03 x10^{-4}	144.01	O
HR 6051	B9V	-7.80	306.00	9.19 x10^{-6}	112.18	Y
HR 6037	A3V	-9.00	106.40	2.77 x10^{-5}	55.55	O
HD 146897	F2/3V	-1.60	55.00	5.39 x10^{-3}	131.49	Y
HR 6507	A8Vp	-36.10	180.00	7.46 x10^{-5}	63.46	O
HD 159082	B9.5V	-11.80	22.00	4.21 x10^{-5}	145.61	O
HR 6534	A5V	-26.00	243.00	3.96 x10^{-5}	46.82	O

Continued on next page

Table D.1 – continued from previous page

Simbad ID	Spectral type	RV [km.s^{-1}]	$v$sin$i$ [km.s^{-1}]	$L_{\rm disk}/L_\star$	Distance [pc]	Age flag
mu. Ara	G3IV-V	-9.29	1.33	1.48 x10^{-5}	15.6	O
HD 164249	F6V	-0.09	20.00	9.73 x10^{-4}	49.61	Y
eps Sgr	B9.5III	-15.00	236.00	9.13 x10^{-6}	43.93	O
HR 6948	F5V	-16.55	–	4.27 x10^{-4}	37.05	O
rho Tel	F6V	0.30	–	2.56 x10^{-5}	58.85	O
HD 181327	F6V	-0.25	16.00	2.98 x10^{-3}	48.21	Y
5 Vul	A0V	-21.20	154.00	3.12 x10^{-5}	71.98	O
c Aql	A0IVp	12.00	90.00	1.28 x10^{-5}	60.67	O
HD 190470	K3V	-7.38	1.40	1.07 x10^{-4}	22.15	O
kap01 Sgr	A0V	-3.40	79.00	2.27 x10^{-5}	68.45	O
phi01 Pav	F0V	-20.00	–	9.21 x10^{-5}	28.29	O
iot Del	A1IV	-3.90	41.00	3.44 x10^{-5}	59.46	O
V AU Mic	M1VeBa1	-4.50	9.68	4.19 x10^{-4}	9.72	Y
HR 8013	F6V	-15.91	13.70	1.75 x10^{-5}	21.28	O
alf Oct	F6(m)pec	85.90	–	2.20 x10^{-5}	44.4	O
HD 202206	G6V	14.68	5.70	9.89 x10^{-5}	46.02	O
HD 207129	G2V	-7.62	0.56	7.79 x10^{-5}	15.56	O
39 Peg	F1V	-18.90	94.00	9.14 x10^{-5}	53.57	O
tau01 Aqr	B9V	15.00	–	3.09 x10^{-5}	108.87	O
V342 Peg	F0+VkA5mA5	-12.60	49.00	2.53 x10^{-4}	41.29	Y
HR 8843	F6V	0.46	–	3.31 x10^{-5}	20.45	O

Appendix E

Tables of Chapter 6

E.1 Parameters of the sample

Table E.1: Main parameters of the sample. Spectral type, heliocentric radial velocity, projected rotational velocity, luminosity ratio L_{disk}/L_{star}, distance and age flag, where "O" stands for older than 100 Myr and "Y" stands for younger than 100 Myr.

Simbad ID	Spectral type	RV [km.s^{-1}]	$v$sin$i$ [km.s^{-1}]	$L_{\rm disk}/L_\star$	Distance [pc]	Age flag
HD 225200	A1V	18.40	341.00	6.14 x10^{-5}	134.46	O
lam01 Phe	A1Va	-2.00	–	1.38 x10^{-5}	56.12	O
HD 3670	F5V	8.92	–	5.15 x10^{-4}	77.59	O
49 Cet	A1V	10.30	196.00	6.93 x10^{-4}	57.06	Y
HD 10472	F2IV/V	12.41	78.20	3.40 x10^{-4}	71.15	O
q02 Eri	A1V	9.50	–	7.36 x10^{-5}	60.96	O
gam Tri	A1Vnn	9.90	254.00	6.76 x10^{-5}	34.43	Y
phi For	A2.5V	19.00	116.80	4.15 x10^{-5}	47.25	O
HD 16743	F0/2III/IV	–	112.20	3.79 x10^{-4}	57.93	O
HD 17390	F3IV/V	7.20	–	2.08 x10^{-4}	48.19	O
41 Ari	B8Vn	4.00	175.00	1.57 x10^{-5}	50.78	Y
V V1229 Tau	A0VpSi+Am	5.00	40.00	2.00 x10^{-4}	139.54	Y

Continued on next page

Table E.1 – continued from previous page

Simbad ID	Spectral type	RV [km.s^{-1}]	$v$sin$i$ [km.s^{-1}]	$L_{\mathrm{disk}}/L_{\star}$	Distance [pc]	Age flag
HD 23863	A7Vn	5.00	165.00	5.77 x10^{-5}	134.25	Y
HD 23923	B8V	9.50	290.00	4.95 x10^{-5}	133.4	Y
kap Lep	B7V	20.80	120.00	4.83 x10^{-6}	223.21	O
HD 34324	A3V	–	–	8.98 x10^{-5}	82.04	O
HD 35150	A0V	–	–	3.74 x10^{-4}	370.67	O
HD 287787	A2	–	–	2.23 x10^{-4}	410.77	O
HD 35332	A0V	–	–	3.44 x10^{-4}	384.18	O
HD 35367	A1IV/V	–	–	1.66 x10^{-4}	365.79	O
HD 287850	A5	–	–	1.30 x10^{-4}	377.57	O
HD 287854	F0	–	–	2.92 x10^{-4}	362.52	O
HD 35625	A0V	–	–	8.51 x10^{-5}	361.96	O
HD 38056	B9.5V	28.10	195.00	4.41 x10^{-5}	128.31	O
HD 46190	A0V	–	–	1.10 x10^{-5}	84.51	O
HD 50571	F5VFe+0.4	26.69	–	1.25 x10^{-4}	34.04	O
bet CMi	B8Ve	22.00	210.00	8.61 x10^{-5}	49.57	O
HD 60995	B8/9V	29.00	316.00	2.72 x10^{-5}	504.64	O
HD 68420	A3V	–	–	1.17 x10^{-4}	411.57	O
30 Mon	A0Va	10.00	134.00	2.71 x10^{-5}	37.5	O
HD 71722	A0V	30.20	–	1.00 x10^{-4}	69.33	O
HD 74374	F3V	16.51	–	1.28 x10^{-4}	153.24	Y
HD 78702	A0/1V	16.90	222.00	2.42 x10^{-4}	104.71	O
HD 79108	A0V	22.60	172.00	5.85 x10^{-5}	115.74	O
HD 88215	F3V	23.60	148.00	3.57 x10^{-5}	27.81	O
HD 93738	B9.5V	4.00	–	1.71 x10^{-5}	154.85	O
HD 98363	A2V	9.60	–	7.28 x10^{-4}	138.59	O
HD 101088	F5IV	19.70	152.00	2.73 x10^{-5}	101.24	O

Continued on next page

Table E.1 – continued from previous page

Simbad ID	Spectral type	RV [km.s^{-1}]	$v$sin$i$ [km.s^{-1}]	$L_{\rm disk}/L_\star$	Distance [pc]	Age flag
bet Leo	A3Va	-0.20	128.00	2.27 x10^{-5}	10.99	O
HD 103234	F2IV/V	13.36	57.00	9.80 x10^{-5}	102.12	O
HD 103266	A1V	-7.50	165.10	3.92 x10^{-5}	83.14	O
HD 103703	F3V	16.01	66.00	4.06 x10^{-4}	107.42	O
HD 104231	F5V	13.51	36.00	1.46 x10^{-4}	102.73	O
HD 104600	B9V	7.60	214.00	1.26 x10^{-4}	104.85	Y
HD 105613	A3V	7.40	–	1.16 x10^{-4}	104.6	O
HD 105857	A2V	7.20	–	1.16 x10^{-4}	112.44	O
HD 105912	F5V	0.40	42.30	7.30 x10^{-5}	48.24	O
HD 106797	A0V	21.00	172.00	1.68 x10^{-4}	105.94	Y
HD 107301	B9V	-8.30	–	1.12 x10^{-4}	97.36	O
HD 107649	F5V	6.10	72.00	1.21 x10^{-4}	108.32	O
HD 107947	A0V	7.90	–	8.25 x10^{-5}	99.13	O
HD 108904	F6V	12.45	64.00	5.33 x10^{-4}	108.02	Y
eta Crv	F2V	0.69	92.00	1.98 x10^{-4}	18.28	O
f Vir	A3V	-6.00	155.40	4.73 x10^{-5}	71.44	O
V MO Hya	F0VkA1mA1_lB	-18.10	138.00	6.55 x10^{-5}	62.57	O
HD 112383	A2IV/V	6.60	–	1.28 x10^{-4}	101.64	O
HD 113457	A0V	15.00	–	1.78 x10^{-4}	105.86	Y
HD 113556	F2V	12.75	49.00	6.50 x10^{-4}	101.54	Y
HD 113902	B8/9V	22.00	–	4.25 x10^{-5}	100.42	Y
iot Cen	kA1.5hA3mA3Va	0.10	90.30	2.24 x10^{-5}	18.02	O
HD 117484	B9.5V	2.00	–	1.99 x10^{-4}	155.5	O
HD 117665	A1/2V	1.50	–	1.69 x10^{-4}	129.17	O
HD 118379	A3IV/V	6.10	–	1.35 x10^{-4}	111.87	O
HD 118588	A1V	1.20	–	5.62 x10^{-4}	135.98	O

Continued on next page

Table E.1 – continued from previous page

Simbad ID	Spectral type	RV [km.s^{-1}]	$v$sin$i$ [km.s^{-1}]	$L_{\mathrm{disk}}/L_{\star}$	Distance [pc]	Age flag
tau Vir	A2IV/V	-6.70	186.00	1.06 x10^{-5}	68.96	O
HD 122705	A2V	6.60	–	6.11 x10^{-5}	122.58	O
HD 124619	F0V	6.90	115.00	8.60 x10^{-5}	131.85	O
HD 127750	A0V	4.40	–	1.59 x10^{-4}	143.43	O
HD 128207	B8V	2.00	–	6.49 x10^{-6}	142.77	Y
HD 131835	A2IV	0.50	–	2.03 x10^{-3}	133.65	Y
HD 132238	B7V	15.00	–	4.41 x10^{-5}	161.67	Y
HD 134888	F3/5V	2.95	37.00	8.73 x10^{-4}	112.31	Y
HD 135454	B9.5V	1.40	–	2.36 x10^{-5}	134.15	O
HD 136246	A1V	-2.70	–	4.03 x10^{-5}	114.18	O
HD 136482	B8/9V	-0.20	–	8.12 x10^{-5}	148.27	O
HD 137015	A1/2V	3.20	119.60	2.05 x10^{-5}	296.42	Y
HD 137119	A2V	-0.70	–	1.53 x10^{-4}	128.34	O
tet CrB	B6Vnne	-25.70	310.00	1.00 x10^{-5}	115.07	O
HD 138813	A0V	-2.54	97.90	9.60 x10^{-4}	137.41	Y
HD 138923	B8V	-3.60	–	1.05 x10^{-4}	134.24	Y
HD 138965	A1V	-2.00	102.70	3.74 x10^{-4}	78.08	O
HD 140840	B9/A0V	–	–	1.65 x10^{-4}	148.16	O
HD 141011	F5V	0.20	83.00	1.44 x10^{-4}	128.6	O
HD 142446	F3V	-1.90	66.00	6.29 x10^{-4}	137.54	Y
HD 144587	A9V	0.00	112.10	3.03 x10^{-4}	144.01	O
HD 145880	B9.5V	-1.80	–	3.65 x10^{-4}	125.62	O
HD 145689	A3V	-9.00	106.40	2.77 x10^{-5}	55.55	O
HD 146606	A0V	-3.43	137.00	7.90 x10^{-5}	137.27	Y
HD 146897	F2/3V	-1.60	55.00	5.39 x10^{-3}	131.49	Y
HD 148657	A0V	-2.70	–	3.01 x10^{-4}	189.92	O

Continued on next page

Table E.1 – continued from previous page

Simbad ID	Spectral type	RV [km.s^{-1}]	$v\sin i$ [km.s^{-1}]	$L_{\rm disk}/L_\star$	Distance [pc]	Age flag
HD 151109	B9IV/V	-2.90	–	1.03 x10^{-4}	174.45	O
HD 153053	A5IV/V	-20.20	102.80	5.82 x10^{-5}	53.25	O
78 Her	A1V	-25.70	–	1.90 x10^{-5}	83.39	O
HD 159082	B9.5V	-11.80	22.00	4.21 x10^{-5}	145.61	O
HD 159170	A5V	-26.00	243.00	3.96 x10^{-5}	46.82	O
gam Oph	A1VnkA0mA0	-7.60	210.00	6.63 x10^{-5}	31.51	O
zet CrA	B9.5Vann	-13.00	–	5.89 x10^{-5}	59.2	O
rho Tel	F6V	0.30	–	2.56 x10^{-5}	58.85	O
alf CrA	A2Va	-18.40	203.20	2.00 x10^{-5}	38.43	O
eta Tel	A0V+M7/8V	13.00	–	1.95 x10^{-4}	48.21	Y
HD 181327	F6V	-0.25	16.00	2.98 x10^{-3}	48.21	Y
5 Vul	A0V	-21.20	154.00	3.12 x10^{-5}	71.98	O
rho Aql	A1Va	-23.00	180.00	4.57 x10^{-5}	47.96	O
HD 192758	F0V	-14.36	–	5.33 x10^{-4}	66.52	O
phi01 Pav	F0V	-20.00	–	9.21 x10^{-5}	28.29	O
3 Peg	A2V	3.00	102.60	2.56 x10^{-5}	88.29	O
del Scl	A0VankB9((_lB))	8.70	299.00	2.78 x10^{-5}	42.14	Y

E.2 Matching interstellar clouds

Table E.2: Clouds in the line of sight or at less than 20° of our targets taken from Redfield and Linsky (2008) LISM database. The name of each target, the radial velocity of each non-photospheric absorption feature, the FWHM of each feature, the name of the cloud found in the line of sight of the target that matches with the radial velocity of the feature (within its FWHM), the radial velocity of this cloud, the name of a cloud found within 20° that also matches with the feature and its corresponding radial velocity.

Name	RV feature [km.s^{-1}]	FWHM feat. [km.s^{-1}]	Cloud line of sight	RV Cloud LoS [km.s^{-1}]	Cloud $< 20°$	RV Cloud $< 20°$ [km.s^{-1}]
41 Ari	16.13±1.17	6.24±0.71	Hyades	14.06±0.91	Aur	14.34±1.03
V V1229 Tau	16.64±1.14	3.83±0.43	–	–	Aur	18.40±0.94
HD 23863	16.00±1.48	5.20±0.76	–	–	Hyades	13.84±0.93
HD 23923	15.74±1.49	6.56±0.96	LIC	22.28±0.98	Hyades	13.84±0.93
	37.39±1.48	4.71±0.69	–	–	–	–
kap Lep	-20.80±1.65	17.67±2.59	–	–	–	–
	2.81±1.48	5.21±0.76	–	–	–	–
	16.26±1.51	8.18±1.20	LIC	20.90±1.04	Blue	13.70±0.91
	23.83±1.48	4.99±0.73	LIC	20.90±1.04	Aur	24.73±0.85
	32.16±1.51	8.48±1.24	–	–	Dor	35.50±0.91
HD 34324	9.07±2.30	5.87±1.34	Blue	13.10±0.95	–	–
HD 35150	-2.88±2.37	14.35±3.28	–	–	Hyades	11.40±1.26
	11.60±2.32	8.79±2.01	–	–	Hyades	11.40±1.26
	22.26±2.31	7.88±1.80	LIC	23.12±0.95	Aur	24.76±0.82
HD 287787	-14.11±1.48	5.41±0.79	–	–	–	–
	0.73±1.48	4.55±0.67	–	–	–	–
	24.70±1.48	5.29±0.78	LIC	23.08±0.95	Aur	24.79±0.82
	31.56±1.47	1.36±0.20	–	–	–	–
HD 35332	10.52±2.39	16.71±3.82	LIC	23.11±0.95	Hyades	11.35±1.26
	23.08±2.29	4.32±0.99	LIC	23.11±0.95	Aur	24.79±0.82
	33.51±2.30	6.16±1.41	–	–	–	–
HD 35367	9.89±1.47	2.34±0.34	–	–	Hyades	11.34±1.27
	22.23±1.48	4.58±0.67	LIC	23.10±0.95	Aur	24.79±0.82

Continued on next page

Table E.2 – continued from previous page

Name	RV feature [km.s^{-1}]	FWHM feat. [km.s^{-1}]	Cloud line of sight	RV Cloud LoS [km.s^{-1}]	Cloud < 20°	RV Cloud < 20° [km.s^{-1}]
	34.45±1.47	2.94±0.43	–	–	–	–
HD 287850	4.54±2.32	8.98±2.05	–	–	Hyades	11.29±1.27
	13.05±2.30	6.53±1.49	–	–	Blue	13.83±0.90
	20.96±2.31	6.93±1.59	LIC	23.10±0.95	Aur	24.81±0.82
	29.66±2.36	13.57±3.10	LIC	23.10±0.95	Aur	24.81±0.82
HD 287854	14.47±2.33	11.09±2.53	LIC	23.08±0.95	Blue	13.84±0.90
	23.42±2.29	3.57±0.82	LIC	23.08±0.95	Aur	24.82±0.82
HD 35625	10.32±1.50	7.05±1.03	–	–	Hyades	11.28±1.27
	18.91±1.82	25.54±3.74	LIC	23.13±0.95	Blue	13.82±0.90
HD 38056	6.07±1.49	6.83±1.00	Blue	12.00±0.96	–	–
	12.86±1.47	3.52±0.52	Blue	12.00±0.96	LIC	15.40±1.21
	22.68±1.51	8.45±1.24	–	–	Dor	23.59±0.91
HD 46190	19.76±2.33	10.18±2.33	Cet	18.20±0.81	–	–
HD 50571	17.11±2.59	5.31±1.37	Vel	16.45±1.01	–	–
bet CMi	19.82±1.05	3.66±0.38	LIC	19.90±1.07	Aur	22.23±1.03
HD 60995	22.33±1.49	6.91±1.01	LIC	16.42±1.18	Aur	22.47±0.94
	31.31±1.49	6.06±0.89	–	–	–	–
HD 68420	0.83±2.36	13.75±3.14	–	–	G	6.40±0.94
	12.39±2.34	11.97±2.74	–	–	Blue	7.37±0.95
	25.55±2.39	16.54±3.78	–	–	Cet	24.09±0.96
30 Mon	15.17±0.78	4.20±0.32	LIC	14.85±1.22	G	15.71±1.31
HD 71722	4.50±2.33	10.30±2.35	G	4.19±0.94	Blue	6.47±0.95
	13.64±2.32	8.84±2.02	Vel	14.33±0.95	Blue	6.47±0.95
HD 74374	11.79±2.32	9.38±2.14	Vel	12.51±0.91	Blue	5.96±0.96
	18.27±2.31	8.40±1.92	Cet	17.53±0.81	–	–
HD 78702	11.38±2.31	7.84±1.79	G	8.69±1.20	Leo	11.20±1.20

Continued on next page

Table E.2 – continued from previous page

Name	RV feature [km.s^{-1}]	FWHM feat. [km.s^{-1}]	Cloud line of sight	RV Cloud LoS [km.s^{-1}]	Cloud $< 20^\circ$	RV Cloud $< 20^\circ$ [km.s^{-1}]
	18.13±2.30	4.83±1.10	–	–	Aur	16.36±1.14
HD 79108	9.07±2.32	9.01±2.06	LIC	11.98±1.28	G	11.55±1.51
HD 88215	18.52±1.05	3.78±0.39	Gem	20.42±0.99	Cet	22.24±0.90
HD 93738	7.01±2.32	8.98±2.05	–	–	Blue	1.64±0.97
	16.21±2.33	10.69±2.44	–	–	–	–
HD 98363	3.89±2.31	7.49±1.71	–	–	Blue	0.85±0.97
	10.05±2.29	2.51±0.57	–	–	–	–
	16.37±2.30	4.84±1.11	–	–	–	–
HD 101088	-4.65±2.30	6.08±1.39	G	-8.90±1.02	Vel	-7.12±0.80
	6.78±2.34	12.13±2.77	–	–	Blue	0.46±1.00
bet Leo	2.21±2.29	3.13±0.72	Leo	0.46±0.78	NGP	2.61±0.75
	13.64±2.30	4.95±1.13	–	–	–	–
HD 103234	0.59±2.31	8.42±1.93	–	–	Blue	-0.35±0.98
	10.73±2.30	6.47±1.48	–	–	–	–
HD 103266	-9.11±1.06	5.10±0.53	–	–	NGP	-7.23±1.05
	3.92±1.06	5.06±0.52	–	–	Gem	3.90±0.98
HD 103703	-9.20±2.29	3.70±0.85	G	-10.67±0.95	Cet	-9.52±0.65
	-1.75±2.30	5.04±1.15	–	–	Blue	-0.37±0.97
	4.81±2.33	10.30±2.36	–	–	Blue	-0.37±0.97
HD 104231	1.40±2.65	13.58±3.51	G	-11.03±0.95	Blue	-0.56±0.98
HD 104600	5.96±1.13	10.64±1.10	–	–	Blue	-0.09±0.99
HD 105613	-7.65±1.05	4.61±0.48	G	-11.52±0.96	Cet	-11.27±0.68
	3.54±1.07	6.70±0.69	–	–	Blue	-0.80±0.97
HD 105857	-9.80±1.09	7.88±0.82	G	-11.79±0.95	NGP	-11.41±1.12
	-0.60±1.08	6.94±0.72	–	–	Blue	-0.95±0.98
	6.74±1.12	10.36±1.07	–	–	Blue	-0.95±0.98

Continued on next page

Table E.2 – continued from previous page

Name	RV feature [km.s^{-1}]	FWHM feat. [km.s^{-1}]	Cloud line of sight	RV Cloud LoS [km.s^{-1}]	Cloud < 20°	RV Cloud < 20° [km.s^{-1}]
HD 105912	-2.17±1.04	3.30±0.34	Leo	-3.66±0.90	Aur	-2.01±1.45
HD 106797	-3.53±1.11	9.41±0.97	G	-11.10±1.00	Blue	-0.60±0.98
	4.31±1.06	5.63±0.58	–	–	Blue	-0.60±0.98
	10.39±1.06	5.66±0.59	–	–	–	–
HD 107301	-5.52±1.09	7.73±0.80	G	-11.23±1.00	Blue	-0.68±0.98
	1.71±1.07	6.06±0.63	–	–	Blue	-0.68±0.98
	6.89±1.09	7.75±0.80	–	–	Blue	-0.68±0.98
HD 107649	-20.79±2.59	4.38±1.13	–	–	–	–
	-3.21±2.67	16.18±4.18	G	-13.04±0.96	Gem	-0.82±1.01
	3.38±2.59	3.74±0.97	–	–	–	–
HD 107947	0.74±1.07	7.10±0.73	–	–	Blue	-0.32±1.03
	8.62±1.06	6.42±0.66	–	–	–	–
HD 108904	-6.47±2.30	4.78±1.09	–	–	–	–
	-0.24±2.30	5.34±1.22	–	–	Blue	-1.21±0.97
	6.93±2.30	5.24±1.20	–	–	–	–
eta Crv	-9.43±2.29	2.49±0.57	–	–	NGP	-9.68±0.95
	-1.12±2.30	6.23±1.42	Gem	-0.11±0.92	Aur	-3.47±1.33
	34.43±2.32	9.15±2.09	–	–	–	–
f Vir	-6.94±2.31	7.81±1.79	Leo	-6.32±0.95	NGP	-8.62±0.88
V MO Hya	-9.10±2.34	11.53±2.64	Leo	-9.10±1.12	Aur	-4.57±1.22
	-1.00±2.31	7.78±1.78	Gem	-3.45±0.95	Aur	-4.57±1.22
HD 112383	-8.52±1.08	7.31±0.75	G	-12.45±1.04	Vel	-13.13±0.92
HD 113457	-9.59±1.08	7.79±0.80	G	-13.51±1.01	NGP	-15.23±1.15
	2.50±1.11	9.68±1.00	–	–	Blue	-1.85±0.98
HD 113556	-14.15±2.29	4.57±1.05	G	-14.71±0.98	NGP	-15.77±1.15
	-5.81±2.31	8.35±1.91	–	–	–	–

Continued on next page

Table E.2 – continued from previous page

Name	RV feature [km.s^{-1}]	FWHM feat. [km.s^{-1}]	Cloud line of sight	RV Cloud LoS [km.s^{-1}]	Cloud < 20°	RV Cloud < 20° [km.s^{-1}]
	2.42±2.29	3.67±0.84	–	–	–	–
HD 113902	-13.64±2.35	12.42±2.84	G	-15.72±0.97	NGP	-16.26±1.15
	-3.17±2.31	8.15±1.86	–	–	Gem	-5.22±1.01
iot Cen	-18.37±2.30	6.70±1.53	NGP	-17.91±1.13	G	-18.81±1.06
HD 117484	-8.06±2.32	9.19±2.10	–	–	Gem	-7.97±1.01
	6.94±2.32	8.98±2.05	–	–	–	–
HD 117665	-8.65±1.06	5.98±0.62	–	–	Gem	-8.26±1.00
	1.97±1.06	6.07±0.62	–	–	–	–
HD 118379	-17.84±1.06	5.57±0.57	NGP	-19.67±1.16	G	-19.56±1.03
	-2.66±1.13	11.27±1.16	–	–	Gem	-9.04±1.00
HD 118588	-8.34±1.06	5.69±0.58	–	–	Gem	-8.92±1.00
tau Vir	-10.92±1.16	7.07±0.79	–	–	Gem	-13.03±0.89
HD 122705	-12.32±1.05	5.33±0.55	–	–	Gem	-10.91±1.02
	-0.98±1.06	5.66±0.58	–	–	–	–
HD 124619	-10.37±1.05	4.56±0.47	–	–	Gem	-11.32±1.02
	-3.17±1.05	4.59±0.47	–	–	–	–
HD 127750	-20.65±2.31	7.75±1.77	G	-21.88±1.02	NGP	-24.37±1.23
	-13.79±2.31	7.88±1.80	–	–	Gem	-14.38±1.02
	-4.65±2.31	8.40±1.92	–	–	–	–
HD 128207	-22.89±2.36	13.99±3.20	NGP	-25.40±1.23	G	-23.23±1.04
	-12.19±2.31	7.03±1.61	Gem	-15.68±1.01	–	–
	-4.39±2.29	3.79±0.87	–	–	–	–
HD 131835	-29.80±2.29	4.63±1.06	NGP	-27.63±1.25	–	–
	-16.08±2.32	9.04±2.07	Gem	-18.56±1.02	G	-24.98±1.06
HD 132238	-27.30±1.05	3.80±0.39	–	–	NGP	-27.58±1.26
	-21.09±1.07	6.15±0.64	Gem	-18.41±1.02	G	-24.71±1.05

Continued on next page

Table E.2 – continued from previous page

Name	RV feature [km.s^{-1}]	FWHM feat. [km.s^{-1}]	Cloud line of sight	RV Cloud LoS [km.s^{-1}]	Cloud < 20°	RV Cloud < 20° [km.s^{-1}]
	-15.92±1.04	3.35±0.35	Gem	-18.41±1.02	–	–
	-11.78±1.05	3.68±0.38	–	–	–	–
HD 134888	-25.16±1.04	3.72±0.38	–	–	G	-26.09±1.07
	-15.13±1.04	4.17±0.43	–	–	–	–
HD 135454	-22.94±2.32	9.31±2.13	G	-24.47±1.05	Gem	-19.12±1.03
HD 136246	-26.28±2.31	7.13±1.63	G	-27.02±1.08	NGP	-30.21±1.28
	-17.83±2.32	9.76±2.23	Gem	-22.25±1.02	Leo	-19.34±1.45
HD 136482	-27.99±1.49	6.66±0.98	G	-25.64±1.06	NGP	-29.37±1.28
	-19.20±1.50	7.52±1.10	Gem	-20.70±1.03	–	–
	-8.95±1.49	6.06±0.89	–	–	–	–
HD 137015	-7.37±1.48	5.41±0.79	–	–	–	–
HD 137119	-14.55±1.48	4.51±0.66	–	–	–	–
	-7.03±1.47	2.56±0.38	–	–	–	–
tet CrB	-17.61±1.17	6.92±0.78	NGP	-19.17±0.99	Oph	-17.85±0.90
HD 138813	-27.51±2.32	9.76±2.23	G	-27.82±1.09	NGP	-31.50±1.29
	-16.08±2.31	8.22±1.88	Gem	-24.16±1.03	Leo	-20.19±1.47
HD 138923	-29.80±2.31	8.37±1.91	G	-26.90±1.07	NGP	-30.97±1.30
	-22.94±2.30	4.86±1.11	G	-26.90±1.07	Gem	-22.96±1.03
	-13.80±2.31	8.47±1.94	–	–	–	–
HD 138965	-18.37±2.29	3.95±0.90	G	-15.95±1.19	Vel	-20.00±1.12
	-11.51±2.29	3.00±0.69	–	–	–	–
HD 140840	-22.94±2.30	6.56±1.50	G	-26.78±1.07	Gem	-23.42±1.04
	-13.80±2.30	6.28±1.44	–	–	–	–
	-4.65±2.30	6.88±1.57	–	–	–	–
HD 141011	-21.78±2.61	8.20±2.12	G	-25.30±1.08	Gem	-21.72±1.04
HD 142446	-23.08±1.52	9.87±1.45	G	-26.72±1.08	Gem	-23.85±1.04

Continued on next page

Table E.2 – continued from previous page

Name	RV feature [km.s^{-1}]	FWHM feat. [km.s^{-1}]	Cloud line of sight	RV Cloud LoS [km.s^{-1}]	Cloud $< 20^\circ$	RV Cloud $< 20^\circ$ [km.s^{-1}]
	-12.16±1.48	4.55±0.67	–	–	–	–
HD 144587	-28.77±2.29	4.29±0.98	G	-28.81±1.09	Gem	-27.48±1.05
	-20.57±2.30	6.88±1.57	–	–	Mic	-22.98±1.20
	-7.83±2.32	8.55±1.96	–	–	–	–
HD 145880	-19.40±2.39	16.25±3.71	G	-26.45±1.11	Gem	-24.55±1.05
HD 145689	-11.51±2.31	7.76±1.78	G	-17.21±1.22	–	–
HD 146606	-27.51±2.31	7.35±1.68	G	-28.52±1.09	Gem	-27.64±1.05
	-20.65±2.29	3.15±0.72	–	–	–	–
HD 146897	-29.30±2.33	10.79±2.47	G	-29.19±1.10	Gem	-28.88±1.05
	-8.51±2.30	4.84±1.11	–	–	–	–
HD 148657	-22.24±1.47	1.07±0.16	–	–	–	–
	-1.60±1.47	3.80±0.56	–	–	–	–
HD 151109	-25.23±2.30	6.52±1.49	G	-26.63±1.15	Gem	-26.61±1.06
	-16.08±2.32	8.91±2.04	–	–	–	–
	-2.36±2.32	9.47±2.17	–	–	–	–
HD 153053	-24.59±0.79	4.97±0.38	G	-22.32±1.23	Aql	-24.86±1.06
	-14.17±0.77	3.17±0.24	–	–	–	–
78 Her	-17.60±1.51	9.15±1.34	LIC	-17.00±1.16	G	-21.40±1.09
HD 159082	-23.35±2.33	10.48±2.40	LIC	-21.03±1.03	G	-26.05±1.07
HD 1591	-29.32±0.79	5.12±0.39	G	-28.63±1.10	Oph	-29.39±0.76
gam Oph	-30.67±1.08	7.04±0.73	Oph	-30.53±0.61	Mic	-27.72±0.97
zet CrA	-25.23±2.32	8.85±2.02	Aql	-18.66±1.05	Mic	-23.02±1.16
rho Tel	-22.75±0.79	5.12±0.39	–	–	G	-19.78±1.48
alf CrA	-23.50±1.12	9.51±0.99	Aql	-19.37±1.06	Mic	-24.00±1.11
eta Tel	-22.94±2.30	5.98±1.37	–	–	G	-18.51±1.51
HD 181327	-22.94±2.29	4.21±0.96	–	–	G	-18.48±1.51

Continued on next page

Table E.2 – continued from previous page

Name	RV feature [km.s^{-1}]	FWHM feat. [km.s^{-1}]	Cloud line of sight	RV Cloud LoS [km.s^{-1}]	Cloud $< 20^{\circ}$	RV Cloud $< 20^{\circ}$ [km.s^{-1}]
5 Vul	-29.80±2.30	5.39±1.23	Aql	-26.30±1.06	Oph	-30.81±0.69
	-20.65±2.30	6.05±1.38	G	-18.05±1.04	Eri	-18.31±1.07
rho Aql	-15.32±0.78	4.39±0.33	Aql	-15.40±1.02	G	-14.95±1.15
HD 192758	-20.51±1.50	8.10±1.19	Vel	-27.47±1.37	Mic	-20.51±1.14
phi01 Pav	-18.47±1.53	3.58±0.54	Vel	-19.40±1.11	–	–
3 Peg	-14.55±1.13	1.61±0.18	–	–	–	–
	-8.95±1.16	6.10±0.69	–	–	LIC	-8.47±1.33
del Scl	-2.36±2.30	6.80±1.55	LIC	0.04±1.38	Cet	-5.25±0.55
	6.78±2.30	5.18±1.19	–	–	–	–

E.3 Reference stars

Table E.3: Comparison stars.

Object of science	Distance [pc]	R$_{search}$ [deg.]	Object of reference	Spectral type	Distance [pc]	θ sep. [deg]
HD 68420	411.57±6.34	3.6	None	–	–	–
HD 78702	104.72±1.66	4.6	None	–	–	–
HD 93738	154.86±6.86	2.7	None	–	–	–
HD 98363	138.59±0.66	2.7	HD 308804	B9	2557.66±277.19	2.42
			HD97320	F3V	57.51±0.14	1.57
HD 101088	101.25±2.44	3.7	HD95881	A0	1185.33±46.37	3.46
			HR4597	B9V	104.85±1.01	2.28
bet Leo	11.00±0.06	3.3	HD 103578	A3V	134.41±4.87	1.92
HD 103234	102.13±0.46	2.6	HD 103703	F3V	107.43±0.50	2.14

Continued on next page

Table E.3 – continued from previous page

Object of science	Distance [pc]	R_{search} [deg.]	Object of reference	Spectral type	Distance [pc]	θ sep. [deg]
			HD 104231	F5V	102.73±0.47	1.03
			HD 105857	A2V	112.44±0.50	2.50
HD 103266	83.14±0.43	4.4	HD 101431	B9V	141.02±4.75	2.73
HD 103703	107.43±0.50	2.6	HD 104231	F5V	102.73±0.47	1.77
			HD 105613	A3V	104.61±0.44	1.78
HD 104231	102.73±0.47	2.6	HD 103703	F3V	107.43±0.50	1.77
			HD 105613	A3V	104.61±0.44	1.77
			HD 105857	A2V	112.44±0.50	1.66
HD 104600	104.85±1.01	3.3	HD 109832	A9V	108.31±0.48	3.26
HD 105613	104.61±0.44	2.7	HD 106906	F5V	103.33±0.46	2.62
			HD 103703	F3V	107.43±0.50	1.78
			HD 104231	F5V	102.73±0.47	1.77
			HD 105857	A2V	112.44±0.50	1.96
HD 105857	112.44±0.50	2.9	HD 106906	F5V	103.33±0.46	1.04
			HD 104231	F5V	102.73±0.47	1.66
			HD 105613	A3V	104.61±0.44	1.96
HD 106797	105.94±0.60	2.7	FH Mus	B8V	114.57±0.59	2.45
			HD 106036	A2V	100.60±0.38	2.30
			HR 4692	B9V	97.36±0.59	0.38
HD 107301	97.36±0.59	3.2	FH Mus	B8V	114.57±0.59	2.08
			HR 4669	A0V	105.94±0.60	0.38
			HD 106036	A2V	100.60±0.38	2.55
HD 107649	108.33±0.62	3.2	CD-50 7023	A0	1018.83±65.69	1.19
			rho Cen	B3V	84.50±2.67	2.14
HD 107947	99.13±0.35	3.3	HD 109026	B3V	102.09±3.99	0.74
HD 108904	108.02±0.38	2.2	None	–	–	–

Continued on next page

Table E.3 – continued from previous page

Object of science	Distance [pc]	R_{search} [deg.]	Object of reference	Spectral type	Distance [pc]	θ sep. [deg]
HD 112383	101.65±0.45	3.3	FH Mus	B8V	114.57±0.59	2.23
			HD 109832	A9V	108.31±0.48	1.90
HD 113457	105.87±0.61	2.5	None	–	–	–
HD 113902	100.43±1.22	3.8	HD 114772	B9.5V	112.23±8.94	2.90
HD 117484	155.51±3.40	2.1	None	–	–	–
HD 117665	129.17±1.16	2.5	HD 117484	B9.5V	155.51±3.40	2.29
HD 118379	111.88±0.81	3.1	HD 120272	F3V	58.30±0.26	2.30
			CD-38 8806	A0	680.49±35.16	2.63
HD 118588	135.99±2.42	2.8	HD 117484	B9.	155.51±3.40	2.55
tau Vir	68.97±0.86	2.3	None	–	–	–
HD 122705	122.59±0.84	3.9	HD 123515	B8V	170.05±3.17	1.63
			HD 125366	B9V	603.42±25.37	3.85
HD 124619	131.85±0.83	3.6	HD 124195	B5V	268.39±4.68	0.89
			HD 123515	B8V	170.05±3.17	2.53
HD 127750	143.44±1.57	4.3	None	–	–	–
HD 134888	112.32±1.02	5.3	HD 136664	B4V	159.24±5.07	4.21
			HD 132955	B3V	151.89±4.26	2.26
			HD 131399	A1V	102.09±0.69	4.09
HD 136482	148.27±2.42	4.8	HD 136664	B4V	159.24±5.07	0.80
			HR 5579	B7V	161.68±3.22	4.54
HD 137119	128.35±1.11	5.0	HD 136664	B4V	159.24±5.07	0.81
			Hip 077286	B8V	124.35±1.79	4.58
HD 138923	134.24±2.17	5.7	HD 136664	B4V	159.24±5.07	4.62
			Hip 077286	B8V	124.35±1.79	2.71
			HD 142630	B9V	64.56±0.46	4.40
			HD 139883	F2V	111.03±0.64	2.15

Continued on next page

Table E.3 – continued from previous page

Object of science	Distance [pc]	R_{search} [deg.]	Object of reference	Spectral type	Distance [pc]	θ sep. [deg]
HD 142446	137.55±0.87	5.2	HR 5999	A7	161.11±1.82	3.31
			Hip 79044	B9V	137.14±1.02	2.49
			HD 142630	B9V	64.56±0.46	2.93
			Hip 077286	B8V	124.35±1.79	2.91
HD 144587	144.01±1.64	4.0	HD 142184	B2V	141.29±2.89	3.10
			HD 144844	B9V	146.33±2.52	0.39
			HD 142990	B5V	146.17±4.38	2.21
			HD 144470	B1V	141.65±7.98	3.29
			HIP 78530	B9V	137.27±1.48	2.35
HD 145880	125.63±0.78	5.5	HR 5999	A7	161.11±1.82	1.34
			HD 148657	A0V	189.93±2.96	3.39
			Hip 79044	B9V	137.14±1.02	3.66
			HD 147683	B4V	295.22±7.90	5.12
HD 146897	131.50±0.93	3.8	HD 144217	B1V	123.92±11.98	3.66
			HD 145502	B2V	135.97±6.46	2.62
			HD 144470	B1V	141.65±7.98	3.05
HD 148657	189.93±2.96	3.0	HD 149533	B9V	166.35±1.75	1.18
HD 151109	174.45±1.95	3.7	HD 148657	A0V	189.93±2.96	3.29
			HD 326320	B0V	1225.71±77.46	2.49
			V923 Sco	F3V	62.22±0.21	3.55
			HD 152249	OC9Iab	2066.61±234.16	2.68
HD 153053	53.25±0.36	3.1	None	–	–	–
78 Her	83.39±0.50	3.5	None	–	–	–
zet CrA	57.50±1.20	4.9	Hip 91956	F2V	74.53±0.95	3.50
eta Tel	48.22±0.49	4.6	None	–	–	–
3 Peg	88.30±0.75	4.0	None	–	–	–

Continued on next page

Table E.3 – continued from previous page

Object of science	Distance [pc]	R_{search} [deg.]	Object of reference	Spectral type	Distance [pc]	θ sep. [deg]
del Scl	42.14±0.39	3.1	None	–	–	–

E.4 Matching features of reference stars

Table E.4: Comparison stars.

Object of science	RV feature [km.s^{-1}]	FWHM feat. [km.s^{-1}]	Reference star	RV feat. ref. [km.s^{-1}]	FWHM feat. ref. [km.s^{-1}]
HD 103234	0.59±2.31	8.42±1.93	HD105857	0.93±0.37	14.83±0.36
	10.73±2.30	6.47±1.48	HD104231	2.12±0.86	11.64±0.94
HD 103266	-9.11±1.06	5.10±0.53	HD101431	-7.64±0.42	5.44±0.43
	3.92±1.06	5.06±0.52	HD101431	5.71±0.05	7.88±0.06
HD 103703	-9.20±2.29	3.70±0.85	HD104231	2.12±0.86	11.64±0.94
	-1.75±2.30	5.04±1.15	HD104231	2.12±0.86	11.64±0.94
	4.81±2.33	10.30±2.36	HD105613	3.76±0.35	5.80±0.32
HD 104231	1.40±2.65	13.58±3.51	HD105857	0.93±0.37	14.83±0.36
HD 104600	5.96±1.13	10.64±1.10	None	–	–
HD 105613	-7.65±1.05	4.61±0.48	HD103703	-0.50±0.37	8.11±0.24
	3.54±1.07	6.70±0.69	HD105857	0.95±0.38	15.03±0.41
HD 105857	-9.80±1.09	7.88±0.82	HD104231	0.42±0.44	19.34±1.08
	-0.60±1.08	6.94±0.72	HD104231	0.42±0.44	19.34±1.08
	6.74±1.12	10.36±1.07	HD105613	3.72±0.31	5.48±0.29
HD 106797	-3.53±1.11	9.41±0.97	HR4692	-6.59±0.37	5.66±0.35
	4.31±1.06	5.63±0.58	FH Mus	5.85±0.31	9.23±0.32
	10.39±1.06	5.66±0.59	HD106036	10.95±0.67	6.49±0.84

Continued on next page

Table E.4 – continued from previous page

Object of science	RV feature [km.s^{-1}]	FWHM feat. [km.s^{-1}]	Reference star	RV feat. ref. [km.s^{-1}]	FWHM feat. ref. [km.s^{-1}]
HD 107301	-5.52±1.09	7.73±0.80	HR4669	-4.29±1.21	9.43±1.04
	1.71±1.07	6.06±0.63	HD106036	1.11±0.34	3.15±0.38
	6.89±1.09	7.75±0.80	FH Mus	5.85±0.31	9.23±0.31
HD 107649	-20.79±2.59	4.38±1.13	CD-50 7023	-17.09±0.13	9.31±0.14
	-3.21±2.67	16.18±4.18	CD-50 7023	-0.99±0.12	15.06±0.15
	3.38±2.59	3.74±0.97	rho Cen	1.47±0.28	8.47±0.30
HD 107947	0.74±1.07	7.10±0.73	HD 109026	3.73±0.49	16.39±0.94
	8.62±1.06	6.42±0.66	HD 109026	3.73±0.49	16.39±0.94
HD 112383	-8.52±1.08	7.31±0.75	FH Mus	-7.13±0.16	4.46±0.16
HD 113902	-13.64±2.35	12.42±2.84	HD 114772	-2.24±0.15	13.27±0.15
	-3.17±2.31	8.15±1.86	HD 114772	-2.24±0.15	13.27±0.15
HD 117665	-8.65±1.06	5.98±0.62	HD117484	-8.06±2.32	9.19±2.10
	1.97±1.06	6.07±0.62	HD117484	6.94±2.32	8.98±2.05
HD 118379	-17.84±1.06	5.57±0.57	CD-38 8806	-7.94±0.23	14.43±0.19
	-2.66±1.13	11.27±1.16	CD-38 8806	-7.94±0.23	14.43±0.19
HD 118588	-8.34±1.06	5.69±0.58	HD117484	-8.24±0.53	9.76±0.55
HD 122705	-12.32±1.05	5.33±0.55	HD 123515	-12.84±1.21	2.96±1.37
	-0.98±1.06	5.66±0.58	HD 125366	2.68±0.18	12.67±0.19
HD 124619	-10.37±1.05	4.56±0.47	HD124195	-10.67±1.16	20.27±1.25
	-3.17±1.05	4.59±0.47	HD124195	-10.67±1.16	20.27±1.25
HD 134888	-25.16±1.04	3.72±0.38	HD136664	-29.23±0.44	6.84±0.46
	-15.13±1.04	4.17±0.43	HD132955	-13.66±0.27	7.40±0.36
HD 136482	-27.99±1.49	6.66±0.98	HD136664	-29.24±0.44	6.93±0.46
	-19.20±1.50	7.52±1.10	HR5579	-20.78±0.89	19.48±1.00
	-8.95±1.49	6.06±0.89	HD136664	-13.62±0.24	10.78±0.27
HD 137119	-14.55±1.48	4.51±0.66	HD136664	-13.62±0.24	10.78±0.27

Continued on next page

Table E.4 – continued from previous page

Object of science	RV feature [km.s^{-1}]	FWHM feat. [km.s^{-1}]	Reference star	RV feat. ref. [km.s^{-1}]	FWHM feat. ref. [km.s^{-1}]
	-7.03±1.47	2.56±0.38	HD136664	-13.62±0.24	10.78±0.27
HD 138923	-29.80±2.31	8.37±1.91	Hip077286	-29.37±0.37	5.22±0.37
	-22.94±2.30	4.86±1.11	HD142630	-26.16±0.49	9.69±0.50
	-13.80±2.31	8.47±1.94	HD136664	-13.60±0.23	11.01±0.19
HD 142446	-23.08±1.52	9.87±1.45	Hip79044	-24.55±0.20	9.43±0.21
	-12.16±1.48	4.55±0.67	Hip79044	-9.77±0.33	4.06±0.33
HD 144587	-28.77±2.29	4.29±0.98	HD142184	-27.55±0.89	16.54±0.58
	-20.57±2.30	6.88±1.57	HD 144844	-17.88±0.82	12.65±2.44
	-7.83±2.32	8.55±1.96	HD 144844	-8.86±0.09	5.57±0.13
HD 145880	-19.40±2.39	16.25±3.71	HD147683	-18.40±0.21	7.13±0.39
HD 146897	-29.30±2.33	10.79±2.47	HD144217	-30.51±0.44	7.25±0.44
	-8.51±2.30	4.84±1.11	HD144470	-9.22±0.05	6.70±0.05
HD 148657	-22.24±1.47	1.07±0.16	None	–	–
	-1.60±1.47	3.80±0.56	HD 149533	1.73±0.34	7.94±0.24
HD 151109	-25.23±2.30	6.52±1.49	HD 152249	-26.75±0.25	10.41±0.38
	-16.08±2.32	8.91±2.04	HD148657	-15.35±0.09	44.43±0.08
	-2.36±2.32	9.47±2.17	HD148657	-1.16±0.11	8.97±0.13
zet CrA	-25.23±2.32	8.85±2.02	None	–	–

E.5 Matching stars within the sample

Table E.5: Comparison stars within our own sample. Object of science, number of comparison stars found within 3°, radial velocity of the features of the object of science, number of stars within the sample having features matching each one of those of the object of science, and the list of these stars. Radial velocity of the features for the comparison stars are not given again here as they have been already presented in previous tables.

Object of science	N nearby stars	RV feature [km.s^{-1}]	N matches	Matching stars within our sample
HD 287850	7	4.54±2.32	6	HD 287787, HD 287854, HD 35150, HD 35332, HD 35367, HD 35625
		13.05±2.30	5	HD 287854, HD 35150, HD 35332, HD 35367, HD 35625
		20.96±2.31	6	HD 287787, HD 287854, HD 35150, HD 35332, HD 35367, HD 35625
		29.66±2.36	6	HD 287787, HD 287854, HD 35150, HD 35332, HD 35367, HD 35625
HD 287854	8	14.47±2.33	7	HD 287787, HD 287850, HD 35150, HD 35332, HD 35367, HD 35625, HD 36444
		23.42±2.29	7	HD 287787, HD 287850, HD 35150, HD 35332, HD 35367, HD 35625, HD 36444
HD 35625	7	10.32±1.50	5	HD 287850, HD 287854, HD 35150, HD 35332 HD 35367
		18.91±1.82	6	HD 287787, HD 287850, HD 287854, HD 35150, HD 35332, HD 35367
HD 38056	0	6.07±1.49	–	–
		12.86±1.47	–	–
		22.68±1.51	–	–
HD 46190	0	19.76±2.33	–	–
HD 50571	0	17.11±2.59	–	–
bet CMi	0	19.82±1.05	–	–
HD 60995	1	22.33±1.49	1	HD 60856

Continued on next page

Table E.5 – continued from previous page

Object of science	N nearby stars	RV feature [km.s^{-1}]	N matches	Matching stars within our sample
		31.31±1.49	1	HD 60856
HD 68420	0	0.83±2.36	–	–
		12.39±2.34	–	–
		25.55±2.39	–	–
30 Mon	0	15.17±0.78	–	–
HD 71722	3	4.50±2.33	2	HD 74374, HD 71043
		13.64±2.32	2	HD 74374, HD 71043
HD 74374	3	11.79±2.32	1	HD 71722
		18.27±2.31	1	HD 71722
HD 78702	0	11.38±2.31	–	–
		18.13±2.30	–	–
HD 79108	1	9.07±2.32	0	–
HD 88215	0	18.52±1.05	–	–
HD 93738	2	7.01±2.32	1	HD 92536
		16.21±2.33	1	HD 92536
HD 98363	0	3.89±2.31	–	–
		10.05±2.29	–	–
		16.37±2.30	–	–
HD 101088	1	-4.65±2.30	1	HD 104600
		6.78±2.34	1	HD 104600
bet Leo	0	2.21±2.29	–	–
		13.64±2.30	–	–
HD 103234	4	0.59±2.31	4	HD 103703, HD 104231, HD 105613, HD 105857
		10.73±2.30	4	HD 103703, HD 104231, HD 105613, HD 105857
HD 103266	0	-9.11±1.06	–	–
		3.92±1.06	–	–

Continued on next page

Table E.5 – continued from previous page

Object of science	N nearby stars	RV feature [km.s^{-1}]	N matches	Matching stars within our sample
HD 103703	3	-9.20±2.29	2	HD 104231, HD 105613
		-1.75±2.30	3	HD 103234, HD 104231, HD 105613
		4.81±2.33	3	HD 103234, HD 104231, HD 105613
HD 104231	5	1.40±2.65	4	HD 103234, HD 103703, HD 105613, HD 105857
HD 104600	1	5.96±1.13	1	HD 101088
HD 105613	5	-7.65±1.05	4	HD 103234, HD 103703, HD 104231, HD 105857
		3.54±1.07	4	HD 103234, HD 103703, HD 104231, HD 105857
HD 105857	4	-9.80±1.09	3	HD 103234, HD 104231, HD 105613
		-0.60±1.08	3	HD 103234, HD 104231, HD 105613
		6.74±1.12	3	HD 103234, HD 104231, HD 105613
HD 105912	0	-2.17±1.04	–	–
HD 106797	3	-3.53±1.11	2	HD 106036, HD 107301
		4.31±1.06	2	HD 106036, HD 107301
		10.39±1.06	2	HD 106036, HD 107301
HD 107301	3	-5.52±1.09	2	HD 106036, HD 106797
		1.71±1.07	2	HD 106036, HD 106797
		6.89±1.09	2	HD 106036, HD 106797
HD 107649	0	-20.79±2.59	–	–
		-3.21±2.67	–	–
		3.38±2.59	–	–
HD 107947	0	0.74±1.07	–	–
		8.62±1.06	–	–
HD 108904	1	-6.47±2.30	1	HD 106036
		-0.24±2.30	1	HD 106036
		6.93±2.30	1	HD 106036
eta Crv	0	-9.43±2.29	–	–

Continued on next page

Table E.5 – continued from previous page

Object of science	N nearby stars	RV feature [km.s^{-1}]	N matches	Matching stars within our sample
		-1.12±2.30	–	–
		34.43±2.32	–	–
f Vir	0	-6.94±2.31	–	–
V MO Hya	0	-9.10±2.34	–	–
		-1.00±2.31	–	–
HD 112383	1	-8.52±1.08	0	–
HD 113457	0	-9.59±1.08	–	–
		2.50±1.11	–	–
HD 113556	3	-14.15±2.29	0	–
		-5.81±2.31	0	–
		2.42±2.29	0	–
HD 113902	0	-13.64±2.35	–	–
		-3.17±2.31	–	–
iot Cen	0	-18.37±2.30	–	–
HD 117484	2	-8.06±2.32	2	HD 117665, HD 118588
		6.94±2.32	1	HD 117665
HD 117665	2	-8.65±1.06	2	HD 117484, HD 118588
		1.97±1.06	1	HD 117484
HD 118379	0	-17.84±1.06	–	–
		-2.66±1.13	–	–
HD 118588	2	-8.34±1.06	2	HD 117484, HD 117665
tau Vir	0	-10.92±1.16	–	–
HD 122705	2	-12.32±1.05	0	–
		-0.98±1.06	0	–
HD 124619	0	-10.37±1.05	–	–
		-3.17±1.05	–	–

Continued on next page

Table E.5 – continued from previous page

Object of science	N nearby stars	RV feature [km.s^{-1}]	N matches	Matching stars within our sample
HD 127750	1	-20.65±2.31	0	–
		-13.79±2.31	0	–
		-4.65±2.31	0	–
HD 128207	1	-22.89±2.36	1	HD 126135
		-12.19±2.31	1	HD 126135
		-4.39±2.29	1	HD 126135
HD 131835	1	-29.80±2.29	1	HD 132238
		-16.08±2.32	1	HD 132238
HD 132238	1	-27.30±1.05	1	HD 131835
		-21.09±1.07	1	HD 131835
		-15.92±1.04	1	HD 131835
		-11.78±1.05	1	HD 131835
HD 134888	0	-25.16±1.04	–	–
		-15.13±1.04	–	–
HD 135454	0	-22.94±2.32	–	–
HD 136246	0	-26.28±2.31	–	–
		-17.83±2.32	–	–
HD 136482	4	-27.99±1.49	0	–
		-19.20±1.50	1	HD 137119
		-8.95±1.49	2	HD 137015, HD 137119
HD 137015	4	-7.37±1.48	2	HD 136482, HD 137119
HD 137119	4	-14.55±1.48	1	HD 136482
		-7.03±1.47	2	HD 136482, HD 137015
tet CrB	0	-17.61±1.17	–	–
HD 138813	0	-27.51±2.32	–	–
		-16.08±2.31	–	–

Continued on next page

Table E.5 – continued from previous page

Object of science	N nearby stars	RV feature [km.s^{-1}]	N matches	Matching stars within our sample
HD 138923	1	-29.80±2.31	1	HD 141327
		-22.94±2.30	1	HD 141327
		-13.80±2.31	1	HD 141327
HD 138965	0	-18.37±2.29	–	–
		-11.51±2.29	–	–
HD 140840	3	-22.94±2.30	2	HD 141327, HD 142446
		-13.80±2.30	2	HD 141327, HD 142446
		-4.65±2.30	2	HD 141327, HD 142446
HD 141011	1	-21.78±2.61	0	–
HD 142446	3	-23.08±1.52	1	HD 140840
		-12.16±1.48	1	HD 140840
HD 144587	0	-28.77±2.29	–	–
		-20.57±2.30	–	–
		-7.83±2.32	–	–
HD 145880	1	-19.40±2.39	0	–
HD 145689	0	-11.51±2.31	–	–
HD 146606	1	-27.51±2.31	0	–
		-20.65±2.29	0	–
HD 146897	4	-29.30±2.33	3	HD 145554, HD 145631, HD 145964
		-8.51±2.30	3	HD 145554, HD 145631, HD 145964
HD 148657	0	-22.24±1.47	–	–
		-1.60±1.47	–	–
HD 151109	0	-25.23±2.30	–	–
		-16.08±2.32	–	–
		-2.36±2.32	–	–
HD 153053	0	-24.59±0.79	–	–

Continued on next page

Table E.5 – continued from previous page

Object of science	N nearby stars	RV feature [km.s^{-1}]	N matches	Matching stars within our sample
		-14.17±0.77	–	–
78 Her	0	-17.60±1.51	–	–
HD 159082	0	-23.35±2.33	–	–
HD 1591	0	-29.32±0.79	–	–
gam Oph	0	-30.67±1.08	–	–
zet CrA	0	-25.23±2.32	–	–
rho Tel	0	-22.75±0.79	–	–
alf CrA	0	-23.50±1.12	–	–
eta Tel	1	-22.94±2.30	1	HD 181327
HD181327	1	-22.94±2.29	1	eta Tel
5 Vul	0	-29.80±2.30	–	–
		-20.65±2.30	–	–
rho Aql	0	-15.32±0.78	–	–
HD 192758	1	-20.51±1.50	0	–
phi01 Pav	0	-18.47±1.53	–	–
3 Peg	0	-14.55±1.13	–	–
		-8.95±1.16	–	–
del Scl	0	-2.36±2.30	–	–
		6.78±2.30	–	–

E.6 Summary and final results

Table E.6: Summary of all the analysis performed and conclusions for the origin of the features. This Table shows the science object, its radial velocity (when available), the radial velocity of each absorption feature, whether the radial velocity of the feature matches with: the radial velocity of the star, a known cloud in the line of sight of the star, a feature in a reference star found in the ESO archive, a feature in another star of our own sample. Finally, a verdict on the most likely origin of the feature. A match is indicated with a ✓, a non match with an ✗, and "–" when no information is available.

Object of science	RV star [km.s^{-1}]	RV feature [km.s^{-1}]	Match RV star	Match Cloud	Match reference	Match within sample	Origin
HD 225200	18.4	-0.08	✗	✓	–	–	ISM
lam01 Phe	-2.0	1.76	✓	✓	–	–	ISM
		6.73	✗	✗	–	–	ISM
HD 3670	8.92	2.38	✗	✓	–	–	ISM
		19.55	✗	✓	–	–	ISM
HD 10472	12.41	4.65	✓	✓	–	–	ISM
gam Tri	9.9	16.31	✗	✓	–	✗	ISM
HD 287850	–	4.54	–	✗	–	✓	ISM
		13.05	–	✗	–	✓	ISM
		20.96	–	✓	–	✓	ISM
		29.66	–	✓	–	✓	ISM
HD 287854	–	14.47	–	✓	–	✓	ISM
		23.42	–	✓	–	✓	ISM
HD 35625	–	10.32	–	✗	✓	✓	ISM
		18.91	–	✓	✓	✓	ISM
HD 46190	–	19.76	–	✓	–	–	ISM
HD 50571	26.69	17.11	✗	✓	–	–	ISM
bet CMi	22.0	19.82	✓	✓	–	–	ISM
HD 60995	29.0	22.33	✓	✓	–	✓	ISM
		31.31	✓	✗	–	✓	ISM
30 Mon	10.0	15.17	✗	✓	–	–	ISM
HD 71722	30.2	4.50	✗	✓	–	✓	ISM

Continued on next page

Table E.6 – continued from previous page

Object of science	RV star [km.s^{-1}]	RV feature [km.s^{-1}]	Match RV star	Match Cloud	Match reference	Match within sample	Origin
		13.64	✗	✓	–	✓	ISM
HD 74374	16.51	11.79	✓	✓	–	✓	ISM
		18.27	✓	✓	–	✓	ISM
HD 79108	22.6	9.07	✗	✓	–	✗	ISM
HD 88215	23.6	18.52	✗	✓	–	–	ISM
HD 93738	4.0	7.01	✓	✗	–	✓	ISM
		16.21	✗	✗	–	✓	ISM
HD 98363	9.6	3.89	✓	✗	✓	–	ISM
		10.05	✓	✗	✓	–	ISM
		16.37	✗	✗	✓	–	ISM
HD 101088	19.7	-4.65	✗	✓	✓	✓	ISM
		6.78	✗	✗	✓	✓	ISM
bet Leo	-0.2	2.21	✓	✓	✗	–	ISM
		13.64	✗	✗	✗	–	ISM
HD 103234	13.36	0.59	✗	✗	✓	✓	ISM
		10.73	✓	✗	✓	✓	ISM
HD 103266	-7.5	-9.11	✓	✗	✓	–	ISM
		3.92	✗	✗	✓	–	ISM
HD 103703	16.01	-9.20	✗	✓	✓	✓	ISM
		-1.75	✗	✗	✓	✓	ISM
		4.81	✗	✗	✓	✓	ISM
HD 104231	13.51	1.40	✗	✓	✓	✓	ISM
HD 104600	7.6	5.96	✓	✗	✗	✓	ISM
HD 105613	7.4	-7.65	✗	✓	✓	✓	ISM
		3.54	✓	✗	✓	✓	ISM
HD 105857	7.2	-9.80	✗	✓	✓	✓	ISM

Continued on next page

Table E.6 – continued from previous page

Object of science	RV star [km.s^{-1}]	RV feature [km.s^{-1}]	Match RV star	Match Cloud	Match reference	Match within sample	Origin
		-0.60	✗	✗	✓	✓	ISM
		6.74	✓	✗	✓	✓	ISM
HD 105912	0.40	-2.17	✓	✓	–	–	ISM
HD 106797	21.0	-3.53	✗	✓	✓	✓	ISM
		4.31	✗	✗	✓	✓	ISM
		10.39	✗	✗	✓	✓	ISM
HD 107301	-8.3	-5.52	✓	✓	✓	✓	ISM
		1.71	✗	✗	✓	✓	ISM
		6.89	✗	✗	✓	✓	ISM
HD 107649	6.1	-20.79	✗	✗	✓	–	ISM
		-3.21	✓	✓	✓	–	ISM
		3.38	✓	✗	✓	–	ISM
HD 107947	7.9	0.74	✗	✗	✓	–	ISM
		8.62	✓	✗	✓	–	ISM
HD 108904	12.45	-6.47	✗	✗	–	✓	ISM
		-0.24	✗	✗	–	✓	ISM
		6.93	✗	✗	–	✓	ISM
eta Crv	0.69	-9.43	✗	✗	–	–	ISM
		-1.12	✓	✓	–	–	ISM
		34.43	✗	✗	–	–	ISM
f Vir	-6.0	-6.94	✓	✓	–	–	ISM
V MO Hya	-18.1	-9.10	✓	✓	–	–	ISM
		-1.00	✗	✓	–	–	ISM
HD 112383	6.6	-8.52	✗	✓	✓	✗	ISM
HD 113457	15.0	-9.59	✗	✓	–	–	ISM
		2.50	✗	✗	–	–	ISM

Continued on next page

Table E.6 – continued from previous page

Object of science	RV star [km.s^{-1}]	RV feature [km.s^{-1}]	Match RV star	Match Cloud	Match reference	Match within sample	Origin
HD 113556	12.75	-14.15	✗	✓	–	✗	ISM
		-5.81	✗	✗	–	✗	ISM
		2.42	✗	✗	–	✗	ISM
HD 113902	22.0	-13.64	✗	✓	✓	–	ISM
		-3.17	✗	✗	✓	–	ISM
iot Cen	0.1	-18.37	✗	✓	–	–	ISM
HD 117484	2.0	-8.06	✗	✗	–	✓	ISM
		6.94	✓	✗	–	✓	ISM
HD 117665	1.5	-8.65	✗	✗	✓	✓	ISM
		1.97	✓	✗	✓	✓	ISM
HD 118379	6.1	-17.84	✗	✓	✓	–	ISM
		-2.66	✓	✗	✓	–	ISM
HD 118588	1.2	-8.34	✗	✗	✓	✓	ISM
HD 122705	6.6	-12.32	✗	✗	✓	✗	ISM
		-0.98	✗	✗	✓	✗	ISM
HD 124619	6.9	-10.37	✗	✗	✓	–	ISM
		-3.17	✗	✗	✓	–	ISM
HD 127750	4.4	-20.65	✗	✓	–	✗	ISM
		-13.79	✗	✗	–	✗	ISM
		-4.65	✗	✗	–	✗	ISM
HD 128207	2.0	-22.89	✗	✓	–	✓	ISM
		-12.19	✗	✓	–	✓	ISM
		-4.39	✗	✗	–	✓	ISM
HD 131835	0.5	-29.80	✗	✓	–	✓	ISM
		-16.08	✗	✓	–	✓	ISM
HD 132238	15.0	-27.30	✗	✗	–	✓	ISM

Continued on next page

Table E.6 – continued from previous page

Object of science	RV star [km.s^{-1}]	RV feature [km.s^{-1}]	Match RV star	Match Cloud	Match reference	Match within sample	Origin
		-21.09	✗	✓	–	✓	ISM
		-15.92	✗	✓	–	✓	ISM
		-11.78	✗	✗	–	✓	ISM
HD 134888	2.95	-25.16	✗	✗	✓	–	ISM
		-15.13	✗	✗	✓	–	ISM
HD 135454	1.4	-22.94	✗	✓	–	–	ISM
HD 136246	-2.7	-26.28	✗	✓	–	–	ISM
		-17.83	✗	✓	–	–	ISM
HD 136482	-0.2	-27.99	✗	✓	✓	✗	ISM
		-19.20	✗	✓	✓	✓	ISM
		-8.95	✗	✗	✓	✓	ISM
HD 137015	3.2	-7.37	✗	✗	–	✓	ISM
HD 137119	-0.7	-14.55	✗	✗	✓	✓	ISM
		-7.03	✗	✗	✓	✓	ISM
tet CrB	-25.7	-17.61	✗	✓	–	–	ISM
HD 138813	-2.54	-27.51	✗	✓	–	–	ISM
		-16.08	✗	✓	–	–	ISM
HD 138923	-3.6	-29.80	✗	✓	✓	✓	ISM
		-22.94	✗	✓	✓	✓	ISM
		-13.80	✗	✗	✓	✓	ISM
HD 138965	-2.0	-18.37	✗	✓	–	–	ISM
		-11.51	✗	✗	–	–	ISM
HD 140840	–	-22.94	–	✓	–	✓	ISM
		-13.80	✗	✗	–	✓	ISM
		-4.65	✓	✗	–	✓	ISM
HD 141011	0.2	-21.78	✗	✓	–	✗	ISM

Continued on next page

Table E.6 – continued from previous page

Object of science	RV star [km.s^{-1}]	RV feature [km.s^{-1}]	Match RV star	Match Cloud	Match reference	Match within sample	Origin
HD 142446	-1.9	-23.08	✗	✓	✓	✓	ISM
		-12.16	✗	✗	✓	✓	ISM
HD 144587	0.0	-28.77	✗	✓	✓	–	ISM
		-20.57	✗	✗	✓	–	ISM
		-7.83	✓	✗	✓	–	ISM
HD 145880	-1.8	-19.40	✗	✓	✓	✗	ISM
HD 145689	-9.0	-11.51	✓	✓	–	–	ISM
HD 146606	-3.43	-27.51	✗	✓	–	✗	ISM
		-20.65	✗	✗	–	✗	ISM
HD 146897	-1.6	-29.30	✗	✓	✓	✓	ISM
		-8.51	✗	✗	✓	✓	ISM
HD 148657	-2.7	-22.24	✗	✗	–	–	ISM
		-1.60	✓	✗	✓	–	ISM
HD 151109	-2.9	-25.23	✗	✓	✓	–	ISM
		-16.08	✗	✗	✓	–	ISM
		-2.36	✓	✗	✓	–	ISM
HD 153053	-20.2	-24.59	✓	✓	–	–	ISM
		-14.17	✗	✗	–	–	ISM
78 Her	-25.7	-17.60	✓	✓	–	–	ISM
HD 159082	-11.8	-23.35	✗	✓	–	–	ISM
HD 1591	-26.0	-29.32	✓	✓	–	–	ISM
gam Oph	-7.6	-30.67	✗	✓	–	–	ISM
zet CrA	-13.0	-25.23	✗	✓	✗	–	ISM
rho Tel	0.3	-22.75	✗	✗	–	–	ISM
alf CrA	-18.4	-23.50	✓	✓	–	–	ISM
eta Tel	13.0	-22.94	✗	✗	–	✓	ISM

Continued on next page

Table E.6 – continued from previous page

Object of science	RV star [km.s^{-1}]	RV feature [km.s^{-1}]	Match RV star	Match Cloud	Match reference	Match within sample	Origin
HD 181327	-0.25	-22.94	✗	✗	–	✓	ISM
5 Vul	-21.2	-29.80	✗	✓	–	–	ISM
		-20.65	✓	✓	–	–	ISM
rho Aql	-23.0	-15.32	✗	✓	–	–	ISM
HD 192758	-14.36	-20.51	✓	✓	–	✗	ISM
phi01 Pav	-20.0	-18.47	✓	✓	–	–	ISM
3 Peg	3.0	-14.55	✗	✗	–	–	ISM
		-8.95	✗	✗	–	–	ISM